Fourier transform holography for magnetic imaging

Submitted by

Thomas Andrew Duckworth

to the University of Exeter as a thesis for the degree of Doctor of Philosophy in Physics, August 2013.

I certify that all material in this thesis which is not my own work has been identified and that no material is included for which a degree has previously been conferred upon me.

. . . . . .

Thomas Andrew Duckworth

Abstract

State-of-the art Fourier transform holography (FTH) techniques use x-ray magnetic circular dichroism (XMCD) as a contrast mechanism for element-specific imaging of magnetic domains. With the soft x-ray Nanoscience beamline at Diamond Light Source in the UK, and the Dragon beamline at the European Synchrotron Radiation Facility (ESRF) in France, the possibility of new methods to study nanostructured magnetic systems has been demonstrated.

The ability to record images without the use of lenses, in varying magnetic fields and with high spatial resolution down to 30 nm has been used to study in-plane magnetism of 50 nm thin permalloy (NiFe alloy) nanoelements. The holographic technique used extended reference objects rather than conventional pinhole references, which allowed a high flexibility on the direction of magnetisation that is probed.

The element specific nature of the imaging, with the additional choice in the directions of magnetisation that are probed has been used to study dipolar interactions in a hard/Ta/soft $[Co/Pt]_{30}$/Ta/Py multi-layered system. Images of the out-of-plane magnetised domains of $[Co/Pt]_{30}$ were found to bare strong spatial resemblance to the in-plane domains of the permalloy. The domain structure is thought to be magnetostatically imprinted into permalloy during the growth stage of the film, where stray fields generated by the adjacent Co/Pt multilayer influence the formation of domains in the permalloy. Strong resemblance between the two layers could be found at remanence within a pristine sample, however the similarities disappear after the sample was exposed to a saturating magnetic field. This disagreed with micromagnetic simulations performed in The Object Oriented

MicroMagnetic Framework (OOMMF) program [1], and an explanation for the observations has been sought in the growth process of the multi-layered film, with conditions that are difficult to recreate in the model.

Optical holography has been used for preliminary insight into implementing a method of FTH in a reflective geometry at soft x-rays wavelength. With scattering chambers at BESSY II in Germany and at the Stanford Synchrotron Radiation Lightsource (SSRL) in California the possibility of reducing scattered noise in a hologram recorded in a reflective geometry has been investigated. Studies into specular and diffuse reflections have been performed optically however the use of extended references alone may alleviate the current problem at x-ray wavelengths which lie in the weak signal given by a reflective point-like reference source.

Acknowledgements

I would like to thank my supervisor Feodor Ogrin for his patience, guidance and support throughout the course of my PhD, and for giving me the opportunity to study under him. My thanks goes out to Gerrit van der Laan who has also been a fantastic help throughout.

I thank the support staff at Diamond, ESRF, BESSY and Stanford synchrotron for all their help during our experiments at the facilities, with special thanks to the beamline scientists Sarnjeet Dhesi, Stuart Cavill, Flora Yakhou-Harris, Radu Abrudan and Andreas Scherz, without whom, the research would not have been possible.

I thank Thomas Moore for providing the interesting samples that have been studied during my PhD and have appreciated all his help with our experiments.

A special thanks goes to Guillaume Beutier and Sean Langdridge for teaching me so much during the first 2 years as a PhD student. Their dedication to the project and support during experiments was vital to the success we had.

My thanks to Paul Keatley and Christy Kinane who have helped a lot with characterising samples at Exeter and at ISIS, and for providing me with a wealth of knowledge in OOMMF modeling.

Thanks to my mentor Peter Petrov who has given his time to discuss the progress of my PhD and for sparking many interesting discussions on application of synchrotron science during this time.

My thanks to the mechanical workshop team at Exeter, especially Russell Edge, Nicholas Cole and Matthew Wears for all their contributions to the research project.

I thank Alasdair Murray for his help proof reading this thesis. He has a far better

grasp of grammar and spelling than I could ever dream of.

A final thanks goes to my friends and colleagues at Exeter, Max Marcham, Toby Davidson, Eygeny Stirokstin, Russell Edge and Paul Keatley who have made the whole research experience more enjoyable. Thanks guys.

Glossary of Acronyms

AFM	Antiferromagnetic
BESSY	Berlin Electron Storage Ring Society for Synchrotron Radiation
CCD	Charge Coupled Device
CDI	Coherent Diffraction Imaging
CXDI	Coherent X-ray Diffraction Imaging
DLS	DIAMOND Light Source
EBL	Electron Beam Lithography
ESRF	European Synchrotron Radiation Facility
FFT	Fast Fourier Transform
FIB	Focused Ion Beam
FM	Ferromagnetic
FOV	Field of View
FT	Fourier Transform
FTH	Fourier Transform Holography
GMR	Giant Magnetoresistance
HERALDO	Holography with Extended Reference by Autocorrelation Linear Differential Operator
IFT	Inverse Fourier Transform
IPA	Isopropanol
LEEM	Low Energy Electron Microscopy
MCA	Magneto Crystalline Anisotropy
MCD	Magnetic Circular Dichroism

MFM	Magnetic Fource Microscope
ML	Multilayer
MOKE	Magneto-optic Kerr Effect
MTJ	Magnetic Tunnel Junction
OOMMF	The Object Oriented MicroMagnetic Framework
PEEM	Photoemission Electron Microscope
PMA	Perpendicular Magnetic Anisotropy
PMMA	Poly(methyl methacrylate)
SEM	Scanning Electron Microscopy
SEMPA	Scanning Electron Microscopy with Polarsation Analysis
SSRL	Stanford Synchrotron Radiation Lightsource
STM	Scanning Tunneling Microscope
STO	Spin Torque Oscillator
STT	Spin Transfer Torque
STXM	Scanning Transmission X-ray Microscope
SXRMS	Soft X-ray Resonant Magnetic Scattering
TEM	Transmission Electron Microscope
TMR	Tunneling magnetoresistance
TXM	Transmission X-ray Microscope
XMCD	X-ray Magnetic Circular Dichroism
XPEEM	X-ray Photo-Emission Electron Microscope

Publications

Magnetic imaging by x-ray holography using extended references

Duckworth T A, Ogrin F, Dhesi S S, Langridge S, Whiteside A, Moore T, Beutier G and van der Laan G, *Magnetic imaging by x-ray holography using extended references*, Optics Express, **19**, Issue 17, pp. 16223-16228 (2011)

Holographic imaging of magnetic nanostructures using extended references

Duckworth T A, Ogrin F, Dhesi S S, Langridge S, Whiteside A, Moore T, Beutier G and van der Laan G, *Holographic imaging of magnetic nanostructures using extended references*, Diamond Light Source Annual Review 2011/12

Holographic imaging of interlayer coupling in Co/Pt/NiFe

Duckworth T A, Ogrin F, Dhesi S S, Langridge S, Whiteside A, Moore T, Beutier G and van der Laan G *Holographic imaging of interlayer coupling in Co/Pt/NiFe*, New Journal of Physics, **15**, Issue 2, 023045 (2013)

Contents

List of Figures

Chapter 1

Introduction

Magnetic domains are the regions that form the microstructure of magnetic materials. Understanding the properties and behaviour of the domains is therefor crucial for designing applications for magnetic materials. Interest in domain analysis has grown in recent years due to the miniaturisation of next generation devices and, naturally, images of magnetic domains form an extensive role in exploring the fascinating microscopic and nanoscopic world. The aim of this research was to add merit and insight to the field of nanomagnetism by developing new imaging techniques for studying magnetic systems.

In an optical instrument, an objective lens ensures that phase information is retained when waves are refracted. A common limitation in many optical systems comes down to imperfections in the optical elements. This is why a large community of scientists work on alternative imaging methods and instruments that do not rely on image forming lenses, with the aim of improving the spatial resolution of images and ultimately achieve resolutions that are only limited by the wavelength of the light that forms them.

State-of-the-art Fresnel zone plates are used as the objective lenses for focusing soft x-rays in highly sophisticated full-field transmission x-ray microscopy (TXM) systems and has proved to be hugely successful for imaging magnetic structure, with spatial resolutions achieved down to 20 nm [2]. Dynamic magnetic processes have also been studied with TXM, where spatial resolutions of 25 nm have been

achieved with sub 100 ps temporal resolutions [3].

Photoemission electron microscopy (PEEM) is another leading instrument used for imaging surface magnetisation with high temporal resolution and spatial resolution down to 20 nm [4] which uses an objective lens for focusing secondary electrons released from the surface of a sample.

The developments of instruments that do not require objective lenses is an active field of research and such techniques provide highly desirable tools for studying the nanoscopic world. Coherent diffraction imaging (CDI) is a general term for lensless techniques where the objective lens used in traditional microscopes is replaced by a mathematical algorithm to convert a reciprocal space coherent diffraction pattern into a real space image. Such an inversion is however challenging because a coherent diffraction pattern only yields the information about the amplitude of the diffracted light. The all important phase information has to be recovered. The research undertaken in this thesis looks at the development of one particular lensless technique called Fourier transform holography.

In 1948 Denis Gabor came up with a brilliant solution to recover phase information by encoding it in the amplitude of a recorded interference pattern [5]. Gabour used a reference beam to form an interference pattern with a wave scattered by a subject, and a complex fringe pattern stored the phase differences as a difference in the measured intensity. This is the concept of holography.

When Gabor first introduced holography, his intentions were to improve upon the resolving power of electron microscopes [6]. Today, however, it is widely used in the x-ray regime at third generation synchrotron radiation sources all over the world to image the nanoscopic structure of materials. Images of magnetic materials using holography were not published until early this millennium [7] but looking back just over half a century, it was in 1952 that El-sum and Kirkpatrick presented the first successful reconstruction from x-ray holograms [8]. Gabor had overlooked this option believing that it would be much easier to use a coherent electron source than to generate a suitably coherent intense source of x-rays. Whilst El-sum and Kirkpatrick were able to generate visible images of thin wires, all other experiments

in the 1950s using x-rays tended to fail because diffraction patterns with a suitable number of interference fringes were extremely difficult to reproduce as most x-ray sources at the time lacked adequate temporal coherence.

During the early 1950s papers were published by many authors using Gabor's in-line projection holographic method [5] but little progress was made in solving the 'twin image problem' (which resulted from the in-line geometry). An off-axis reference was required to alleviate this problem but a source with sufficient coherence was not available until much later [9].

A defining point in the history of holography came with the invention of the optical laser and its ability to produce spatially coherent light. This enthused scientists and research interest using holographic methods grew once again. In 1963 Emmett N. Leith and Juris Upatnieks produced the first successful laser holograms that exploited the spatial coherence of the laser to produce a coherent off-axis reference beam [10]. This result demonstrated the first reconstruction with a solution to Gabours 'twin image problem'.

In recent years, holography has been used by the magnetic community to image the nanoscopic magnetic domain structure in thin magnetic films which exhibit perpendicular magnetic anisotropy (PMA) [7, 11, 12, 13, 14, 15]. Other studies include magnetic coupling between different magnetic layers in all PMA stacks [16, 17]. Its application to image dynamic behaviour, stroboscopically, has also been explored in detail [18, 19].

Most recently the use of the technique for single shot magnetic imaging has been investigated [20, 21, 22] with bright 4th generation x-ray sources. This shows promise for exiting new discoveries in the magnetic community with the contribution of sequential snapshot imaging of samples to generate a movie of excited state dynamics at atomic length scales and femtosecond time scales.

Owing to limitations associated with the experimental geometries of magnetic imaging with holography, very little work has been reported where holography has been used to image magnetic specimen where the direction of magnetisation lies in the plane of the sample [23]. Most of the experiments on magnetic materials

reported so far have focused on systems with out-of-plane magnetisation. This thesis is devoted to investigate two holography experimental setups that will extend the technique's application for simultaneous imaging of in-plane and out-of-plane magnetic components. The two geometries are:

- Transmission holography at off-normal incidence
- Reflection holography

The main objective of this thesis is to use holography to investigate and to further understand magnetisation in magnetic nanostructures with in-plane and out-of-plane magnetic components, which is important from the fundamental point of view and is crucial for their technological applications.

1.1 Review of Magnetic Imaging and Lensless Based Techniques

The ability to control thin film growth has led to enormous interest in research on magnetism and magnetic materials over the past forty years. Understanding the static and dynamic magnetisation in magnetic nanostructures such as magnetic thin films, isolated and arrays of magnetic dots, spin valves and magnetic tunnel junctions have all been of particular importance in the last 15 years. The magnetism in confined nanostructures, as review by Bader [24] in 2002, discussed their importance in the context of theoretical and experimental studies in addition to emerging applications such as magnetic data storage devices (for example, magnetic random-access memory) and sensor technologies (for example, giant-magnetoresistance and magnetic-tunnel-junction reading heads).

In the 1980s the field of spintronics emerged which explores the intrinsic spin of the electrons and the associated magnetic moments as well as their electronic charge. One of the questions this field of research is answering is,
How does the magnetisation of a material responds to a sudden change of the external magnetic field or with the addition of applied electric or spin currents?

To answer such a question a range of powerful tools for studying the magnetic behaviour of nanostructures have been developed over the years. The techniques that involve directly imaging the magnetic structure of a material such as Kerr microscopy, x-ray microscopy, transmission electron microscopy and mechanical scanning techniques are all critically review in Section 2 of this thesis, and the reader should skip ahead to this section for further details and comparisons of the various approaches for magnetic imaging techniques. In this section, we review the motivations for developing magnetic imaging tools and attempt to provide a snapshot of where the field of lensless magnetic imaging has been, with an eye to the more speculative issue of where it will go to next.

In the early 1970s, the first magnetic nanostructures were introduced. They included magnetic bubbles for bubble-domain memory devices that were developed based on perpendicular domains in yttrium iron garnet (YIG) films [25, 26], however, they could not compete with the other memory devices available at the time [27]. In 1988, however, the giant magnetoresistance (GMR) effect was independently discovered by Fert and Gruüberg in antiferromagnetically coupled Fe/Cr/Fe trilayers. In a device with successive ferromagnetic layers, because of the GMR effect, the resistance in the device will dramatically reduce if the magnetisation in the different layers is aligned in the same direction. This effect is of great importance in today's modern magnetic devices along with a related effect known as Tunneling magnetoresistance (TMR).

Tunneling magnetoresistance (TMR) was an effect first described in 1975 by Julliere [28] and was later independently established by Moodera *et al.* [29] and Miyazaki *et al.* [30]. TMR is a spin-dependent tunneling effect of electrons. The electrons can tunnel across an insulating barrier between two ferromagnetic electrodes and the resistance will depend on the relative orientation of the two magnetic layers. TMR is the mechanism behind magnetic tunnel junctions (MTJs) which are used in modern devices (for example, read-heads and MRAM).

Applied magnetic fields can be used to classically control magnetic states, however in 1996, an alternative was suggested for controlling and manipulating mag-

netic states using the spin-transfer-torque (STT) effect from spin-polarised currents [31, 32]. In this situation the angular momentum carried by a spin-polarised current exerts a torque on the magnetic moments in the device that leads to reversal or continuous precession of the magnetisation vector. Current-induced switching of the magnetisation offers promising applications in future magnetic random access memory (for example, STT-MRAM), whilst current-induced magnetisation precession enables magnetic nanostructures to be used as a new type of nanoscale oscillators which can be tunable to high-frequencies. These are known as spin-transfer nano-oscillators (STNOs) and a review of their physics can be found in [33], and a discussion of potential applications for new technologies can be found in [34, 35, 36].

With any conventional imaging microscopy, the spatial resolution of the technique is ultimately limited by the wavelength of the radiation or the particle used. There is a good incentives to carry out experiments using smaller wavelengths than visible light, such as x-rays, for studying nanostructures because it allows an increase in spatial resolution. Using resonant absorption, one can can gain element specific contrast and use it to probe the properties of specific elements within a material. Soft x-ray resonant magnetic scattering [37, 38] has had a huge impact on the study of magnetic structure because the resonant absorptions energies to determine the magnetic structure of ferromagnets, is in the soft x-ray regime. Along side this, x-rays provide information on the nanometer length scale. Its applications include characterisation of the electronic and magnetic properties of domain systems, providing details of interface roughness between layers and layer resolved magnetic moments [39, 40, 41].

Synchrotron radiation allows us to tune the energy and polarisation of the x-ray source. If the energy of circular polarised x-rays is tuned to the resonant absorption edge of an element, x-ray magnetic circular dichroism (XMCD) [42, 43, 44, 45] can be used in SXRMS experiments for detailed analysis of magnetic structure of a sample with element specificity. Durr *et al.* [46] demonstrated this by measuring diffracted intensity in reflection geometry from the periodic stripe domains in FePd

thin films. Magnetic peaks around the central, specularly reflected X-ray beam were observation. The magnetic peaks were only observed when the energy of the x-rays was within a few electron volts of the Fe absorption edge, which confirmed their magnetic origin. The peaks indicated a domain structure with striped magnetic domains of a transverse real space period of 90 nm [46].

Other studies include the work of Chesnel *et al.* [47, 48] where periodic arrays of nanolines, coated with a Co/Pt multilayer, were studied with SXRMS. The Co/Pt exhibited perpendicular magnetic anisotropy (PMA). The magnetic satellites of the SXRMS revealed antiferromagnetic order, which is generated by the interline dipolar coupling. A study, also by Chesnel *et al.* [49], of the magnetic memory in [Co/Pd] IrMn multilayers induced by exchange bias showed that the film exhibits no memory at room temperature but when cooled <275K the system acquired a high degree of magnetic memory.

An x-ray source can be made coherent by using spatial and spectral filters at the sacrifice of photon flux. If one performs SXRMS uses coherent x-rays, magnetic speckle can be observed in a far field diffraction pattern. Speckle is random variations in the intensity of scattered coherent radiation from a random sample. This is caused by variations in the path length to the detector in the far field, which leads to interference. The speckle patterns can give information on particular magnetic structural configuration in a sample whereas if incoherent light was used, the structural information would be average over the entire structure.

Coherent SXRMS measurements therefor provide a probe for the local magnetic structure of a sample and can also be used for studying the evolution of magnetic configurations within applied fields [50].

Work by other groups who have used coherent SXRMS include, Beutier *et al.* [51, 52, 53] where magnetic anisotropy in FePd alloy thin film were quantified [53]. Pierce *et al.* [54, 55, 56] used coherent SXRMS to investigate the magnetic memory in Co/Pt multilayers as a function of induced disorder and the multilayers roughness, and Kinane *et al.* [57] investigated magnetic satellite peaks from permalloy in a [Co/Pt]Ta/Py multilayer that indicated magnetic structure in the permalloy

with a period equivalent to that of the Co/Pt multilayer.

The Development of Magnetic FTH

In 2003, Eisebitt *et al.* reported how the polarisation dependencies in SXRMS can influence coherent interference experiments such as holography. When linearly polarised light diffracts through a pinhole, the polarisation of the sample does not change, whilst resonant magnetic scattering rotates the linearly polarised beam by $\pi/2$. For these two situations (magnetic scattering and non-magnetic scattering) the radiation is scattered into orthogonal polarisation channels and as a result, cannot interfere. For application of magnetic holography if the incident radiation is linearly polarised, there is no interference between a reference wave propagating from an open reference pinhole and the magnetic scattering from the domain structure a sample, however, this is not the case for circularly polarised light. Right (or left) circular polarised x-rays scatter into the same polarisation state and can therefor interfere with a pinhole reference wave in the far field.

Magnetic holography using coherent SXRMS and magnetic dichroism with circularly polarised x-rays was the pioneering work of Eisebitt *et al.* [58, 7] with the first experiments revealing real-space images with magnetic contrast using Fourier transform holography reported in 2004 [7]. The technique exploits XMCD for magnet contrast. A charge-coupled device (CCD) camera records a far field interference pattern of a reference wave and magnetic sample for each helicity of circularly polarised x-rays. By subtracting one diffraction patterns from the other, the resulting image contains only magnetic scattering information as charge scattering cancels out. The work reported by Eisebitt *et al.* [7], used photon energies tuned to the Co L_3 absorption edge (778 eV). Resonant scattering of the Co in a Co/Pt ML revealed out-of-plane domains with perpendicular magnetic anisotropy. The spatial resolution reported in this experimental was 50 nm and prior to this, the highest spatial resolution that had been achieved with x-ray holography was 60 nm, as reported by McNulty *et al.* [59], who imaged gold particles.

Holography provides a solution to the phase problem by encoding the phase in-

formation as an amplitude measurement (in the form of interference fringes) which can be recorded on a CCD detector. Since the 1980s, iterative algorithms have been developed to recover phase information using numerical solutions. The approach combines coherent scattering and oversampling techniques to retrieve phase information and reconstruct a real space image [60, 61, 62, 63]. A common problem with phase recovery using an algorithm (aside form getting the algorithm to converge) is being able to determining whether the solution the algorithm provides is unique [60].

Iterative phase retrieval approaches have proved successful for imaging a variety of samples in recent years [62, 64, 65] and more recently, magnetic samples have been investigated [66, 21], however, without improving upon spatial resolutions that can be achieved with magnetic FTH.

The spatial resolution in conventional holography is limited by the size of the reference hole, and so a phase retrieval technique that could achieve resolutions without lens or aperture aberration would be highly desirable. The ability to image a sample without ambiguity is however a clear advance of holography and other microscopy techniques over phase retrieval.

A common iterative phase retrieval approach uses a sample support [67] in order to converge. A lower resolution image can be used to define the support and provide the algorithm with an input which is close to the real solution [68]. In a combined approach like this, holography can be used to define the lower resolution starting image [69], with the added advantage that the same experimental setup could be used to record the high-resolution diffraction pattern for phase retrieval [70, 71].

The application of Fourier transform holography for magnetic imaging have been impressive over the past decade. After the work reported by Eisebitt *et al.* [7], images of domain evolution in a Co/Pt multilayer under applied field have been demonstrated [11] alongside the switching behaviour in small arrays of nanospheres capped with Co/Pd [72] and switching fields for Co/Pd multilayer nanodots based on bit patterned media devices [73]. An array of antidots patterned into a Co/Pt

multilayer film has also been investigated [13].

An important phenomenon which is used in modern technology (for example reliable spin-valve read head [74], manufacturing magnetic recording heads [75], pinning hard layers in MTJs [74] and the development of magnetic random-access memory cells [76]) is the pinning of the magnetisation direction of a ferrromagnet (FM) by coupling it to an antiferromagnet (AFM). This is an effect referred to as exchange biasing [77].

In 2009, the magnetic properties of perpendicular exchange biased FM/AFM $[Pt/Co]_n$/IrMn systems were investigated with FTH [14]. Here the robustness of the technique against external magnetic fields was demonstrated, providing direct images of the magnetisation reversal of the perpendicular ex-change biased FM/AFM system. It was observed that the magnetic domain configuration had an asymmetric nature during the reversal, which agrees with other observation in both in-plane [78] and perpendicularly biased FM/AFM systems [79].

The quantum mechanical interaction known as exchange coupling is another important phenomenon to understand for device application. This is the parallel or antiparallel alignment of magnetisation between two closely situated magnetic layers separated by a non-magnetic spacer. FTH has been used to image magnetic reversal in perpendicular anisotropy antiferromagnetically coupled ferromagnetic multilayers [17]. It has also been shown that domain replication induced by temperature can occur in dipolar coupled ferromagnetic layers separated by a thick layer of Pd [16].

Magnetic FTH has been demonstrated in scanning mode where the holographic mask that is typically integrated with the sample, was separated allowing for the sample to be scanned across the mask [12]. This was used to investigate the magnetic domain structure of an exchange-coupled Co/Pt multilayer film, over a larger area than had been achieved before with FTH due to the restrictions in the size of the field of view.

In recent years a number of dynamic studies have relied on femtosecond x-ray pulses, and therefore have to rely on producing a signal having only collected a

limited number of photons. A large amount of work to development FTH for use with next generation x-rays sources is underway [80]. It has been shown that using multiple reference pinholes in an FTH setup can enhanced the signal strength of the reference without compromising the spatial resolution [81] and it was also demonstrated that a large array of holes can be used as a reference when combined with a Hadamard convolution [82]. These development has been toward single shot imaging with the desire for short intense pulses of x-rays from Free electron laser sources [83, 84, 85, 86, 87].

The work by Pfau *et al.* [88] reports on a new experimental approach where linearly polarised light was successfully used to image magnetisation. This was achieved by using an elliptical polarisor. It is important for further developments of magnetic FTH with next generation x-ray sources because circular polarisation is only available at certain resonant energies [88, 89]. In 2012, Sacchi *et al.* [20] reported the use of linearly polarised light to achieve magnetic contrast by passing the reference wave through a magnetic film such that the scattered reverence wave experienced the same rotation in polarisation as the light that scattered through the magnetic sample. This allowed for interference at the detector because the reference and object waves were scattered into the same polarisation channels [58].

The Development of HERALDO Imaging

In general, a limitation of FTH lies with the low contrast in the reconstruction, which can only be improved by increasing the reference signal. Typically by increasing the size of the reference pinhole one can improve the image contrast but at the cost of reducing the resolution of the image. Multiple reference sources that form several images that can be combined to improve the brightness [90, 81] however this doesn't completely decouple the strength of the reference signal from the final resolution of the image.

In a recent development of FTH, the work of Podorov *et al.* [91, 92] and Guizar-Sicairos *et al.* [93, 94] have shown the use of extended objects as holographic references. The method developed by Podorov *et al.* [91], placed an object confined

within a rectangular support that was uniformly illumined. The far field diffraction pattern is then modified in such a way that a particular solution upon Fourier inversion is retrieved. The approach was later generalised by Guizar-Sicairos *et al.* [93] who illustrated that a number of extended objects could be used as a holographic reference providing it contained a sharp feature. The generalised approach was dubbed 'Holography with extended reference by autocorrelation linear differential operation' (HERALDO). Since its introduction HERALDO has been used for soft x-ray FTH imaging [95, 96] and has recently been applied to single shot imaging with the aim of decreasing the exposure time required to form an image due to the increased flux form the larger references [97, 85]. The HERALDO technique forms an extensively part of the work in this thesis.

1.2 Aims and Objectives of This Research

To date, very little work has been reported where holography has been used to image magnetic specimen where the direction of magnetisation lies in the plane of the sample [23]. In 2010, the in-plane magnetisation of a Co microscopic element was imaged with FTH [23] using an off-normal geometry. The spatial resolution was not explicitly commented upon, however, it was ultimately limited by the size of the reference hole, which was ∼65 nm. Here, an inclined reference hole was milled into the holographic mask and this allowed for imaging at an off-normal incidence to obtain magnetic contrast. By milling the reference holes at an angle, the sample plane could be rotated within the x-ray beam and still permit light through it. The spatial resolution of this approach was limited by the fabrication of the reference holes, which is technically challenging because it requires FIB milling of narrow holes through ∼ 800 nm thick layers of gold, with the sample plane rotated within the FIB beam. To ultimately achieve images with spatial resolutions of sub-10 nm, one would find it challenging if proceeding with FIB milling of inclined reference pinholes.

The motivations of this thesis are to develop a technique that will extend the applications of conventional FTH into a more flexible technique for simultaneous

imaging of in-plane and out-of-plane magnetic components with a high spatial resolution. In this thesis, we have investigated two holography experimental setups to achieve this goal. The two geometries are:

- Transmission holography at off-normal incidence
- Reflection holography

For transmission holography at off-normal incidence we investigate the use of extended references to allow a sample to be rotated within an x-ray beam using a method of FTH known as HERALDO [93, 91]. In using extended references for soft x-ray holography, Zhu *et al.* [95] have reported high spatial resolutions of less than 20 nm. When imaging in an off-normal geometry the resolution can be expected to match those reported by Zhu *et al.* [95]. The spatial resolution for off-normal FTH imaging using HERALDO can be expected to be higher than the resolution previously reported where inclined references holes were used [23] because of the ease with manufacturing extended reference compared to inclined pinholes.

In addition to the expected increase in resolution from previous in-plane measurements with FTH, using extended references decouples the signal of the reference wave from the resolution of the image. This is because in HERALDO the resolution of the image is not determined by the size of the holographic reference, instead, it depends on the sharpness of the reference's features. When using a narrow hole as a holographic reference, to improve the resolution one has to decrease the size of the reference hole, which in turn, decreases the signal strength of the reference beam [98].

Using HERALDO the off-normal rotation angle is flexible and can be changed during the experiment. In comparison, with inclined reference holes the angle of incidence is fixed to a pre-defined small range. The HERALDO technique is element specific, sensitivity to in-plane and out-of-plane magnetisation and can provide high spatial resolutions. Such a technique is extremely valuable to the magnetic community and can further our understanding of the magnetic properties in complex magnetic systems for technical applications.

As we have discussed above, a technique that can produce high spatial resolutions is very desirable for studying magnetic nanostructures. In addition to this, the ability to simultaneous image the in-plane and out-of-plane magnetic components allows one to understand the magnetic system to a greater extent.

In this thesis, holography with extended references (HERALDO) has been used to allow an FTH sample to be rotated within an x-ray beam and permit light through the reference. This opens up FTH for magnetic imaging sensitive to in-plane magnetic components with expected spatial resolutions of less than 20 nm which are much higher than previously reported using FTH.

The main motivation for investigating reflection holography was to provide a lensless imaging technique, complimentary to transmission holography at off-normal incidence, but also suitable for imaging magnetic materials with in-plane magnetisation. In the reflection geometry the substrate for growing magnetic samples would not be limited to Si_3N_4 membranes because the sample would not necessarily have to be x-ray transparent. A reflection technique would also be suitable for imaging systems that can only be grown as bulk crystals.

A reflection geometry for holographic imaging has been investigated in this thesis for the purpose of magnetic imaging. In this geometry, the FTH technique is sensitive to magnetic scattering from in-plane magnetic moments and would provide a new experimental geometry that has not been previously been reported on for studying magnetic specimen.

Chapter 2

Imaging Magnetic Domains

2.1 Introduction

In this chapter we outline the development of magnetic domain theory which has lead to our modern understanding of magnetic microstructure.

Section 2.2 introduces the history of Weiss domains and how the idea was remarkably developed by theory before any pictures of domains were available.

Section 2.2.1 presents the different interactions and associated energies of a ferromagnetic system. This leads to a discusses on the definitive work of Landau and Liftshitz and their quantitative solution to describe the static and dynamic properties of ferromagnetic materials.

Section 2.2.2 looks at the formation of magnetic domains in more depth. We discuss the characteristics of domain walls and show some common types of domain ground states that form in various ferromagnetic systems such as films with in-plane and perpendicular magnetic anisotropy, and sub-micron sized elements.

In the remainder of this chapter we discuss a number of scientific instruments and experimental methods for observing magnetic microstructure. A critical re-

view of magneto-optical methods (Section 2.3), transmission electron microscopy (Section 2.4), mechanical probing (Section 2.6) and x-ray techniques (Section 2.7) are presented.

Section 2.8 contains a comparison of the imaging methods reviewed in this chapter and in light of this, we discuss the importance of lensless imaging to the research field of magnetic imaging and emphasise why the HERALDO technique [93] is an important tool for new research into magnetic systems.

2.2 Background Theory of Ferromagnetism

Progress towards understanding magnetic behaviour began in 1905 when Langevin used the methods of statistical thermodynamics to develop a theory of paramagnetism [99]. Two years after, Weiss expanded on this idea and introduced the concept of a molecular field [100]. Weiss' theory was successful in determining the general shape of the temperature dependence of magnetic saturation and predicted that at any temperatures below the Curie point, the state of magnetic saturation was the thermodynamic equilibrium state. Weiss' molecular field followed the direction of the average magnetisation. This means the magnetisation vector is always fixed in magnitude, however, its direction remains arbitrary. Many researches at the time had observed that a ferromagnetic crystal exhibited zero overall magnetisation at temperatures far below the Curie point but it was Weiss who suggested that the reason for this was because magnetisation vectors vary in different parts of the crystal and to achieve a demagnetised state the vectors must cancel each other out. He proposed the idea that ferromagnetic crystals are split into small regions (domains) which are always magnetically saturated yet the direction of the molecular field in each domain was randomly orientated and resulted in zero overall magnetisation in any given direction. With the introduction of quantum mechanics came the realisation that Weiss' molecular field was infact a much simplified understanding of a more complicated quantum mechanical effect, the exchange interaction, which is the interplay between the Coulomb interaction

between electrons and the Pauli Exclusion. Pieces of the puzzle were still missing at this point in time, however, a solution came in 1935 by the pioneering work of Landau and Lifshitz who presented the first quantitative description for static properties of ferromagnetic materials. It explained that the ground state of any static magnetic system is the solution with the minimum total free energy.

2.2.1 Interactions Between Atomic Magnetic Moments

Magnetic domains in ferromagnetic materials form in order to minimise the sum of all the energy terms of the system, e.g. the exchange, the magnetostatic, the anisotropy and the Zeeman energies [101].

In the case where a magnetic film has infinite lateral dimensions and uniform magnetisation in the film plane, the magnetostatic energy would be zero. When faced with a film of finite size one has to consider surface charging, resulting in a demagnetising field. The demagnetising field causes the film to separate into domains with magnetisation vectors in different orientations such that the magnetostatic energy is reduced. The domains are separated by boundaries called magnetic domain walls. Inside the wall, the spins gradually rotate to reorientate themselves in alignment with the neigbouring domain. In this section the magnetic energy terms (exchange, magnetostatic, anisotropy and the Zeeman energies) are introduced with the conclusion that the formation of magnetic domains is the result of the system minimising its total free energy.

Energy Terms in Ferromagnetic Systems

Exchange Energy

The exchange interaction has a short range (on lengths scales of 5 to 10 nm) and favours parallel alignment of spins between neigbouring atoms. It competes against thermal effects which increase the kinetic energy of the magnetic moments, and if the temperature of the system is such that the thermal effects overcome the exchange interactions, (known as the Curie temperature), the ferromagnet becomes paramagnetic. The exchange interaction energy density, $E_{exchange}$, between two

spin vectors $\mathbf{S}_i$ and $\mathbf{S}_j$, scales with the exchange integral, J, and can be written as

$$E_{exchange} = -J_{ij}\mathbf{S_i} \cdot \mathbf{S_j}. \tag{2.1}$$

One can estimates the exchange energy in a magnetic domain wall using a model of continuous spin rotation across a one-dimensional boundary [102]. Here the total exchange energy inside the wall (E_{wall}) is

$$E_{wall} = A\left(\frac{d\theta}{dx}\right)^2 \tag{2.2}$$

where A is the exchange stiffness constant and θ is the angle of the spins with respect to the easy axis of magnetisation. The exchange energy decreases with smaller rotations between spins in neigbouring atoms and so the exchange energy tends to promote a more gentle rotation of spins across a domain wall. This ultimately leads to domain walls having a well defined width. A discussed of domain walls is presented later in Section 2.2.3.

Anisotropy Energy

Magnetocrystalline Anisotropy

Anisotropy describes the affect that directions have on the energy level. Magnetocrystalline anisotropy (MCA) was briefly mentioned above when describing the exchange energy within a domain wall, which increases as the spins rotate away form the easy axis of magnetisation. This is the magnetocrystalline anisotropy (MCA) and results from spin-orbital interactions that couple the isotropic spin moments to the crystal lattice. The magnetisation will preferentially align to a particular crystallographic axis of a material, known as the easy axis. If the bias of the magnetic moments in a material is towards one particular direction (the easy axis), the material is said to have uniaxial anisotropy. The uniaxial anisotropy energy density can be expressed as [103],

$$E^i_{uni} = K_1 \sin^2\theta_i \tag{2.3}$$

where K_1 is the primary uniaxial anisotropy constants of a material. This term is temperature dependent and attained through experiment measurements.

Cubic crystals (such as nickle and iron [103]) have a bias towards many particular directions. These material have multiple easy axes. Cubic anisotropy is another form of magnetocrystalline anisotropy and the energy density is expressed as [104],

$$E_{cub} = K_0 + K_1(m_x^2 m_y^2 + m_x^2 m_z^2 + m_y^2 m_z^2) + K_2 m_x^2 m_y^2 m_z^2 + ... \tag{2.4}$$

where K_i is the ith order anisotropy constant. Higher order terms greater than 2 aren't significant at room temperature, however become important in low temperature studies.

Uniaxial and cubic anisotropy are forms of magnetocrystalline anisotropy because their properties arise from the crystalline structure of the material. It is worth noting here that some materials, such as permalloy, are considered isotropic from a crystalline perspective (i.e. $\mathrm{K}_1 = \mathrm{K}_2 = 0$), and there is no contribution from anisotropy to the total energy.

Volume and Interface/Surface Anisotropy

Anisotropy can also be induced by breaking the symmetry of a crystal structure such as at the surface of a specimen or an interfaces [105]. When working with thin films this becomes important because of missing neigbouring atoms at the boundaries of the material. The orientation of the easy axis for many magnetic thin films lie in the plane of the film. There are highly anisotropic materials, or specifically grown systems where the easy axis of magnetisation lies out-of-plane, and these are said to exhibit perpendicular magnetic anisotropy (PMA). In such cases magnetic films with out-of-plane uniaxial anisotropy form with a surface energy density of

$$E_s = K_s \sin^2\theta, \tag{2.5}$$

where K_s is the surface anisotropy constant and θ is the angle between the z-axis and the magnetisation vector. The volume anisotropy in these thin films is not negligible and can be defined as

$$E_V = K_{u1} \sin^2\theta + K_{u2} \sin^4\theta, \tag{2.6}$$

where K_{ui} is the ith term unaxial volume anisotropy constant and θ is the angle between the magnetisation and anisotropy axis.

The total anisotropy energy density in a magnetic thin film is the sum of the volume and surface anisotropies and depends on the film thickness (d),

$$E_{uni} = E_V + \frac{E_s}{d}. \tag{2.7}$$

Magnetorestrictive and Shape Anisotropy

Magnetostriction is an another type of anisotropy (stress anisotropy) caused by the contraction and expansion of ferromagnets along the magnetisation direction [103]. Additionally there is a direction the magnetisation will prefer to lie based on the physical geometry of the sample. This is known as shape anisotropy [106].

Magnetostatic Energy

The magnetostatic energy is a magnetic dipolar interaction and relates to the demagnetising field, $\mathbf{H}_d$, generated by the ferromagnetic body itself. Each spin moment in the material can be considered as a circulating current loop. The circulating current loop generates its own magnetostatic field that can be considered equivalent to a pair of magnetic charges of opposite sign, separated in space. Although the interaction is several orders of magnitude weaker than the exchange interaction, it has a long range which makes it a crucial component for a complete understanding of a ferromagnetic system. If one considers a specimen with a single finite domain, its magnetostatic energy will be large. If magnetisation is broken up into localised regions (domains) the magnetostatic energy can be reduced, for example when the domains provide flux closure at the ends of the specimen. If the decrease in the magnetostatic energy is greater than the energy that is required to form magnetic domain walls, a static ground state with multiple domains will arise in the specimen.

If we consider a film with magnetisation, $\mathbf{M}$, which creates a stray field H_{stray} - due to surface charging, a field exists inside the film which has the same amplitude as H_{stray} but is opposite in direction to $\mathbf{M}$. This is called the demagnetising

field, H_d. For a solid of homogeneous susceptibility the demagnetising field can be characterised by the demagnetisation factors, N_d. This is a function of the shape of the object and it is common in micromagnetic studies for the shape of nanomagnets to be approximated as an ellipsoid because analytical solutions for N_d of solid ellipsoids are convenient [107, 108] compared to other such approximations [109, 110, 111]. The demagnetising field inside a material is given by,

$$\mathbf{H_d} = -\mathbf{N}(\mathbf{r}) \cdot \mathbf{M} \tag{2.8}$$

where $\mathbf{N}(r)$ is the demagnetising tensor. The associated magnetostatic energy density is then,

$$E_{dipole} = -\mu_0 \int_V \mathbf{M} \cdot \mathbf{H_d} \mathbf{dV}. \tag{2.9}$$

Zeeman Energy

The Zeeman energy describes the interaction energy of the magnetisation vector $\mathbf{M}$ with an externally applied magnetic field $\mathbf{H}_{ex}$. The Zeeman energy is

$$E_{Zeeman} = \mu_0 \int \mathbf{M} \cdot \mathbf{H_{ex}} \mathbf{dV}. \tag{2.10}$$

Total Energy

The total energy density, E_{total}, is a sum of all the contributing terms discussed in the section above. It can be expressed in the following form,

$$E_{total} = E_{exchange} + E_{anisotropy} + E_{dipole} + E_{Zeeman} \tag{2.11}$$

where $E_{anisotropy}$ includes all the anisotropy terms of the magnetic system.

The Landau-Liftshitz-Gilbert Equation

The Landau-Liftshitz-Gilbert equation (LLG) describes what happens when a single magnetic moment is subject to an external magnetic field. It was first introduced by Landau and Liftshitz in 1935 [112] and later modified by Gilbert in 1955

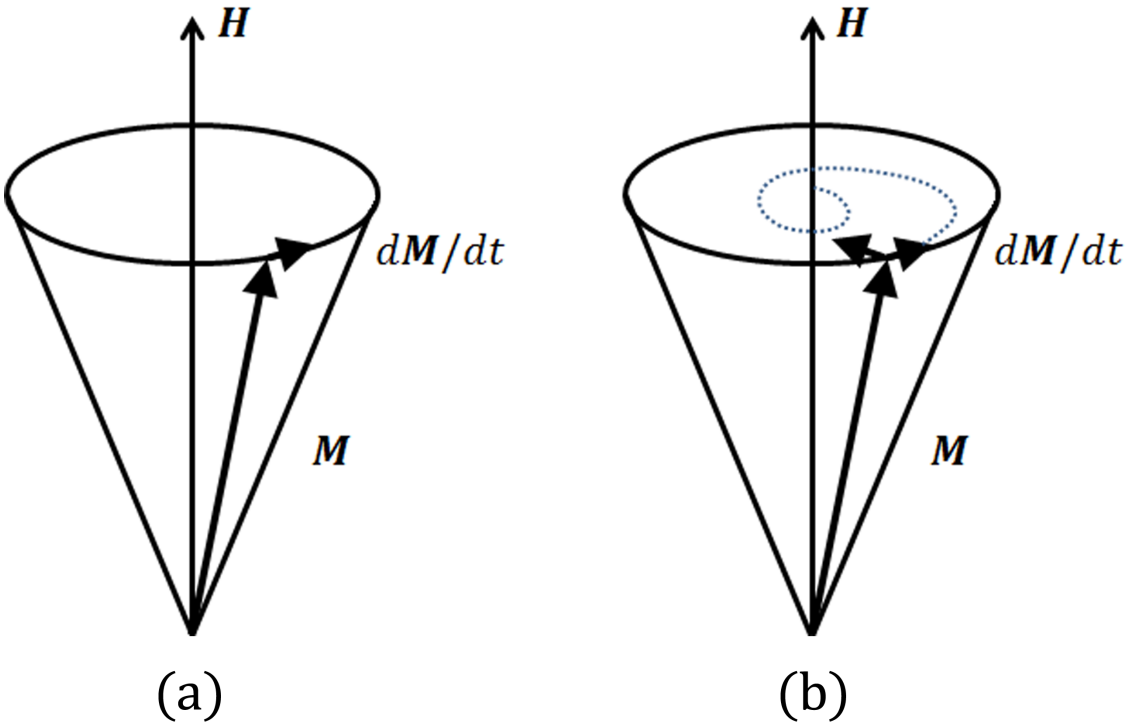

Figure 2.1: Sketch illustrating the magnetisation dynamics in a Ferromagnet (a) without damping term and (b) with damping term.

[113] who introduced a phenomenological damping term. It is used to describe dynamic magnetisation processes, and associated relaxation taking the form,

$$\frac{\mathrm{d}\mathbf{M}}{\mathrm{d}t} = -\gamma_0 \left[\mathbf{M} \times \mathbf{H}_{eff}\right] - \frac{\alpha}{M_s}\mathbf{M} \times \left[\mathbf{M} \times \mathbf{H}\right] \tag{2.12}$$

where γ_0 is the gyromagnetic ratio and α is a dimensionless phenomenological damping parameter introduced by Gilbert.

The first term in (2.12) ($-\gamma_0 \left[\mathbf{M} \times \mathbf{H}_{eff}\right]$) describes the processional motion of the magnetic moment around the direction of the field that will continue indefinitely in the absence of a damping. The second term ($-\frac{\alpha}{M_s}\mathbf{M} \times \left[\mathbf{M} \times \mathbf{H}\right]$) describes damping which causes the amplitude of the processional motion to decay, following a spiral trajectory, until the magnetisation reaches an equilibrium state where it lies along the direction of the effective field $\mathbf{H}_{eff}$. An illustration of the magnetisation dynamic with and without the damping term is shown in Figure 2.12.

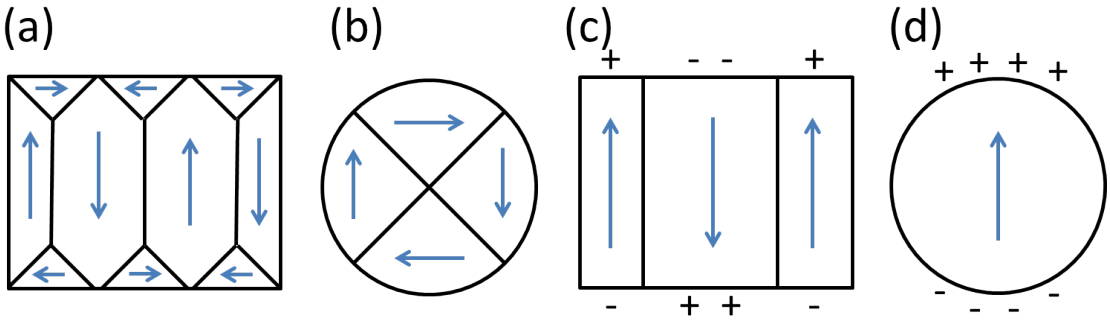

Figure 2.2: In (a) and (b) a biaxial particle with low anisotropy forms flux-closed domain patterns. In (c) and (d) an uniaxial particle with a high anisotropy forms open domain patterns.

2.2.2 Static Magnetic Domains

The minimisation of the energy terms in (2.11) leads to the formation of domains in ferromagnetic materials and was the pioneering work of Landau and Lifshitz. The domains can be thought of as the elements of the microstructure within a magnetic material where the magnetisation is aligned in parallel. Across the entire specimen the average magnetisation is reduced to zero (in zero field) because the magnetisation direction of each domain has no particular direction. If placed within a saturating magnetic field, no individual domains form in a magnetic sample and the overall magnetisation is uniform. Once the field is reduced, domains will begin to form in order to minimise the overall energy of the system. The domains are separated by boundaries called domain walls in which the magnetic moments within the boundaries rotate to align with the magnetisation of the neigbouring domain.

In large crystals with small anisotropies the assumption by Landua and Lifshitz of flux-closed domain patterns Figure 2.2 (a) and (b) was well justified. In small elements or even uniaxial crystals, Kittel calculated that large anisotropies lead to open structures [114, 115] as shown in Figure 2.2 (c) and (d). At length scales on the order of nanometers there are several common states that can occur in magnetic samples. These result as the system attempts to reduce its overall energy. Common metastable states of magnetisation are shown in Figure 2.3. A single-domain state

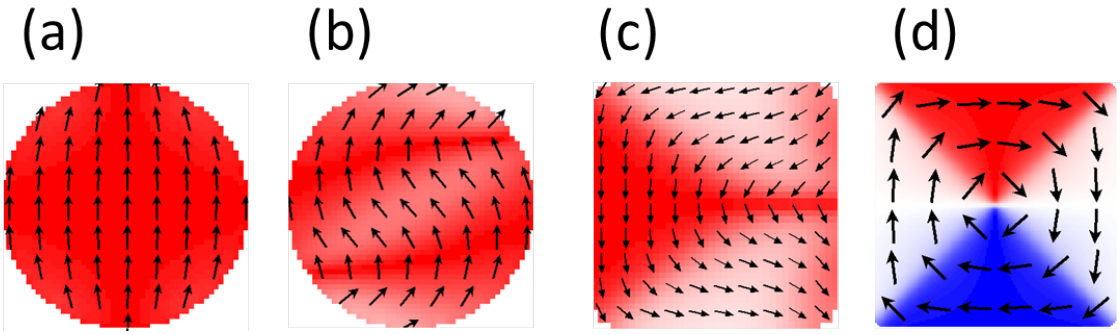

Figure 2.3: Illustrations of some common metastable states of magnetisation in microstructures. (a) Single-domain state. (b) S state. (c) C state. (d) Vortex state. The colours and arrows indicate the in-plane direction of magnetisation

which occurs when a saturating external field is applied to the material is shown in Figure 2.3 (a). In small particles, this state can occur at remanence if the exchange energy is the dominating term in the overall energy of the system. Figure 2.3 (b) and (c) are known as the S and C states respectively because the magnetisation curves in much the same way as the shape of the letters. Further examples of the S and C states can be seen in [116]. A flux-closed vortex state is shown in Figure 2.3 (d). Interesting flux closure structures also form in rectangular and circular magnetic rings [117, 118] known as "onion" states. Here, a stable bi-domain state with a head-to-head and a tail-to-tail domain wall can be observed.

2.2.3 Domain Walls

An important contribution that micromagnetics offers to the analysis of magnetic domains are the calculations of the domain wall structure. This is because experimentally, information about the domain walls is difficult to access - the properties of a domain wall can change at a specimens surface which is where most observation take place and the domain walls are also difficult to isolate from their neighbors and often they interact with each other in complex networks rather than behaving as singular elements. Both these points make theoretical calculations of the energy and structure of the walls the method of choice over determining values experimen-

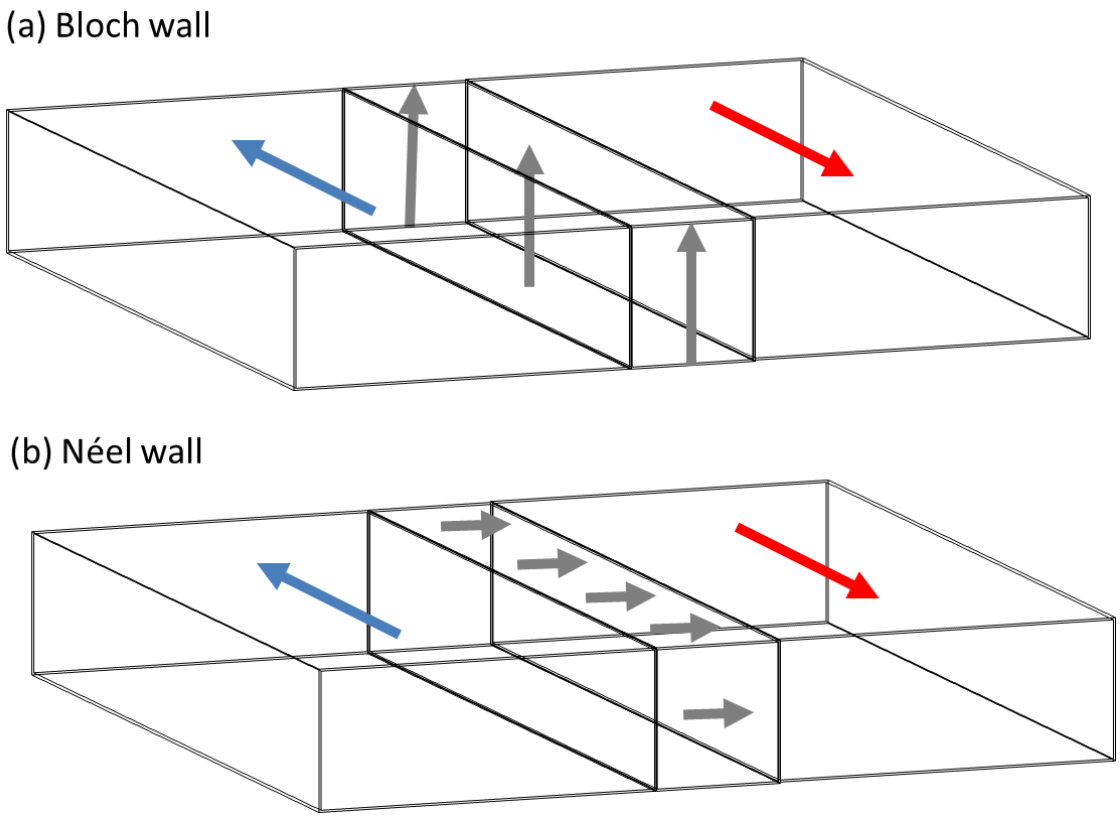

Figure 2.4: Most common types of domain walls in magnetic materials. (a) In a Bloch wall the magnetisation vector rotates through the plane of the wall. (b) In a Néel wall the magnetisation rotates in the plane of the wall.

tally. Theoretical approaches are well founded and relatively straight forward to carry out as first demonstrated by Landau and Lifshitz [101]. Here we will simply discuss the basics behind domain wall energy and structure. For additional material and an overview of the many interesting details of domain walls the reader is directed to [119, 102]. The are two types of domain wall which are most commonly found in magnetic materials. these are illustrated in Figure 2.4.

Bloch Walls

A Bloch wall is the narrow transition between neigbouring magnetic domains where the magnetisation rotates 180° through the plane of the domain wall (Figure 2.4(a)). If the spins between neigbouring domains switched abruptly, the exchange energy cost would be very high. This results in a gradual rotation of the

spins across the width of the domain wall as they reorientate their magnetic moment. This leads to domain walls of a certain width. The domain wall width is mainly determined by competition between the exchange energy and anisotropy energy. The exchange between neigbouring moments tends to increase the width of the wall because a rotation of the spins over a larger length between two neigbouring domains will cause a lower exchange energy. Whilst the wider wall may reduce the exchange energy, it results in higher anisotropy energy because inside the wall the direction of the spins are not aligned with the magnetocrystalline easy axis. The specific wall energy γ_w is the total energy per unit area of the wall. This can be expressed as an integral over the expressions for exchange energy density (2.2) and anisotropy energy density (2.3), yielding the result [102]

$$\gamma_w = 4\sqrt{AK}, \tag{2.13}$$

note here that γ_w, is per unit wall area and not per volume. The domain walls form continuous transitions between two domains and so a single definition for the domain wall width isn't apparent. The most commonly used definition was introduced by Lilley [120] and defines the Bloch wall width as,

$$\delta_B = \pi\sqrt{A/K}. \tag{2.14}$$

Typical length scales of δ_B range between 2-3 nm in magnetically hard materials and 100-1000 nm in soft materials [121].

Néel Wall

A Néel wall is the narrow transition between neigbouring magnetic domains where the magnetisation rotates within the plane of the domain wall (Figure 2.4(b)). Néel walls are very common in thin films where the exchange length is very large compared to the thickness of the film. In the case of the Néel wall, the free energy density can be approximated as,

$$\sigma_N = A\frac{\pi^2}{\delta_N} + K_u\frac{\delta_N}{2} + \left(\frac{2\mu_0 M^2}{\pi}\right)\delta_N arctan\left(\frac{t}{\delta_N}\right), \tag{2.15}$$

where δ_N is the wall thickness. In the limiting case where the film thickness (t) is small, i.e. for $t/\delta_N \leq 1$, the energy density σ_N can be expressed as,

$$\sigma_N \approx \pi t M_s^2 \tag{2.16}$$

and the wall thickness, δ_N, follows as

$$\delta_N \approx \pi \left(\frac{2A}{K}\right)^{1/2}. \tag{2.17}$$

Domain Walls in Thin Films

Magnetic films tend to be described as thin, if their thickness is comparable to the Bloch wall width. There are two basic geometries for the magnetisation in these films, (1) films with in-plane anisotropy and (2) films with perpendicular anisotropy. In-plane magnetisation lies in the plane of the film where the anisotropy may be either uniaxial or biaxial. In films with perpendicular anisotropy the direction of the magnetisation in the domains is perpendicular to the films surface. This requires a small saturation magnetisation and a large anisotropy.

Walls in Films with In-Plane Anisotropy

In 1955 Néel [122] first realised that the standard theory of Bloch walls did not hold true for thin films. He discovered that when the film thickness becomes comparable to the wall width there is a type of wall (Néel wall) that exists which has a lower energy than the Bloch wall. A Néel wall (as illustrated in Figure 2.5) will form in favor of a Bloch wall in films such as permalloy layers with a thickness of 50 nm [123].

Walls in Films with Perpendicular Anisotropy

If the preferred axis for magnetisation is out of the plane and the anisotropy is sufficiently strong then films with perpendicular anisotropy can arise. They typically have regular Bloch walls however towards the surface within the wall region the stray fields from the domains either side of the wall act on the walls moments

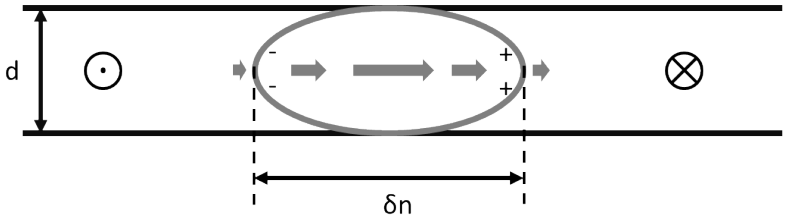

Figure 2.5: Néel's interpretation of domain walls in thin films with in-plane anisotropy. He showed that a mode with lower energy than classical Bloch wall existed when the thickness (d) of the film was comparable with the wall width.

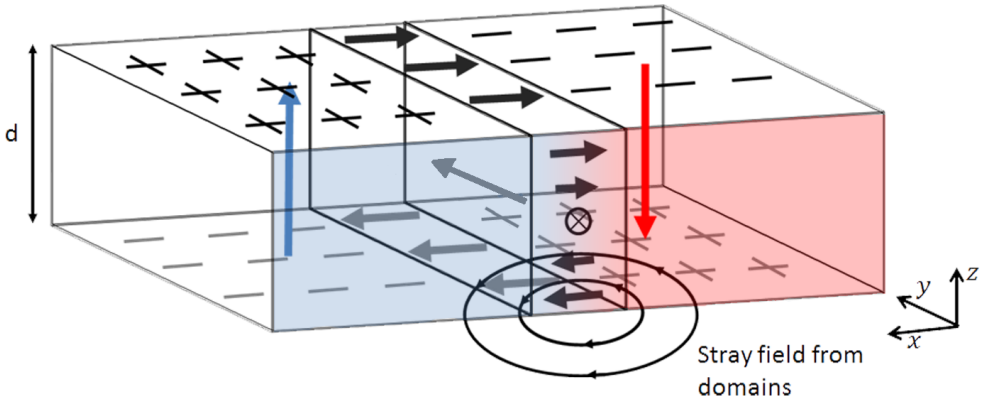

Figure 2.6: Bloch wall that form in thin films with perpendicular magnetisation. Here the domains are connected with stray fields which twists the magnetisation into a Néel wall at the surface.

and twist the magnetisation into a Néel wall [124]. An illustration of this complex situation is shown in Figure 2.6 [102].

For systems with perpendicular magnetic anisotropy, there are many different domain patterns that can form in the material with equivalent values of external applied perpendicular field. Hysteresis effects strongly influence domain generation, annihilation and their transformation which leads to some very intriguing phenomenon which is both interesting for fundamental studies and for memory devices.

In recent years, PMA has been observed in metallic multilayers composed of an alternating ferromagnetic transition metal layer and nobel metal layer, with examples such as Co/Pt, Co/Pd or Fe/Pd [125]. In many cases, the origin of

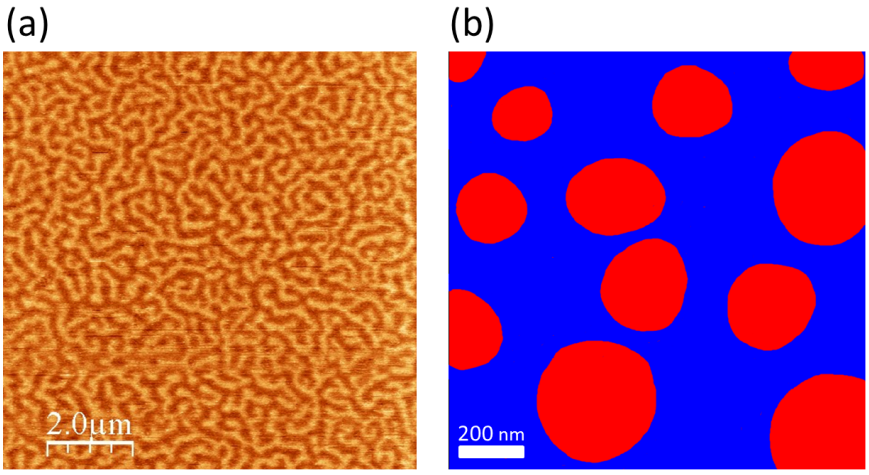

Figure 2.7: (a) Magnetic force microscopy measurement a Co/Pt multilayer thin film at remanence. (b) Illustration of magnetic bubble domains when a large perpendicular magnetic field is applied to the film. The colour in (b) represent magnetisation directions in and out of the surface plane.

PMA in thin films is not completely clear, but it is believed to be attributed to the altered hybridisation, reduced symmetry [126], and atomic mixing [127] at the interface regions. A lot of interest surrounds Co/Pt multilayers because both the large magneto-optical (MO) Kerr rotation these films exhibit [128, 129] and PMA makes them a desirable material applicable for short wavelength MO media [130]. The typical width of the Bloch walls in CoPt multilayer film is < 10 nm [131, 102] which is much less than the size of the domains themselves. Figure 2.7 (a) shows an MFM image of a $[Co/Pt]_{30}$ ML at remanence. It reveals perpendicular maze domains (also commonly referred to as worm-domains [132, 15]). When an external magnetic field is applied to a $[Co/Pt]_{30}$ ML the size of the domains expand to form "bubbles" [133, 134, 135, 136]. These are isolated cylindrical domains which have scope for application in magnetic storage devices [27].

Vortex structures

Magnetic vortex structures occur in soft ferromagnetic films and patterned elements (such as thin permalloy discs and squares) as a result of the balance between ex-

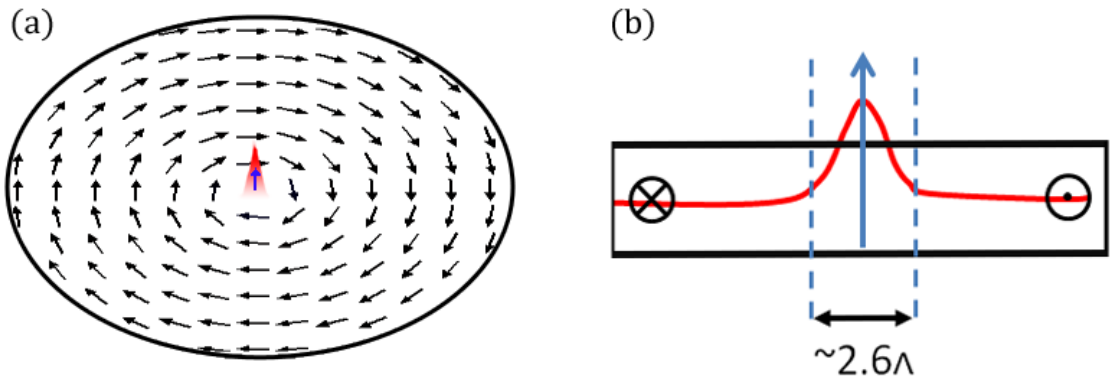

Figure 2.8: (a) Illustration of a typical vortex state that forms in thin permalloy elements as the result of a balance between the exchange and dipolar energies. The curling magnetisation is forced perpendicular to the surface at the centre of the element and forming the vortex core. (b) A profile of the element shows that the width of the core can be estimated from the exchange length as defined by (2.18)

change and dipolar energies. In a vortex state the magnetisation curls around the element in the plane of the sample with a core at the centre, where the magnetisation is forced out of the plane. The exchange length is calculated as,

$$\Lambda = \sqrt{\frac{2A}{\mu_0 M_s^2}} \tag{2.18}$$

where A is the exchange constant and M_s is the spontaneous magnetization. Using typical values of these parameters for permalloy ($M_s = 800$ kA/m and $A = 13$ pJ/m [137]) one can estimate the exchange length $\Lambda = 5.7nm$. The width of the vortex core can be estimated as $\sim 2.6\Lambda$ [121], giving an core width between $15-20$ nm for a permalloy element 40 nm thick and 500 nm in lateral size [138]. Figure 2.2.3 (a) illustrates the vortex state that typically forms at remanence in a thin permalloy disc element (40 nm thin and 500 nm in lateral size). In Figure 2.2.3 (b) the profile of the magnetisation is illustrated across the disc. The red curve simulates the out-of-plane magnetic moment which dominates at the centre of the disc forming the vortex core.

Application to Multibit Memory Storage Devices

The magnetic vortex state that forms in nanopatterned elements has drawn alot of interest in recent years with the possibility of multibit storage [139, 3, 2, 140, 141]. Here a vortex state is used as a logic unit which can be in one of four states (two given by the polarity of the core and two given by the circulation direction). For applications, independent control of both the polarity and circulation is required.

It has been shown that the polarity of the core can be flipped by applying a large static out-of-plane magnetic field [142] or by driven gyrotropic precession [143]. It has also been demonstrated that a pulsed magnetic fields can be used to reverse the direction of the circulation [3, 139].

A recent study by Im *et al.* [2] reported that symmetry breaking occurs in the formation of magnetic vortex states implying that a preferable state can be found out of the four. It is thought that this could lead to interesting applications of magnetic vorticies for magnetic sensors or logic elements [144, 145]. There is a lack of experimental techniques that are able to simultaneously image both in-plane and out-of-plane magnetic components in nanostructures and therefore most experiments have focused on either the polarity of the vortex core, or the chirality of the in-plane curling magnetisation. HERALDO imaging could open up new insight in the mechanisms of vortex switch behaviors by providing a magnetic imaging technique capable of simultaneous imaging of both in-plane and out-of-plane magnetisation.

2.2.4 Summary

Micromagnetic simulations have formed an important role in our understanding of domain theory however theoretical prediction alone cannot replace the value that experimental observation provides. We have discussed the formation of magnetic domains and the primary interactions at their boundaries within the domain walls. Different types of metastable ground states have been presented with particular focus on thin films systems and the minimisation of energy in nano- and micron-sized elements. We have seen that flux-closed vortex structures form in small

elements with fascinating properties that are actively being explored for use in high-density magnetic storage devices. The basic properties of maze and bubble domains that form in thin films with a large perpendicular anisotropy have also been introduced. Finally the LLG equation has been introduced which describes what happens when a single magnetic moment is subject to an external magnetic field.

2.3 Magneto-Optical Effects

Linearly polarised light that passes through (Faraday Effect [146]) or reflects off (Kerr Effect [147]) a magnetically ordered sample will undergo a rotation of the polarisation and a change of ellipticity. For experimental purposes, measuring the Faraday rotation requires the sample to be transparent to the incident light. This is not a restriction when measuring the Kerr rotation. The Magneto-optic Kerr Effect (MOKE) is a flexible tool used to characterise magnetic materials and study their magnetic properties by analysing the reflected light from a sample's surface [148, 149]. For a review of the magneto-optical effects in transition metal systems the reader is referred to [150].

In MOKE magnetometry a laser beam is linearly polarised and upon incidence with a sample, it excites electrons which, in turn, oscillate. The oscillating electrons experience a Lorentz force due to the presence of an externally applied field or from spin-orbital interactions in the magnetic material itself, generating an effective magnetic field. The Lorentz force reorientates the axis of oscillation and the reflected light contains a small component of polarisation perpendicular to the incident polarisation. By analysing each polarisation component of the reflected beam one can directly determine the magnitude of Kerr rotation and infer information about the magnetisation of the sample. This effect can be used to study magnetic specimen within applied external magnetic fields. There are three different geometries for MOKE magnetometry which are illustrated in Figure 2.9. They depend upon the magnetisation orientation with respect to the plane of incidence and the sample surface.

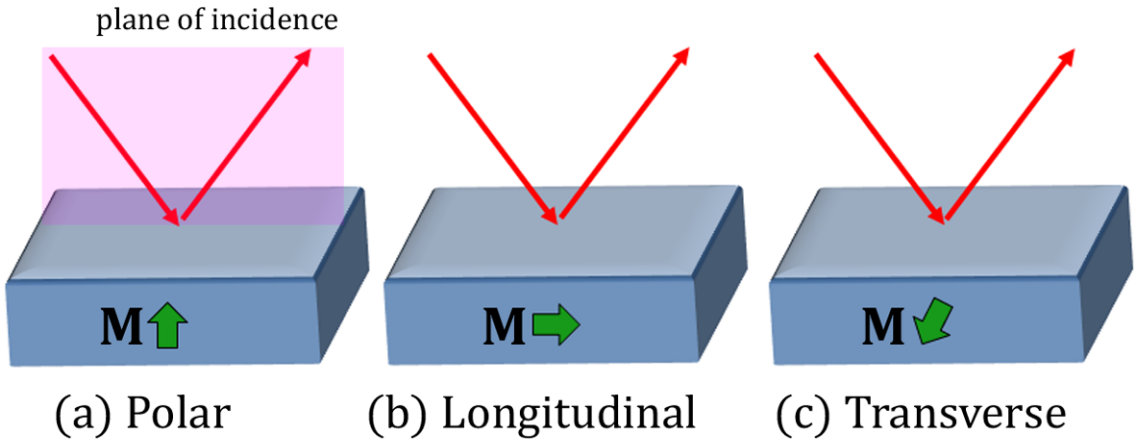

Figure 2.9: MOKE geometries. (a) Polar: Magnetisation is parallel to the plane of incidence and normal to the sample surface. (b) Longitudinal: Magnetisation is parallel to the plane of incidence and to the sample surface. (c) Transverse: Magnetisation is normal to the plane of incidence and parallel to the sample surface.

Polar MOKE is used to study magnetisation that is perpendicular to the plane of the sample and is often carried out at near-normal angles of incidence. It is therefore common to use polar MOKE to study films which exhibit PMA. A Lorentz force will therefore always exist and hence Kerr rotation. Figure 2.10 shows a schematic of the polar MOKE setup that was used in this study to characterise samples and examine their magnetisation. Resulting curves for a number of samples predominantly studied during this research project are shown in Figure 2.11. Figure 2.11 (a) shows several hysteresis loops for $[Co/Pt]_n$ multilayers (ML) with various stack repetition values n. The loops indicate that the samples possess PMA, with a reduction in the remanent magnetisation as the number of stacks is increased from 5 to 30. Figure 2.11 (b) shows several polar MOKE curves for a more complex system where a permalloy (NiFe alloy) layer was deposited onto of a $[Co/Pt]_n$ ML. In such systems, the Co/Pt ML generate stray fields just above their surface which interact with the permalloy film during deposition, and an in-plane domain pattern is magnetostatically imprinted into a permalloy layer by the adjacent Co/Pt ML. The optical laser probe in the MOKE measurements does not penetrate deep into the sample and therefore the hysteresis loops shown in

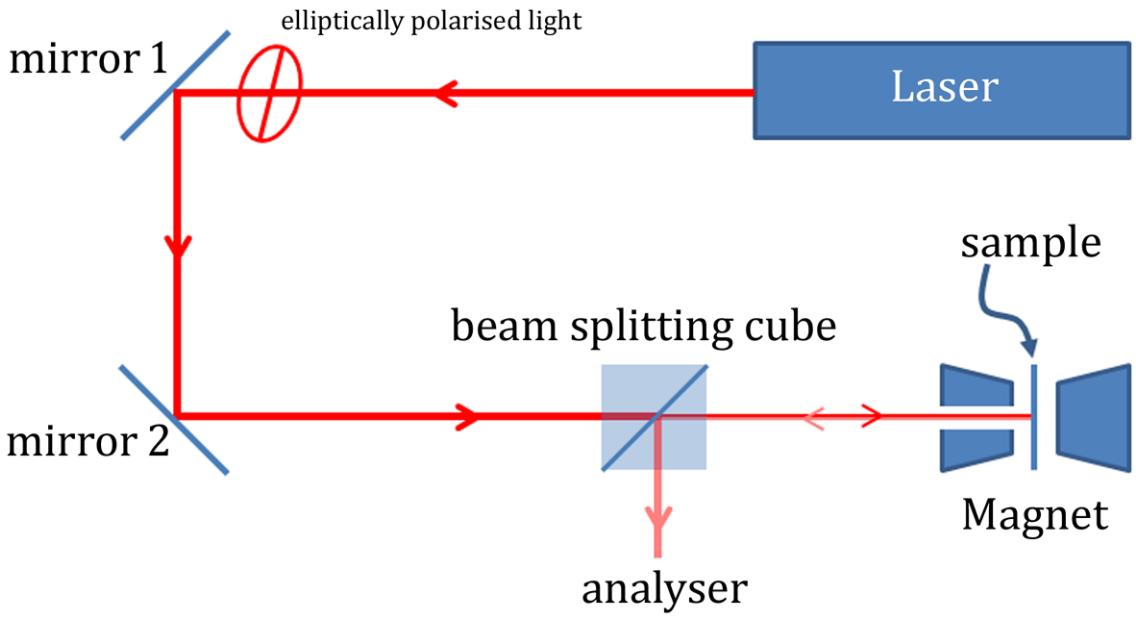

Figure 2.10: Polar MOKE experimental setup. Elliptically polarised light is passed through a beam splitting cube and directed onto a sample positioned between the two poles of a magnet. The front pole contains a small hole that does not disrupt the applied magnetic field and allows the laser light to reflect from the sample surface. The sample plane is orthogonal to the beam's direction so the beam is reflected straight back along the optical axis towards the beam splitting cube where it is reflected into an analyser. The analyser independently measures the two polarisation components that constitute the elliptically polarised light. The analysis is performed for several applied magnetic fields and the magnetisation of the sample for each field value can be determined by the polarisation rotation measured at the analyser.

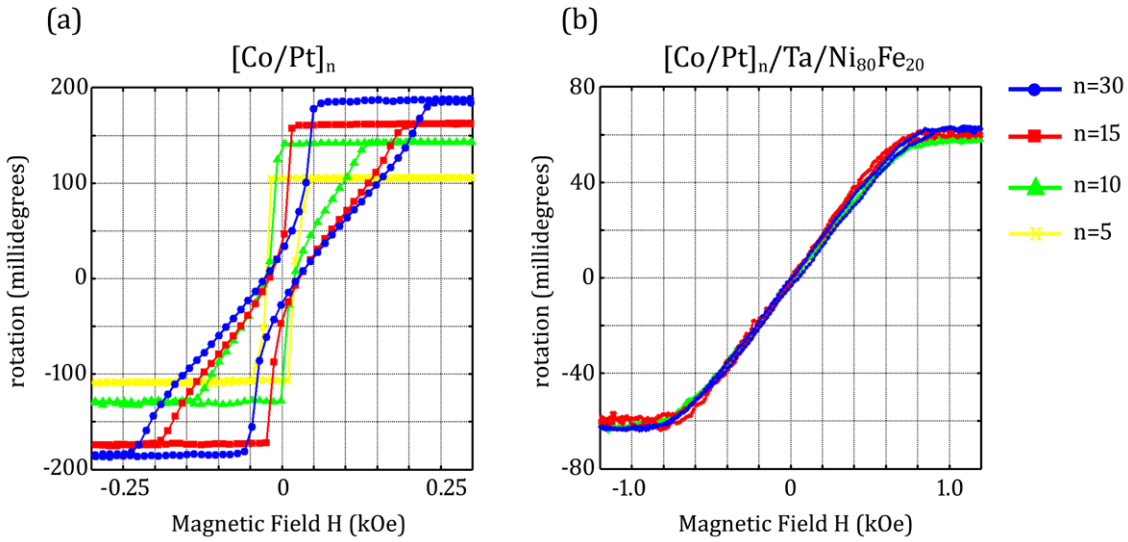

Figure 2.11: Polar MOKE loops. (a) Hysteresis loops of $[\text{Co}(0.4\text{ nm})/\text{Pt}(1\text{ nm})]_n$ multilayers with various stack repetition values n. (b) Polar MOKE curves of $[\text{Co}(0.4\text{ nm})/\text{Pt}(1\text{ nm})]_n/\text{Ta}(8\text{ nm})/\text{Ni}_{80}\text{Fe}_{20}$ (5 nm) systems with equivalent $[\text{Co/Pt}]_n$ stack repetition values to those shown in (a).

Figure 2.11 (b) are independent of n and measures the response from only the top thin Py layer and not the buried Co/Pt ML. These loops show similar responses, as expected, which are characteristic of the field dependence for in-plane magnetic anisotropy. Soft x-ray holography measurements have been performed to examine the nanoscopic magnetic domain structure of the systems and a more rigorous discussion of the samples shown in Figures 2.11 (a) and (b), where $n = 30$, can be found in later chapters of this thesis.

2.3.1 Kerr Microscopy

Standard Kerr microscopes can provide high resolution, distortion-free images using a lens with a high numerical aperture and incident light of short wavelength. Imaging domains with narrow width of 150 nm have been achieved [151] but ultimately the spatial resolution of this technique is limited by the optical microscope of the setup.

The small penetration depth of light, which can be 10-20 nm in metals, means

that it is common for the surface of samples to be prepared before magnetic contrast can be achieved with Kerr microscopy. Mechanically polishing soft metals is usually damaging to the surface layer and the damaged layer is often too thick yield satisfactory images. Mild heat treatment is typically performed after polishing to allow the surface to reconstruct [102]. On the other hand, hard metals can be prepared by diamond polishing alone without the need to for heat treatment as the damaged layer is thin enough in most cases. Some samples do not require any surface preparation, e.g. thin films, as they already have a sufficiently perfect surface providing they have not been handled before domain observation.

Using laser illumination provides a highly stable and intense source with the ability to use short pulses to stroboscopically observe periodic magnetisation processes in pump-probe experiments [152].

Time Resolved Kerr Microscopy (TR-MOKE)

Stroboscopic measurements can be made by varying the time delay of the probing laser pulse with respect to the pump. The magnetisation can then be mapped by recording the MOKE signal at each time delay and periodic magnetic processes can be observed [153, 154, 155]. An intense laser pulse can be used to excite the magnetisation dynamics [156], or alternatively, a time-varying magnetic field can be synchronised to, or triggered by a laser [157]. Sub-100 femtosecond pulses used as a pump leads to sample heating and can cause the temperature of the metal to rise above the Curie point, resulting in ultrafast demagnetisation [156]. To enhance the resolution of TR-MOKE a scanning optical microscope can be used. This approach is referred to as time-resolved scanning Kerr microscopy (TR-SKM) [158]. Here, the magnetic sample can be integrated with a micron-sized planar waveguide so that magnetisation dynamics can be excited by a pulsed [159] or harmonic magnetic field [160]. The high spatial and temporal resolution of TR-SKM makes it a powerful tool for studying the dynamic magnetic processes of micron-sized ferromagnetic elements [161].

2.3.2 Laser Scanning Optical Microscopy

Instead of using a conventional (wide field) setup with parallel illumination, a scanning optical microscope can be used for Kerr microscopy. Their advantage is that the signal can by analysed point by point giving local quantitative information about the sample with an enhanced resolution [195]. The main disadvantages with scanning methods are their high price and slow scanning speed compared to standard imaging microscopes. An approach whereby the sample is mechanically scanned under a fixed laser is ofter the preferred method as it significantly lowers costs, however, this reduces the scanning speed further. Another disadvantage when using a scanning probe is the problem with local heating of the sample. This is more of a challenge with scanning setups and can result in the probe influencing the magnetic domains in the material. With fast scanning speed this effect could be minimised by repeatedly scanning areas quickly, however such scanning speeds are not available.

2.3.3 Summary

The advantages of standard Kerr microscopy are:

- The sample is not damaged during observation.
- The observation is direct without any ambiguity of the magnetisation.
- Providing the effects of sample heating are suppressed, the observation does not influences the magnetisation state.
- Quantitative information on the magnetisation vector field at the surface can be obtained.
- Periodic dynamic processes can be observed stroboscopically.
- The technique is suitable for imaging specimen in extreme environments such as high/low temperatures or external applied fields.

- The conventional setup can easily be switched to scanning mode and local measurements can be made.

The drawbacks are:

- Samples have to be specially prepared so that they are flat and smooth to scales below the desired resolution.
- The spatial resolution is limited and domains smaller than ~ 150 nm cannot be resolved.
- The technique is only sensitive to surface magnetisation with a penetration depth of ~ 10 nm.

Using a laser scanning mode can provide an enhanced resolution however this suffers from low scanning speeds and can cause changes in the magnetisation of the sample due to localised sample heating. Along with the high costs of the setup we can conclude that their value lies in time-resolved magnetic measurements (for example, imaging processional magnetisation dynamics in isolated submicron ferromagnetic elements [162]) or the imaging of qualities other than magnetisation.

2.4 Transmission Electron Microscopy (TEM)

Transmission electron microscopy (TEM) offers magnetic imaging of local domain structure with high spatial resolutions typically between 1-20 nm [163]. An advantage of the technique lies in the additional information about the materials structural and electronic properties that can be gained from any one region on the sample. This is possible because of the large number of interactions that occur when a beam of high-energy electrons is incident upon a material.

2.4.1 Magnetic contrast in TEM

In classical beam optics, the electrons interact with magnetic induction and are deflected as particles by the Lorentz force ($\mathbf{F}_l$),

$$\mathbf{F}_l = q_e(\mathbf{v}_e \times \mathbf{B}) \tag{2.19}$$

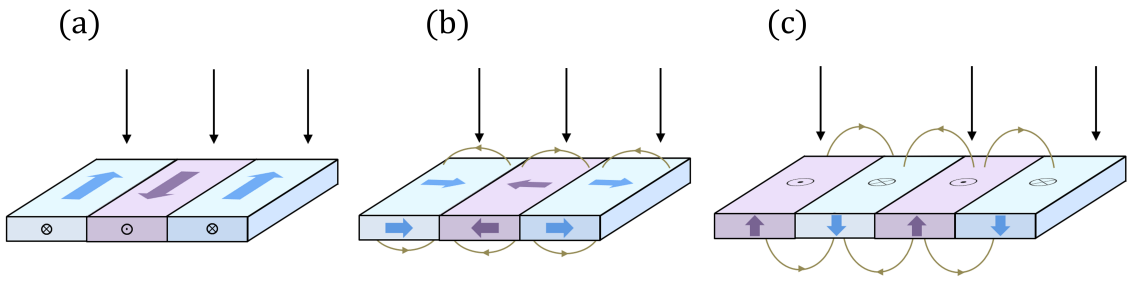

Figure 2.12: Lorentz deflections in basic sample arrangements [102]. (a) In-plane domains yield an overall deflection from the Lorentz force for an electrons beam perpendicular to the sample. (b) The deflection due to the magnetic domains is canceled out with deflection by the stray fields around the sample. Only the edges of the sample will give rise to contrast. (c) The Lorentz force is zero inside the sample because the magnetisation of the domains runs (anti)parallel to the beam. Any deflection from stray fields above and below the sample cancel.

where q_e is the charge and $\mathbf{v}_e$ is the velocity of the electrons. $\mathbf{B}$ is the magnetic flux density.

For imaging magnetic materials a beam of fast electrons is incident onto the sample which gets deflected by magnetic fields resulting in light and dark bands of contrast which corresponds to the local changes in the magnetic field strength. Three basic sample arrangement are shown in Figure 2.12. It demonstrates that with some magnetic configurations the overall Lorentz force is zero. This restriction to certain magnetic orientations is a limitation of any of the microscopy modes discussed below which rely on the Lorentz force to provide magnetic contrast.

2.4.2 Lorentz Microscopy

Lorentz microscopy has been used for imaging magnetic specimen for the past 50 years. It is a powerful high resolution technique capable of 1 nm spatial resolution and 30 ms time resolution in static magnetic imaging [164] and has aided in the study of magnetic domain structure and the mechanisms of magnetisation reversal in magnetic thin films and elements.

In this section we describe the common imaging modes, which are the Fresnel (defocused) mode and the Foucault mode. Differential phase contrast imaging will also be introduced. Reviews of the Lorentz microscopy technique can be found in [165, 166, 167]. In the Fresnel imaging mode (Figure 2.12 (a) and (b)) the objective lens is defocused so that a defocused image of the sample is formed. With this arrangement, the domain walls appear as bright and dark contrast lines in the final image because the electrons are converged into the wall or diverged away from it by the magnetisation of the domains that surround the walls. The direction of magnetisation within the domains is revealed by ripples in the image which always orientated perpendicular to the direction of magnetisation. In the Foucault mode (Figure 2.12 (c) and (d)) the objective lens remains in focus however an aperture in the diffraction plane is laterally displaced to block one of the spots.

The Lorentz force contrast depends on small changes to the paths of the electrons. Large deflections caused by scattering from the samples core electrons, or form collisions with nuclei, generate background effects which ultimately limits the maximum sample thickness of films to less than a few hundred nanometers. A disadvantages of the technique comes apparent when imaging nanostructured elements. The edges of the elements contribute to the contrast in the image and this can become significant as the dimensions of the element is reduced. This can result in the imaging of the magnetic structure hard to characterise.

Differential Phase Contrast Imaging (DPC)

This mode of imaging is normally implemented with a scanning transmission electron microscope (STEM) instrument. Here, the local Lorentz deflection is determined by a detector segmented into quadrants and positioned in the far-field. Two difference signals are obtained from opposite segments which provides a measure of the two components of the Lorentz deflection and a map of the magnetisation vectors perpendicular to the electron beam can be constructed. Using the total signal received by the detector, a map of the samples structure (without magnetic contrast) can be built. This added functionality gives DPC an advantage over the

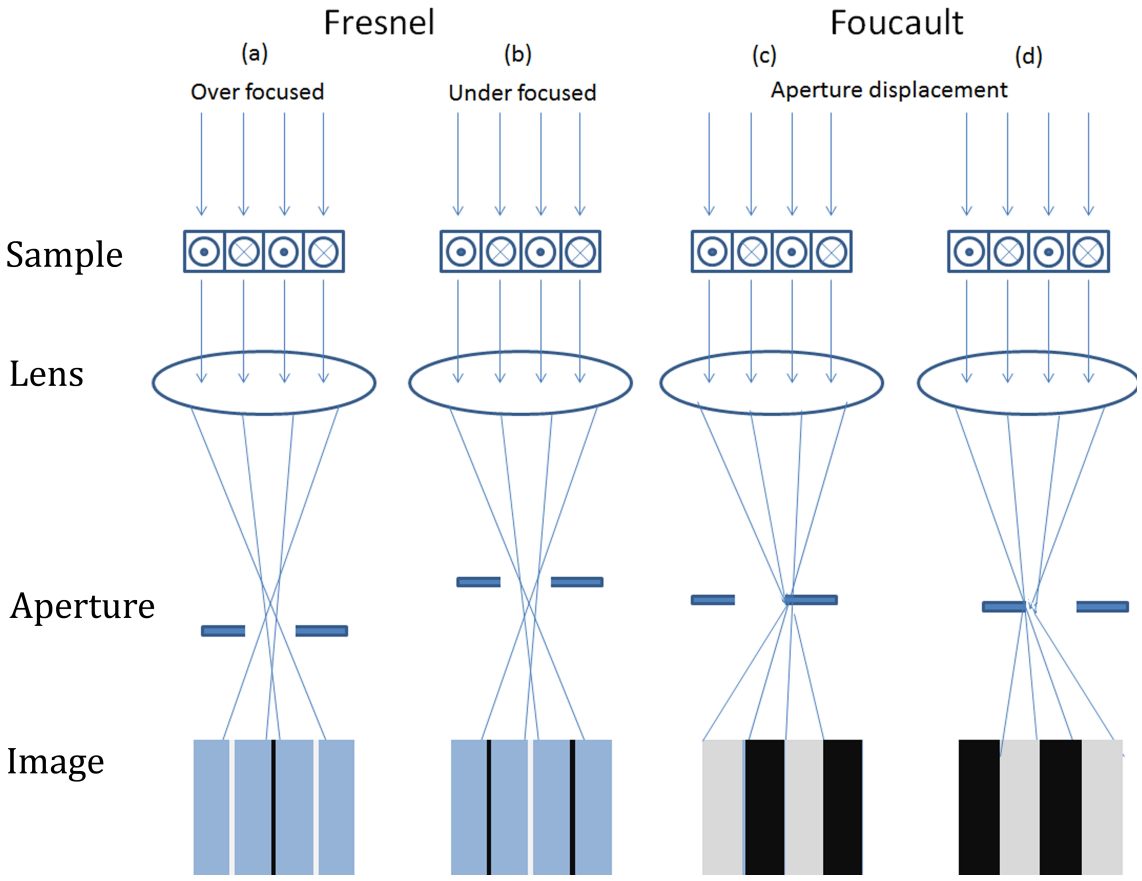

Figure 2.13: Lorentz Micorpscopy Modes reproduced from [163]. Illustration of the contrast that can be expected from the two common imaging modes (Fresnel and Foucault) of Lorentz microscopy.

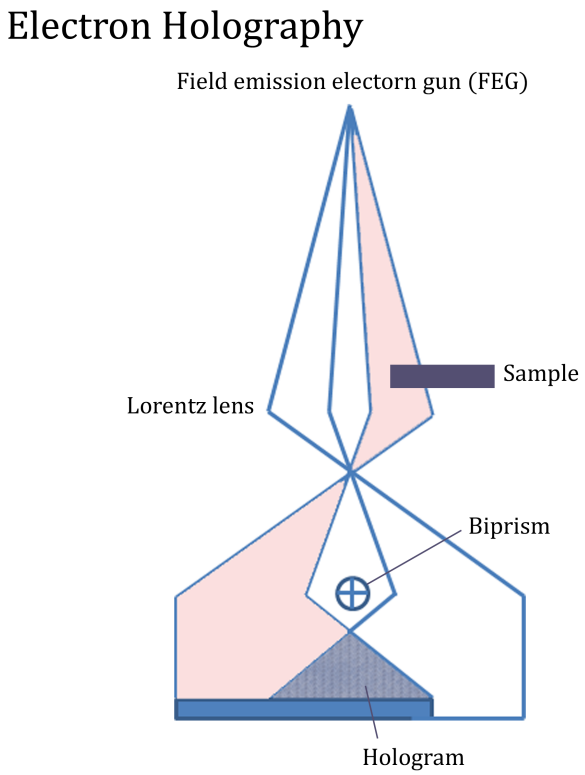

Figure 2.14: Schematic of Electron Holography reproduced from [163]. A coherent electron beam is needed for electron holography. This is provided by the electron field emission gun (FEG). An electrostatic biprism is used to cause an overlap between the reference beam (coloured white) and the object beam (coloured pink).

other imaging modes discussed above because the topography of the material can be studied alongside the magnetisation.

The main disadvantage with DCP is the added complexity in the instruments setup and it can be difficult to operate compared to other fixed beam modes. In addition the raster scanning nature of DCP restricts the technique to time-independent events due to the added recording time required.

2.4.3 Electron holography

Electron holography is a high resolution TEM technique that yields a two-dimensional vector map of magnetic flux. Most TEM imaging modes cannot be used to charac-

terise the magnetic fields which surround a sample because they are not sensitive to the changes in the phase of the electron beam. Electron holography offers an alternative approach which can capture long range magnetic fields by recording the amplitude and the phase of the electron wave after the electrons have passed through the sample [168]. The phase change of the electron wave is directly related to the magnetic fields of the sample it passes through and a high resolution image revealing magnetic structure can be achieved. A review of electron holography can be found in [169, 167, 170] where twenty different forms of the technique have been identified. The most common method used is off-axis electron holography (Figure 2.14). In this standard approach, the sample is placed within a coherent electron beam, leaving part of the beam to pass by undiffracted. This is used as the reference beam. The reference and object beam are brought together using a biprism (consisting of two plates and a charged wire) and an interference pattern is recorded. In principle the technique is capable of achieving spatial resolutions of magnetic material better than 1 nm, however, practical limitations (with signal-to-noise ratios, phase resolution and optical aberrations) the spatial resolution is estimated between 10-20 nm [171, 172]. Due to multiple scattering effects the sample thickness is limited to $\sim$ 500 nm to ensure the quality of the hologram is not degraded [163].

2.4.4 Recent Application to Magnetic Materials

Off-axis electron holography can be used to determine the magnetic fields in and around closely-spaced nanoparticles and wires. It has been demonstrated by Dunin-Borkowski *et al.* [171] that cobalt nanoparticles can self-assemble into rings < 100 nm in diameter, which support chiral flux closure states that can be switched with coaxial magnetic pulses. More recently electron holography has been used to determine the dimensions of vortex cores in head-to-head domain walls and quantitatively measured their in-plane and out-of-plane magnetization [173]. Recently the technique was used to image switching in ferromagnetic nanoscale double disk structures [174]. Here electron holograms demonstrated a single domain state that

exists between two 250 nm disks. This was followed by a series of Lorentz microscope images and electron holograms which followed the magnetic switching with an applied magnetic in-plane field. these images recorded the remanent configuration of the magnetisation after the switching field was removed. Whilst the temporal resolution of TEM is limited, time-elapsed imaging of vortex core precession in permalloy nano-sized elements has been demonstrated by Pollard *et al.* [175] using Lorentz microscopy measured under AC excitation. Here the orbit amplitude of the vortex core gyration was measured with spatial resolution < 5 nm.

2.4.5 Summary

The advantages of TEM techniques are:

- The technique provides high contrast of small variation in the magnetisation.
- High spatial resolutions < 10 nm are readily achievable with electron holography and modes of Lorentz microscopy.
- Very high resolution quantitative images of domains and walls can be obtained with DPC microscopy.
- Measurements of the stray fields above and below the sample can be combined with quantitative information from DPC microscopy and a complete three-dimensional magnetization map can in principle be derived mathematically.

The drawbacks and and limitations:

- Sample thickness is generally limited to a few hundred nanometers.
- In electron holography the sample thickness is restricted further to samples < 100 nm.
- The field of view is restricted to less than a few hundred microns.
- The equipment is expensive and in general, once adjusted for imaging magnetic materials it cannot be used for other purposes.

- The temporal resolution is limited to ~ 30 ms for dynamic studies.
- Imaging within an externally applied magnetic fields is difficult.
- The magnetisation and stray fields can counteract each others effect on the contrast in the recorded image.
- Whilst electron holography is useful for investigating magnetic fields outside a sample, it is less useful for direct imaging of magnetic domain structure.

2.5 Electron Diffraction and Scattering

In this section we look at two mechanisms for surface sensitive imaging. When an electron beam hits a ferromagnet two kinds of re-emitted electrons can be distinguished. (i) Electrons that are elastically backscattered from the samples surface and (ii) secondary electrons that are emitted by the atoms when excited by the electron beam.

2.5.1 Low Energy Electron Micorscopy (LEEM)

In low energy electron microscopy (LEEM), incident electrons with high energy from the illuminating system are deaccelerated to low energies typically between 1-100 eV. The low energy electrons probe the surface of the sample and are reflecting back. The incident and image electron beams are separated by a magnetic sector field and an objective lens forms an image of the sample from the backscattered electrons which is projected onto a microchannel plate (MPC) - florescent screen image detection system. The image that is produced on the fluorescent screen is then recorded with a CCD camera.

The technique is highly sensitive to the sample's surface and the probe depth can be tuned by varying the energy of the illuminating electrons [176]. A review of LEEM can be found in [176, 177]. For magnetic contrast, spin polarised electrons can be used rather than the conventional unpolarised illuminating electron beam. In the situation where spin polarised electrons are used, the number of

electrons that are elastically backscattered from the samples surface depends on the orientation of the local magnetisation with respect to the spin of the electrons [178, 179].

2.5.2 Spin polarised low energy electron microscopy (SPLEEM)

A spin polarised low energy electron microscope (SPLEEM) instrument is a LEEM that uses a spin-polarised illumination system [180]. It offers a high resolution on the order of 10 nm, which is limited by spherical and chromatic aberrations of the objective lens. It is also highly surface sensitive. These features make the technique particularly suited to growth studies. SPLEEM has frequently been used for studying single layers with the aim of understanding how magnetisation direction and the magnetic domain structure evolves as film thickness is increased [181, 182, 183].

It is worth noting that in SPLEEM the polarisation state of the imaging electrons is not needed to achieve magnetic contrast and so a spin analyser is not required, unlike in SEMPA (see Section 2.5.3). This provides a highly efficient technique because the available electron polarisors are more efficient than polarisation analysers. It is also a full field technique and faster acquisition times are achievable compared to other scanning methods.

The instrument is complex and any contamination of the sample's surface can eliminate magnetic contrast. This makes imaging sample *ex-situ* more challenging as the sample has to be treated before the surface can be probed e.g. with capping layers that decreases the magnetic contrast [184]. External fields cannot be applied in the plane of the sample because this would cause the electron beam to be deflected. The technique is however suitable for extreme temperature measurements [183]. Sample cooling to 118 K has been demonstrated [184] with the expectation of further cooling to 10 K using liquid helium.

2.5.3 Scanning Electron Microscopy with Polarisation Analysis

In scanning electron microscopy with polarisation analysis (SEMPA) [185, 186, 187, 188, 189], the spin polarisation of secondary electrons that are emitted by a magnetic samples are analysed to obtain an image of the sample magnetisation. A scanning electron microscope (SEM) provides a primary beam of electrons which is raster scanned over the sample. When the primary electron beam hits a ferromagnetic material, spin-polarised secondary electrons are created at the surface of the sample. The mean free path of the secondary electrons is short ($\sim$1-2 nm [190]) which makes SEMPA a highly surface sensitive technique. This method is therefore more surface-specific than Kerr microscopy which typically measures to a depth of 20 nm in metals specimen.

The advantages of SEMPA are the high spatial resolutions of less than 10 nm [188] and the simultaneous SEM measurement that allows one to directly compare magnetic structure with the topography of the sample.

A drawback with SEMPA is the low efficiency of the spin polarised detectors compared with intensity measurements. It has been demonstrated to take $\sim 10^4$ times longer to record a polarisation measurement compared to an intensity measurement with the same signal to noise statistics [191]. It can typically takes about 15 minutes to record an image [192] which limits the technique for time resolved studies of magnetisation dynamics. A further limitation is the ability to image domains within an external magnetic field. Electron beams are deflected in the presence of a magnetic field and complicated corrections are necessary. Limited success has been achieved with the use of weak fields (10-15 Oe) [187, 193] with fewer problems arising when the field is applied perpendicular to the surface [187] along the direction of the electrons motion. Other success with field measurements have been achieved by using a weak but strongly localised magnetic applied field and the reversal of magnetic nanoparticles could be observed [194]. Further details of SEMPA and its applications can be found in [192, 195, 196, 191, 197].

2.5.4 Summary

The advantages of electron reflection methods for domain observation are:

- With high surface-sensitivity the technique can provide quantitative images of the surface magnetization.
- Using electron polarisation methods offers high spatial resolutions on the order of 10 nm.
- Magnetic domain images can be combined with SEM images revealing sample topography.

The drawbacks and limitations are:

- The spatial resolution is poor compared with non-magnetic electron microscopy techniques.
- The instruments are extremely expensive especially if ultra high vacuums are needed.
- Non-conducting samples require a metallic coating to avoid surface charge distorting the image.
- Measurements in external magnetic fields are only possible in certain geometries but limited by the conditions of the electron microscope.
- The temporal resolution is limited as typically images can take a few seconds to several minutes to acquire.
- Contamination of the sample surface can easily reduce magnetic contrast.

2.6 Mechanical Scanning Techniques

In this section we discuss a range of scanning probe methods (SPM). All experimental SPM approaches are based on force or tunneling microscopy which will be discussed here in more detail.

2.6.1 Magnetic Force Microscopy (MFM)

Magnetic force microscopy (MFM) [198, 199] is a variation on the principles that govern atomic force microscopy [200], however, much smaller forces are measured in MFM than in AFM. MFM is a well established technique and extensively used to characterise magnetic domain structure [201, 202]. In this section we limit the discussion to an outline of the basic principles and discuss its advantages, drawbacks and limitations in brief. The reader is directed to a range of literature [201, 102, 203] for further details of the technique.

MFM probes the magnetic stray fields above a very flat sample by mounting a small ferromagnetic tip onto a cantilever spring that is lowered very close to the surface of the sample. The force on the magnetic tip as it is scanned above the surface is detected by measuring how far the tip is displaced. Typically these displacements are on the order of nanometers and are detected by optical means. The principles of the MFM are illustrated in Figure 2.15.

The tip profiles the topography of the sample in tapping mode [204] before being raised to a distance $\sim$ 30 nm from the surface and re-traces the profile. Interactions between the magnetised tip and the sample generates an image of the magnetic field gradients, independent of the surface topography. The technique is highly desirable for simultaneously producing an image of the samples topography and magnetic profile, with a spatial resolution routinely better than 50 nm [205].

The image produced does depend on the type of the tip and magnetic coating, and problems can arise due to tip-sample interactions disturbing the sample's magnetisation. The advantages of MFM are the high spatial resolutions on the order of 10 nm [206] and the techniques sensitivity to magnetic contrast of samples with surface coatings, such as conductive or capping layers. Imaging under applied field is somewhat limited [201].

In Summary, MFM is an imaging technique that can readily provide qualitative images with high resolution. Its drawbacks lie in the lacking quantitative information of fine details. The orientation of the magnetisation in domains is not directly probed and so magnetisation configurations in complex samples can

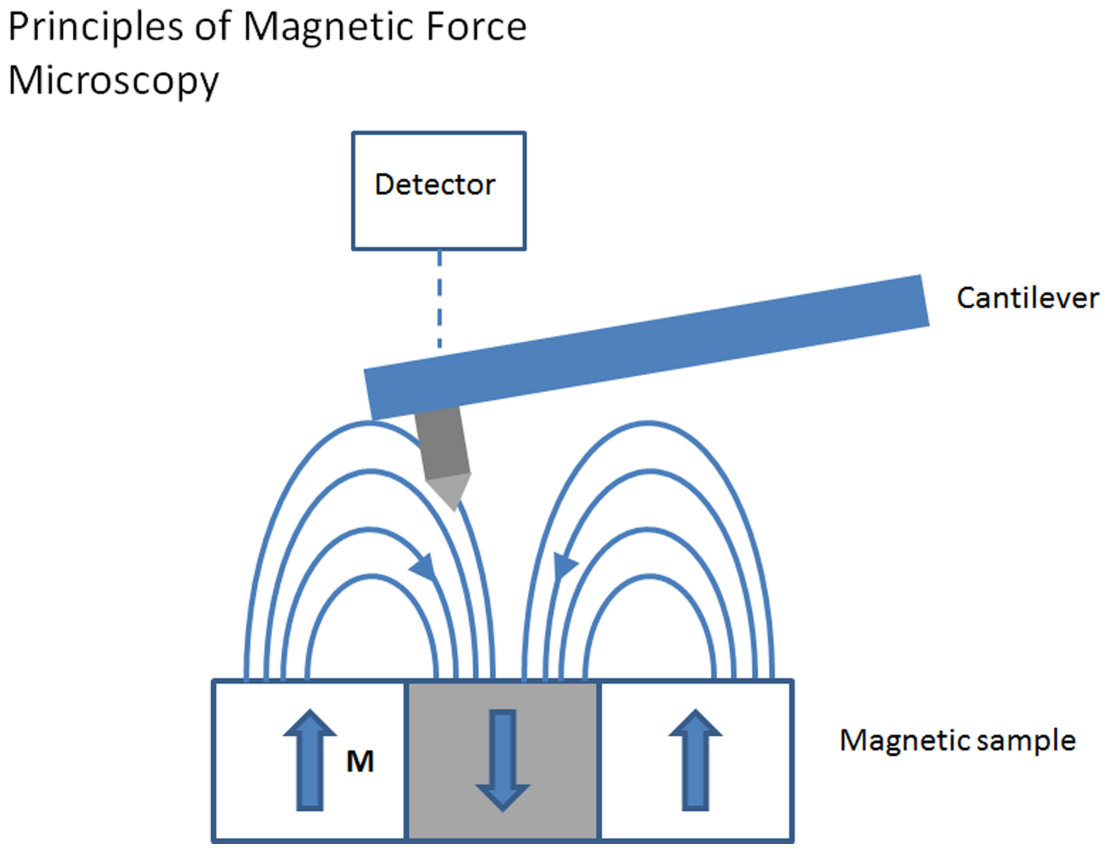

Figure 2.15: Principles of MFM. A cantilever probes the magnetic stray fields above the surface of a magnetic material. A detector measures how much the cantilever is effected by the stray fields and a map of the magnetisation in the sample is constructed as the cantilever tip is scanned over the sample just above the surface.

remain obscured.

2.6.2 Near-Field Optical Scanning Microscopy

With conventional magneto-optical microscopes the resolution is diffraction limited and spatial resolutions are at best a few hundred nanometres. With scanning nearfield optical microscopy (SNOM) the diffraction limit is circumvented by forcing the light through a submicroscopic aperture. When the probe is sufficiently close to the sample, the aperture can be scanned over the sample and magneto optical contrast [207] can be achieved with spatial resolutions of ~ 100 nm [208].

The drawbacks of this technique mainly lie in the available geometries of the experimental setup. It would be difficult to obtain an image using the Kerr effect which limits its application. A further drawback is the techniques sensitive to environmental conditions and so suitable sample preparation is needed.

2.6.3 Spin Polarised Scanning Tunneling Microscopy (SP-STM)

A scanning tunneling microscope (STM) sensitive to spin would provide an incredibly powerful instrument for magnetic surface characterisation and in theory, with such a tool it would be possible to investigate individual spins in the topmost atomic layer of a sample.

In STM [209] the signal is the tunneling current between a conductive tip and conductive sample. Sample-tip distances are typically 0.1 nm. The technique is capable of achieving atomic spatial resolutions < 1 nm for both the atomic and magnetic structure which is ultimately limited by the sharpness of the tip.

In SP-STM the electronic charge of the electrons that tunnel between the magnetic tip and the sample maps the surface topography, and the polarisation probes the spin structure of the sample.

The are several drawbacks with this instrument that stem from it's complexity, special sample and tip requirements and cost. Samples are required to have atomically clean surfaces and once the probing tip is transfered to the SPM it has to

be cleaned *in-situ* before magnetic contrast can be achieved. Measurements also have to be performed in ultra high vacuum. Similar to MFM, using magnetic tips can also cause stray fields that influence the samples magnetisation. For a detailed comparisons of magnetic contrast between SP-STM and MFM see [210].

2.6.4 Magnetic Field Sensor Scanning

Other scanning probe microscopy tools can be used for magnetic imaging without detecting forces. In SQUID (scanning super conducting quantum interference device), scanning Hall and magneto-resistance sensors [211] near surface fields or magnetic flux is measured.

In SQUID microscopy [212], quantitative imaging of magnetic stray fields is possible with sub-micron resolution with high field sensitivity of 200 pT [213]. In scanning Hall probe microscopy (SHPM) [214], typical resolutions down to 120 nm can be achieved [215].

These main advantages and applications of these techniques are when quantitative detection of near-surface magnetic fields, at fairly high resolutions is required. One particular disadvantage of SQUID worth noting is that it has to be operated under cryogenic conditions. Further details of scanning probe methods of magnetic imaging can be found in [216]

2.6.5 Summary

In summary, scanning force microscopes are the most versatile and widely used scanning probe instruments allowing for AMF and MFM. MFM requires minimal sample preparation which in contrast are quite demanding in STM and SNOM due to their sensitivity to environment conditions. The main application of STM and SNOM are to dedicated research areas where the efforts in preparing the samples are justified by the gain of incredible spatial resolutions and sensitivity, such as detections involving a small amount of spin.

2.7 Domain Observation with X-ray Techniques

A description of all the state-of-the-art magnetic imaging techniques that probe mater with soft x-rays are presented in this section. Their magnetic contrast arises from the polarisation of the exciting radiation, often using circularly polarised light (XMCD).

2.7.1 X-ray Magnetic Circular Dichroism (XMCD)

XMCD is a useful contrast mechanism particularly for imaging ferromagnetic systems. The mechanism is particularly effective for transition metal L_{2-3} absorption edges due to a strong dichroic effect and a highly intense signal.

Dichroism is a spectroscopic effect describing the polarisation dependent absorption of light. The way in which a ferromagnetically ordered material interacts with circularly polarised x-rays provides a contrast mechanism which allows one to quantitatively map the magnetisation of a sample. Since the experimental discovery of x-ray magnetic circular dichroism (XMCD) [217], it has been widely used as an element-specific probe of magnetic samples in a myriad of synchrotron techniques [163]. XMCD spectromicroscopy was first demonstrated in 1993 [44] and now offers many capabilities for studying the elemental, chemical and structural properties of materials. It can probing to large depths, has a wide range of spatial dimensions and is sensitivity the orientation and the size of the magnetic moments of the material. Its application as a contrast mechanism in Fourier transform holography (FTH) was experimentally realised in 2003 [58], where resonant coherent scattering from magnetic domains were recorded in a Gabour in-line geometry. The first off axis interference holograms consisting of magnetic speckle were recorded the following year [7] and since, FTH has proved to be a robust imaging technique for studying magnetic domains in thin ferromagnetic films and multilayers providing the sample substrate is suitably transparent to x-rays [11, 13, 14]. XMCD is also the mechanism used for magnetic contrast behind XPEEM, TXM and STXM.

This section is aimed at providing the reader with the basic ideas behind XMCD which are used later in this thesis as a contrast mechanism in magnetic FTH trans-

mission experiments. The reader is referred elsewhere for a more comprehensive introduction [218].

We will first consider the absorption of x-rays in $3d$ transition metals by the excitation of a core electron into a higher energy state above the Fermi level. We restrict ourselves in this discussion to transitions where a $2p$ core electron is excited to a $3d$ state, because these transitions are relevant to the work carried out in this thesis. Due to the spin-orbit interaction, the $2p$ states are energetically split into separable $2p_{1/2}$ (L_2) and $2p_{3/2}$ (L_3) levels. The absorption of x-rays is thus determined by the occupied density of states in the $2p$ core levels and the unoccupied density of states in the $3d$ levels above the Fermi energy. If we now consider $2p \rightarrow 3d$ transitions that are excited by circularly polarized x-rays, these transitions will exhibit a spin polarisation dependence due to selection rules [219], as illustrated in Figure 2.16. selection rules!!

This means that for each helicity of light, more electrons of one spin direction are excited into unoccupied $3d$ states than the opposite spin direction. In effect, using XMCD one can determine the density of unoccupied states in the $3d$ level for each spin polarisation. In a ferromagnet there is difference in the number of unoccupied $3d$ states for each spin polarisation [see Figure 2.16 (a)], which will lead to a distinct difference in the absorption spectra for opposite helicities of light, and this provides a direct way of quantifying the spin magnetic moment of the material. An x-ray absorption spectra for Fe is illustrated in Figure 2.17. This illustrates resonant absorption at the L_2 and L_3 edges of Fe.

The XMCD contrast depends upon the degree of circular polarization of the x-rays, and the magnetic absorption cross section normalised to the atomic cross section absorption. The absorption signal is also proportional to the projection $\mathbf{M} \cdot \mathbf{k_i}$ of the magnetisation $\mathbf{M}$ onto the wave vector of the incident light $\mathbf{k_i}$. In transmission imaging experiments, when the sample plane is orthogonal to the incident beam the magnetic signal is maximal for perpendicular magnetisation and vanishes for in-plane magnetisation. Due to demagnetisation effects, the orientation of the average magnetic moment in many magnetic thin films is in the plane of the

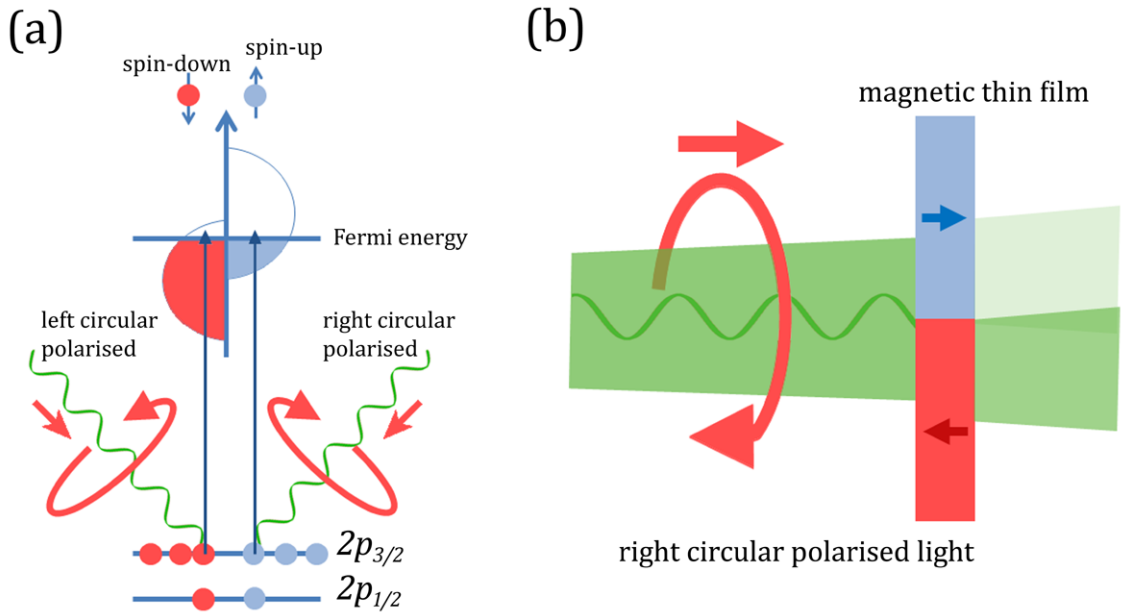

Figure 2.16: Principles of XMCD absorption, figure reproduced from [218]. (a) $2p \rightarrow 3d$ transitions are spin dependent and depend on the polarisation of the absorbed light. Any spin flips are forbidden in x-ray absorption and so the measured resonant absorption intensity directly relates to the number of empty states in the $3d$ level for a particular spin. (b) The dichroism is used as a contrast mechanism for magnetic imaging. The transmission of circularly polarised x-rays through a magnetic thin film is illustrated. For right circularly polarised x-rays, the absorption of one magnetisation direction is much stronger than others, thus the magnetisation direction of different magnetic domains is revealed.

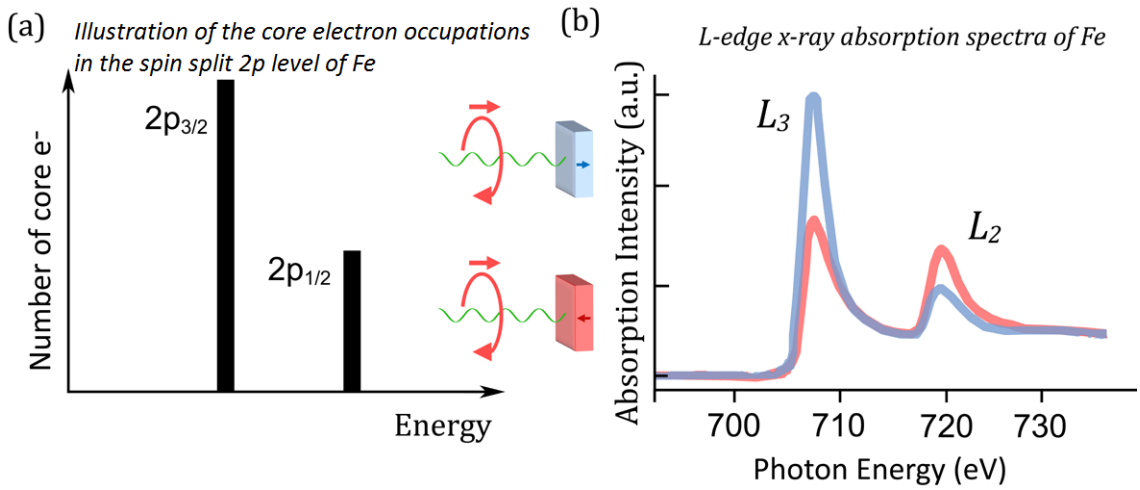

Figure 2.17: (a) Schematic revealing the core electron occupation in $3d$ transition metals in the spin split $2p$ level. Absorption of right (left) circularly polarised light mainly excites spin-up (spin-down) photoelectrons. (b) Fe L-edge XAS. In XMCD spectroscopy reversing the polarisation of light whilst keeping the magnetisation direction fixed, is equivalent to changing the magnetisation direction with a fixed photon helicity. The XAS spectra shown illustrates resonant absorption at the L_2 andL_3 edges of Fe.

sample, and only highly anisotropic materials, or specifically grown systems exhibit PMA.

2.7.2 Photoemission Electron Microscopy (PEEM)

A photoemission electron microscope (PEEM) instrument is similar to the LEEM instrument described in Section 2.5.1, however, in PEEM the spatial distribution of electrons that are emitted from a solid sample surface and captured and used to form an image of the sample on a two dimensional detector [220]. The main advantages of the PEEM are its fast image acquisition time, similar to that of an optical microscope, and the ability to image domain structure of microscale and nanoscale elements with a spatial resolution of a few tens of nanometres. There is one particular mode of PEEM which is of interest for magnetic imaging which exploits XMCD to achieve magnetic contrast. An XPEEM image of magnetic domains was first demonstrated in 1987 with an example that showed when the x-ray beam energy was tuned to the Fe K edge, absorption of circularly polarised x-rays depended on the magnetisation state of the Fe sample [217]. The tunable nature of the x-ray beams at third generation synchrotron sources make XPEEM a very powerful tool for studying magnetic structure. The energy of the x-ray beam can be tuned to an elements absorption edge making the technique element-specific. In this mode one can gain access to magnetic signal of buried layers to a depth of up to ~ 5 nm. Further details of the XPEEM technique can be found in [221] and additional reviews of its applications to magnetic imaging can be found in [74, 222, 223, 224, 225, 226].

To form a magnetic image in XPEEM the XMCD signal in the photo-absorption process is translated into an electron yield via the emission of Auger electrons. The core-holes are filled causing a radiative x-ray fluorescence or a non-radiative Auger process. In the soft x-ray regime, the Auger transitions are much more probable. The yield Auger electrons is proportional to the absorption signal. The Auger electrons pass through the sample and suffer from multiple inelastic scattering events which leads to a cascade of secondary electrons. The secondary electron are

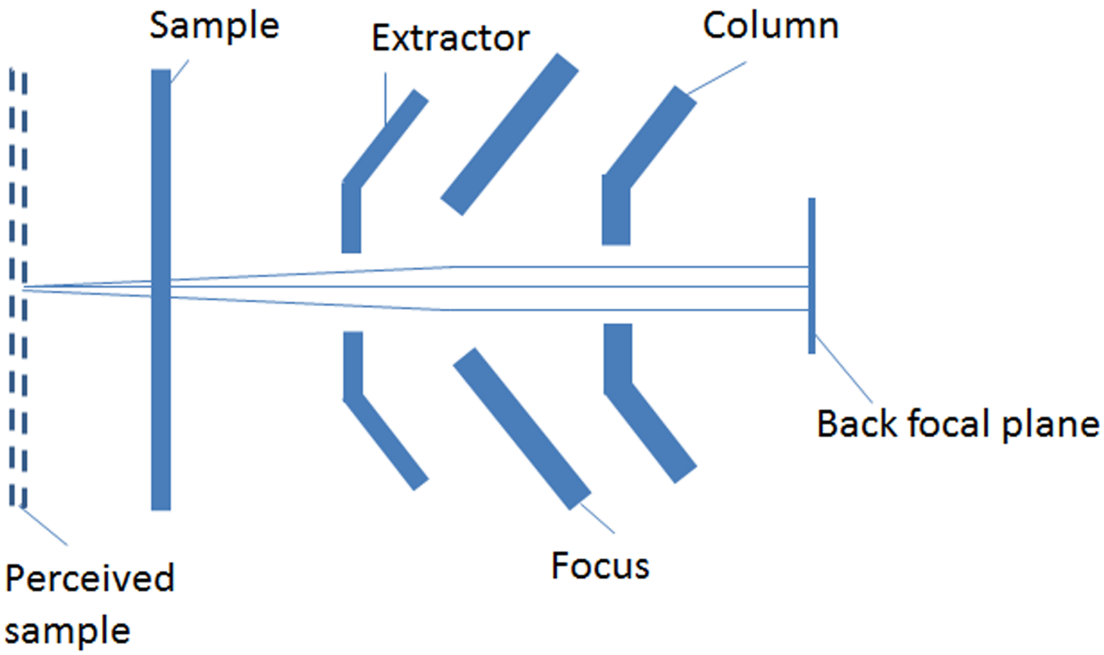

Figure 2.18: Schematic of an electrostatic cathode lens reproduced from [224]. The extractor/focus/column electrodes perceives a sample shown in the diagram as the dashed outline.

of lower energy but yield the same chemical information as the Auger electrons. In short, the XMCD signal is transfered into a dichroism in the Auger electron yield, which in turn translates into a helicity-dependent secondary electron yield proportional to the XMCD absorption signal [227].

The cathode lens forms a main part of the emission microscope because it determines the size of possible field of views and its aberrations determine the lateral resolution of the image. Typically the field of view can be changed between $\sim$ 1 mm down to a few microns in size making the microscope ideal for investigating magnetic structure. For studying magnetic samples, any magnetic fields close to the sample must be avoided to prevent influencing the domain structure of the sample. Thus, an electrostatic lens system is advantageous.

Figure 2.18 shows an illustration of an electrostatic cathode lens. An approximation for the aberrations taken form [224] can be calculated by considering how the extractor/focus/column electrodes perceives the sample. It will 'see' a virtual

image of the sample which gives an apparent electron starting energy of,

$$E^{'} = E_0 + E_{gain} \tag{2.20}$$

where E_0 is the true starting energy of the electrons and E_{gain} is the energy the electrons gain having left the surface before they reach the extractor electrode. The perceived starting angles of the electrons can be written as,

$$\alpha^{'} = \alpha_0 \left(\frac{E_0}{E'} \right)^{\frac{1}{2}} \tag{2.21}$$

where α_0 if the true starting angle of the electrons with respect to the surface normal.

The expression for the perceived chromatic aberration (δ_c) can be written as,

$$\delta_c = C_c \alpha^{'} \frac{\Delta E}{E'} \tag{2.22}$$

where C_c is a coefficient of aberration characterised by the lens itself, $\alpha^{'}$ is the apparent starting angle of the secondary electrons with respect to the sample normal. $E^{'}$ and E are the apparent and true starting energy of the electrons respectively. The perceived spherical aberration (δ_s) can be written as,

$$\delta_s = C_s \alpha^{'3} \tag{2.23}$$

where C_s is a coefficient of aberration characterised by the lens itself. The contrast aperture in the back-focal plane of the objective lens defines the angle $\alpha^{'}$, as the diameter of the contrast aperture determines the cone of electron starting angles on the sample surface that are accepted by the microscope optics for a given starting energy. Therefore the contrast aperture does effect the the size of the aberrations in (2.22) and (2.23). For small aperture diameters a diffraction contribution to the aberrations must also be considered where,

$$\delta_d = \frac{0.61\lambda}{\alpha^{'}} \tag{2.24}$$

where λ is the wavelength of the electrons after they are accelerated to the column potential. The total aberration is given by a sum of all the aberrations terms expressed as,

$$\delta_{total} = \sqrt{\delta_c^2 + \delta_s^2 + \delta_d^2} \tag{2.25}$$

For magnetic imaging the photon energies used are in the soft x-ray regime. Typically the energy width of the secondary electrons is large at these photon energies which leads to chromatic aberration and a reduction in the spatial resolution of the final image. The aberrations can be reduced by using smaller contrast apertures, however, this reduces the intensity.

Once the electrostatic immersion objective lens has collected the secondary electrons emitted by the sample, an image of the sample is projected onto a microchannel plate (MPC) - florescent screen image detection system. The image that is produced on the fluorescent screen is then recorded with a CCD camera. An experimental schematic is shown in Figure 2.19.

It is worth noting that XPEEM can be used in a scanning mode where the illuminating beam is focused onto the sample (usually with a Fresnel zone plate). In scanning photoelectron emission microscopy (SPEM) peak resolutions of ~ 200 nm have been achievable [223] which gives PEEM a significant advantage over SPEM in terms of the lateral resolution.

Time Resolved XPEEM

This novel technique of time resolved XPEEM (TR-XPEEM) is is very attractive for real-time observation of dynamics of surface magnetisation processes in the picosecond regime.

Using a pump-probe setup, TR-PEEM has been used for stroboscopic imaging of a permalloy layer to study nucleation processes [4]. The growth of reversed domains was observed with a temporal resolution limited to only a fews tens of picoseconds determined by the width of the probing synchrotron x-ray pulses. It has been used to observed coherent magnetisation rotation in a Py ring [229], to observe a pair of well spaced, micron-sized Py elements in response to pulsed field excitation [230] and more recently, to observe the evolution of magnetisation patterns in an exchange-coupled Py/Cr/Py trilayer, following excitation with a magnetic field [231]. For extensive details of the technique and further examples of its applications the reader is directed to [229, 232, 233, 230, 231].

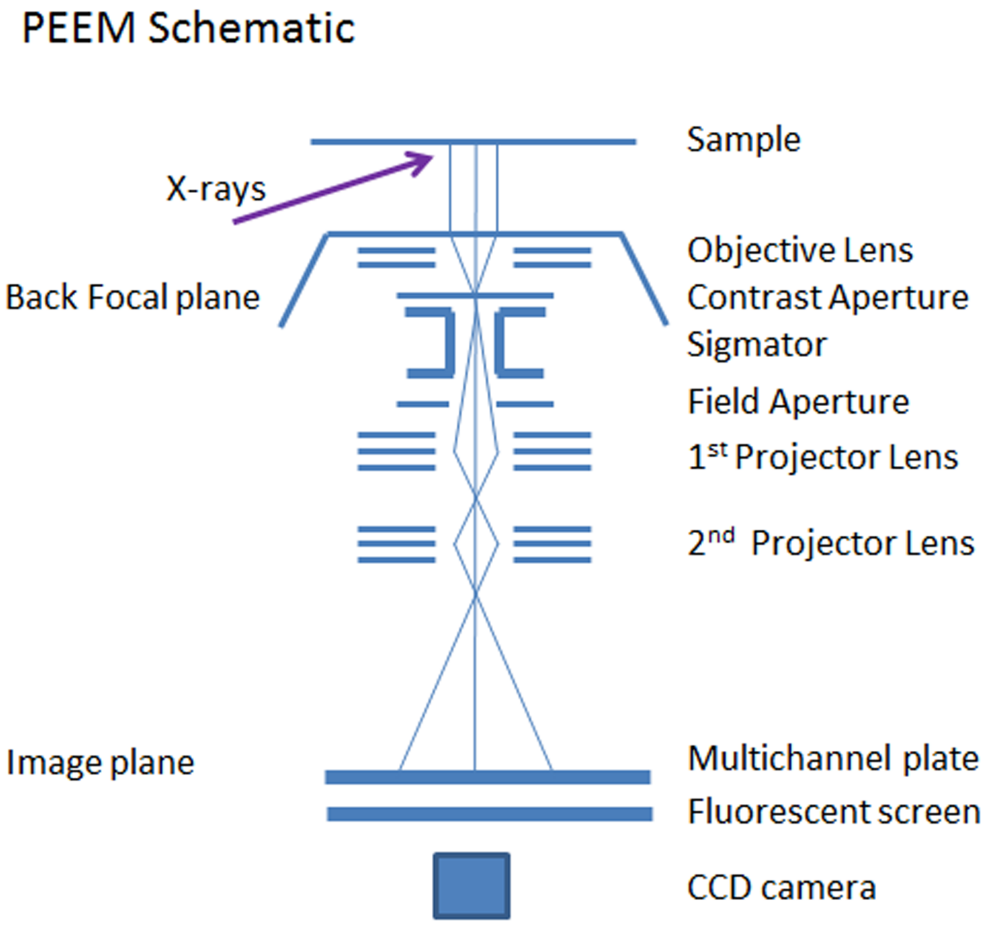

Figure 2.19: XPEEM Schematic reproduced from [228]. The sample is illuminated and radiates secondary electrons. These are collected by the objective lens and projected onto a multichannel plate, a fluorescent screen and a CCD camera to form an image of the sample.

Towards Aberration-Corrected Instruments

In order to achieve a resolution of sub-10 nm with XPEEM instruments which correct spherical and chromatic aberration are being developed. Two particular aberration-corrected instruments are SMART [234, 235] and PEEM3 [236]. This incorporates a band pass energy filter in a mode known as spectroscopic photoemission and low-energy electron microscope (SPELEEM). Predictions for spatial resolutions down to 2 nm have been made for SMART [234], however crucial influencing factors which determine this are the start energy of the electrons and their energy spread.

Summary

The advantages of XPEEM are:

- Provides fast parallel image acquisition.
- Has a wide range of zooms.
- Provides high spatial resolutions on the order of 20 nm.
- TR-PEEM can provide temporal resolutions in the range of fews tens of picoseconds.

The drawbacks of PEEM are:

- Measurements with high applied fields are not available.
- Spatial resolution is limited by aberrations of the objective lens, however, the development of aberration-corrected instruments aims to improve resolution limits to several nanometers.

2.7.3 Soft x-ray microscopy

Modern development of soft x-ray microscopes based on diffraction optics began around 30 years ago in the early 1980's [237]. Fresnel zone plate lenses of various forms are of high interest in todays instruments because they can form an image

with high resolution approaching the diffraction limit and are typically manufactured using electron beam lithography [238]. The focusing properties of Fresnel zone plate lenses can be found in [239]. There are two main types of zone plate based microscopes: transmission x-ray microscopes (TXM) and scanning transmission x-ray microscopes (STXM) (Figure 2.20). In a TXM (Figure 2.20 (a)), a zone plate magnifies a sample onto a two dimensional detector and in STXM (Figure 2.20 (b)), the sample is raster scanned through the focal point of an x-rays beam. Both modes can be used for element-specific measurement of material by tunning the energy of the x-ray beam to an absorption edge. The technique is also suitable for studying samples with applied fields [240] or environments with extreme temperatures or mechanical sample stress. For reviews on x-ray transmission microscopy see [241, 242, 243]

Transmission X-ray Microscopy (TXM)

The main advantages of TXM are its simplicity and ability to form high resolution images with short exposure times. The lateral resolutions is determined by the wavelength of the illuminating source and the width of the outer zones of the micro-zone plate [241] and typically sub-20 nm resolutions can be achieved for magnetic imaging. The micro-zone plate projects a full-field image onto a CCD camera, with exposure times of a few seconds [238]. The field of view is about 10 μm however the sample can be raster scanned to increase the field of view [244]. An experimental illustration is shown in Figure 2.20 (a).

The magnetic vortex state in nanopatterned elements has been a popular applications of TXM in recent years. A study in 2012 found that contrary to prior assumption, during the formation process of a magnetic vortex state, a magnetic nanodisc experiences symmetry breaking and a preferable state can be found [2]. This could lead to magnetic vortex structures having some potential in applications such as magnetic sensors or logic elements.

The vortex core sizes in 500 nm Py disk structures [137] is another recent application where it was shown that as the thickness of the nanoscopic Py element

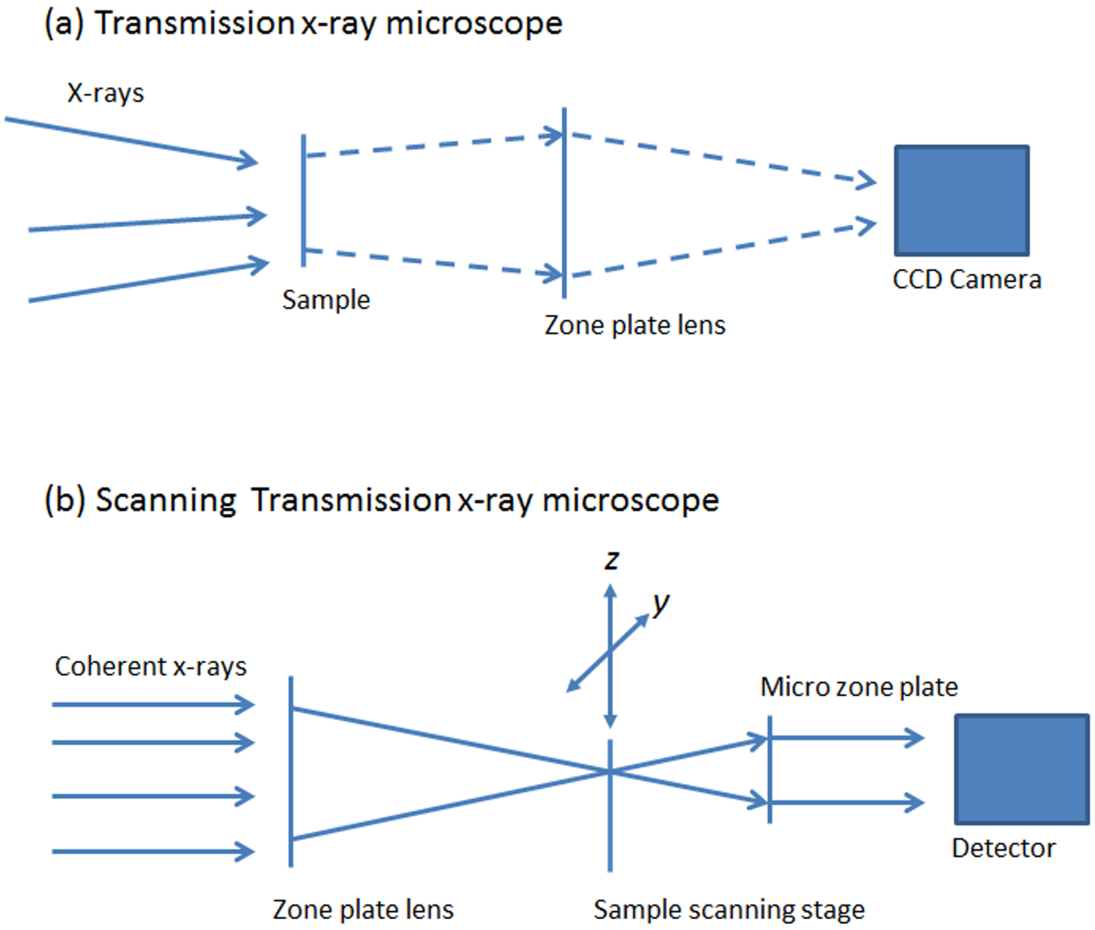

Figure 2.20: The two most common transmission x-ray microscopes that use zone plate lenses. (a) A soft x-ray transmission x-ray microscope (TXM) forms a complete image on a CCD detector. (b) A scanning transmission x-ray microscope (STXM) in which the sample is scanned through the focus point of an x-ray beam and the transmitted intensity is detected. The image of the samples structure is constructed pixel by pixel.

was decreased from 150 nm to 50 nm, the radius of the vortex core decreased from approximately 38 nm to 18 nm.

Scanning Transmission X-ray Microscopy (STXM)

The setup for a scanning transmission x-ray microscope [245, 246] is illustrated in Figure 2.20 (b). The technique requires a spatially coherent soft x-ray source which is focused to a spot on the samples surface. The lateral resolution of the final image is limited by the width of the outermost zones of the focusing lens in accordance with the Rayleigh criterion as shown in [239]. To form the image, the x-rays transmitted through the sample are detected as the sample is scanned through the focal point of the illuminating source. Because the focal point of the zone plate lens changes with the photon energy of the x-rays, the sample position has to be scannable along the beam direction in order to perform spectroscopic studies.

Typical image acquisition times can be several minutes because a large amount of intensity is lost when spatial filtering is performed to provide a coherent beam. The scanning approach also suffers from loss in spatial resolution at high scanning speeds due to the nanometer inaccuracies of the sample position when scanning.

Time Resolved TXM (TR-TXM)

The inherent timing structure of the synchrotron which provides x-ray flashes, provides a way for stroboscopic measurements to be carried out for periodic dynamic magnetisation processes. Time-resolved TXM (TR-TXM) have been performed by Stoll *et al.* [247] where ferromagnetic micron-sized elements were excited with a microcoil, and the processional frequencies of the elements were observed. The approach has since been used to image the resonant motion of the vortex core in micron-sized Py elements with spatial resolutions better than 25 nm and temporal resolutions 70 ps [248]. Further details of time resolved x-ray microscopy for magnetic dynamic studies can be found in [249, 250, 251].

Summary

The advantages of magnetic x-ray microscopy are:

- The technique is relatively simple compared with others.
- High spatial resolution of sub-20 nm can be achieved.
- Measurements are element-specific.
- Buried layers can be imaged.
- Samples can be imaged within external fields.
- Measurement of samples in extreme environments (such as low temperatures) can be performed.
- Stroboscopic measurement can be performed for periodic dynamic processes with temporal resolutions of 70 ps.

The drawbacks are:

- The resolution is limited by the diffractive optics, such as Fresnel zone plate lenses.
- The samples and substrate have to be transparent to soft x-rays.

2.7.4 Transmission Spectro-Holography (FTH)

The principles of optical and x-ray Fourier transform holography (FTH) are described in full in Section 3 so here we shall only give an overview summarising its key advantages and drawbacks in comparison to other magnetic domain imaging techniques.

The first magnetic images using x-ray FTH were published in 2004 by Eisebitt *et al.* [7], where XMCD was exploited to obtain magnetic contrast of the magnetic domains in a Co/Pt multilayer. The spatial resolution was ∼50 nm and comparable to SXTM at the time. The spatial resolution of FTH has since seen considerable improvement with the manufacturing of smaller holographic references.

To reconstruct an image of magnetic domains, a far field interference pattern is recorded between a magnetic film contained within a field of view, and a close-by reference beam. The energy of the x-ray beam in [7] was tuned to the Co L_3 absorption edge and diffraction patterns for each helicity of circular polarised light were recorded on a CCD camera. The difference between the two diffraction patterns gives a signal from just the magnetic structure in the sample and this is used to reconstruct a real space image of the magnetic domains. The reconstruction algorithm used to form the image is simply a Fourier inversion as the phase information is encoded as in the amplitude of the interference pattern and does not need to be recovered by other means.

Since its first application to magnetic imaging, FTH has been used to demonstrate domain reversal and switching processes with applied magnetic fields in many systems. Ferromagnetic films [11], nanospheres [72], exchange-coupled ferromagnetic-antiferromagnetic systems [98, 17] and dipolar coupled film with perpendicular anisotropy [16] are just some examples.

Its limitation to out-of-plane magnetisation has also been addressed by using a samples rotated within an x-ray beam [23]. Attempts have also been made to increase the size of the limited field of view (typically <2 μm) by decoupling the holographic mask (containing the object field of view and reference hole) from the sample to allow the technique to be used in a scanning mode [12]. The application of FTH to study the dynamic behaviour of magnetic bubble domains in nanoelements is feasible [18, 19] and the possibly to study periodic dynamic processes using standard pump-probe methods at 3rd generation synchrotrons is being investigated.

HERALDO imaging

Holography with extended reference by autocorrelation linear differential operation (HERALDO) is a technique where extended reference object can be used for FTH. This will prove useful for FTH imaging of magnetic structure because an extended reference could be rotated within an x-ray beam and still permit light through the reference. With this geometry, the technique becomes sensitive to in-plane

magnetisation.

Secondly, HERALDO decouples the signal of the reference wave from the spatial resolution. This means that for experiments where there is a low flux, or limited number of photons (for example in single shot imaging), the signal from the reference can be increased, making sure the signal is out of the noise level of the experiment, without decreasing the final spatial resolution of the image.

Summary

To summarise what has been discussed so far, the advantages of x-ray magnetic FTH are:

- The spatial resolution is not limited by lens aberrations.
- The reconstruction algorithm to invert the diffraction pattern to a real space image is simply a Fourier transform.
- High spatial resolution of sub-30 nm can be readily achieved.
- Measurements are element-specific.
- Buried layers can be imaged.
- Samples can be imaged within external fields.
- Measurement of samples in extreme environments (such as low temperatures) can be performed.
- Stroboscopic measurement could be performed for imaging dynamic processes.

The drawbacks are:

- Requires coherent illumination.
- The field of view is limited by the coherence of the illumination.
- Integrated holographic masks typically have to be manufactured for each sample.

- Difficult to achieve magnetic contrast for in-plane magnetisation (perpendicular to the illuminating source).
- Spatial resolution is limited by the size of the holographic reference.

2.8 Comparison of Domain Observation Techniques

One can identify three length scales with different orders of magnitude which are important for magnetic imaging because impact to the overall properties of the material can occur at each level. On the larger side at length scales of $\sim$1 μm, lies many magnetic structures (such as spin valve heads) that are lithographically fabricated for applications. Secondly, the typical size of crystallographic grains in magnetic materials are on the order of $\sim$10 nm and finally the atomic sizes on the order of 0.1 nm. Whilst many of the domain observation techniques can provide spatial resolutions below 1 μm, when imaging structures that are micron-sized, it is still desirable to have a spatial resolution below 100 nm [45].

Whilst understanding structure is crucial, it is also important to be able to understand the dynamics of the magnetic domains. In recent years the dynamics of patterned nanostructures has attracted enormous interest as access to these processes has become more accessible with the advances in temporal and spatial resolutions of instruments with surface sensitivity. For magneto-optical Kerr microscopy alone meeting all these demands has becoming challenging because the spatial resolution is limited by the photon wavelength. Lorentz microscopy is an alternative technique that whilst providing high resolution images, it lacks surface sensitivity and temporal resolutions are somewhat limited in comparison to other techniques. MFM is another widely used and highly versatile technique that can provide high resolution images of surface magnetisation. The orientation of the magnetisation in domains is not directly probed and so magnetisation configurations in complex samples can remain obscured. Along with this disadvantage MFM is a slow scanning technique and so does not allow the opportunity for dynamic imaging. SPLEEM, SEMPA, SNOM [252] and SNOM [253] provide high resolu-

tions of surface layers, however in general, the focus of these techniques are for quasi-static magnetic images.

XMCD can be used for XPEEM, x-ray microscopes and FTH in full-field and scanning modes as a mechanism for magnetic contrast with element specificty. In comparison with magneto-optical Kerr microscopy, the wavelengths of the x-rays are much shorter and so much higher resolutions can be achieved with the x-ray techniques. Whilst the spatial resolution may not match the atomic resolutions that can be achieved with SP-STM, synchrotron based techniques offer high temporal resolutions and the unique advantage of providing element-specific contrast with sensitivity to buried layers in the sample. In addition, the XMCD contrast mechanism is directly correlated with the local spin and orbital moments in the specimen and each of these component contributions can be separated with sum rules [254, 255, 256]. There are three sum rules which can be used for determining information about the electronic and magnetic properties of the sample. The sum rules quantitatively link the intensities of the x-ray scattering signal to, the charge distribution [256], the spin moments [255] and the orbital moments [254] of the magnetic material. Further details of the sum rules can be found in [257].

Compared with parallel imaging techniques, scanning approaches are generally slower and often the temporal resolution is not suitable for real-time studies of magnetisation. This makes XPEEM, TXM and x-ray FTH particularly suited for the study of magnetic dynamic processes.

As a rule of thumb, buried layers can be "seen" by an imaging technique providing their depth is no greater than three times the sampling depth of the probe [45]. In XPEEM the probe depth is at most $\sim$5 nm and because of this high sensitivity to surfaces, capping layers can become problematic if they are too thick. With soft x-ray transmission techniques i.e. TXM, STXM and x-ray FTH, the soft x-rays can typically penetrate through about 100 nm of ferromagnetic material [45]. The limitation with x-ray transmission approaches are the requirement for the sample substrate to be transparent in the soft x-ray regime. Silicon nitride membranes are typically used as substrates because they are mechanically robust and incred-

ibly thin membrane films ($\sim$ 30 nm thick) can be manufactured [258]. The thin membrane films are particularly useful for transmission x-ray experiments because they are largely transparent to x-rays. Because the transmission techniques are photon-in photon out, they are unaffected by the presence of magnetic fields which is a limitation in XPEEM measurements because of the influence fields have on the secondary electrons used for imaging.

X-ray FTH is a highly desirable technique because it provides many of the advantages that are associated with x-ray microscopes, with the addition that the resolution of the image is not limited by the aberrations of diffractive optics, but instead by the size of the reference.

Compared with XTM, holographic imaging requires additional sample preparation because a holographic masks has to be integrated onto one side of the sample. Whilst this is less convenient and requires the use of nanofabrication tools such as FIB, the procedure is relatively straight forward and can be automated to batch process samples [19].

A second advantage of XTM over FTH is the difference in the restrictions of the field of view. In XTM is is limited to $\sim$10 μm compared with $\sim$2 μm in FTH (as determined by the size of the coherent region of the beam). Whilst this is not ideal for studying large areas of a sample, it is adequate for studying individual sub-micron sized elements and the microscopic structure of thin films.

Further still the magnetisation orientations that conventional FTH is sensitive to is limited by the geometry of the setup. The XMCD signal used for magnetic contrast scales with the dot product of the incident wave vector of the x-rays and the magnetisation vector. Typically a pinhole provides a holographic reference in FTH and the sample plane is placed orthogonal to the incident x-rays to allow the x-rays to be transmitted through the sample. In this geometry the XMCD contrast is only sensitive to magnetisation in and out of the plane of the sample. To achieve in-plane magnetic contrast the sample is typically rotated within the beam so that the in-plane magnetic moments are no longer orthogonal to the direction of the incident x-rays. In x-ray microscopy this is not a challenge because the sample

can simply be rotated, however in FTH, due to the integrated holographic mask, this become significantly more challenging because the narrow reference hole no longer permits light to pass through it if rotated within a beam. In-plane imaging using FTH has been achieved [23], however it will be difficult to improve the spatial resolution of this technique to match those that can be achieved with TXM simply because of the difficulty associated with fabricating the special inclined reference pinholes required with the technique.

2.9 Summary

In this chapter we have review the background theory behind ferromagnetism and critically reviewed many imaging techniques that are used in modern day experiments of characterising and imaging magnetic samples. In the last section we directly compared all the imaging techniques that have been discussed concluding that whilst conventional FTH may not require optics to form an image, it does suffer from other drawbacks which limits it's flexibility as a versatile magnetic imaging technique.

Using extended references overcomes some of the limitations associated with conventional FTH which will now be discussed.

The Need for Lensless Magnetic HERALDO Imaging

The difficulty of accessing in-plane magnetic contrast is a major restriction of FTH that HERALDO imaging can resolve. Because the holographic reference is not limited to a pinhole, a large object can be used that can be rotated within an x-ray beam and still permit light to transverse through it. This will make the FTH imaging a more flexibility tool with rotation capabilities that will allow one to control the signals sensitivity to in-plane and out-of-plane magnetisation.

A second advantage with the HERALDO technique over conventional FTH is the decoupling of the size of the reference with the resolution of the image. In conventional FTH, the size of the reference is reduced to improved the spatial

resolution at the cost of providing a significantly weaker reference signal. This problem is alleviated in HERALDO because the resolution is not determined by the size of the reference but instead by the sharpness of its features. With HERALDO a reference structure can be tuned so that the signal from the reference is equivalent in amplitude to the signal from the object and this will maximise the contrast of the interference fringes in the recorded hologram.

With regards to reflection holography in the x-ray regime, a difficulty lies in the weak signal from reflected x-rays. If using a pin structure to provide a reflective point source, the signal is expected to be incredibly weak. By using HERALDO in reflection geometry a larger reference structure can provide a much stronger reflected signal. An Investigation of x-ray HERALDO imaging in reflection geometry is presented in Section 8.

Chapter 3

Principles of Optical and Soft X-ray Holography

The field of optics has steadily progressed since the 1930s and has been the driving force behind many important achievements in physics. Its history is full of examples where Fourier synthesis techniques have greatly advanced the fields of signal-and-image-processing. In 1960 the first optical laser (a ruby laser) was built by Theodore Maiman which is still considered one of the most important modern inventions mankind has made. The ingenuity came from Einstein [259] in 1916 when he suggested the concept of stimulated emission and the idea of lasing.

3.1 Stimulated Emission

If one considers a two level quantum system as a simplistic model of an atom, when light is shone onto the atom, absorption of a photon can occur if the energy of the photon, $\hbar\omega$, is equal to the finite energy gap between the levels. The process of absorption is illustrated in Figure 3.1. Absorption will promote an electron from the lower energy level, E_a, to an upper state, E_b.

The lifetime for which the electron remains in the exited state is finite because the system will naturally relax into its lowest energy state. After an average lifetime, τ, the electron will spontaneously fall back down to the lower energy level

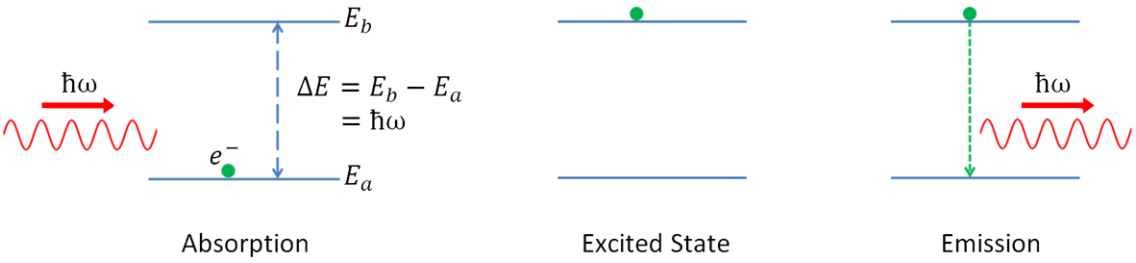

Figure 3.1: Illustration of photon absorption and spontaneous emission by an atom modelled as a two state quantum system

Figure 3.2: Illustration of stimulated emission where an input photon prompts an electron to fall from an excited state causing it to emit a second photon which is coherent to the input photon.

resulting in the emission of a photon with the same energy as the energy gap ΔE. In this two state model there is no higher energy level above the excited state so the electron cannot be promoted further. If an electron is already in the excited state, and before spontaneous decay it is subjected to an external photon with the same energy as ΔE, stimulated emission will occur, Figure 3.2. The external photon prompts the electron to fall down to the lower energy state and emit a photon which is coherent to the stimulating photon.

In quantum mechanics the spontaneous emission of an electron is in fact stimulated emission in disguise. If the atom in an excited state is within a vacuum, the stimulation for decay comes from zero point fluctuations in the vacuum energy. For ease of understanding it is often more useful to consider spontaneous emission and stimulated emission as two distinct processes. Stimulated emission is the key principle behind understanding how a laser operates. It requires some statistical thought and the manipulation of electron populations in the different energy levels

within an atom. The rate of absorption, emission and the lifetime of electrons in the excited state are therefore important factors for designing a laser. When absorption occurs, there will be an associated rate of absorption relating to the population of electrons, N_b, in the upper state within a time dt. This will depend upon the population of electrons, N_a, in the lower state, and the energy density of photons, $\rho(\omega)$, with the associated energy ΔE.

$$R_{absorption} = B_{ab} N_a \rho(\omega), \tag{3.1}$$

where B_{ab} is an absorption constant. There is also a rate of emission, which is the rate at which the upper state is depopulated. This depends upon the spontaneous emission, and thus number of electrons in the upper state, and also the stimulated emission.

$$R_{emission} = A N_b + B_{ba} N_b \rho(\omega), \tag{3.2}$$

where A is an emission constant relating to spontaneous emission and B_{ba} is an emission constant relating to stimulated emission. The constants A, B_{ab} and B_{ba} are known as Einstein coefficients and are derived by considering the system in a state of dynamic equilibrium, i.e. $R_{absorption} = R_{emission}$. At equilibrium the energy density according to Einstein's approach is

$$\rho(\omega) = \frac{A}{B_{ab}(\frac{N_a}{N_b}) - B_{ba}}. \tag{3.3}$$

In blackbody radiation theory, Max Planck defines energy density as

$$\rho(\omega) = \frac{\hbar\omega^3}{\pi^2 c^3} \frac{1}{exp(\frac{\hbar\omega}{k_B T}) - 1}. \tag{3.4}$$

The Boltzmann distribution can be used to describe the population of electrons in the two energy states, $N_a \propto exp(\frac{-E_a}{k_B T})$ and $N_b \propto exp(\frac{-E_b}{k_B T})$ and for Einstein's equation to agree with Plancks law, B_{ab} must be equal to B_{ba}. i.e. the coefficient associated with absorption is equal to the coefficient associated with stimulated emission and thus absorption and stimulated emission occur at the same rates when in a state of equilibrium. Einstein's equation for the energy density is equivalent to Plancks law if

$$\rho(\omega) = \frac{A}{B} \frac{1}{exp(\frac{\hbar\omega}{k_B T})} \tag{3.5}$$

where $B_{ab} = B_{ba} = B$. An operational laser requires a system out of an equilibrium state and requires the conditions that stimulated emission is greater than (i) spontaneous emission and (ii) absorption. The Boltzmann distribution will no longer apply when the system is out of equilibrium however the Einstein coefficients A and B remain constant whether the system is in equilibrium or not. The conditions where stimulated emission supersedes spontaneous emission is proportional to the cube of the frequency of emitted radiation ($A = \frac{\hbar\omega^3}{\pi^2 c^3} B \propto \omega^3$). Frequencies in the x-ray regieme are larger tham frequencies in the optical regieme, which is why it is particularly challenging to make an x-ray laser whereas optical, infrared or microwave lasers are relatively straight forward to build. Suppose we write

$$\begin{aligned} \frac{R_{emission}}{R_{absorption}} &= \frac{BN_b\rho(\omega) + AN_b}{BN_a\rho(\omega)} \\ &= \left(\frac{B\rho(\omega) + A}{B\rho(\omega)}\right)\left(\frac{N_b}{N_a}\right) \\ &= \left(1 + \frac{A}{B\rho(\omega)}\right)\left(\frac{N_b}{N_a}\right), \end{aligned} \tag{3.6}$$

to increase the rate of stimulated emission with respect to the spontaneous emission one can increase either the rate of stimulated emission or absorption. When this first condition is met, $\frac{A}{B\rho(\omega)} \to 0$ and thus

$$\frac{R_{emission}}{R_{absorption}} \approx \left(\frac{N_b}{N_a}\right) \tag{3.7}$$

For a system where stimulated emission dominates over absorption, a state of population inversion needs to be maintained. Population inversion is simply a state where the population of electrons in N_b is greater than the population of electrons in N_a, however, such a state is not possible to attain with a two level quantum system because it becomes saturated once equilibrium is reached. A way to create a population inversion that can be maintained is to use a higher ordered set of energy levels such as a three level quantum system which is the basis of the ruby laser.

If we consider a two level system but now with an additional metastable energy level, E_c, which lies between E_a and E_b, we can begin to understand how lasing can be achieved. If we pump electrons from the ground level E_a to the excited level

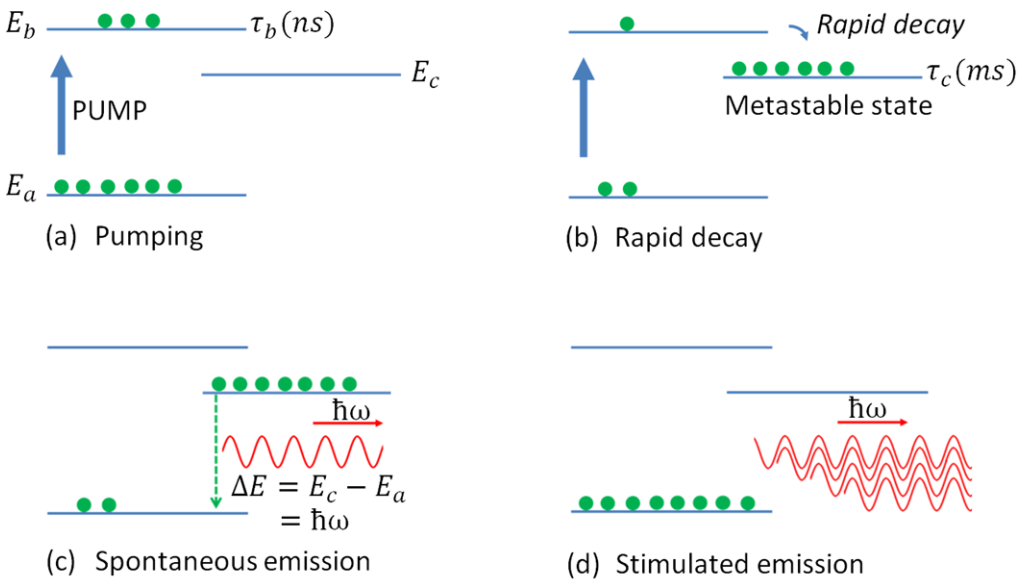

Figure 3.3: Lasing from a three level quantum system. (a) Electrons are pumped from the ground level into an excited state which has a short average lifetime on the order of nanoseconds. (b) The electrons rapidly decay from the excited state into a metastable state. The metastable state has a much longer average lifetime on the order of milliseconds and population inversion is achieved between the metastable state and the ground level. Spontaneous emission eventually occurs and an electron from the metastable state falls to the ground level. (d) The spontaneous emission of a photon acts as a seed for many stimulated emissions of perfectly coherent photons.

E_b, the number of electrons in E_b will always remain lower than the population within E_a, as is the case with the two level quantum system, and no population inversion occurs between levels E_a and E_b. Now suppose the lifetime, τ_b, of level E_b was very short. The electron from E_b rapidly decay into the metastable level E_c which has a much larger left time, τ_c. The energy level E_c fills with electrons and a population inversion is achieved between level E_c and E_a. Spontaneous emission will eventually occur and an electron from E_c will fall to E_a and emit a photon. This single photon will trigger the stimulated emission of another electron from E_c to E_a which results in a second photon being emitted with total coherence to the first. An avalanche effect then occurs and an exponential amount of coherent photons are emitted. The lasing transition in Figure 3.3 is between E_c and E_a, but this is not the only possible way to achieve lasing in a three level system. If E_b was a metastable state instead of E_c, then the lasing transition could occur between E_b and E_c, with rapid decay occurring between level E_c and E_a.

3.2 The Helium-Neon Laser

A laser is typically named after the active medium which is lasing. A HeNe laser is pumped by electrically exciting a low pressure mixture of helium and neon gases within a Fabry-Perot cavity. The pump is a collision based method and its mode of operation is through continuous pumping rather than a pulsed excitation. The laser operation can be summarised by five steps. (1) A DC electrical discharge or radio frequency (RF) excites He atoms. (2) Collisions with the excited atoms efficiently transfer energy to the Ne atoms which promote electrons to the metastable $3s^2$ energy state. (3) Lasing occurs as electrons fall to one of several Ne $2p$ states. (4) Spontaneous emission occurs causing the Ne $2p$ electrons to rapidly fall to the 1s state. (5) Collisions with the cavity walls cause Ne atoms to lose energy and electrons fall from the 1s state to the ground state. Standing waves resonate in the cavity but only certain frequencies are amplified. The length of the cavity is chosen so that those frequencies include the quantum lasing frequency. Additional frequencies around the lasing energy gap exist because the stimulated emission is

not a delta function but instead a Gaussian distribution. Higher harmonics also occur due to the several modes the cavity amplifies. The laser used for all optical diffraction experiments throughout this thesis was a Melles Griot, class II, 1 mW HeNe laser. This is a green laser where $\lambda = 543.5nm$. The beam diameter is 0.63 mm with a beam divergence of 1.26 mrad (as given by Melles Griot product data sheets [260]).

The coherent properties of lasers are, as the name suggests, very important in coherent diffractive imaging (CDI). The HeNe laser has a high complex degree of coherence encompassing both temporal and spatial aspects that are intimately related to its oscillation mode-structure. The temporal coherence depends on the spread of frequencies emitted by the source while the spatial coherence is directly related to the beams divergence.

The bandwidth of a laser is a distribution of frequencies centred about the fundamental frequency. Broadening, δv_{nat}, of the natural linewidth occurs due to the uncertainty in energy of the lasing transition. The broadening has a Lorentzian profile and typically we get $\delta v_{nat} \cong 16$ MHz for a green HeNe laser [261]. This, and other broadening effects are small in comparison to Doppler broadening $\delta v_{doppler}$. The spectral linewidth depends on the velocity of the atom relative to the observer and due to the distribution of velocities of the radiating atoms in the HeNe gas, the fundamental linewidth is broadened as described by a Gaussian profile. Considering a HeNe laser and assuming a temperature $T = 300$ K, $\delta v_{doppler} \cong 1.7$ GHz corresponding to a longitudinal coherence length of ~ 20 cm.

Laser light has the potential for generating Gaussian beams with very high spatial coherence, arising from the existence of resonator modes that define spatially correlated field patterns. As far as optical holography is concerned, a HeNe laser provides a highly directional beam with near-perfect spatial coherence if oscillating in any single transverse mode. Almost all commercially available lasers oscillate in the lowest order mode TEM_{00} (transverse electric and magnetic field), or can be adjusted to.

This is in contrast to x-rays produced at synchrotron facilities. Synchrotron

radiation is an electromagnetic wave that radiates as a charged electron accelerates. Each radiating electron is mutually incoherent and therefore a small part of the x-ray beam has to be extracted (using a pinhole as a spatial filter [239]) so that the coherent properties are sufficient to perform holographic or indeed other coherent scattering experiments. Calculating the degree of coherence is discussed further in Section 3.4. An insertion device is a component of a synchrotron light source that is positioned into the main storage ring of the synchrotron, forcing the stored electrons to undergo oscillations as they pass through the device. We will now discuss the key concepts of undulator radiation.

3.3 Undulator Radiation

An undulator is an insertion device consisting of periodic dipole magnets generating a static magnetic field that alternates through the length of the undulator. As electrons from the main storage ring transverse through the device, they are forced to oscillate and thus radiate an electric field and orthogonal magnetic field [see Figure 3.4 (a)]. The electrons travel at relativistic speeds so the radiation pattern in the frame of reference moving with the electrons is very different from that of a stationary laboratory reference frame. In the laboratory frame of reference the wavelength of the light (λ) is perceived with a much shorter wavelength than the magnetic period (λ_u) of the undulator. The short wavelength in the laboritory frame is a result of Lorentz contraction and a relativistic Doppler shift.

In the frame of reference moving with an electron, the electron percieves the magnetic periods of the undulator moving towards it with a contracted period (λ') due to relativistic Lorentz contraction. This is given by

$$\lambda' = \frac{\lambda_u}{\gamma} \tag{3.8}$$

where $\gamma = 1/\sqrt{(1 - v^2/c^2)}$, v is the relative velocity and c is the velocity of light in a vacuum. From the perspective of the observor in the laboratory reference frame, the radiation of the electrons is reduced further by relativistic Doppler

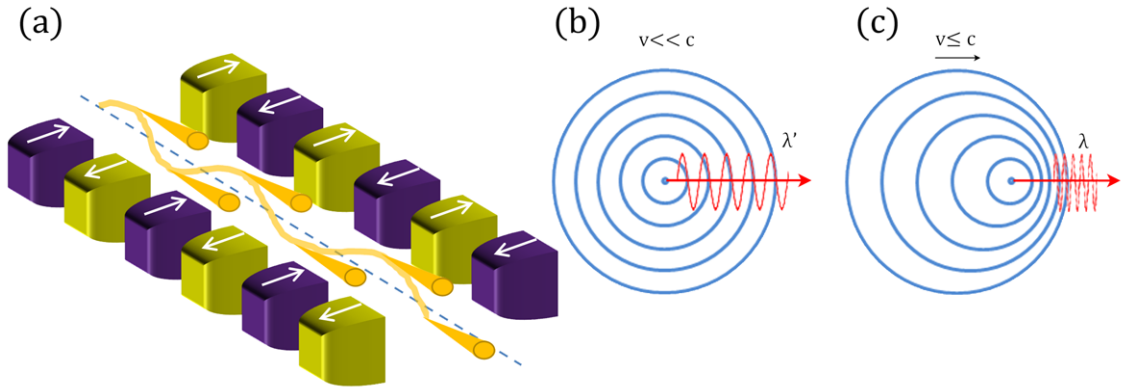

Figure 3.4: Undulator insertion device. (a) Periodic magnets (purple/yellow) generate a static magnetic field which forces a stream of electrons (orange line) to oscillate. As the electrons accelerate they radiate and an intense beam of x-rays (orange cones) is produced. The radiation from a charged electron oscillating in a direction into and out of the page is shown for (b) non-relativistic speeds and (c) at relativistic speeds. (c) The separation between successive wavefronts is dramatically compressed and the observed radiation in the stationary reference frame has a wavelength several orders of magnitude smaller than would be observed in the frame of reference moving with the electrons.

shifting. This angular dependent Doppler shift is illustrated in Figure 3.4 (b). In the frame moving with the electron, they radiate light with a wavelength as defined by (3.8). In the laboratory reference frame, the electrons appear as if they are moving at velocities approaching c. The separation between successive wavefronts is thus dramatically compresses and thus reduce the wavelength of the radiation in laboratory reference frame by several orders of magnitude. The Lorentz contraction and Doppler shift is why light in the x-ray regieme is observed in the laboratory reference frame.

The observed wavelength in the laboratory reference frame can be determined as [239],

$$\lambda = \frac{\lambda_u}{2\gamma^2} \tag{3.9}$$

This can be extended to a more general form known as the undulator equation

[239],

$$\lambda = \frac{\lambda_u}{2\gamma^2}\left(1 + \frac{K^2}{2} + \gamma^2\theta^2\right) \tag{3.10}$$

where θ is the observation off-axis angle and K=0.9337$\mathrm{B_0(T)}\lambda_u$(cm), $\mathrm{B_0}$ is the magnetic field of the undulator magnets. The undulator equation is what describes the short x-ray wavelengths that are generated by undulators which scales as a factor of $\lambda_u/2\gamma^2$. Tuning the wavelength of radiation can achieved by varying K by changing the magnet gap, which is a practical way for tuning λ [239].

3.4 Coherence

In the following section we build upon our discussion of the complex degree of coherence. The temporal coherence provides a time for which a wave will propagate with longitudinal coherence. For holographic experiments, the longitudinal coherence length must be at least equal to the total difference in path length between interfering beams. The spatial coherence describes the phase relation between two points along any one wavefront, and it is worth noting that a non-laser source is far from being spatially coherent and filtering procedures have to be taken to achieve a partially coherent beam.

Longitudinal Coherence

In Figure 3.5 we consider two waves with slightly different frequencies that are initially emitted in phase. The longitudinal coherence length, ξ_l, is the distance over which the phase difference between the two waves becomes π. It is directly related to the beams monochromaticity as discussed above and typically defined in terms of wavelength, frequency or beam energy;

$$\xi_l = \frac{\lambda^2}{\delta\lambda} = \lambda\frac{v}{\delta v} = \lambda\frac{E}{\delta E} \tag{3.11}$$

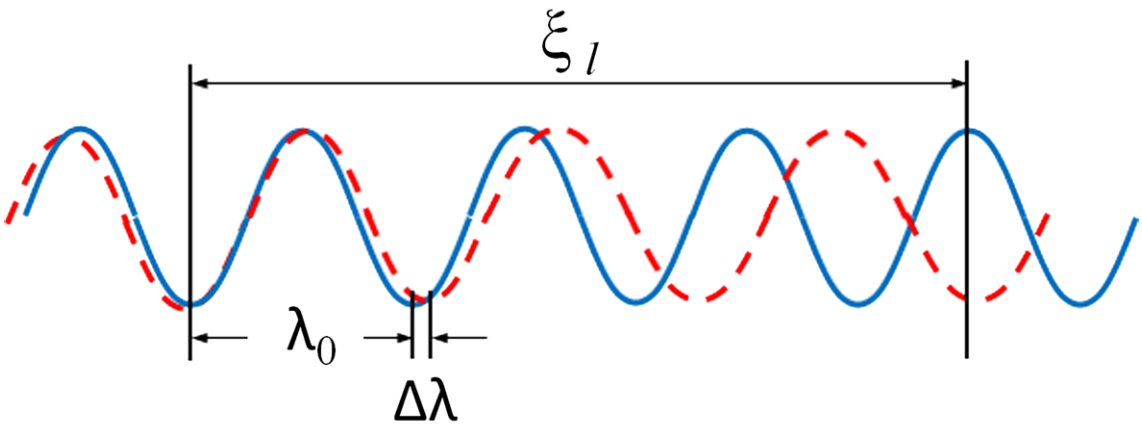

Figure 3.5: Longitudunal coherence

Transverse Coherence

The divergence of a Gaussian beam is given as $\theta = \lambda/2\pi d$, where d is the width of the source. For experimental purposes many refer to a transverse coherence length that defines a region for which the beam is spatially coherent. This improves with the propagation distance z. If we define the transverse coherence length as $\xi_t = z\theta$, one can write

$$\xi_t = \frac{\lambda z}{2\pi d} \tag{3.12}$$

This result can be described by the van Citter-Zernike theorem that states: *the degree of spatial coherence between the complex electric fields at two points is given by the spatial Fourier transform of the intensity distribution of the source.*

Note: the van Citter-Zernike theorem is valid for a quasi-monochromatic source which is made up of spatially incoherent points confined within a small area, and this area is much smaller than the distance the wave propagates before the spatial coherence is defined. A thorough explanation of the van Citter-Zernike theorem can be found in Chapter 10 of Born and Wolf [262].

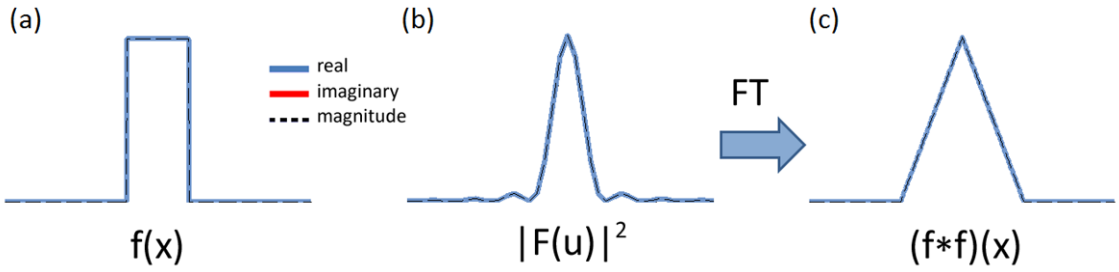

Figure 3.6: An example of Fourier transform relationships. (a) A real space top hat function. (b) The square of the Fourier transform of a top hat function produces a $sinc^2$ function (where $sinc(x) = sin(x)/x$). (c) The Fourier transform of (b) produces an autocorrelation of the top hat function in (a).

3.5 Fourier Optics

Fourier analysis provides linear operations for describing periodic behaviour within symmetric systems. It is common to see the Fourier transform applied to functions that are periodic in time, for example, the simple harmonic motion of a swinging pendulum. We, however, shall concentrate on the transform cast in the space and frequency domain. Such systems with perhaps complicated spacial periodicity can then be simplified and described by a set of discrete spatial frequencies. We define the one dimension Fourier transform as

$$\mathcal{F}[f(x)] = F(u) = \int_{-\infty}^{\infty} f(x)e^{-i2\pi ux}\,\mathrm{d}u \tag{3.13}$$

where $f(x)$ is a complex function in real space and $F(u)$ is its Fourier transform, where u represents the reciprocal space coordinate. $\mathcal{F}$ denotes the Fourier transform operator. $f(x)$ and $F(u)$ are described as Fourier integral pairs and have interesting properties which are utilized for many purposes in signal processing. By introducing a second spatial dimension, these special relationships between Fourier pairs become relevant for image processing and form the basis of the mathematics behind FTH.

The square of the Fourier transform, $\mathcal{F}|f(x)|^2$, is known as the power spectrum or intensity distribution. From convolution theory [263] (see Appendix B), it can be shown that a Fourier transform of this intensity distribution gives the autocor-

relation of $f(x)$, i.e. $\mathcal{F}\{|F(u)|^2\} = (f * f)(x)$. This is demonstrated in Figure 3.6 where a top hat, or rectangular function shown in Figure 3.6 (a) describes a real space signal. This is analogous to the transmission of coherent light through a single aperture. The power spectrum is shown in Figure 3.6 (b), which produces a $sinc^2$ function. Figure 3.6 (c) shows the Fourier transform taken of the power spectrum, which produces a triangular function resulting from the autocorrelation of the original top hat.

Let us now consider a complex function that contains some arbitrary values separated in space from a top hat function. We can consider this as a function $f_2(x)$, with two separate components $f_2(x) = f(top\,hat) + f(arb.)$. If the width of the top hat is sufficiently narrow, it can be taken to be a Dirac delta function. Figure 3.7 (a) illustrates the function $f_2(x)$, and is analogous to the transmission of coherent light passing through a single aperture that is separated in space from an arbitrary object with non-uniform density. The power spectrum of $|F_2| = \mathcal{F}|f_2(x)|^2$ is shown in Figure 3.7 (b). When a Fourier transform of Figure 3.7 (b) is taken, it produces the autocorrelation of $f_2(x)$ which is shown in Figure 3.7 (c). This features several components, but of specific interest are the two mirror images of the arbitrary function that result from the cross-correlation of the $f(top\,hat)$ with $f(arb.)$. The complex information is preserved in this procedure with both cross-correlations producing exact mirrored magnitude and real curves about the vertical axis. The imaginary component shows that the mirror images are in fact conjugate pairs. This illustration forms the basis of FTH when the analogy is extended from a 1 dimensional signal, to a 2 dimensions image.

3.5.1 Diffraction

Diffraction theory is a vital tool in any branch of physics or engineering where a description of wave propagation is desired. There are many authors who discuss the theory of diffraction in great depth and provide a more comprehensive look at the principles than what will be discussed here. In this section we shall begin with the so-called Huygens-Fresnel principle. Despite this being a scalar approximation,

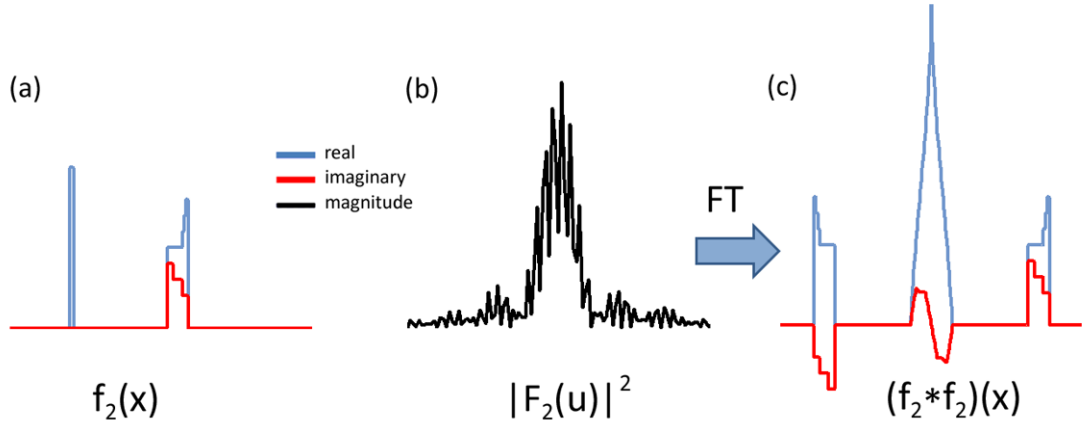

Figure 3.7: (a) A real space top hat function is separated from an arbitrary complex function. (b) The power spectrum of (a). (c) The Fourier transform of (b) demonstrates the basis of reconstructing images in FTH. Two conjugate mirror images form about the y-axis as a result of the cross-correlation of the top hat function with the complex arbitrary function.

as it neglects the vectorial nature of the electromagnetic fields, it still yields results that are remarkably similar to experimental data. The derivation that follows can be found in Section 4.1.2 and 4.2 of Goodman [264]. Figure 3.8 defines geometries that one can use to then define the Huygens-Fresnel principle as

$$E(P_0) = \frac{1}{i\lambda}\iint_{\Sigma} E(P_1)\frac{e^{ik\mathbf{r_{01}}}}{r_{01}}cos(\theta)\mathrm{d}s \tag{3.14}$$

Here $k = 2\pi/\lambda$ where λ is the wavelength. The vector $\vec{r}_{01}$ points from P_0 to P_1, with $cos(\theta) = z/\mathbf{r_{01}}$. To further simplify the principle, a binomial expansion can be used to approximate the distance $\mathbf{r_{01}}$. This yields the result for the wavefield at a distance z from the aperture as

$$E(u,v) = \frac{e^{ikz}}{i\lambda z}e^{i\frac{k}{2z}(u^2+v^2)}\int_{-\infty}^{\infty}\iint\left\{E(x,y)e^{i\frac{k}{2z}(x^2+y^2)}\right\}e^{-i\frac{k}{\lambda z}(ux+vy)}\mathrm{d}x\mathrm{d}y \tag{3.15}$$

Here the wavefield at the aperture is $E(x,y)$ and the field of the diffracted wave is $E(u,v)$. The result of 3.15 is known as the Fresnel diffraction integral. It is the Fourier transform of the complex wavefield immediately after the aperture,

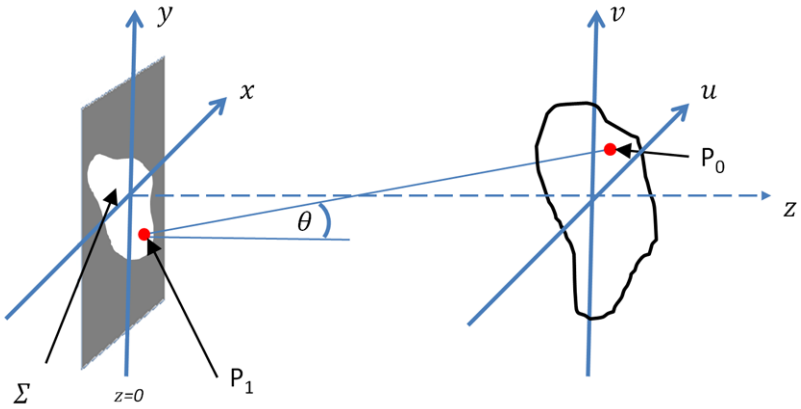

Figure 3.8: Diffraction geometry [264]. If an apertures lies in the (x, y) plane which is then illuminated in a positive z direction, one can calculate the wavefield across a (u, v) plane, at a distance z from the aperture. The (u, v) plane is parallel to the (x, y) plane.

multiplied by a quadratic phase exponential and some additional scaling factors. When $z >> \pi(x^2 + y^2)/\lambda$ then the quadratic phase exponential will approach unity over the whole aperture, and the diffracted field (bar the additional scaling factors) can be directly determined from a Fourier transform. This special case of the Fresnel approximation is known as the Fraunhofer approximation.

3.5.2 Fraunhofer Diffraction

The region where Fraunhofer diffraction becomes a valid approximation for the diffracted wave is referred to as the far field. Here

$$E(u,v) = \frac{e^{ikz}e^{i\frac{k}{2z}}(u^2+v^2)}{i\lambda z}\iint_{-\infty}^{\infty}\left\{E(x,y)e^{-i\frac{k}{2z}(ux+vy)}\right\}\mathrm{d}x\mathrm{d}y \tag{3.16}$$

which, excluding the multiplicative phase factors prior to the integral, is simply the expression for the Fourier transform of the aperture distribution. Fraunhofer diffraction occurs when,

$$\frac{W^2}{\lambda} << z \tag{3.17}$$

where W is the aperture size, λ is the wavelength. For example, at a wavelength 1.59 nm (typical of x-rays used for magnetic imaging), and an arbitary aperture of

width 10 μm, the observation distance z must satisfy,

$$z >> 0.06\, meters \qquad \text{(x-ray regime)}$$

A way to observe Fraunhofer diffraction patterns at much closer distances is for the observer to position a positive lens in place after the aperture. Using a lens in this way is often done in the optical regieme if placing the detector in the far field (as defined by (3.17)) would be experimentally impractical.

Circular aperture

If we consider a circular aperture that has a radius w, the electric field amplitude transmission function t will be,

$$t(x,y) = circ\left(\frac{\sqrt{x^2+y^2}}{w}\right) \tag{3.18}$$

If the aperture is illuminated by a fully coherent plane wave at normal incidence, $E_0(\xi,\eta)$, the complex field amplitude distribution in the Fraunhofer diffraction pattern can be calculated by substituting the intensity transmitted by the aperture into (3.16), and calculating the Fourier transform. More details of this step can be found in Goodman [264]. The complex electric field amplitude in the far field is

$$E(u,v) = e^{ikz}e^{i\frac{kR^2}{2z}}\frac{\pi w^2}{i\lambda z}\left[2\frac{J_1(kwR/z)}{kwR/z}\right] \tag{3.19}$$

where $R = \sqrt{u^2+v^2}$ is the radial coordinate in the observer plane and J_1 is a Bessel function of the first kind and order one.

It is however intensity patterns that can be detected ($I = |E(u,v)|^2$) and so upon measuring in the far field, the complex phase terms are lost. We are left with an intensity distribution

$$I(R) = \left(\frac{\pi w^2}{i\lambda z}\right)^2\left[2\frac{J_1(kwR/z)}{kwR/z}\right] \tag{3.20}$$

This is known as the Airy pattern as illustrated in Figure 3.9. The positions of the maxima and minima of the successive rings can be calculated from the known

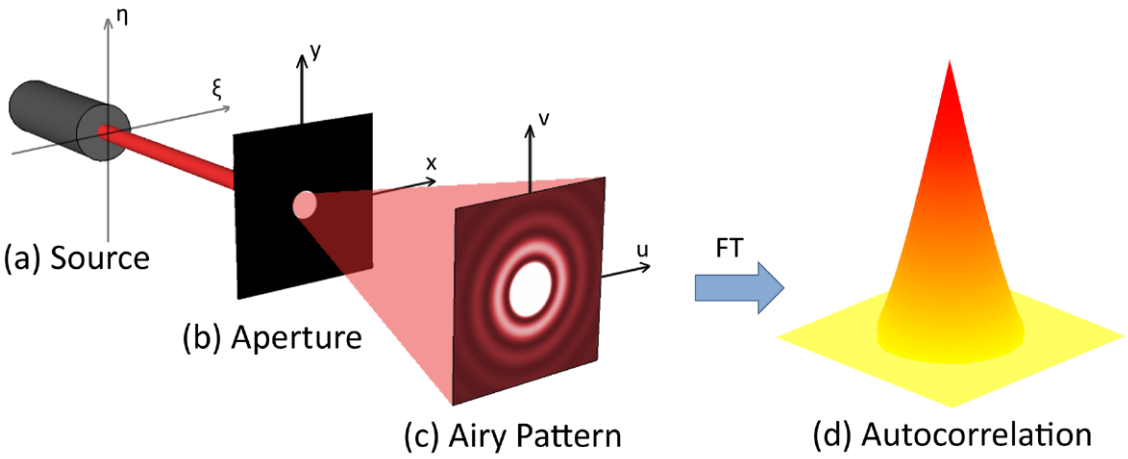

Figure 3.9: Diffraction from a circular aperture. (a) a fully coherent plane wave illuminates mask (b). (b) The mask consists of a circular aperture with radius w, which diffracts the source wave. (c) The far field diffraction forms an Airy pattern providing the observation is made along the optical axis at a distance $z >> \pi(w^2)/\lambda$. Here the central bright lobe has a width $W_{airy} = 1.22(\lambda z/w)$ measured along the u or v axis. The image thresholding has been scaled so that the successive rings are visible, because the peak intensity of the first ring is <2% of the central lobes peak intensity. The second ring is $\sim$ 0.4%. (d) Shows the fourier transofrm of the Airy pattern. It illustrates that a fourier transform of two functions that are multiplied together in reciprocal space, forms a cross-correlation of the two functions in real space. When the circular aperture is cross-correlated with itself, it gives the circles autocorrelation, producing a cone function. The width of the base of the cone is twice the size of the aperture width in (b).

roots of the J_1 Bessel function and its derivative J_1'. The width of the first central lobe measured along the u or v axis is then given by

$$W_{airy} = 1.22\frac{\lambda z}{w} \tag{3.21}$$

In Figure 3.9, a fully coherent source Figure 3.9 (a) illuminates a circular aperture Figure 3.9 (b), which diffracts the plane wave. The airy pattern that forms in the far field is shown in Figure 3.9 (c). This is an intensity pattern so contains no complex terms relating to the phase factors, as shown in (3.20). Figure 3.9 (d) shows the inverse Fourier transform of the airy pattern, revealing an autocorrelation of the illuminated aperture in Figure 3.9 (b). The cone function that can be seen is analogous to the single dimensioned triangular function discussed in Figure 3.6.

Young's Double Aperture Experiment

Thomas Young was a highly talented polymath who made many insightful contributions to science in the fields of visual perception, solid mechanics and the theory of light. Young is particularly well known for his double-slit (aperture) experiment which demonstrated the probabilistic nature of quantum mechanical phenomena and established the wave theory of light. His experiment utilises the setup shown in Figure 3.9, however, Young introduced a second aperture positioned on the mask in close proximity to the first (Figure 3.10). The Fraunhofer diffraction pattern exhibits fringes where the diffracted light from both apertures interfere with one another in the far field. This concept is fundamental to holography and in this short section we shall look at the principles that we will later build upon to explain how a reconstruction is achieved in Fourier transform holography. First we consider a mask to contain two identical apertures of width w and separation $2L$. The transmission function t will be

$$t(x,y) = circ\left(\frac{\sqrt{(x-L)^2+y^2}}{w}\right) + circ\left(\frac{\sqrt{(x+L)^2+y^2}}{w}\right) \tag{3.22}$$

By treating each aperture as separate components, the transmitted electric field at the mask will be

$$E(x,y) = E_o[t_1(x-L,y) + t_2(x+L,y)] \tag{3.23}$$

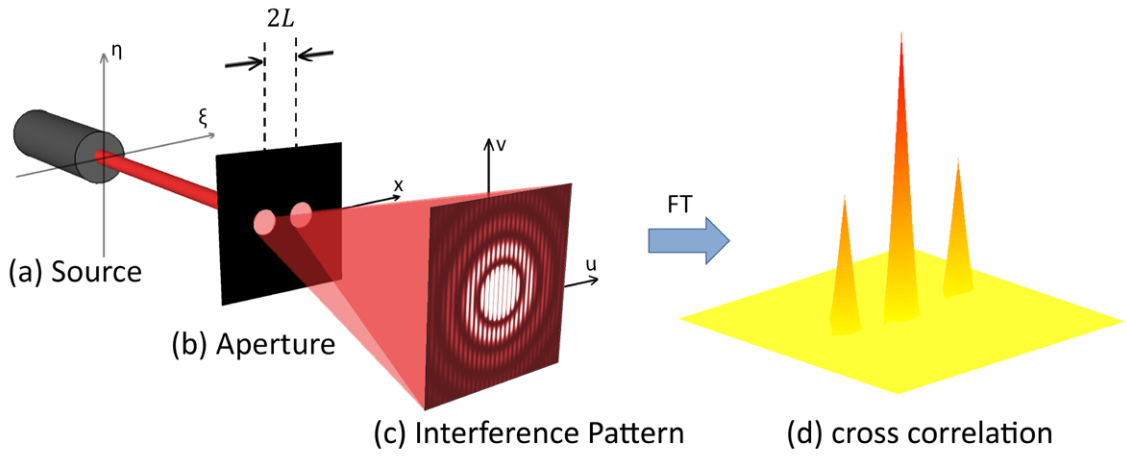

Figure 3.10: Young's interference. (a) A fully coherent plane wave illuminates mask (b) which contains two circular apertures with radius w, separated by length $2L$. (c) The far field diffraction forms an interference pattern showing fringes across an Airy pattern that would normally form from a single aperture. (d) Shows the Fourier transform of the (c). It shows three distinct peaks that come from cross-correlations of the functions defined by the illuminated mask (b). The central cone is an addition of the two autocorrelations from each aperture, and the two cones either side are cross-correlations of the two apertures with each other. The peak-to-peak separation between the central autocorrelations and either cross-correlation is given by the separation $2L$ between the apertures.

where t_1 and t_2 are the transmission function of each aperture and E_0 is the electric field of the coherent source. Taking a Fourier transform of $E(x, y)$ gives the electric field amplitude in the far field thus,

$$\begin{aligned} E(u, v) &= \mathcal{F}\{E(x, y)\} \\ &= \mathcal{F}\{E_1(x - L, y) + E_2(x + L, y)\} \end{aligned} \tag{3.24}$$

Shift theorem (see Appendix B) can be used to change the spatially different apertures so that their Fourier transforms only differ by an additional phase term.

$$E(u, v) = \mathcal{F}\{E_1(x, y)\} e^{-i\frac{k}{z}Lu} + \mathcal{F}\{E_2(x, y)\} e^{i\frac{k}{z}Lu} \tag{3.25}$$

Substituting this into 3.16, the electric field in the far field is

$$E(u, v) = \frac{e^{ikz}e^{i\frac{k}{2z}}(u^2 + v^2)}{i\lambda z}\left[\mathcal{F}\{E_1(x, y)\} e^{-i\frac{k}{z}Lu} + \mathcal{F}\{E_2(x, y)\} e^{i\frac{k}{z}Lu}\right] \tag{3.26}$$

The intensity can then be determined to be

$$\begin{aligned} I(u, v) &= |E(u, v)|^2 \\ &= \left(\frac{\pi w^2}{i\lambda z}\right)^2 \left|E_1(u, v)e^{-i\frac{k}{z}Lu} + E_2(u, v)e^{i\frac{k}{z}Lu}\right|^2 \end{aligned} \tag{3.27}$$

Upon expanding, we receive four terms that form the basis behind the reconstruction method in Fourier transform holography.

$$\begin{aligned} I(u, v) = \left(\frac{\pi w^2}{i\lambda z}\right)^2 &(|E_1(u, v)|^2 + |E_2(u, v)|^2 + \\ &E_1(u, v)E_2^*(u, v)e^{-2i\frac{k}{z}Lu} + E_2(u, v)E_1^*(u, v)e^{2i\frac{k}{z}Lu}) \end{aligned} \tag{3.28}$$

$|E_1(u, v)|^2$ and $|E_2(u, v)|^2$ each give the same result as in 3.20, forming Airy intensity patterns in the far field. The latter two terms are responsible for the fringes present in Figure 3.10 (c), where the fringe frequency $f_u = 2L/\lambda z$.

The resulting Fourier transform of the interference pattern is shown in Figure 3.10 (d). When two functions are multiplied together in Fourier space, the result in real space is a convolution of the two functions. Here, the central conical function is the sum of both autocorrelations from each aperture. The cone functions either side of the central autocorrelations in Figure 3.10 (d) are identical to each other. Each one is equivalent to Figure 3.9 (d). One cone is a cross-correlation of the two apertures, whilst the other is a convolution. They are thus a conjugate images.

3.6 Fourier Transform Holography

In the following section we will look at how an image is formed in Fourier transform holography and shall see that there are direct similarities with Young's double slit experiment, as laid out above. We shall discuss conventional methods for reconstructing an image using point-like holographic references but also, we will look at newly emerging approaches that relay on sharp features in extended objects to provide a holographic reference wave. In both cases we will look at the ideas behind the techniques followed by a mathematical treatment of the concepts illustrated.

3.6.1 Conventional Point Source References

If we replace one of the apertures from Young's interference experiment, with an aperture that can be approximated by a Dirac delta function, this will provide a well-characterised function with specific convolution properties. If we then replace the second aperture in Figure 3.10 (b) with an unknown sample, the setup for FTH is complete. Here, the well-defined delta function will act as a reference and the unknown sample will provide the object. As with Young's double slit experiment, a coherent light source illuminates both the object and the reference causing the light to diffract. We illustrate this in Figure 3.11 (a) with a simulation assuming a monochromatic light source with full transverse coherence, but providing the source is sufficiently coherent the imaging can be implemented successfully. Treatment of a partially coherent source is discussed in Section 3.4.

A Fourier transform of the electric field at the plane of the object (o) and reference (r) mask will give the Fraunhofer approximation of the electric field in the far field. If we calculate the far field intensity by squaring the magnitude of the electric field, we retrieve a hologram as shown in Figure 3.11 (b). This contains interference fringes caused by the light diffracted by the object, interfering with the scattered light from the reference. It is worth remembering that phase information is lost upon detecting intensities. Holography provides a way for phase information to be encoded as an amplitude via the method of interference. The diffracted light from the object provides an object wave, and similarly the light diffracted by the

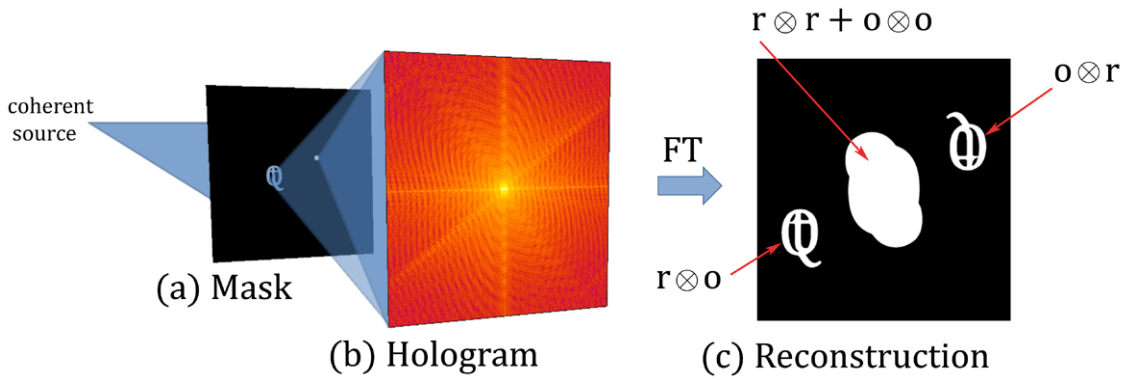

Figure 3.11: Fourier transform holography (FTH). (a) A fully coherent plane wave illuminates a mask that contains a narrow reference hole and an object. The light is scattered by the mask and a diffraction pattern forms in the far field. (b) The recorded diffraction pattern (hologram) contains interference fringes that encode phase information from the object as modulations in the intensity. A Fourier transform of the hologram gives the reconstruction in (c). In (c) there is a cross-correlation between the reference and the object ($r \otimes o$). Separated in real space, their is cross-correlation of the object with the reference ($o \otimes r$) and at the centre of the reconstruction the autocorrelation of the reference and the object ($r \otimes r + o \otimes o$). Provided there is sufficient separation between the object and reference in the mask, the central autocorrelation terms in the reconstruction will not overlap with the cross-correlation terms, and isolated images of the object can be retrieved.

reference give a reference wave. The interference in the hologram relates to a variation in phase between the object and reference waves that results from either a path length difference acquired during wave propagation or any additional phase changes induced by the objects structure.

A real space reconstruction, Figure 3.11 (c), is retrieved by taking a two dimensional Fourier transform of the recorded hologram that is typically done using a fast computer algorithm. The reconstruction is a complex image, recovering information about the object's phase. The object then appears in the reconstruction as a convolution of the reference with the object.

The mask in Figure 3.11 (a) contains an object and a reference, which is illu-

minated by a monochromatic, fully coherent source. The transmission functions $t_{ref}(x, y)$ for the reference, and $t_{obj}(x, y)$ for the object, can be treated independently such that the electric field transmitted by the mask is given by

$$\begin{aligned} E(x, y) &= E_0(t_{ref}(x, y) + t_{obj}(x, y)) \\ &= r(x, y) + o(x, y) \end{aligned} \tag{3.29}$$

where $r(x, y)$ and $o(x, y)$ are the electric fields transmitted by the reference and object. The electric field amplitude in the far field is thus

$$\begin{aligned} E(u, v) &= \mathcal{F}\{r(x, y) + o(x, y)\} \\ &= R(u, v) + O(u, v) \end{aligned} \tag{3.30}$$

where $R(u, v)$ and $O(u, v)$ are the Fourier transforms of the reference and object in the far field respectively. The intensity given by the square of the electric far field amplitude is then

$$\begin{aligned} I(u, v) &= |E(u, v)|^2 \\ &= |R(u, v) + O(u, v)|^2 \\ &= |R(u, v)|^2 + |O(u, v)|^2 + R(u, v)O^*(u, v) + R^*(u, v)O(u, v) \end{aligned} \tag{3.31}$$

and is a breakdown of all the terms which comprise the recorded hologram. The simulation of the recorded hologram [Figure 3.11 (b)] can be reconstructed by calculating the two dimensional Fourier transform of I, which reveals a real space image with spatially isolated reconstructions of the object $o(x, y)$ as illustrated by Figure 3.11 (c). The electric field amplitude of the reconstruction is,

$$\begin{aligned} E_{rec}(x', y') &= \mathcal{F}\{I(u, v)\} \\ &= \mathcal{F}\left\{|R|^2\right\} + \mathcal{F}\left\{|O|^2\right\} + \mathcal{F}\{RO^*\} + \mathcal{F}\{R^*O\} \\ &= r \otimes r + o \otimes o + r \otimes o + o \otimes r \end{aligned} \tag{3.32}$$

where '$\otimes$' denotes a cross-correlation and x', y' are real space variables in the reconstruction. The term $o \otimes r$ indicates a cross-correlation between the object and the reference that forms in the reconstruction. The reference is a real function so a convolution of $o * r$ is equivalent to the cross-correlation $o \otimes r$. $r \otimes o$ and $o \otimes r$ are conjugate pairs, the latter of which forms a twin image that is separated in real

space to form a second isolated object images in the reconstruction. They are identical in nature so no additional information can be attained from the twin image. When the reference r is approximated to a delta function, the term $r \otimes o = o$, giving the resulting image of the original object. In practice, the reference will contain some finite width that blurs the image of the original object and provides a limit upon the spatial resolution achieved in the reconstruction. The reference here is chosen to be much smaller than the sample so that the fine structure of the object can be resolved. This leads to a weak scattering contribution from the reference resulting in a reconstruction that is low in contrast. To improve the contrast, one has to increase the size of the reference hole allowing more light through. This typically renders a high resolution reconstruction with high contrast impractical.

3.6.2 Extended References

In a general sense the solution to the problem of low contrast reconstructions, without compromising resolution, is to use multiple reference sources forming several images that can be combined to improve the brightness [90, 81]. The placement of additional references must be such that overlapping does not occur in the reconstruction and thus the number of pixels available to image the sample is restricted. Numerous efforts have now been made in the field of coherent diffractive imaging (CDI) to overcome the inherent phase problem with non iterative solutions. Specially chosen complicated reference objects [265, 266] can be used in conjunction with numerical deconvolution; however, these present difficulties associated the missing frequency content of the chosen extended reference. Additional approaches include the work by Podorov *et al.* [91, 92], Enders *et al.* [267] and Guizar-Sicairos *et al.* [93, 94, 96]. The method developed by Podorov *et al.* [91], placed an object confined within a rectangular support that was uniformly illumined. The far field diffraction pattern is then modified in such a way that a particular solution upon Fourier inversion is retrieved. The approach was later generalised by Guizar-Sicairos *et al.* [93] who illustrated that a number of extended objects could be used as a holographic reference providing it contained a sharp feature.

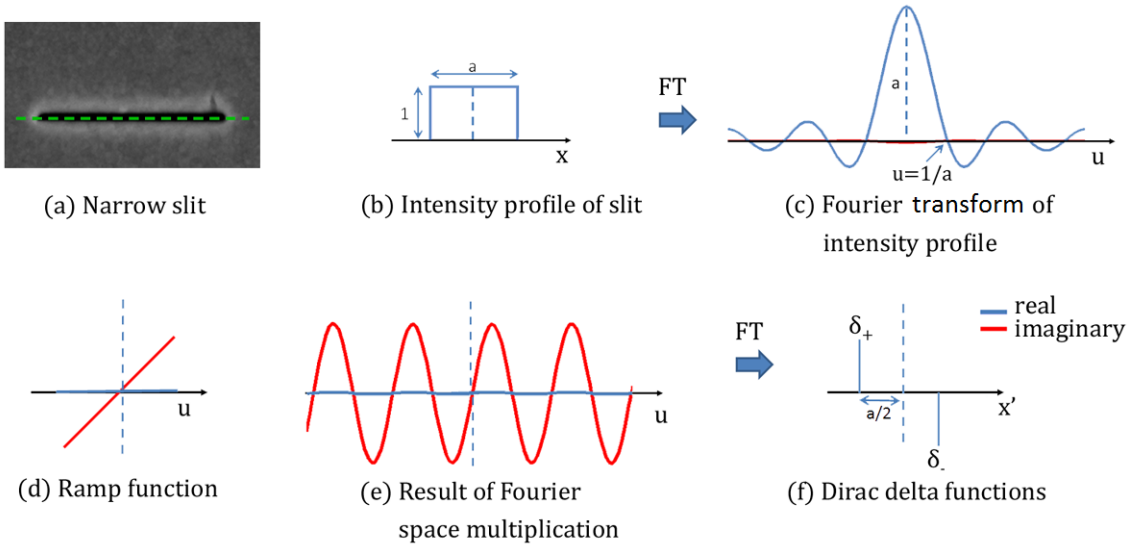

Figure 3.12: Extended reference slit. (a) Scanning electron micrograph of a narrow slit that has been patterned into a gold mask using focused ion beam milling. (b) A simulation of the intensity profile when the slit is illuminated by coherent light. (c) A one dimensional Fourier transform of (b) reveals a sinc function, equivalent to the profile through the centre of the Fraunhofer diffraction pattern of the slit. (d) A ramp function, defined as $2\pi iuR(u)$, is multiplied to (b) so that upon Fourier inversion, (e) a real space derivative of the slit attained as given by the Fourier property in (3.33). (f) The direction derivative of the extended reference slit reveals two Dirac delta functions with opposite polarity that form at either end of the slit.

One can imagine that the simplest example of an extended reference object would be to take a point-like hole and stretch it in one direction. This would give a narrow slit $r_{slit}(x, y)$ that terminates sharply at both ends. Figure 3.12 (a) is an SEM image of an extended reference, r_{slit}, that was manufactured by milling the structure with a focused ion beam (FIB) into a gold film. Figure 3.12 (b) shows a simulated profile taken along the length of the slit and revealing a broad top hat function that can also be considered as two back-to-back Heaviside step functions. The one dimensional derivative of Figure 3.12 (b) in the x direction gives two Dirac delta functions with opposite polarity forming at either end of the slit. From (3.32) we have seen that in FTH, a reconstructed image forms by a cross-correlation of the sample object with the reference. If however we could mathematically modify the hologram in such a way that the resulting cross-correlation of the object forms, not with the reference, but the derivative of the reference, the extended slit would behave as if it had been replaced with a Dirac delta function at either end.
Using derivative properties of the Fourier transforms (see Appendix B) we have the identity,

$$\frac{\mathrm{d}r(x)}{\mathrm{d}t} = \mathcal{F}\left\{2\pi i u R(u)\right\} \tag{3.33}$$

where $\mathcal{F}\left\{r(x)\right\} = R(u)$. This Fourier relationship is convenient for the technique with extended references because the derivative of a reference can be determined by a straight forward multiplication to its Fourier transform. The application of this Fourier relationship is illustrated in Figures 3.12 (c-f) where the Fourier transform of the top hat function from Figure 3.12(b) is multiplied by a complex ramp function. The Fourier transform of the resulting multiplication reveals two Dirac deltas that were digitally obtained. The next short section reveals how this concept is used in holographic imaging by taking a mathematical approach. It shows that a directional derivative of the a reconstruction will reveal isolated reconstructions that form a cross-correlation between the object and Dirac delta function rather than a broad top hat function that is defined by the extended reference.

The derivation that follows is based on the concepts illustrated above and can

be found in Guizar-Sicairos *et al.* [93]. If one assumes that for a specific choice of reference, $r(x, y)$, there exists a linear differential operator $\mathcal{L}^{(n)}\{.\}$, that when applied onto $r(x, y)$ we receive a point Dirac delta function centred at (x_0, y_0), plus an additional arbitrary function $g(x, y)$.

$$\mathcal{L}^{(n)}\{r(x,y)\} = \sum_j = A_j\delta(x - x_0, y - y_0) + g(x, y) \tag{3.34}$$

Where A_j is a arbitrary complex-valued constant. In the discussion above where a slit was used as an extended reference, $g(x, y)$ is simply a second Dirac delta separated from (x_0, y_0) by the length of the slit. If we apply the linear operator to the electric field autocorrelation from (3.32) we obtain,

$$\begin{aligned}\mathcal{L}^{(n)}\{E(x',y')\} = \mathcal{L}^{(n)}\{r\otimes r\} + \mathcal{L}^{(n)}\{o\otimes o\} + \\ \mathcal{L}^{(n)}\{r\otimes o\} + \mathcal{L}^{(n)}\{o\otimes r\}\end{aligned} \tag{3.35}$$

Using the derivative theorem for the cross-correlation of two functions (see Appendix B), we can obtain the identity

$$[h \otimes g(x, y)]' = -h \otimes g'(x, y) = h' \otimes g(x, y)] \tag{3.36}$$

where $f'(x) = \delta f(x)/\delta x$. From this identity, we write (3.35) as

$$\begin{aligned}\mathcal{L}^{(n)}\{E_{rec}(x',y')\} = \mathcal{L}^{(n)}\{r\otimes r\} + \mathcal{L}^{(n)}\{o\otimes o\} + \\ \left[\mathcal{L}^{(n)}\{r\}\otimes o\right] + (-1)^n\left[o\otimes\mathcal{L}^{(n)}\{r\}\right]\end{aligned} \tag{3.37}$$

Using the shifting properties of Dirac delta functions, from (3.35) we obtain the following;

$$\begin{aligned}\mathcal{L}^{(n)}\{E_{rec}(x',y')\} = \mathcal{L}^{(n)}\{r\otimes r\} + \mathcal{L}^{(n)}\{o\otimes o\} + (-1)^n o\otimes g + g\otimes o + \\ (-1)^n A^* o(x_0 + x, y_0 + y) + Ao * (x_0 - x, y_0 - y).\end{aligned} \tag{3.38}$$

This forms the main result from Guizar-Sicairos *et al.* [93] and is the basis behind the technique dubbed holography with extended reference with applied linear differential operator (HERALDO). The last two terms of (3.38) show that providing one can find a suitable reference and linear operator pair such that (3.34) is satisfied, when the linear operator is applied to the electric field autocorrelation,

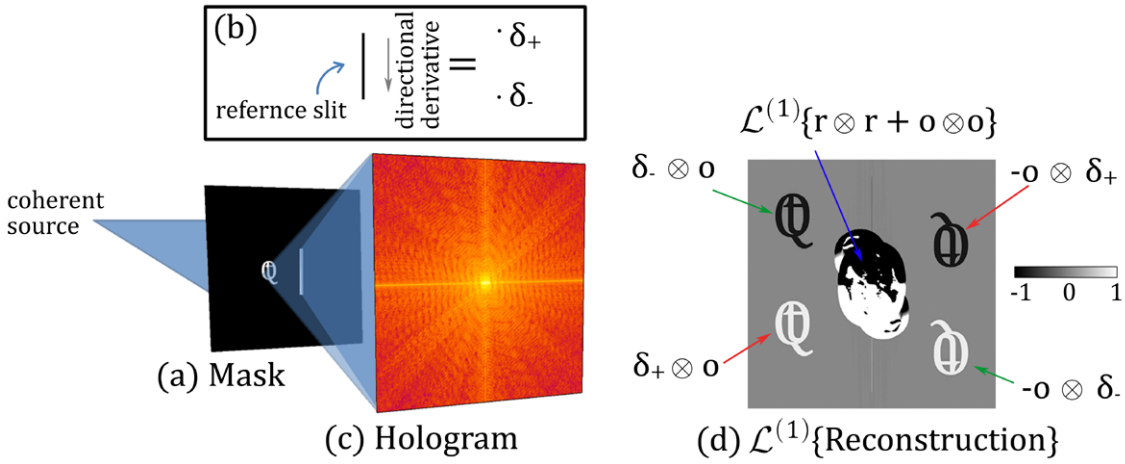

Figure 3.13: FTH with an extended reference slit. (a) A mask contains an object and a narrow slit which is used as an extended holographic reference. The inset (b) show that a direction derivative of the narrow slit reveals two Dirac delta functions labeled δ_+ and δ_-. These form at either end of the slit. The simulated hologram of the mask is shown in (c). The hologram is digitally multiplied with a linear differential filter so that when the inverse Fourier transform is taken, the reconstruction in (d) produces cross-correlation terms that result from taking a direction derivative of the reconstruction.

it results in a cross-correlation of the sample object with a Dirac delta function. Figure 3.13 is a simulation which demonstrates HERALDO imaging. In Figure 3.13 (a) a mask containing an object sample and extended reference slit is illuminated with fully coherent light. Figure 3.13 (b) illustrates that a direction derivative taken along the slit will give two Dirac delta functions at either end of the slit. These have been labeled as δ_+ and δ_-. The recorded hologram in Figure 3.13 (c) contains a bright streak which is a result of the light scattered by the slit. The hologram is multiplied by a ramp function so that a derivative of the reconstruction is obtained upon a Fourier inversion. Figure 3.13 (d) reveals that an object is reconstructed from the cross-correlation $\delta_+ \otimes o$. The image also contains a complex conjugate given by $-o \otimes \delta_+$. Note that the negative sign infront of this term is the reason for the reversal of colour contrast in the objects complex conjugate. If a second order differential operator were used to form the Dirac delta, it can been seen from (3.38) that both the object and its complex conjugate would be of the same sign. A second pair of conjugated object reconstructions can be seen in Figure 3.13 (d) that result from the cross-correlation between the Delta function δ_- that forms from the lower end of the slit. Examples where sharp corners are used as extended reference objects, such as intersecting edges of square or triangular apertures, can be found in Guizar-Sicairos *et al.* [93]. In the case of a corner reference, a second order linear differential operator is applied to satisfy (3.34), but the principles to attain the result in (3.38) remains the same.

Resolution

The resolution of the resulting reconstruction has limitations based on a number of factors. First and foremost is the fundamental limit imposed by the wavelength of the illuminating source. In the optical regime, this is typically hundreds of nanometers whereas x-ray wavelengths are much shorter and for soft x-ray magnetic imaging are on the order of 1 nm. The Rayleigh criterion is the most widely accepted criterion for determining the minimum resolvable detail. If we begin by looking at two point sources in close proximity which radiate quasi-monochromatic

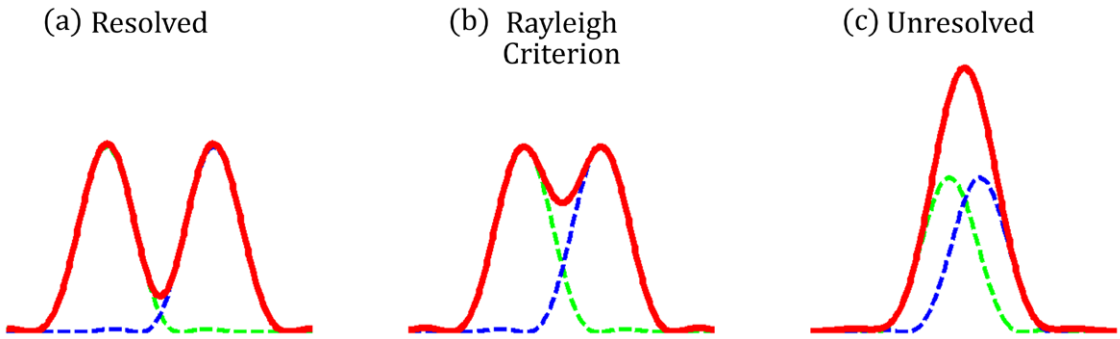

Figure 3.14: The Rayleigh Criterion. A linescan through the centre of two Airy patterns in close proximity are analysed. When evaluating the sum (red curve) of two Airy functions (blue/green dashed lines), any overlapping intensities add up. (a) Two distinct peaks are visible and the functions are considered resolved. (b) The Rayleigh criterion is such that the diffraction maximum from one peak coincides with the first minimum from the other. This is the limit in which the two peak are still considered to be resolved. (c) The two peaks overlap considerably and their individual structure is not clear from a summation. These peaks are considered unresolved by the Rayleigh criterion.

radiation such that they each form an Airy intensity patterns in the far field. In this example both sources are mutually incoherent, so the fields do not form an interference pattern, but instead the overlapping intensities add. By the Rayleigh criterion, as the two peaks are brought closer together, they can be individually resolved upto the point where the diffraction maximum from one source meets the first minimum from the other, as illustrated in Figure 3.14. As the two Airy patterns are brought closer to one another, the overlapping region between the two individual peaks increases, and it gradually becomes harder to discern the two individual Airys.

A common test of resolution is known as the knife edge test [239]. This is advantageous because it can be implemented with relative ease. If we consider a knife edge that is convolved with an Airy pattern, from the Rayleigh criterion the resolution will be equivalent to the width from the Airy's centre to the first zero. Figure 3.15 (a) shows the convolution of an Airy pattern with a knife edge.

We see that the resolution inferred from the Rayleigh criterion is equivalent to the difference between 10% and 90% of the intensity in the convolved knife edge.

In FTH, the reconstructed imaged will be given by the convolution of the reference with the sample object. Figure 3.15 (b) shows a convolution of a circular function (which is the typical transmission function of a pinhole reference) with a knife edge. From this, we can determine a general rule for determining the highest resolution one can achieve when using a reference pinhole of a certain size. Using the 10-90% Rayleigh criterion method, we can achieve a resolution of $\sim 30\%$ less than the diameter of the reference hole.

A second constraint is given by the maximum angle of scattered light that can be recorded with sufficient fringe contrast. This largely depends on the size of the detector, or rather, its field of view (FOV) of the far field diffraction pattern. In comparison to conventional FTH, the fringe contrast at large scattering angles in HERALDO is amplified due to a higher relative intensity transmitted by the reference. Whilst collecting a large FOV of the diffraction pattern is essential for achieving a high resolution in the reconstruction, it is also important that the fringes in the hologram are recorded with sufficient resolution as given by the Nyquist−Shannon sampling theorem. The period f_u of the fringes in a hologram is given by

$$f_u = \frac{x}{\lambda z} \tag{3.39}$$

where x is the real space separation between the interfering functions, λ is the wavelength of the illuminating source and z is the distance from the sample to the detector. In Young's interference experiment (Figure 3.10), two apertures were separated by $2L$. We see from (3.39) that the frequency of these fringes in Figure 3.10 (c) are $f_u = 2L/\lambda z$. The period of fringes is given by $1/f = \lambda z/x$, and so the shortest fringe period in a recorded hologram can be determined by taking x as the largest spacing S between the object and the reference. The Nyquist-Shannon sampling theorem states that a spatial frequency f_u can only be completely determined if it is sampled by a series of points spread no greater than $1/2f_u$ units apart. Thus, the detector is required to record each fringe period with at least two

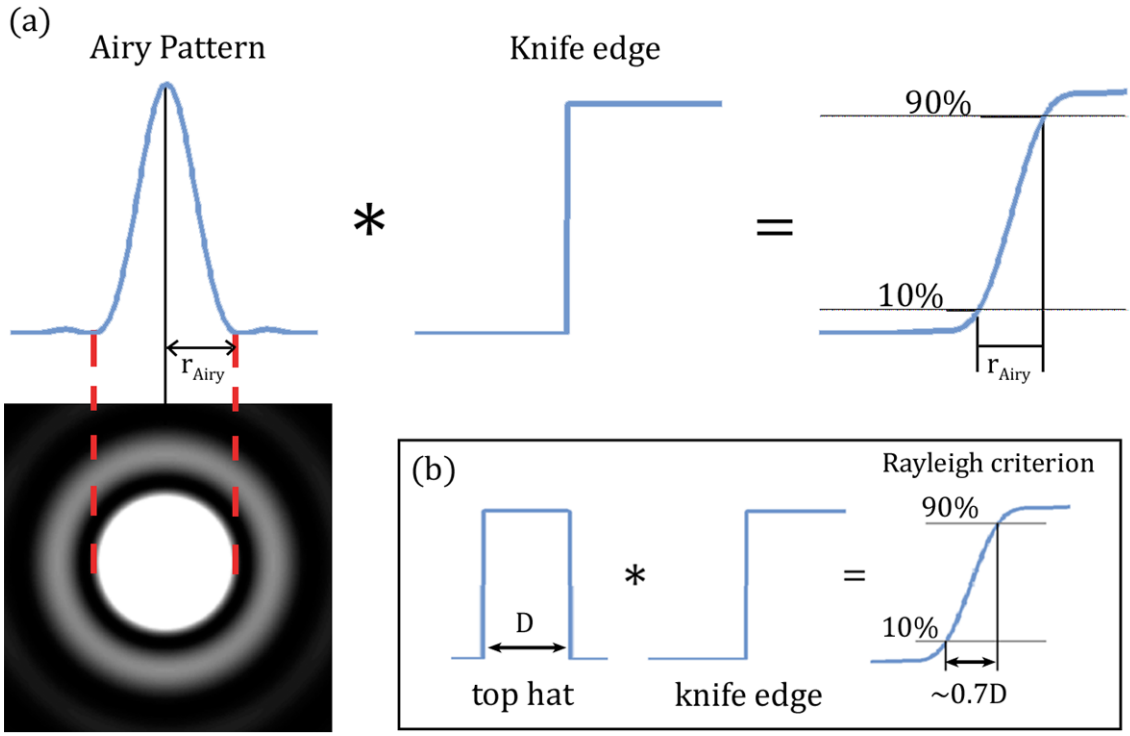

Figure 3.15: Knife edge test for a point source illumination. (a) An array pattern forms at the detector plane when a point source is illuminated. The intensity profile across the centre of the Airy pattern is numerically scanned across a knife edge/step function. The resulting convolution is shown on the right. Upon comparison with the resolution as given by the Rayleigh criterion, it can be seen that this correlates to a 10% to 90% variation in the intensity. (b) Examining the resolution that can be achived from FTH using a pinhole reference. The refernce is given by a circular function which is represented by a narrow top hat with width D. The resolution is determined by the Rayleigh criterion and is equal to $\sim$ 70% of the reference hole's diameter.

pixels. This places a upper limit on the width of each pixel that makes up the detector as $W_{u,v(pixel)} = \lambda z/2S$.

The real space reconstruction is made up of pixels and the size that each pixel represents is determined by the detectors FOV of the diffraction pattern. In the x-ray regime the Fraunhofer diffraction approximation can be measured without the use of lenses, and so the detector's FOV, and thus the largest angle of scattered light that is detected, depends on how far the detector is positioned downstream from the diffracting object-reference mask. This is illustrated in Figure 3.16 where a plan view of the experimental setup from Figure 3.11 is shown. The magnitude of the scattering vector $\mathbf{q}$ is given by

$$q = \frac{4\pi sin(\theta)}{\lambda} \tag{3.40}$$

where λ is the wavelength of x-rays and θ is the angle between the incident beam and the direction of the scattered light. The scattering from a periodic function is inversely proportional to vector $\mathbf{q}$, with a real space period given by $2\pi/q$. Rearranging (3.40) we find

$$real\,space\,period = \frac{\lambda}{2sin(\theta)} \tag{3.41}$$

From the small angle approximation we find $\theta_{max} = D_{u,v}/2z$, where $D_{u,v}$ are the appropriate dimensions of the detector and z is its position downstream from the scattering mask shown in Figure 3.16 (a). The size of each pixel in the reconstruction shown in Figure 3.16 (c) is referred to as the sampling period and relates to q_{max}. The real space width of each pixel in the reconstruction is given as

$$W_{X',Y'(pixel)} = \frac{\lambda z}{D_{u,v}} \tag{3.42}$$

In the optical regime, placing a detector in a region where the Fraunhofer approximation holds true is impractical, and so the far field diffraction pattern is generated by placing a Fourier transforming lens infront of the diffracting mask. The detector is then positioned at the focal point of the lens and the reconstructed pixel size is determined from the magnification factor of the lens as given by

$$u_{pixel(X',Y')} = \frac{(\lambda\sqrt{4fl^2 + D_{u,v}^2}}{2D_{u,v}} \tag{3.43}$$

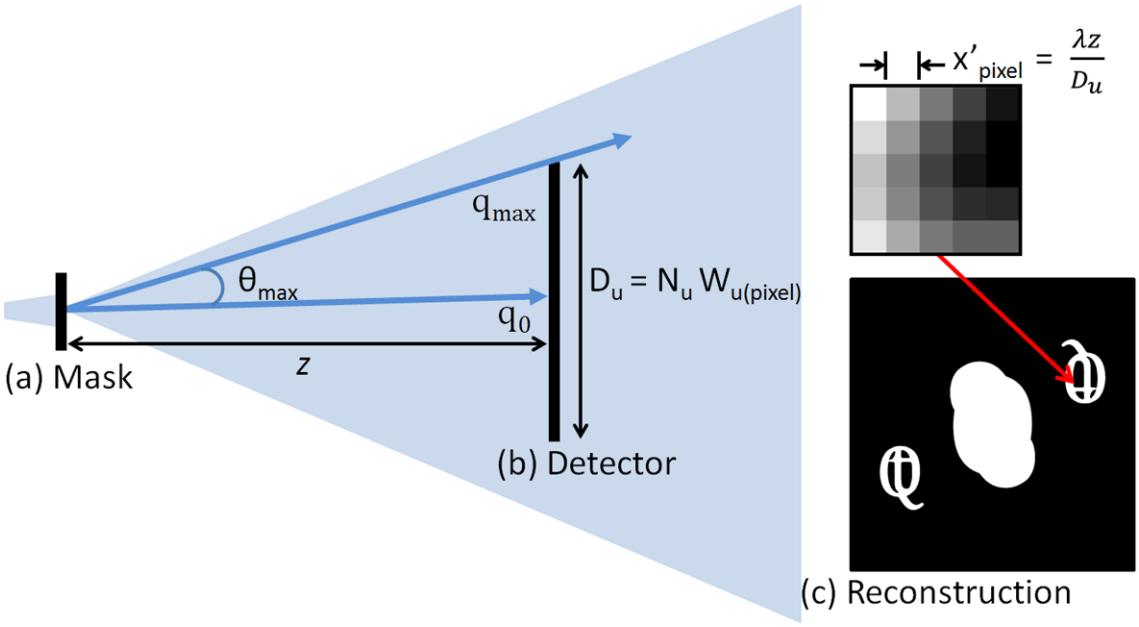

Figure 3.16: Plan view of FTH setup (a) The mask diffracts the light with a scattering vector **q**. The vector **q** depends on the size of the scatterer and the wavelength of light, with smaller particles scattering light to a higher **q**. (b) At the detector plane, the recorded intensity of the largest scattering vector depends on the size of the detector and its position downstream from the mask in (a). The size of the detector in the direction u, is given by the width ($W_{u(pixel)}$) of each pixel and the total number of pixels (N_u) in the horizontal plane. (c) A holographic reconstruction is determined from a Fourier transform of the intensity pattern at the detector. It is made up of pixels which each correspond to a real space size. The real space size that each pixels in the reconstruction represents is determined by the maximum scattering vector q_{max} which is recorded by the detector. If one finds that the reconstructed pixel size is large, the resolution of the reconstruction may be limited by q_{max}. This restriction can be overcome by simply moving the detector closer to the sample mask. This allows for higher **q** vectors to be recorded which correspond to the scattering from smaller particles.

Here, fl is the focal length of the lens. If the size or quality of the holographic reference (i.e. the size of a pinhole or the width and edge sharpness of extended references) is significantly worse than the pixel size in the reconstruction, then the reference will limit the final resolution and not the sample period.

Fringe Visibility

The visibility of the interference fringes is all-important for the reconstruction as it directly determines the precision of the phase measurements. High fringe contrast in the hologram implies a bright reconstructed image and is quantitatively measured by the fringe visibility, defined as

$$V = \frac{I_{max} - I_{min}}{I_{max} + I_{min}} \tag{3.44}$$

where I_{max} and I_{min} are the maximum and minimum intensities of the interference fringes within a small region of the recorded hologram. The visibility depends on the ratio of their intensities at the observation plane and the complex degree of coherence between the interfering object and reference waves. A point-like holographic reference has a total area that is typically much greater than the sample object area, and often this leads to a large ratio between the two contributing intensities. One can increase the size of the reference hole to improve the contrast of the image, but at the cost of lowering the resolution [98]. This problem is somewhat alleviated with HERALDO imaging and an extended reference object can be chosen so that the relative intensities from the object and reference are much more alike. If we assume the ratio of the intensities between the object and reference are equivalent and we find that the visibility is still less than unity, it implies that the illuminating beam is partially coherent.

Measuring Coherence

A Michelson interferometer is a form of amplitude division and will allow one to compare the phase of the wave at various points along the direction of its prop-

agation. Using (3.44) and a Michelson interferometer, the temporal coherence of a laser can be measured. An equivalent form of amplitude division at soft x-ray wavelength has yet to be discovered however the temporal coherence of a beamline can be measured with a grating spectrometer that can resolve the spectral bandwidth. If one assumes perfect temporal coherence, the visibility of fringes as given by (3.44) in Young's double aperture experiment (see Figure 3.10) can be used to deduce the spatial coherence of a source.

3.7 Interactions of Light with Matter

The Thomson scattering mechanism describes the interactions between incident photons with the charge density of electrons in a sample. X-ray diffraction is a powerful tool for characterising the structure of crystalline materials and here we discuss its development for probing magnetic materials.

It was in the 1970s when x-ray scattering was first thought to be sensitive to magnetism [268] and 10 years on, Platzman and Tzoars' theory was experimentally confirmed [269]. This led to the so called 'non-resonant magnetic scattering' where the incident electromagnetic wave is scattered by the spin and orbital moments of the electrons. The non-resonant magnetic scattering is much weaker than the charge scattering, however in 1988, a large resonant enhancement (a factor of 50 greater) in the magnetic absorption intensity was observed by Gibbs *et al.* [270] when the energy of the incident x-rays was tuned to the L_3 absorption edge of holumium metal.

When an electromagnetic wave meets an interface, it will be reflected or refracted. The incident wave will be scattered into a wave with wavevector $\mathbf{k}'$ or $\mathbf{k}''$ and polarisation $\mathbf{e}'$ or $\mathbf{e}''$ as defined by Figure 3.17. When x-rays interact with matter it is convenient to write the complex refractive index as

$$n = 1 - \delta(w) + i\beta(w) \tag{3.45}$$

where $1 - \delta$ and β represent the frequency dependent dispersion and absorption of light in the medium. In some literature, β is commonly referred to as the

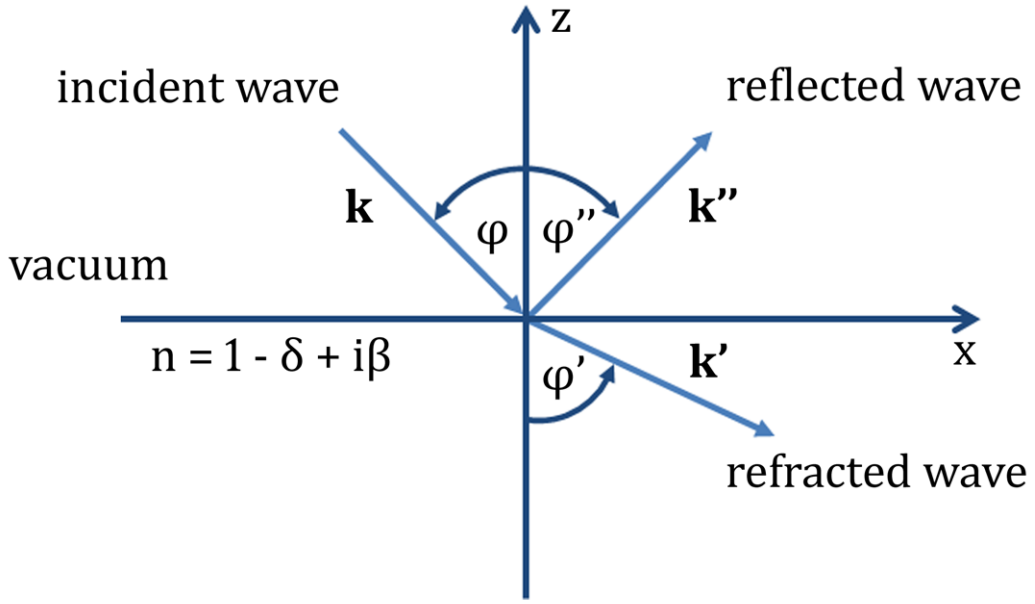

Figure 3.17: Interference geometry for incident, reflected and refracted waves [239].

extinction coefficient as it describes the attenuation of the wave as it is absorbed by the medium. The intensity of light that is transmitted through a slab of finite thickness is described by Beer's Law [271]

$$I(z) = I_0 e^{-\alpha z} \tag{3.46}$$

where I_0 is the incident intensity and $\alpha = 4\pi\beta/\lambda$ is the intensity absorption coefficient.

3.7.1 Resonant Magnetic Scattering

The phenomena of resonant absorption was discussed in Section 2.16 along with a basic introduction to x-ray magnetic circular dichroism (XMCD) as a magnetic contrast mechanism in synchrotron imaging techniques. From a scattering perspective, XMCD can be described by the effect that local magnetic moments have on the resonant coherent scattering amplitude $fa(w)$. For resonant magnetic scattering dipole transitions, the scattering amplitude is given by [272]

$$fa = F_c(\mathbf{e}' \cdot \mathbf{e}) - iF_{m1}(\mathbf{e}' \times \mathbf{e}) \cdot \mathbf{M} + F_{m2}(\mathbf{e}' \cdot \mathbf{M})(\mathbf{e} \cdot \mathbf{M}) \tag{3.47}$$

where $\mathbf{e}$ ($\mathbf{e}'$) is the polarisation of the incident (scattered) x-rays and $\mathbf{M}$ is the local magnetic moment. The term F_c concerns itself with charge scattering that becomes very large near absorption edges. The term F_{m1} gives scattering which linearly depends on the magnetisation direction but is also comparable to the charge scattering near certain absorption edges. The term F_{m2} has a quadratic dependence with the magnetisation and is much weaker than F_c and F_{m1}. Due to its small size, it will not significantly contributing to the magnetic scattering and shall be neglected in further steps.

The measured signal in FTH experiments is given by the scattered intensity as discussed in Section 3.5.2. The magnetic diffraction intensity is a function of both ω and the scattering vector $\mathbf{q} = \mathbf{k}' - \mathbf{k}$, where $\mathbf{k}$ ($\mathbf{k}'$) is the wave vector of the incident (scattered) beam. One obtains [38]

$$I(\mathbf{w}, \mathbf{q}) \propto \left| \sum_n f a_n(\omega) e^{i\mathbf{q}\cdot\mathbf{r_n}} \right|^2 \tag{3.48}$$

where the position vector r_n with a resonant electric dipole scattering amplitude is summed over all the lattice sites.

If we consider the FTH setup shown in Figure 3.11, replacing the object with a sample that possesses magnetic properties, we can insert (3.47) into (3.48) by following the steps in Section 3.5.2 and obtain a measured intensity

$$I(\mathbf{q}) \propto \left| \widetilde{F}_c(\mathbf{q}) + \widetilde{M}(\mathbf{q}) + \widetilde{R}(\mathbf{q}) e^{i\alpha} \right|^2 \tag{3.49}$$

where $\widetilde{F}_c(\mathbf{q})$ and $\widetilde{M}(\mathbf{q})$ refer to the Fourier transforms of the charge and magnetic contributions of the sample object respectfully. $\widetilde{R}(\mathbf{q})$ is the Fourier transform of the contribution from the reference object, where α describes the phase difference between the object and reference scattered waves. $\widetilde{F}_c(\mathbf{q})$ represents the electron density structure factor and $\widetilde{M}(\mathbf{q})$, the magnetisation density structure factor, of the object. $\widetilde{R}(\mathbf{q})$ gives the structure factor which comes from the reference, whether this be a pinhole or extended object. Typically the reference will only produce structural diffraction without any magnetic scattering, however in circumstances, for instance where the holographic mask is separated from the magnetic sample to provide a scanning mode [12], or a Faraday polariser for the reference [20], the

reference wave will also pass through a nanoscopic region of the magnetic sample film.

Upon reversing the helicity of circular polarised x-rays the magnetic scattering amplitude will change sign, whereas the charge scattering will remains the same. A difference image of opposite polarisations thus provides a way to extract only the magnetic scattering from an FTH reconstruction, as any charge information cancels out,

$$\begin{aligned} I(\mathbf{q})^{+} - I(\mathbf{q})^{-} \propto & \widetilde{M}(\mathbf{q})\widetilde{F}_c^{*}(\mathbf{q}) + \widetilde{F}_c(\mathbf{q})\widetilde{M}^{*}(\mathbf{q}) + |M|^2 \\ & + \widetilde{R}(\mathbf{q})\widetilde{M}^{*}(\mathbf{q})e^{i\alpha} + \widetilde{M}(\mathbf{q})\widetilde{R}^{*}(\mathbf{q})e^{-i\alpha}. \end{aligned} \tag{3.50}$$

A Fourier inversion of (3.50) then gives a holographic reconstruction with only magnetic contrast. The last two terms of (3.50) produce a convolution of the magnetic structure with the reference that are separated in space from the central cross-correlations.

$$\mathcal{F}\left\{\widetilde{R}(\mathbf{q})\widetilde{M}^{*}(\mathbf{q})e^{i\alpha}\right\} = \mathcal{F}\left\{\widetilde{R}(\mathbf{q})\right\} \otimes \mathcal{F}\left\{\widetilde{M}(\mathbf{q})\right\} \tag{3.51}$$

This result concludes our discussion on the underline theory of Fourier transform holography, and how the technique is implemented for imaging magnetic structure. It was mentioned at the end of Section 2.16 that the polarisation dependent magnetic absorption signal is proportional to the projection $\mathbf{M}\cdot\mathbf{k_i}$ of the magnetisation $\mathbf{M}$ onto the wave vector of the incident light $\mathbf{k_i}$. It is important to note here that this comes from the second term in (3.47) where the magnetic scattering amplitude is scaled by a dot product with the magnetisation vector. This is important in holographic magnetic imaging because accessing the components of magnetisation that are in-plane require different experimental geometries to those that probe out-of-plane magnetisation. In the next section we will look at an experimental overview of the research, and the progress that has been made in finding a geometry that will allow one to probe several direction of magnetisation *in-situ*.

Chapter 4

Experimental Overview

An obstacle to overcome with any magnetic imaging technique that exploits XMCD to provide magnetic contrast, is the direction of magnetisation that can be probed. From (3.47) we see that it is important for the direction of magnetisation to be (anti)parallel with the direction of the wave vector of the probing light in order to maximise the soft x-ray resonant magnetic scattering (SXRMS) signal.

Magnetic holography in a transmission geometry is a well established imaging technique. Here, an x-ray transparent substrate is positioned within the x-ray beam, with the sample plane perpendicular to the beams direction, and the forward scattering transmitted through the sample is recorded as a hologram in the far field [7]. Whilst this allows one to measure the magnetisation of thin films with perpendicular magnetic anisotropy, it does not allow one to directly probe any magnetisation vector that is in the plane of the film. Overcoming this issue in other magnetic synchrotron techniques, such as scanning transmission x-ray microscopy (STMX), is not a problem because the sample can be rotated within the beam which allows one to access the in-plane magnetic moments [273]. Unfortunately, in holography, this solution is not as trivial as it might first sound. If we consider a conventional sample used for magnetic holographic imaging [7], the sample is integrated with a fixed holographic mask that contains an object aperture and a narrow reference hole. If such a sample is rotated to an off-normal geometry within the x-ray beam, the narrow holographic reference hole will stop any throughput of

light and an interference hologram can no longer be measured.

This chapter explores several methods for measuring in-plane magnetism using holographic experiments in transmission and reflection geometries. The proposed methods are discussed in detail in the chapters that follow and provide the main results of this thesis. We start the discussion with a description of focused ion beam (FIB) and e-beam nanofabrication, which provided an invaluable tool for manufacturing many of the sample for this research. An outline of some of the main components for the experiments is then given, followed by a discussion of various experimental geometries that were used to perform the holographic imaging. For specific details about the sample design for each experiment, the reader should refer to the corresponding chapters that follow, and should note that this chapter provides an overview of the various setups and sample manufacturing tools.

4.1 Sample Fabrication

Focused Ion Beam (FIB) and e-beam nanofabrication were performed to pattern many aspects of the holographic samples. Figure 4.1 shows the Nova 600 system from FEI. This system is a dual-beam unit that provides the capability to undertake ion-beam milling and electron-beam lithography (EBL), as well as standard scanning electron microscopy (SEM).

In x-ray transmission magnetic holography experiments, the reference objects and viewing apertures were fabricated into an integrated x-ray opaque gold mask using FIB milling. Nanoscopic elements were also fabricated with FIB by etching a small region of a magnetic thin film that left an isolated nanoscopic disc or square element at the centre of the etched region. The FIB provided a key tool in the fabrication process with results that would have been difficult to achieve with electron beam lithography (EBL).

EBL provides a means of patterning large areas across a substrate with high resolution and precision. The ability to automate large area patterning is a feature that the FIB lacked, due to the small patterning field of view at the required low beam currents. This meant that lithography was the wiser choice for initial test

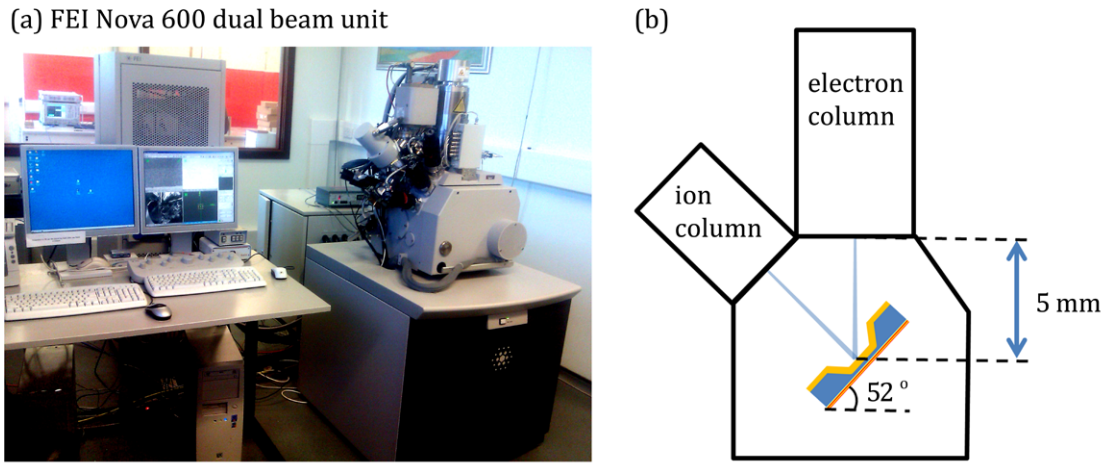

Figure 4.1: FEI Nova 600 dual-beam system. (a) FIB, EBL and SEM system in the physics department at the university of Exeter. (b) By tilting the stage to 52°, FIB milling can be performed with the ion beam.

samples that were manufactured for reflection holography experiment, as these test devices were large compared to the FIB's patterning FOV. The EBL procedure is illustrated in Figure 4.2. The method involves spin coating a substrate with a positive (negative) electron beam resist [Figure 4.2 (b)]. An image pattern file is then created that defines exactly which regions, within a certain field of view, will be exposed to the electron beam, as shown in Figure 4.2 (c). The region that are exposed become soluble (insoluble) in a developer solution. During the development stage the soluble regions are removed, as shown in Figure 4.2 (d), and what remains is a negative (positive) pattern in the resist that matches the image pattern file. Metal can then be deposited over the entire substrate [Figure 4.2 (e)]. The metal is deposited directly onto the substrate where the resist has been removed, however, every other region has a resist coating which acts as a barrier between the metal and the substrate. Finally a 'lift-off' step is performed which dissolves any resist that was not removed in the development stage. Any metal that lies on the resist, peels off from the surface, as the resist is removed. This leaves metal behind on the substrate as a positive (negative) pattern of the original image pattern file as shown in Figure 4.2 (f).

Poly(methyl methacrylate) (PMMA) was used as a positive e-beam resist [Fig-

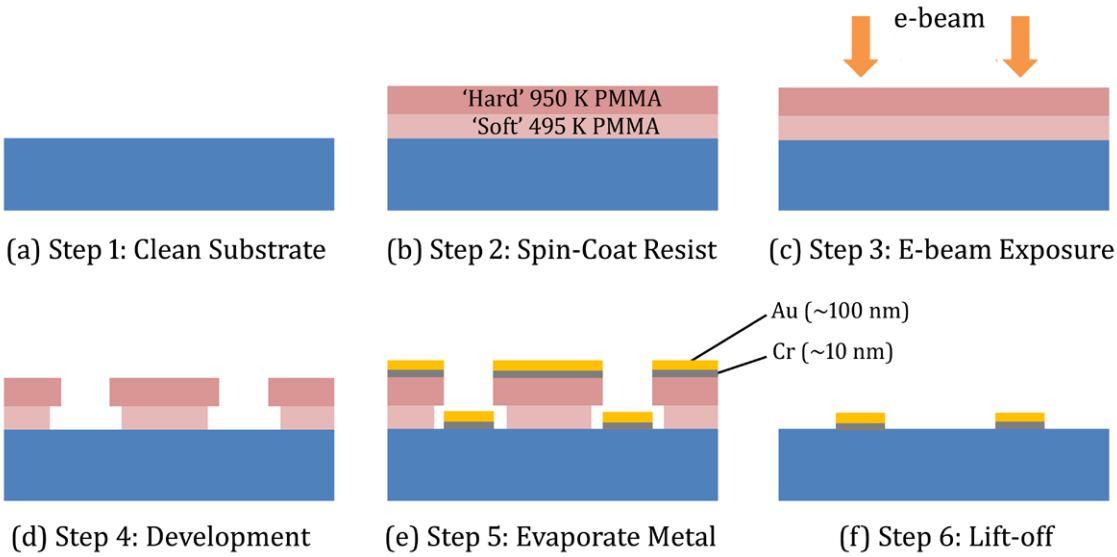

Figure 4.2: Positive E-beam lithography. The process of applying e-beam lithography to make samples for reflectivity measurements is illustrated.

ure 4.2 (b)]. In Figure 4.2 (c), exposure to the e-beam breaks the bonds in the polymer chains, making these regions soluble in a dilute isopropyl alcohol (IPA) solution. The IPA was diluted with distilled water (DW) in a ratio of 9 parts DW:1 part IPA. The e-beam exposed samples were developed in this solution for 50 seconds [Figure 4.2 (d)]. They were then placed in a solution of pure IPA for a further 5 seconds and immediately rinsed in DW and dried with nitrogen gas to stop the development continuing. After the development stage, the desired metal was deposited via thermal evaporation onto the substrate [Figure 4.2 (e)]. Typically this included a thin chromium layer (5-10 nm thick) followed by a gold film. The Cr acted as an intermediate layer which helped the Au bond to the substrate. The maximum thickness of the Au film was determined by the thickness of the resist that remained after the development stage. If a metal layer is deposited which is too thick, the Au which fills in exposed area of the PMMA becomes connected to the Au layer which is deposited onto the unexposed PMMA that remains after development. This would be problematic, and in the lift-off stage the desired pattern can also be removed as the rest of the Au peels off from the surface. The lift-off is performed by soaking the sample in acetone for ∼20 hours [Figure 4.2 (f)]. In

some cases, boiling the acetone can encourage regions to peel free from the surface more easily. Another way to achieve a successful lift-off is to use a bilayer of resist which has been illustrated in Figure 4.2 (b). Here, a 'soft' PMMA resist (495K PMMA A2) is spin-coated onto the substrate, followed by a 'hard' PMMA resist (950K PMMA A4). In this case, the bonds in the 'soft' polymer are broken with smaller exposures to the e-beam and an undercut profile in the exposed pattern, as shown in Figure 4.2 (d), can be achieved. This reduces the likelihood of a connection being made between the metal that makes up the desired pattern, and the metal to be removed in lift-off. The total thickness of the PMMA bilayer was ∼300 nm, which allowed for an Au film of up to 100 nm thick to be evaporated and still permit a successful lift-off.

X-ray Transparent Substrates

Silicon nitride (Si_3N_4) can be specially tailored into a robust thin film that is transparent at the soft x-ray energies used for magnetic imaging. It has a low atomic number and the absorption of soft x-rays is weak. 100 nm thick Si_3N_4 membranes are commercially available and were purchased from Silson Ltd. in the UK. The membranes were supported by a 200 μm thick silicon substrate frame and are made via a chemical wet etch procedure [274]. Figure 4.3 shows a schematic of these sample substrates where multiple membrane windows have been etched into a single 5×5 mm silicon support frame. The illustration shows windows that were 0.50 mm square (however 0.25 mm square windows were also used). The separation between each window was 0.38 mm (the minimum separation the fabrication etch angle would allow [258]).

4.2 Detection Mechanisms

Charged Coupled Device Cameras

A CCD camera has a large square array called a parallel register that contains many potential wells (pixels). Charge accumulates in the potential wells when the

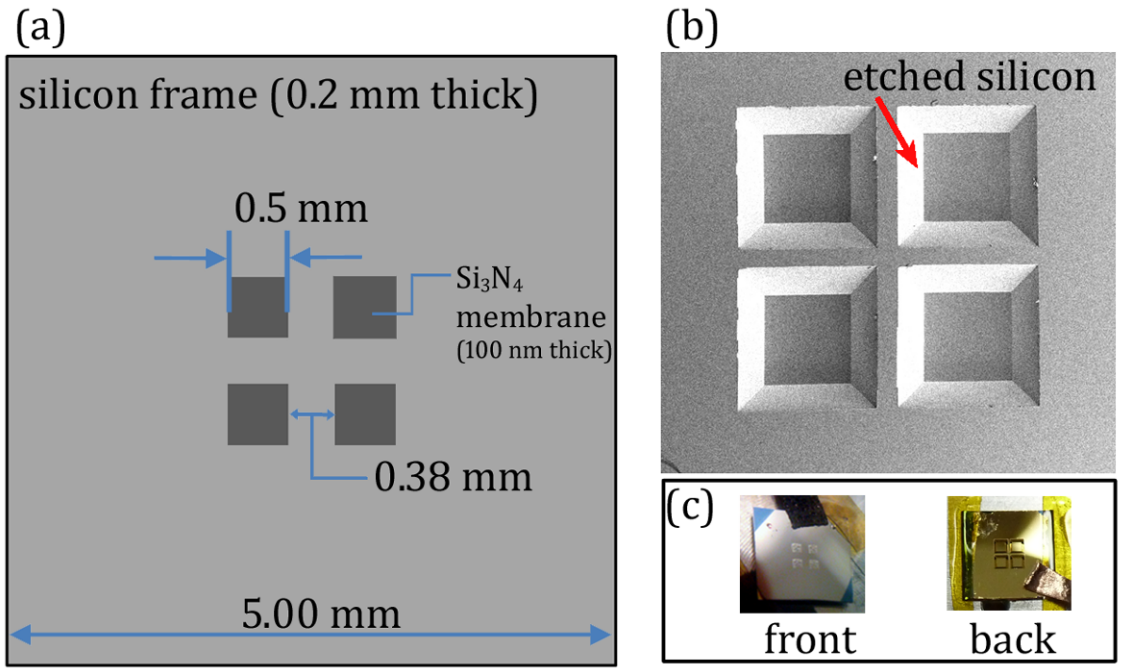

Figure 4.3: Silicon Nitride Membranes - purchased form Silson Ltd., UK. (a) Schematic of the front side of the samples. (b) Scanning electron micrograph of the back side of the sample showing four square regions where the silicon frame has been etched to form the thin membrane windows. (c) Photographs of the sample from the front and back sides. A Co/Pt magnetic ML has been deposited onto the front of the sample substrate and a thick Au film to the back side.

CCD is exposed to light, which is shifted and read out to form an image. For optical holography experiments, a Lumenera Lu170M camera was used to record the holograms. This 8-bit camera features 1280×1024, 5.2 μm square pixels, and operates at room temperature. The number of photon counts for each pixel is converted into a digital number between 0 and 255, which then signifies a greyscale value of the pixel in the image. The camera wasn't capable of detecting the large dynamic range of the Fourier intensity pattern, and so several frames with different exposure times were stitched together to improve the dynamic range of the recorded holograms.

The soft x-ray CCD cameras are back-illuminated. This means that the substrate of a conventional CCD is reduced in thickness to approximately 10 μm and the photons are detected on the back of the parallel register. This avoids the soft x-rays having to pass through polysilicon gates on the front surface of the array that generally become opaque at wavelengths <400 nm [275]. During operation, the CCD cameras were cooled to -50°C to minimise thermal noise or dark current. The x-ray CCD cameras produced 16-bit images, providing a large dynamic range. Parts of the beam will pass through the sample with little scattering and produce an intense region of the direct beam on the CCD. A beamstop is helpful for blocking this central region so that the detection of weaker scattering signals at high $\mathbf{q}$ values can be achieved that would otherwise would be lost within noise. Overexposed images can damage the CCD resulting in 'hot' or 'dead' pixels. This meant that several frames with different exposure times could not be taken when measuring with soft x-rays, and the maximum exposure was determined by the point at which any central pixel became fully saturated.

Photodiodes

In x-ray experiments, photodiodes are excellent detectors for alignment procedures because they can measure over a large dynamic range. A photodiode was used to position a pinhole into the centre of the x-ray beam that acted as a spatial filter and defined the spot size of the beam on the sample. The pinhole was aligned

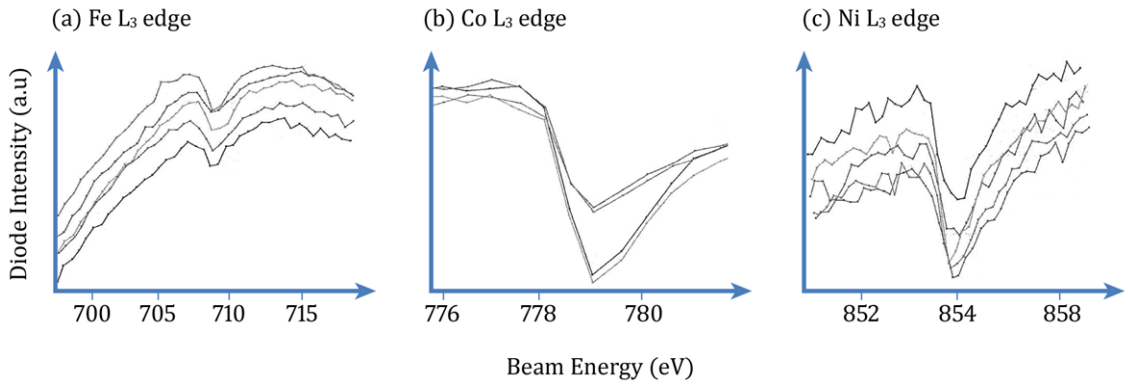

Figure 4.4: L_3 absorption edge of Fe (a), Co(b) and Ni(c). The transmitted intensity through a magnetic thin film containing Fe, Co and Ni is measured with a photodiode over a range of energies. 4-5 repeated scans of each energy range are shown. (a) X-rays with energy 708 eV absorb more strongly due to the presents of Fe in the sample. 708 eV corresponds to the Fe L_3 absorption edge. (b) X-rays with energy 778 eV absorb more strongly due to the presents of Co in the sample. 778 eV corresponds to the Co L_3 absorption edge. (c) X-rays with energy 854 eV absorb more strongly due to the presents of Ni in the sample. 854 eV corresponds to the Ni L_3 absorption edge.

by raster scanning it through beam as the transmitted intensity was measured on the photodiode. Aligning the sample was also achieved in the same fashion. The photodiodes were sensitive to visible light, so all the view ports on the chamber were covered and visible light sources within the chamber, such as pinhole position encoders, were switched off.

To achieve chemical sensitivity the energy of the x-ray beam was tuned to a specific element's L_3 absorption edge. Energy scans were performed with the photodiode measuring the transmitted intensity through a thin magnetic sample film which contained Fe, Ni and Co. The scans are shown in Figure 4.4 and reveal dips in the recorded intensity which correspond to the L_3 absorption edges of Fe (a), Co (b), and Ni (c).

4.3 Soft X-ray Transmission FTH

The imaging experiments concerning magnetic samples were carried out at large 3rd generation synchrotron facilities where a bright x-ray beam is provided. These beamlines provide a partially coherent soft x-ray beam, with circularly polarisation and a high photon flux density. The photon energy can be tuned to the Fe, Ni, or Co L_3 absorption edge [see Figure 4.4] which in turn provides element specific absorption measurements.

Transmission measurements have been performed at the Diamond Light Source synchrotron and the European Synchrotron Radiation Facility (ESRF) where magnetic imaging using extended holographic references was demonstrated. A method for imaging in-plane magnetisation was developed by designing a holographic mask with an extended reference slit that could be rotated within the x-ray beam and provide a non-zero in-plane component of the SXRMS signal. This is discussed in Section 7.2.2.

4.4 Soft X-ray Reflection FTH

By recording the reflected light from a magnetic thin film, one can achieve a non-zero component of the SXRMS signal from in-plane magnetisation. A holographic approach in reflection, as first proposed by Winthrop and Worthington [276], has been investigated along-side the transmission experiments. Measurements in reflection geometry were performed at the BESSY II synchrotron at the Helmholtz-Zentrum Berlin and at the Stanford Synchrotron Radiation Lightsource (SSRL).

Before imaging of magnetic samples commenced it was important to gain a perspective on the effectiveness of the technique with non-magnetic samples. We therefore performed preliminary test experiments at the synchrotron that were based on experiments performed at Exeter University in the optical regime as a test for x-ray experiments.

4.5 Optical Holography

A system was built at Exeter university to perform holographic measurements in transmission and reflection geometries in the optical regime. Samples were designed that could be implemented in the soft x-ray regime. Optical tomography was explored, where several holographic reconstructions are taken as an object is rotated through 360° [277]. Filtered back projection [278] can then be used to construct a three dimensional rendering of the object from the two dimensional slices. Little insight was found into how the method could be implemented to gain a clearer understanding of the $3d$ magnetic profile in ferromagnetic films.

Chapter 5

Optical Holography at Exeter University

In this chapter we describe the optical setups that were constructed at the university of Exeter to perform holographic measurements in a transmission and reflection geometry. The motivation behind these experiments was to provide insight into methods that could be implemented in the soft x-ray regime for imaging magnetic structure.

5.1 Transmission FTH

5.1.1 Experimental Setup

A schematic of the experimental setup for transmission measurements is illustrated in Figure 5.1 (a), with a photograph of the imaging components shown in Figure 5.1 (b). Here the beam from a HeNe laser (Melles Griot, class II, 1 mW, wavelength 543.5 nm) is attenuated by a neutral density filter before being expanded by a lens (focus length $fl = 100$ mm) and further expanded and recollimated by a 5× beam expander to obtain an approximately planer monochromatic input beam. The beam illuminated a test sample containing a holographic device. A planoconvex lens ($fl = 200$ mm) was placed 5 mm downstream from the sample, and focused onto a CCD camera (Lumenera Lu170M). This lens ensured that a far field diffrac-

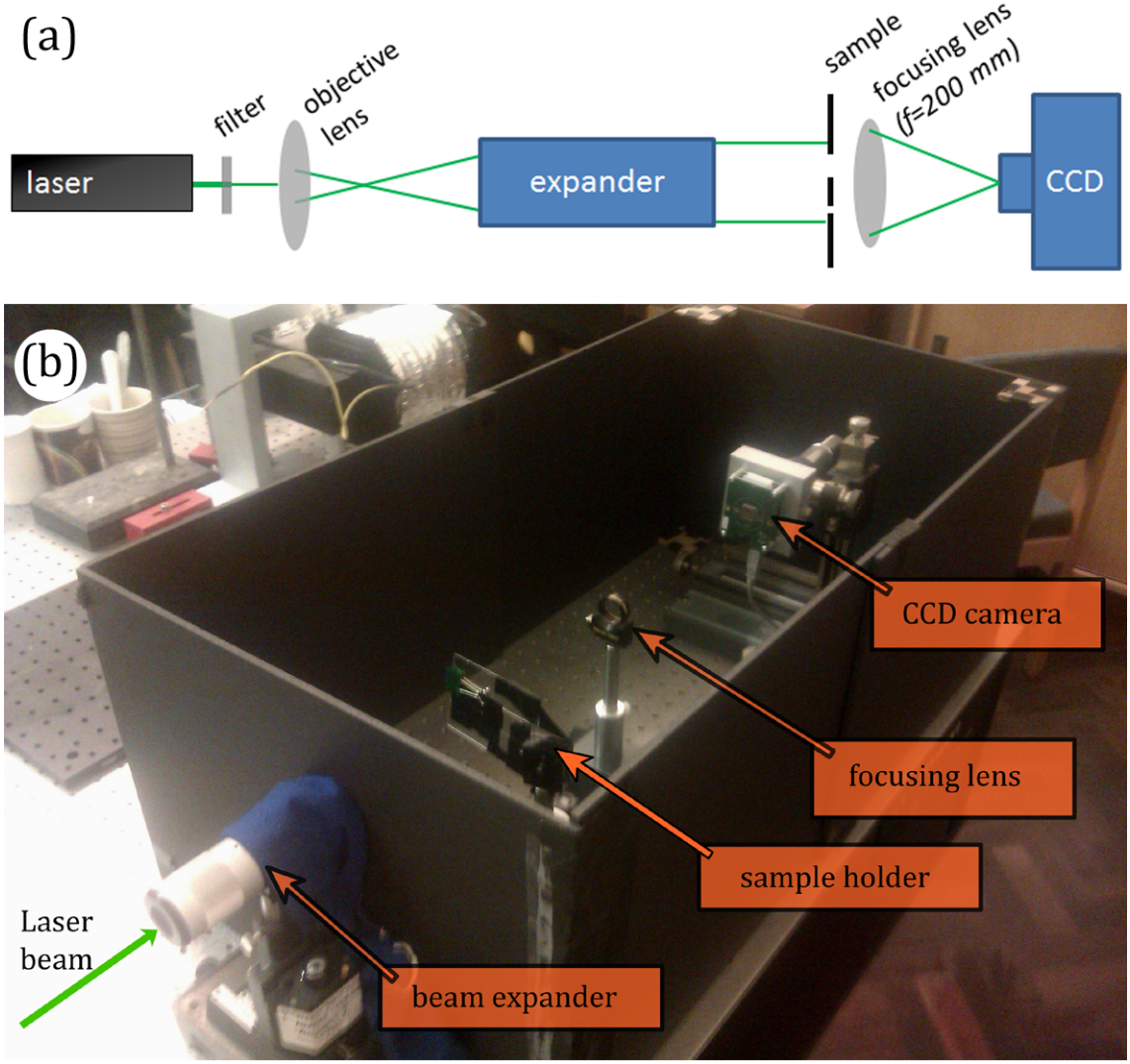

Figure 5.1: Experimental setup for transmission FTH. (a) Schematic of the optical imaging system. (b) Photograph of the imaging components. Here the focusing lens has been further away from the sample so that it can be seen clearly in the photograph.

tion pattern formed at the detector that was compatible with the size of the CCD array.

5.1.2 Sample Design and Fabrication

To fabricate optically opaque holographic masks, a 300 nm thick film of Ag was deposited onto a SiO_2 substrate. A bilayer of PMMA was spin coated onto the Ag

film and EBL was used to expose a pattern of an object arrow (1 mm in size) and a close-by reference pinhole (100 μm in diameter) in the resist. After the E-beam exposure, the sample was developed. The Ag mask was chemical etched with a dilute potassium iodide solution, such that the Ag was removed in the regions of the sample where the PMMA resist had been exposed to the E-beam. The sample was then rinsed in Acetone and IPA.

This sample was suitable for conventional FTH. A comparison between the reference hole and an extended reference was then drawn by manufacturing an extended reference slit. The extended reference was assembled using overlapping razor blades [92] and formed a slit, $\sim$100 μm wide. The Au mask containing the optically transparent arrow and pinhole reference, was mounted in close proximity to the extended reference slit. The ensemble was positioned into the laser beam and a comparison between measurements from the conventional and extended references were made by imaging the object arrow in a transmission geometry. Figure 5.2 (a) shows a photograph of the sample.

5.1.3 Experimental Results

A measured diffraction pattern from the object arrow was recorded at the CCD and is shown in Figure 5.2 (b). To capture the large dynamic range of the Fourier intensity patterns, we stitched frames with five different exposure times (ranging from 0.1 to 1000 ms). For each exposure we averaged 100 frames of data to reduce the noise and subtracted dark frames. Each of the stitched images were scaled appropriately and the resulting hologram was multiplied by a linear differential operator with a direction determined by the intense visible streak in the hologram. The resulting FFT is shown in Figure 5.2 (c) and shows the reconstructed object having used a conventional narrow reference hole, and an extended reference slit.

Figure 5.3 (a) shows a microscope image of the object patterned into an Ag film. The reconstruction of the object from the 100 μm reference hole is shown in Figure 5.3 (b). An image of the extended reference slit is shown in Figure 5.3 (b). An enlargement of a region over the slit is shown in the inset which reveals a

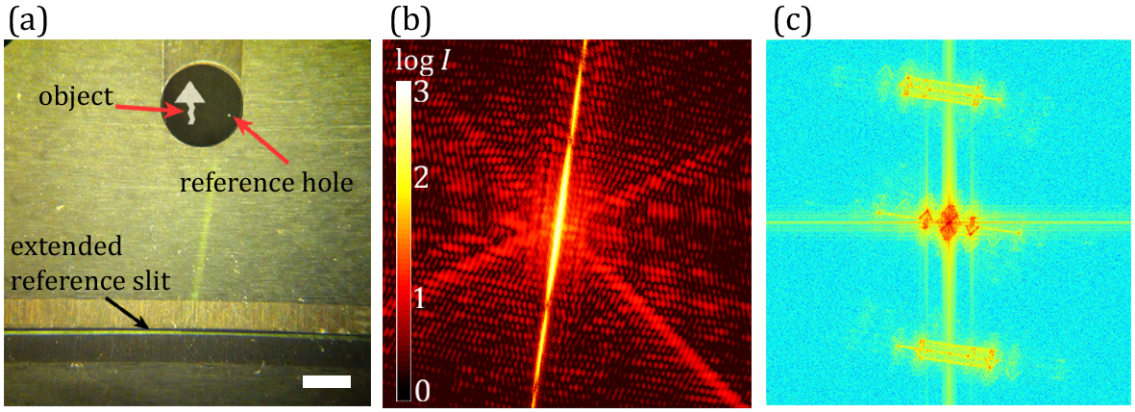

Figure 5.2: (a) Schematic of the sample showing the object arrow and reference pinhole positioned within a circular aperture. Below the aperture is the extended reference slit assembled from four razer blades (white scale bar = 1 mm). (b) Far field diffraction pattern of the sample. (c) Reconstruction of the object arrow from the reference pinhole (central cross-correlations with high contrast) and the extended reference slit (outer cross-correlation with low contrast). Streaks have formed between the object reconstructions from the ends of the reference slit which is caused by roughness along the straight edges of the razer blades.

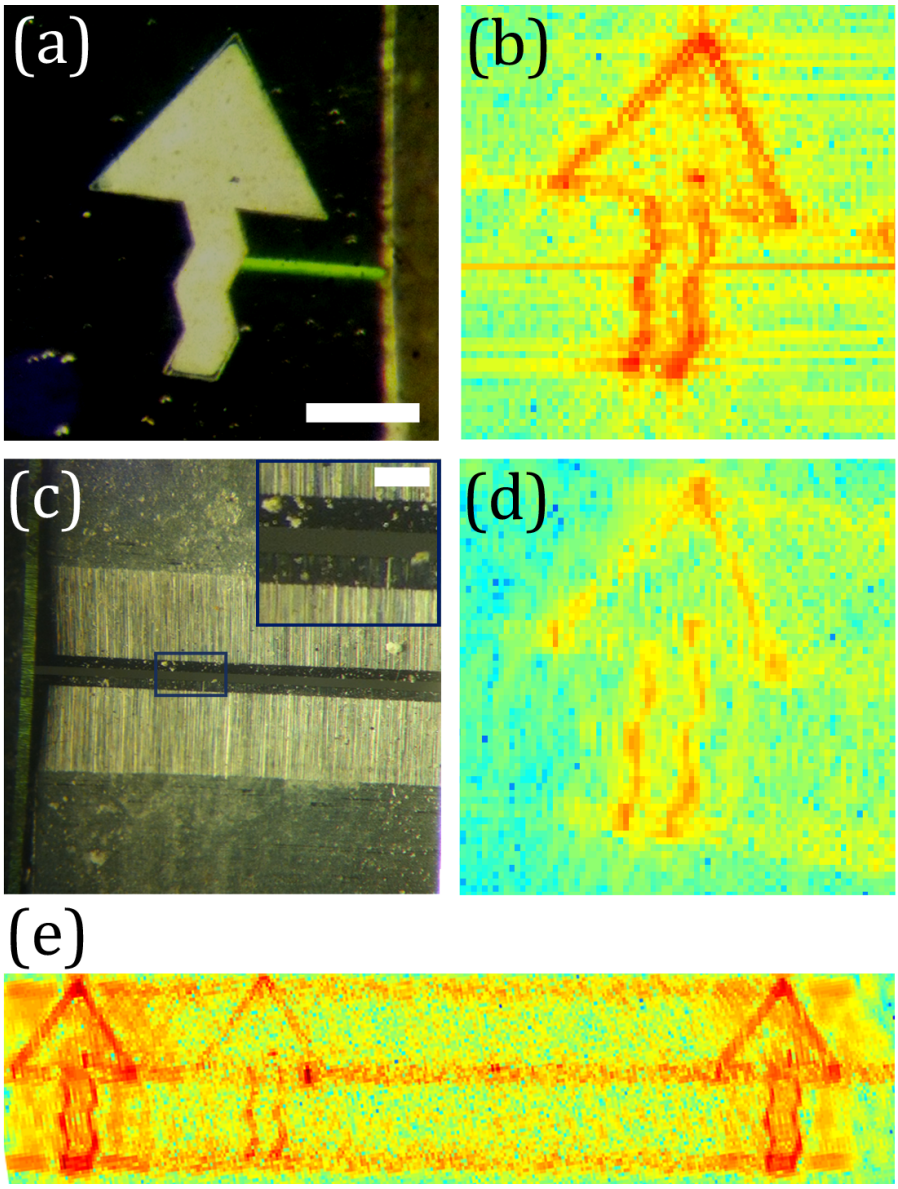

Figure 5.3: (a) Amplitude of the object arrow (white scale bar = 500 μm. (b) FTH Reconstruction from the 100 μm reference pinhole. (c) Microscope image of the extended reference slit. The inset shows an enlargement over a small region of the slit. It reveals microscopic contamination along the sharp edge of the razer blades which cause additional cross-correlations to form in the reconstructed image (Inset white scale bar = 200 μm). (d) FTH reconstruction from one end of the reference slit. (e) Cross-correlation from the entire reference slit and object after the application of the differential filter to the hologram. The contrast has been enhanced to amply the additional reconstruction that formed along the edge of the slit, due to a disruption of the sharp edge of the razer blades as shown in (c).

disruption to the sharp blade edge of the razer which has caused an additional cross-correlation, seen in Figure 5.2 (c), to form along the reference slit. The HERALDO reconstruction from the edge of the slit is shown in Figure 5.3 (d) and aids as a comparison between the extended reference imaging and conventional FTH. An in depth comparison between the conventional FTH methods and HERALDO imaging can be found in [95]. Here, we present transmission reconstructions to provide a direct comparison of the image quality between transmission measurements and results measured in reflection geometry.

We can see in Figure 5.2 (c) that multiple reconstructions have formed during the HERALDO imaging. We determined that microscopic disruptions to the sharp edge of the razer blades that make up the reference slit cause additional object-reference cross-correlations to form in the reconstruction. Whilst these additional cross-correlations were undesirable, it demonstrates the importance of the extended reference to possess sharp edges for the differential filtering to be implemented most successfully. The result does however present an interesting concept where by an object is inserted into the beam to provide a holographic reference signal. This approach has been demonstrated optically by Podorov *et al.* [92], but could be applied in the x-ray regime where a nanoscopic structure could be inserted into a beam to provide a suitably small extended holographic reference.

5.2 Reflection FTH

5.2.1 Experimental Setup

The experimental setup for a reflective geometry is shown in Figure 5.4 (a), with a photograph of the imaging components shown in Figure 5.4 (b). The samples were tailored to reflect light from a test object and holographic reference and the CCD camera was positioned to detect Bragg scattering. Measurements were taken of samples for three rotations, namely with the sample plane rotated to 45°, 22.5° and 8°, off-parallel from the optical axis. A plan view of the three experimental setup is illustrated in Figure 5.8.

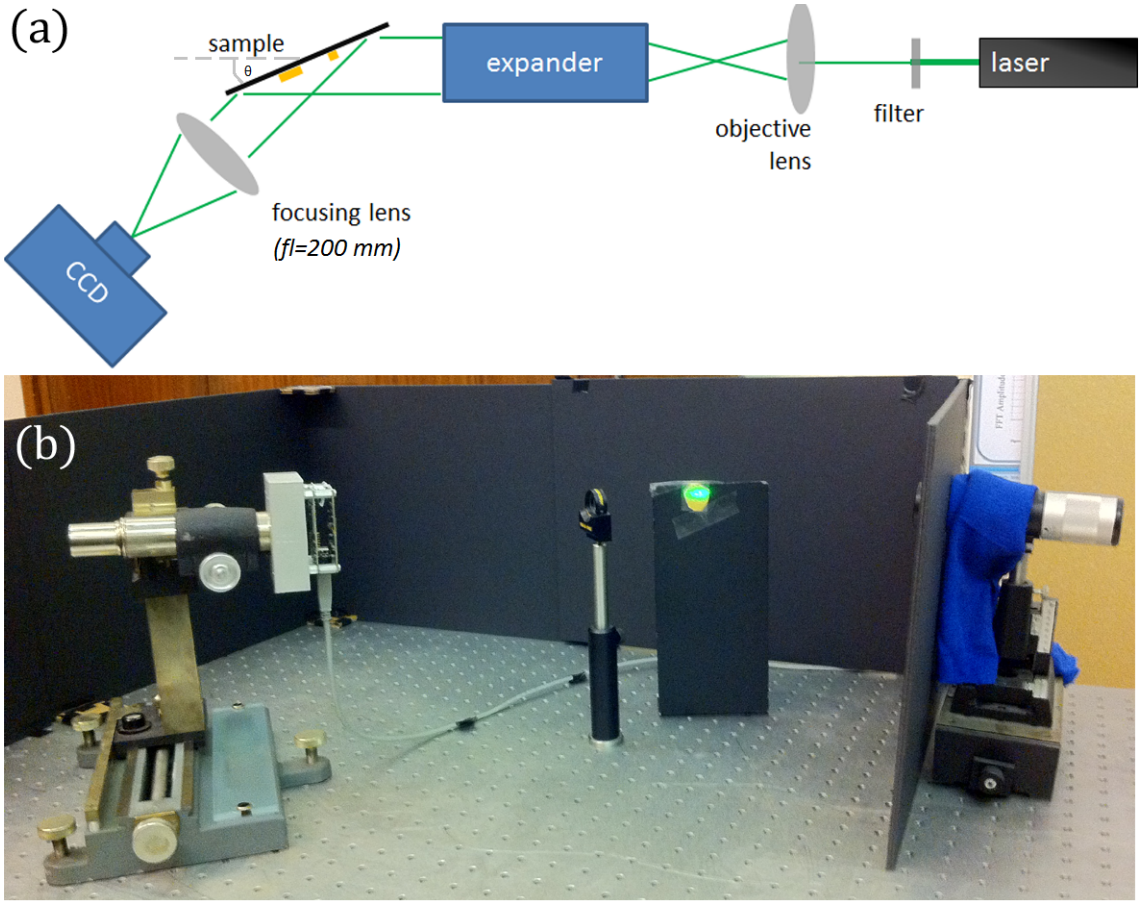

Figure 5.4: Experimental setup for reflection FTH. (a) Schematic of the imaging system with the plane of the CCD chip at 45° to the optical axis and positioned at the focus point of the lens (i.e. 200 mm away from the focusing lens). The surface plane of the sample was positioned in parallel with the beam direction, then rotated to 22.5°. (b) Photograph of the imaging components.

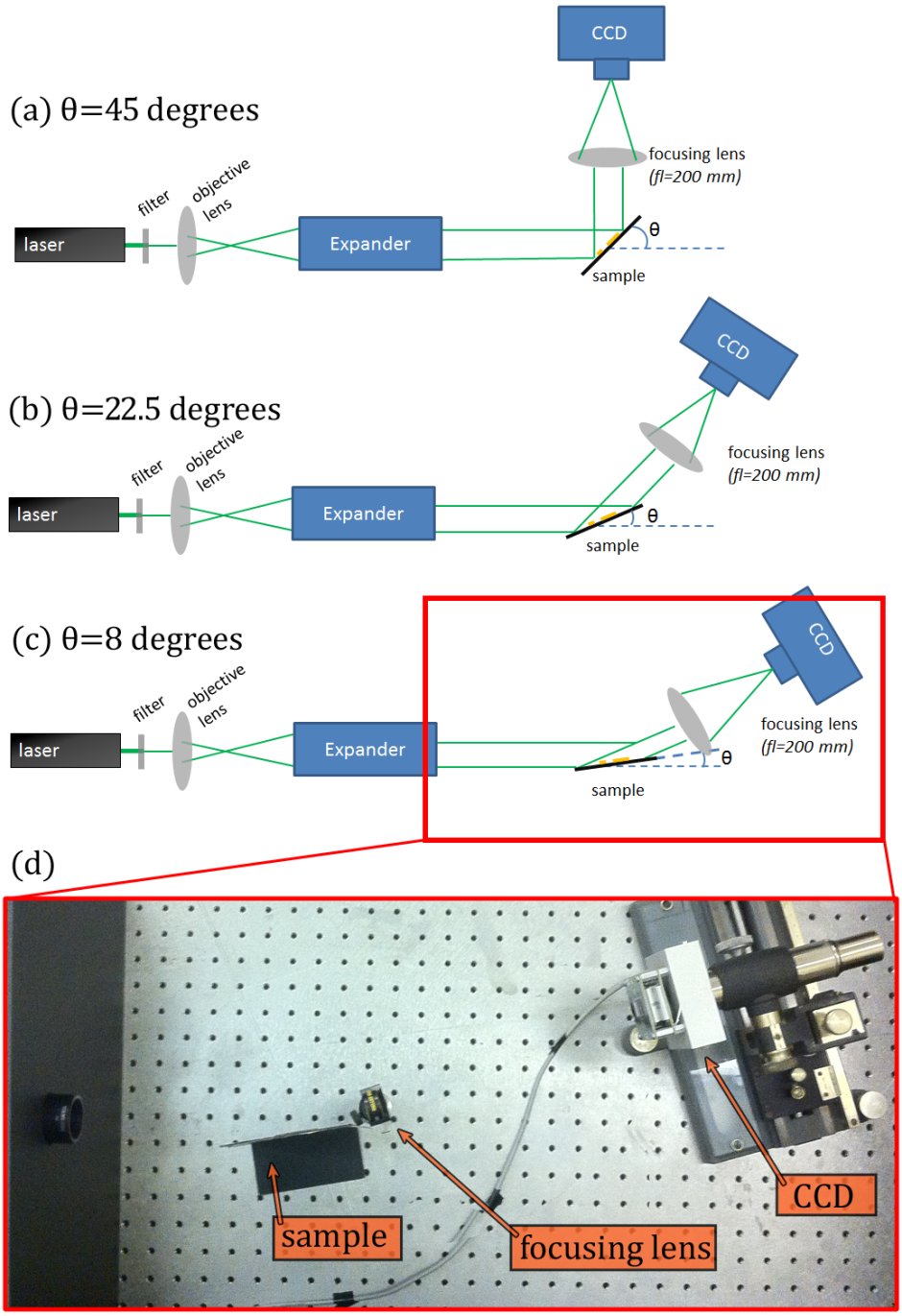

Figure 5.5: Experimental setup for reflection FTH at various angles of incidence. The sample was rotated to (a) 45°, (b) 22.5° and (c) 8°, off-parallel to the optical axis. The CCD camera was positioned so that the plane of the chip was rotated to (a) 90°, (b) 45° and (c) 16°, off-parallel to the optical axis. The CCD recorded the light reflected from the sample. In each setup the CCD camera was placed at the focus point of the lens (i.e. 200 mm away from the focusing lens). (d) Shows a photograph of part of the setup illustrated in (c).

5.2.2 Sample Design and Fabrication

Three variants of samples were manufactured for reflection holography. They were designed such that equivalent samples could be manufactured for reflection experiments in the soft x-ray regime.

Variant #1

A bilayer of PMMA was spin coated onto SiO_2 substrate and EBL was used to expose a pattern of a 1 mm sized object arrow into the resist, and a close-by reference pinhole 100 μm in diameter. These structures were equivalent to those fabrication for transmission experiments in Section 5.1.2. After the E-beam exposure, the sample was developed and 100 nm thick Au film was deposited over the substrate. Lift-off was performed to remove the Au material from around the reflective holographic features. Here, the SiO_2 substrate and the Au holographic structures both provide strong reflected signals. An optical image of the sample is shown in Figure 5.6 (a). Samples were fabricated for measurements in the x-ray regime based on this design and are discussed in Chapter 8.

Variant #2

A low reflective holographic mask was placed in contact with an optical mirror and was positioned into the beam as demonstrated in Figure 5.4. The mask contained an arrow shaped test object ($\sim$ 5 mm in length) and circular reference hole ($\sim$ 1000 μm in diameter). Here, the holographic structures provided a strong reflective signal whereas background reflections were cut out by the non-reflective mask. An optical image of the sample is shown in Figure 5.6 (b). Samples were fabricated for measurements in the x-ray regime based on this design and are discussed in Chapter 8.

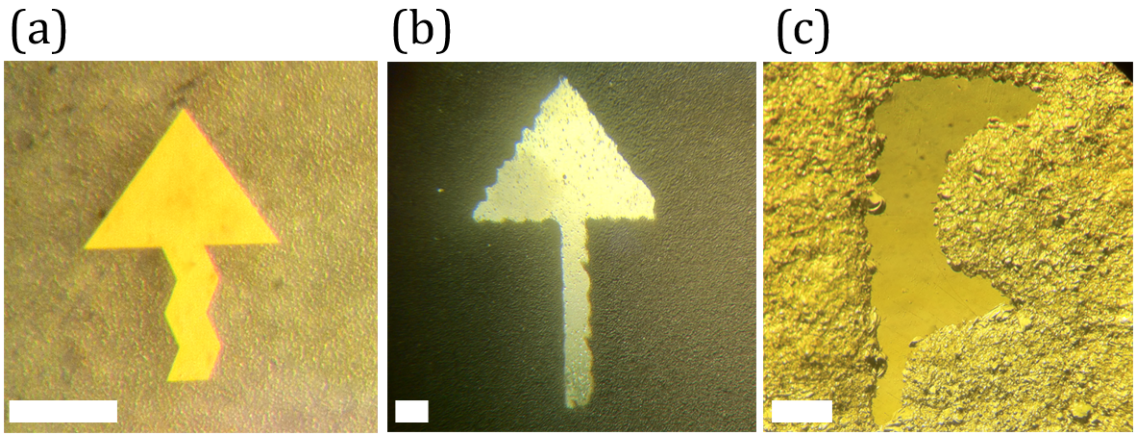

Figure 5.6: Sample schematics for reflection FTH. (a) Sample variant #1 - high reflective signal from holographic features and substrate (white scale bar = 0.5 mm). (b) Sample variant #2 - low reflective mask providing a high reflective signal from holographic features (white scale bar = 0.5 mm). (c) Sample variant #3 - high reflective signal from holographic features, diffuse scattering from substrate caused by inducing roughness into the substrate around the holographic features (white scale bar = 0.5 mm)

Variant #3

A highly reflective 300 nm Au film was deposited onto a SiO_2 substrate. Epoxy resin was used to structure an object letter 'F' ($\sim$ 3 mm in length) and a circular reference pin ($\sim$ 500 μm diameter) and mask the Au layer beneath. Sandblast etching was then used to induce roughness to the reflective surface of the sample. Here, the holographic structures provided a strong reflective signal whereas background scattering was diffuse due to the induced roughness. An image of the sample is shown in Figure 5.6 (c).

5.2.3 Experimental Results

Figure 5.7 shows the results for each of the sample variants with the sample plane rotated to 45° off parallel to the beam direction. To capture the large dynamic range of the Fourier intensity patterns, we stitched holograms recorded by the CCD with five different exposure times (ranging from 0.1 to 1000 ms). For each

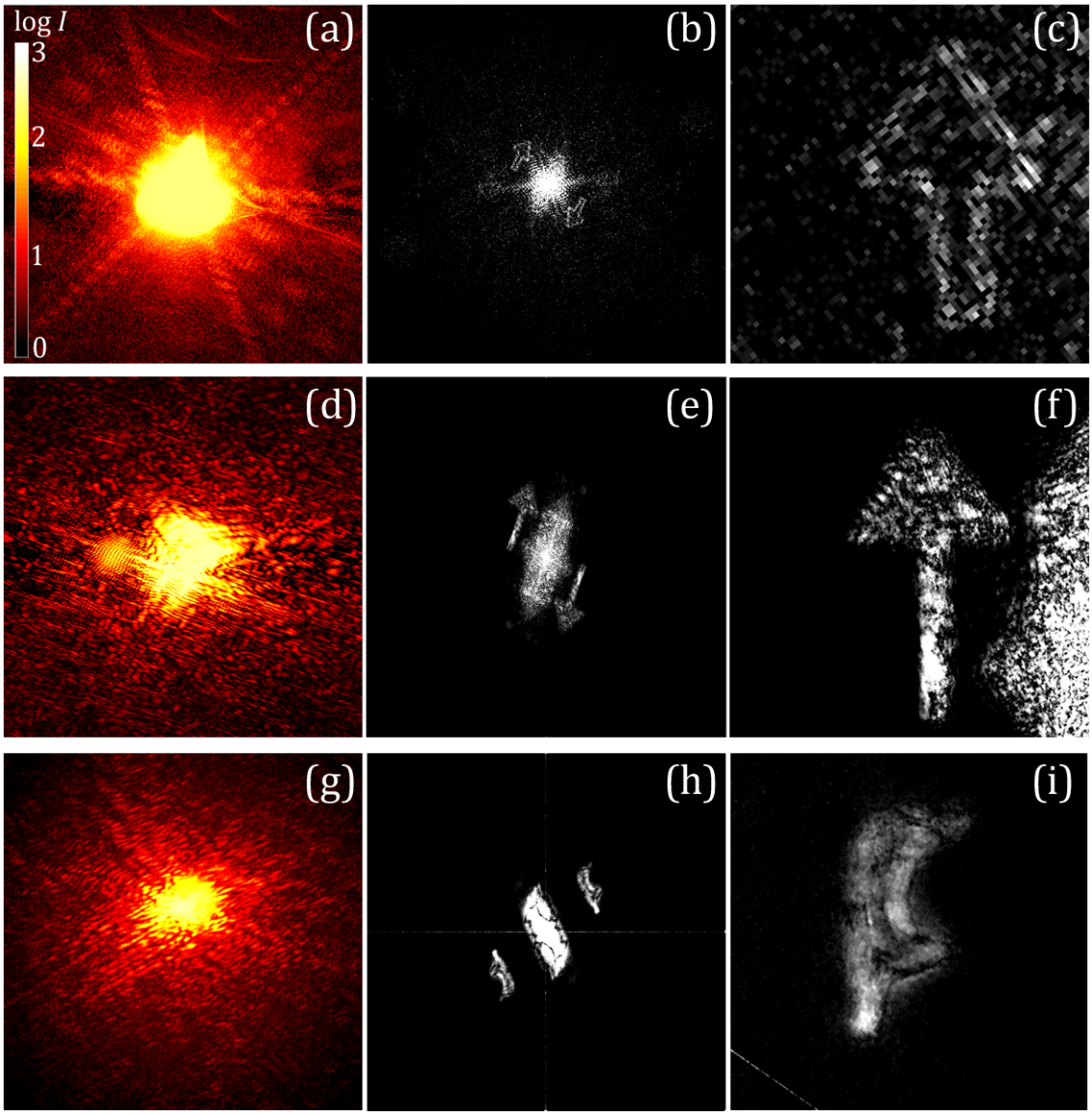

Figure 5.7: Reflection FTH for a sample rotation of 45°. (a-c) Shows the measured hologram, reconstruction and an enlargement of the reconstructed object for sample variant #1, respectively. (d-f) Similarly, shows the results of sample variant #2 and (g-i) shows the results of sample variant #3.

exposure we averaged 100 frames of data to reduce the noise and subtracted dark frames. Each of the stitched images were scaled appropriately.

Figure 5.7 (a) shows the measured reflection hologram of sample variant #1. The FFT of the hologram is shown in Figure 5.7 (b) with an enlargement of the reconstructed object shown in Figure 5.7 (c). Similarly, Figures 5.7 (d-f) show the

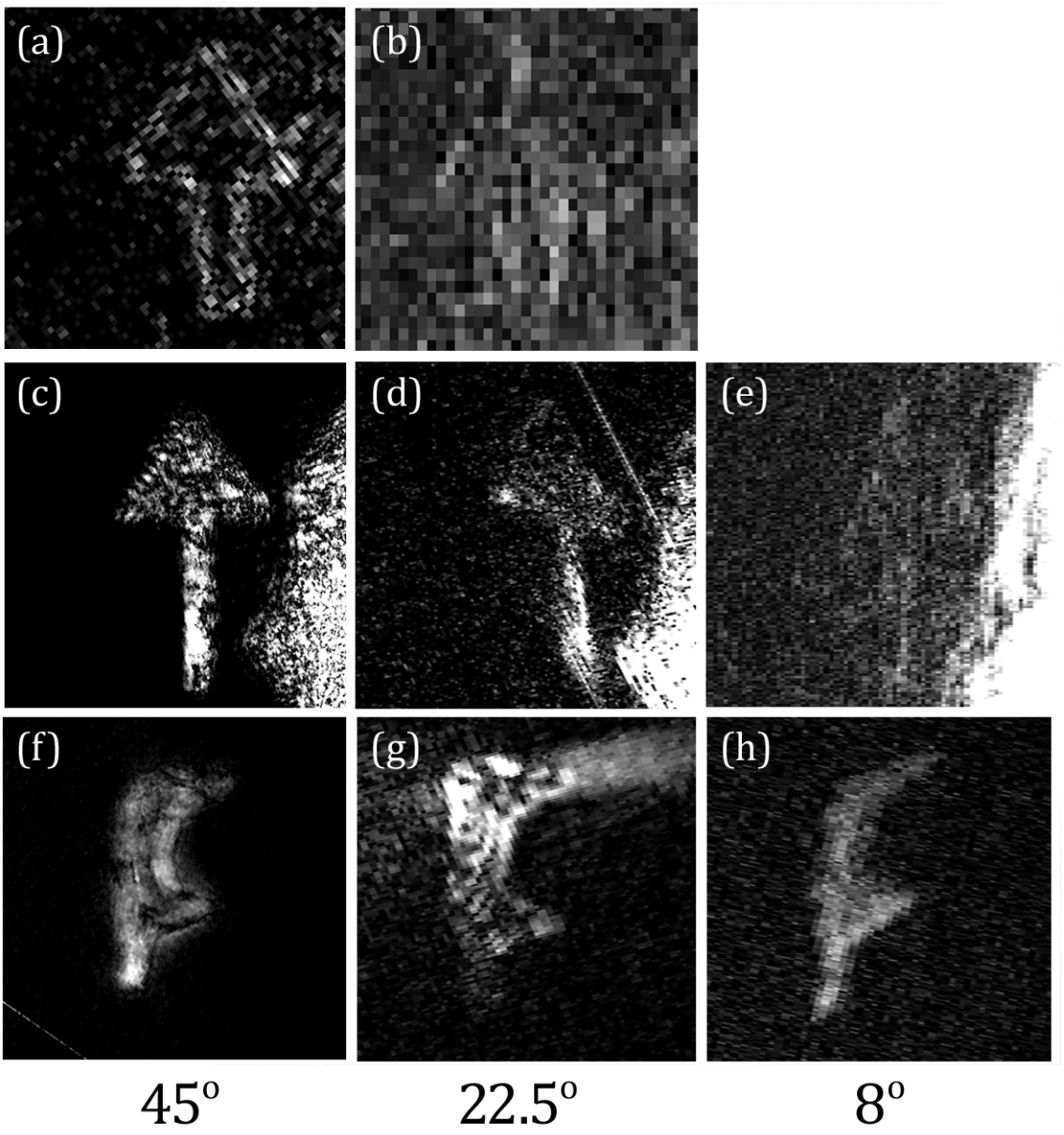

Figure 5.8: Comparison of reflection FTH reconstructions for sample rotations 45°, 22.5° and 8°. (a-b) Reconstructed object of sample variant #1 at sample rotations of 45° and 22.5°, respectively. (c-e) Reconstructed object of sample variant #2 at sample rotations of 45°, 22.5° and 8°, respectively. (f-h) Reconstructed object of sample variant #3 at sample rotations of 45°, 22.5° and 8°, respectively.

results from sample variant #2 and Figures 5.7 (g-i) show the results from sample variant #3. Directly comparing the reconstruction in Figure 5.7 (c) with the result of Figure 5.3 (b) gives one an qualitative indication of the image quality one can expect from FTH in reflection when compared to transmission measurements.

A plan view of the experimental setup is illustrated in Figure 5.8 and a comparison of the reconstructed object of sample variants #1-3, at different angles of incidence is shown in Figure 5.5. The contrast and resolution of the reconstructed objects suffer as the angle of incidence approaches zero. We found that sample variant #1 did not provide any recognisable features when imaging at an angle of incidence of 8°. For implementing the technique in the x-ray regime, the strength of the reflected x-ray signal is maximised at glancing angles of incidence and decays by several orders of magnitude with an increase of only a few degrees [279]. From Figure 5.5, we found sample variant #3 produced the most successful reconstructions and believe that diffuse scattering from the substrate to produce a weak background reflected signal, could provide a way for lensless imaging of structure at soft x-ray wavelength, in reflection geometry.

5.3 Conclusions

We have demonstrated optical FTH in transmission geometry using a narrow reference holes and an extended reference slit. We illustrate the importance for an extended reference to maintain sharp edges to prevent additional cross-correlation terms forming in the reconstruction. If deformations to the sharp edge of a reference slit are comparable to the width of the slit, then additional cross-correlations can distort the view of the intended reconstruction especially if the distortions are within the vicinity of the slit ends. In principle, one could use nanoscopic structures as extended reference objects rather than use FIB to machine a reference apertures into an opaque film.

We have directly compared reconstructions of an equivalent object fabricated with EBL for optical transmission and reflection FTH measurements. We find the reconstruction in the transmission geometry to provide a much clearer recon-

structed object, despite equivalent counting times and measured intensities. The degraded resolution in the reflection approach is apparent in the stretching of the object across many pixels in the lateral dimension and the increased reflected signal from the background reflection of the substrate. Preliminary methods were undertaken to cut out the background reflected signal from the substrate via the use of an unreflective mask, and by inducing roughness into the substrate to encourage diffuse scattering over specular scattering. We found the more successful method out of the two approaches for improving the contrast of the reconstructions was to induce roughness into the sample substrate around the holographic device.

Whilst the reflection FTH setups described in this section were largely successful in the sense that an image of the object structure was reconstructed, it it shown later in Section 7 that using the geometries described here in the x-ray regime proved to be more challenging due to the flux available at third generation synchrotrons, and the very small reflected light at soft x-ray wavelengths. A hologram recorded in reflection with x-rays with sufficient fringe contrast was not achieved, however, an alternative approach to achieve an x-ray reflection image is discussed. The experimental geometry has been reported by Roy *at al.* [280] where successful reconstructions were achieved at soft x-ray energies. Their setup is illustrated in Figure 5.9. It consists of a conventional holographic mask used in transmission experiments which is separated from a sample and placed into the path of the light reflected from a sample. The reflected beam is split into a reference and object source an interference pattern is recorded in the far field by a CCD camera.

As will be discussed later in Section 7 and Section 9, the approach reported by Roy *at al.* [280] shows promise for imaging magnetic samples in an FTH reflection geometry. For future experiments in the optical regime it would be useful to investigate a setup as described in Figure 5.9. This would lead to insight for implementing the setup in the x-ray regime for magnetic imaging.

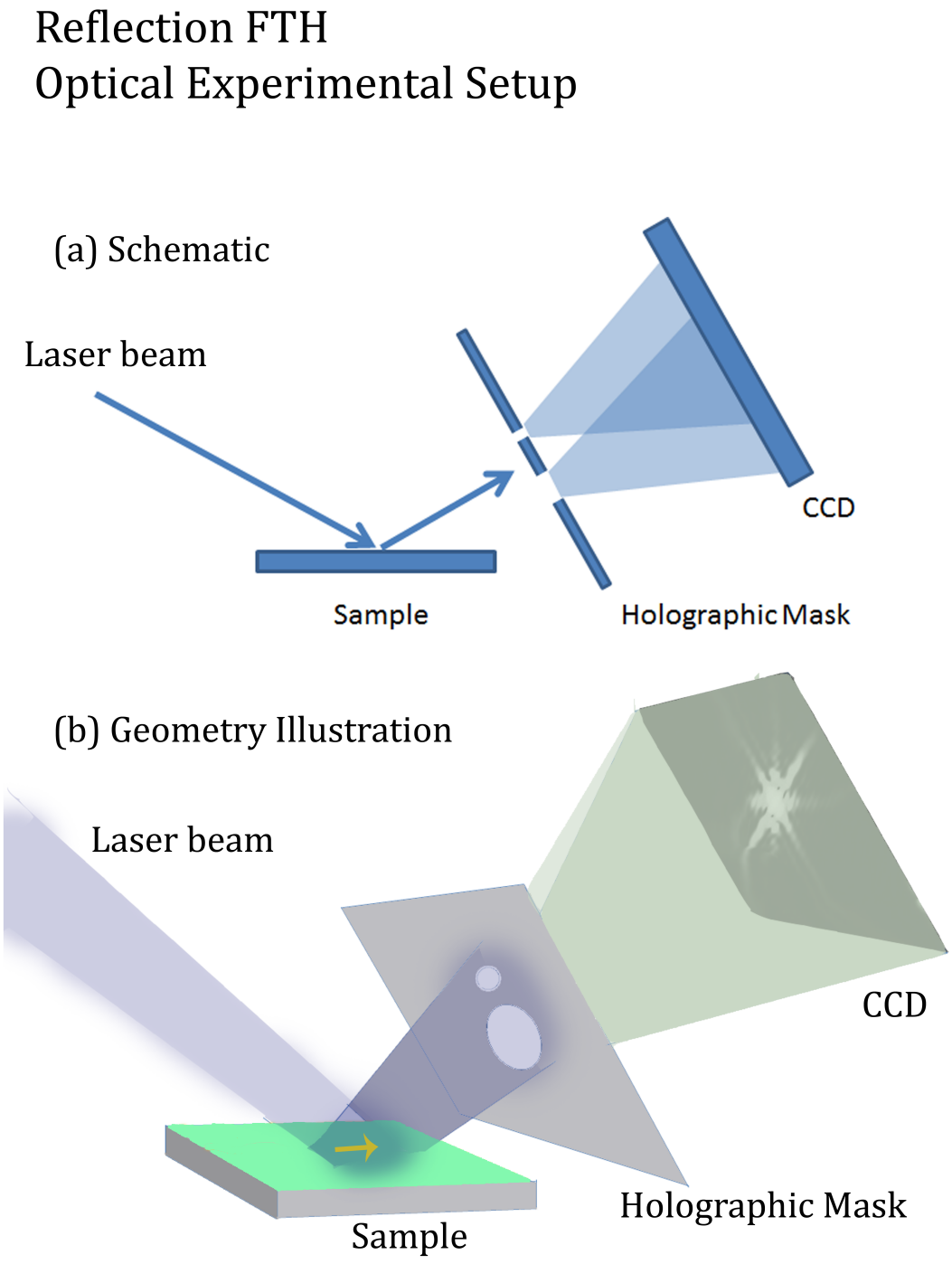

Figure 5.9: (a) Experimental schematic for reflection FTH in the optical regime. Here a traditional transmission FTH mask is placed in the path of the beam reflected from the sample. The mask splits the beam into a reference and object wave that interfere at the detector. (b) Illustration of the reflection FTH experimental setup reported by Roy *et al.* [280].

Chapter 6

Establishing Magnetic Holography at Diamond Light Source

The nanoscience beamline I06 at Diamond Light Source contains a branch line that provides a partially coherent soft x-ray beam, with circularly polarisation and a high photon flux density [281]. The energy range of first harmonic circularly polarised x-rays at IO6 is 106 - 1300 eV which deems it possible to tune the photon energy to the Fe, Ni, or Co L_3 absorption edge and perform element specific analysis of magnetic systems. The aim of this chapter is to introduce the setup that was constructed on the beamline IO6 to perform high resolution magnetic imaging using conventional FTH and holography with extended references.

6.1 Experimental Setup

The branch line was fitted with a diffraction chamber end station that allows one to perform soft x-ray resonant magnetic scattering (SXMRS) experiments such as lensless Fourier transform holography. The experimental setup at IO6 for performing transmission coherent x-ray diffraction measurements is shown in Figure 6.1. A photograph of the endstation is shown in Figure 6.2.

The x-rays first pass through a 'holey mirror' (shown in Figure 6.1). A close up photograph of the mirror is shown in Figure 6.3 (a). This was positioned in the

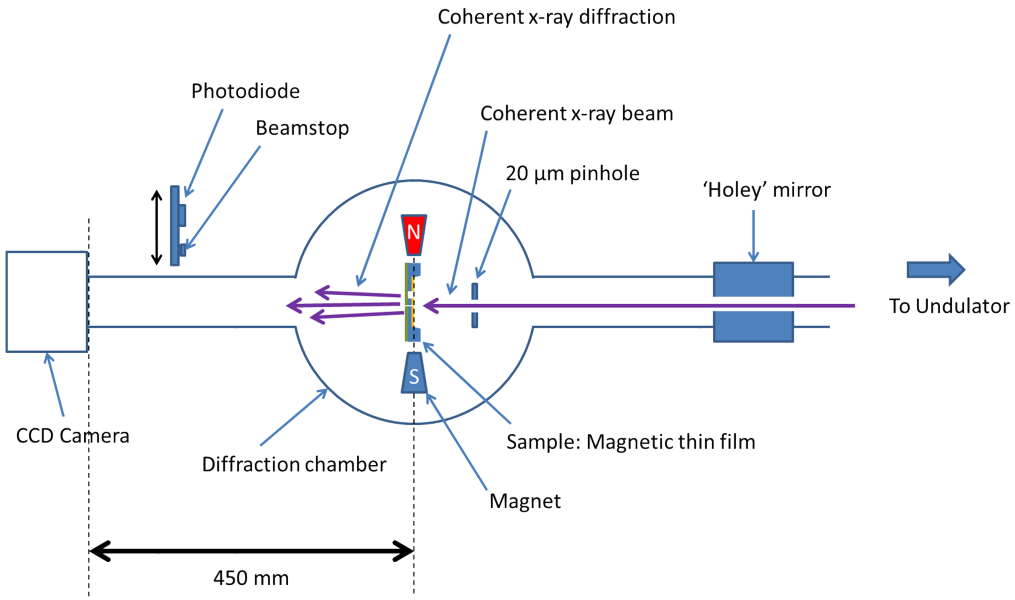

Figure 6.1: Coherent X-ray Diffraction Experimental Schematic at Diamond Light Source at beamline IO6. In this diagram, partially coherent x-rays from the beamlines undulator enter the experimental setup at the end of the branch line. First the x-rays pass through a mirror which contained a 2 mm circular hole. Next the x-ray beam passes into the diffraction chamber where the scattering from the sample takes place. Before it reaches the sample, the beam passes through a 20 μm pinhole which acts as a spatial filter and ensures the x-ray beam has sufficient spatial coherence once it reaches the sample. Next the sample diffracts the x-rays. After the diffraction chamber there is a photodiode detector and beamstop which can be moved in and out of the beams path. The photodiode is used for aligning the pinholes and sample into the centre of the beam. Once in position, the coherent x-ray diffraction signal can be recorded on the CCD camera at the end of the branch line. The beamstop is positioned into the centre of the beam to protect the CCD camera from intense x-rays that pass through the sample unscattered.

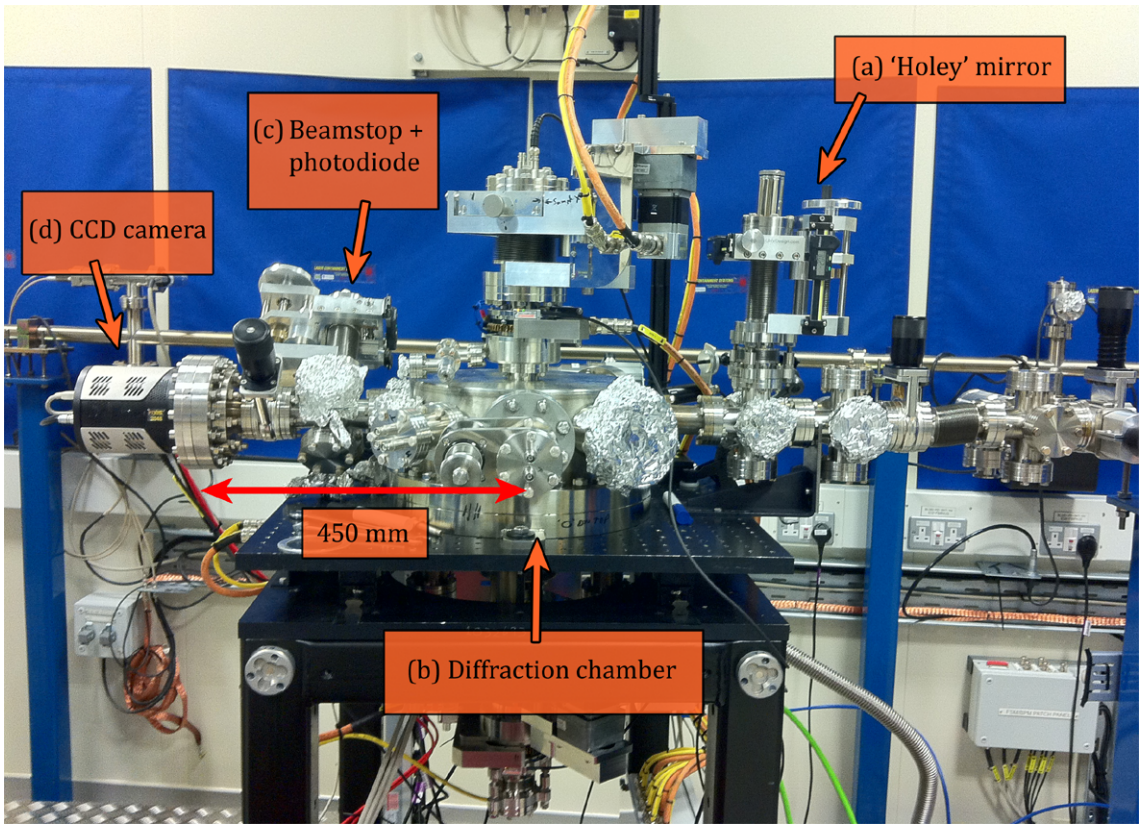

Figure 6.2: IO6 - Branch line at DIAMOND Light Source, UK. This photograph shows the key components of the setup for performing coherent x-ray diffraction experiments such as Fourier transform holography. A schematic of the experimental setup is shown in Figure 6.1.

beams path to block stray light that was found to dominate the CCD recordings. After passing through the 'holey' mirror, the x-rays enter the diffraction chamber (shown in Figure 6.1). A photograph of the inside of the chamber is shown in Figure 6.4 (a). This contained a spatial filter pinhole, the sample, and a magnet. The spatial filter pinhole was used to skim the x-ray beam, extracting a small fraction with nearly full transverse coherence, and define the spot size on the samples.

Figure 6.2 (c) shows a mount that was attached to the end of the diffraction chamber. The mount held an arm that could be wound into the beam so that different components attached to the arm could be individually positioned in the beam. Attached to the arm was a photodiode and a beamstop. The role of these component are discussed later in the chapter in more detail, but in short the photodiode is used for positioning the sample and the beamstop is to protect the CCD from intense x-rays.

A Princeton Instruments CCD camera was mounted to the end of the branch line, as shown in Figure 6.1 and Figure 6.2 (d). The CCD had 2048×2048, 13.5 μm square pixels, and recorded 16-bit images. It was positioned ∼450 mm away from the sample that meant the CCD was capable of detecting light with a maximum scattering vector $\mathbf{q}_{max} = 240\ \mu\text{m}^{-1}$. In real space this corresponds to a spacing of ∼30 nm.

'Holey' Mirror

A circular mirror contained a 2 mm hole machine drilled through it at a 45° angle, as shown in Figure 6.3 (a). The mirror was placed in the beams path to block stray light from reaching the CCD camera used to record the holograms. The source of the stray light was undiscovered, however, its origin was found to be upstream from the diffraction chamber. Figures 6.3 (b) and (c) compares images recorded on the CCD with and without the mirror in position. Figure 6.3 (b) shows that without the mirror, the recorded holograms are contaminated with false information at high scattering angles which significantly reduced the quality and resolution of the reconstructions.

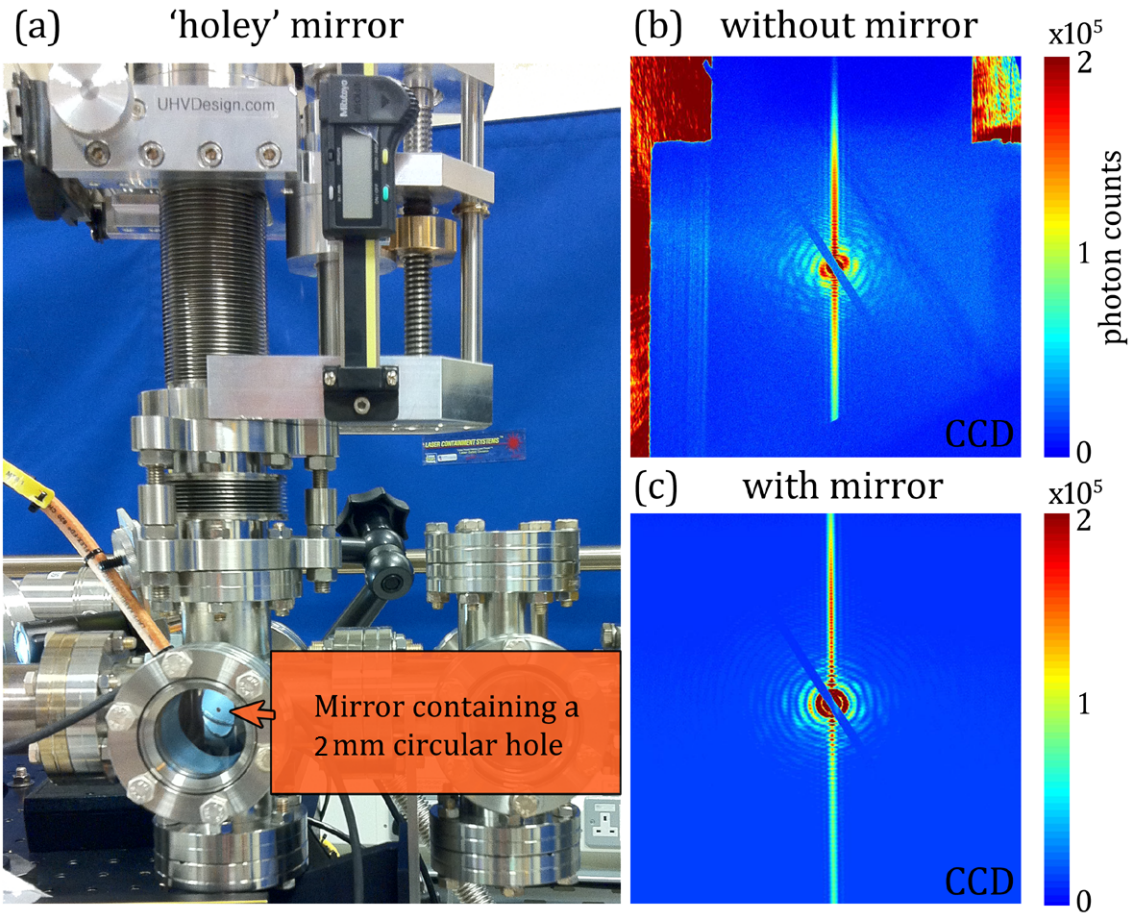

Figure 6.3: IO6 - 'holey' mirror. (a) Illustrated photograph of the mirror. The central hole allows the x-ray beam to pass directly through undisturbed whereas the stray light was blocked by the mirror. (b) CCD image without the mirror in position. The intense stray light can be seen at high **q** values. At low **q** values, the stray light is blocked by the sample holder in the diffraction chamber and an outline of the holder is seen in the image. A shadow of the beamstop can also be seen toward the centre of the CCD image. (c) CCD image with the mirror in position. Here the stray light does not cause any contamination to the hologram as it is all blocked upstream by the mirror.

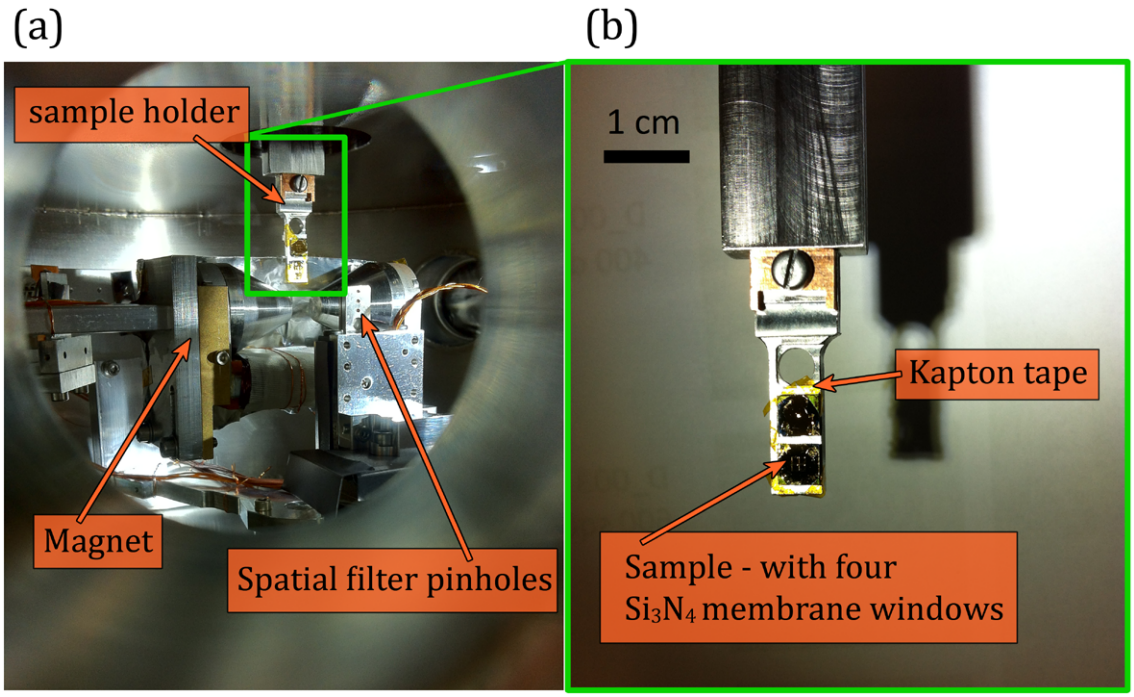

Figure 6.4: IO6 - Diffraction chamber. (a) Photograph of the inside of the diffraction chamber. (b) Close up photograph of the sample holder. Each of the sample were held to the holder with vacuum compatible Kapton tape.

Diffraction Chamber

The diffraction chamber is illustrated in Figure 6.4 (a). The size of the beam is 200 μm (H) $\times$ 20 μm (V) when it enters the chamber and so a pinhole, 20 μm in diameter, was placed 30 mm upstream from the sample. The beam divergence is small having passed through the 20 μm pinhole and so the beam spot size on the sample was close to 20 μm.

The samples were attached to the sample holder with vacuum compatible Kapton tape as shown in Figure 6.4 (b). Several samples could be mounted into the chamber at any one time, and using sample stage motors, the different samples could be moved into the beam.

6.1.1 Sample Design and Fabrication

As stipulated in the Chapter 4, a large portion of the sample fabrication was performed using powerful nano fabrication systems such as FIB. The procedures for creating suitable samples for imaging magnetic thin films with FTH is outlined in Figure 6.5. First, a silicon nitride membrane was mounted onto a suitable support so that the membrane was stable in vacuum conditions. Secondly, a [Co (0.4 nm)/Pt (1 nm)]$_n$ magnetic multilayer (ML) film was sputter deposited onto the front side of the membrane. These film possess PMA and are suitable for imaging with FTH with the sample plane at normal incidence. On the reverse side of the membrane, an x-ray opaque Au film (∼600 nm thick) was sputter deposited onto the sample, and the passage of x-rays through the magnetic film was controlled by FIB milling through specific regions of the Au. A schematic of the sample is shown in Figure 6.6 (a). A polar MOKE hysteresis loop of the magnetic film is shown in Figure 6.6 (b) that reveals characteristics of perpendicular magnetic anisotropy. This is supported by the MFM image, shown in Figure 6.6 (c) that reveals the typical maze pattern of antiferromagnetically coupled up and down domains formed in the multilayer at remanence.

The sputtering of the mask and the magnetic layer was performed in the physics department at the university of Leeds. Due to the stress on the membrane window during the deposition of the magnetic ML film, the membrane surface became buckled, as shown in Figure 6.7 (b). The buckling was not a problem during the x-ray experiments because the variations in the height of the membrane over the microscopic regions of interest were insignificant. When performing MFM, however, the buckling became more problematic if one desired images with a large FOV and achieving high quality images of magnetic domains over a 20 μm square scan was difficult. The large variation in height across the samples surface meant the MFM tip had difficulty tracing the surface tomography accurately. This resulted in a poor magnetic image when the tip retraced the surface in lift mode. The buckling of the membranes may be preventable by switching the order of the steps 2 and 3 in Figure 6.5, as the addition of the thick Au film deposited on the reverse of

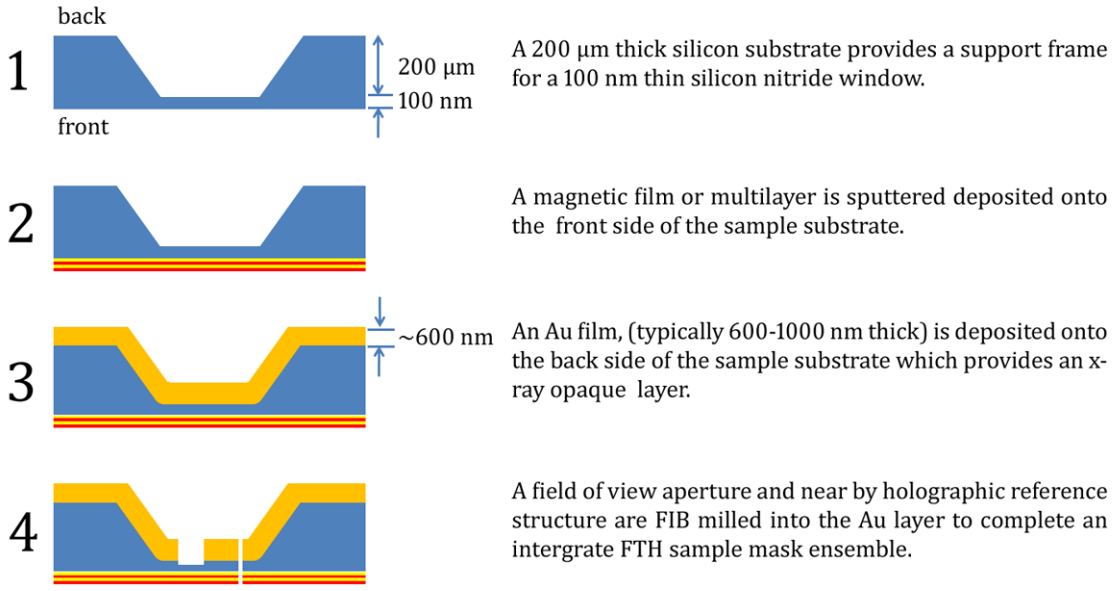

Figure 6.5: Sample fabrication of a magnetic multilayer film deposited onto a silicon nitride membrane substrate with a gold holographic mask machined on the reverse side of the membrane substrate. These samples were used for x-ray holography transmission experiments.

the membrane may ease the strain on the window during the deposition of the magnetic ML [282]. This however has not been tested.

The fourth step from Figure 6.5 illustrates the nano fabrication performed using FIB to create the holographic mask by milling through the thick Au film on the reverse side of the membrane. A field of view (FOV) aperture, $\sim$2 μm in size, was milled through the Au only as far as the Si_3N_4 window beneath. A second structure near to the FOV aperture was milled through the entire Au mask/substrate/magnetic ML ensemble that provided a holographic reference source. The reference was either a narrow hole $<$100 nm in size, or an extended reference slit with a length greater than the size of the FOV aperture, and a width of $\sim$30 nm. For simplicity, a single 'aperture-reference pair' will now be referred to as a 'holographic device'.

In the experiments, the x-ray beam spot was centered onto a single holographic device. The beam was scattered by the charge and magnetic structure within the FOV aperture, and diffracts through the close-by reference structure. The

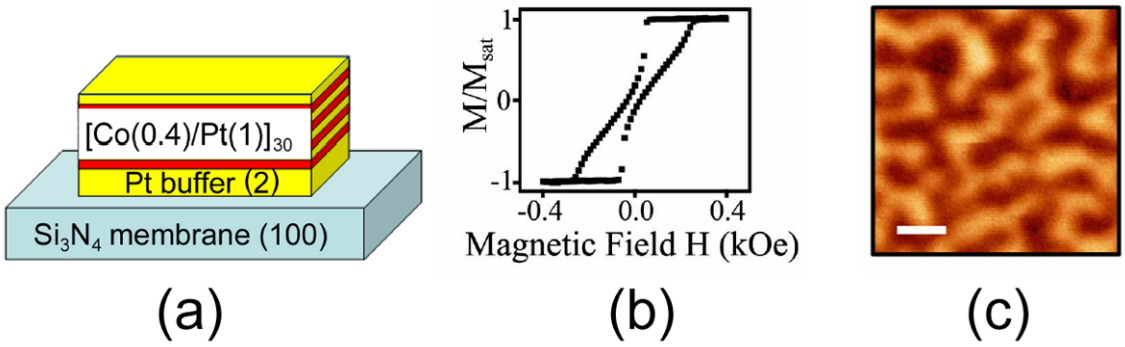

(a) (b) (c)

Figure 6.6: Characterisation of the $[Co/Pt]_n$ ML films. (a) Sample structure of the $[Co/Pt]_{30}$ ML with corresponding thickness values in nanometers in the parentheses. (b) Polar MOKE hysteresis loop of the sample film. (c) MFM image showing perpendicular maze domains of the Co/Pt at remanence (white scale bar = 500 nm).

interference pattern between the two waves in the far field is then recorded on the CCD.

Figure 6.7 shows a scanning electron micrograph of several holographic devices that were patterned across a single membrane window and were measured in the x-ray experiments. Figure 6.7 (a) shows a 250 μm square membrane window that was patterned with twenty holographic devices, placed into two columns. Several test devices can also be seen in both corners on the right hand side of the window. The separation between each device was $\sim$25 μm, which is greater than the size of the beam spot on the sample and each device could be independently imaged. Figure 6.7 (c) shows a conventional FTH device where a 1.5 μm circular FOV aperture is centred about three $\sim$60 nm reference holes. A conjugate pair of reference-aperture cross-correlations was produced in the final reconstructed image for each of the three reference holes. Each cross-correlation revealed a separate image of the magnetic domain structure within the FOV aperture. In Figure 6.7 (d), a 1.5 μm circular FOV aperture is separated by 3 μm from an extended reference slit that was used to perform HERALDO imaging of the magnetic film. Once the digital filter required for HERALDO imaging is applied to the hologram,

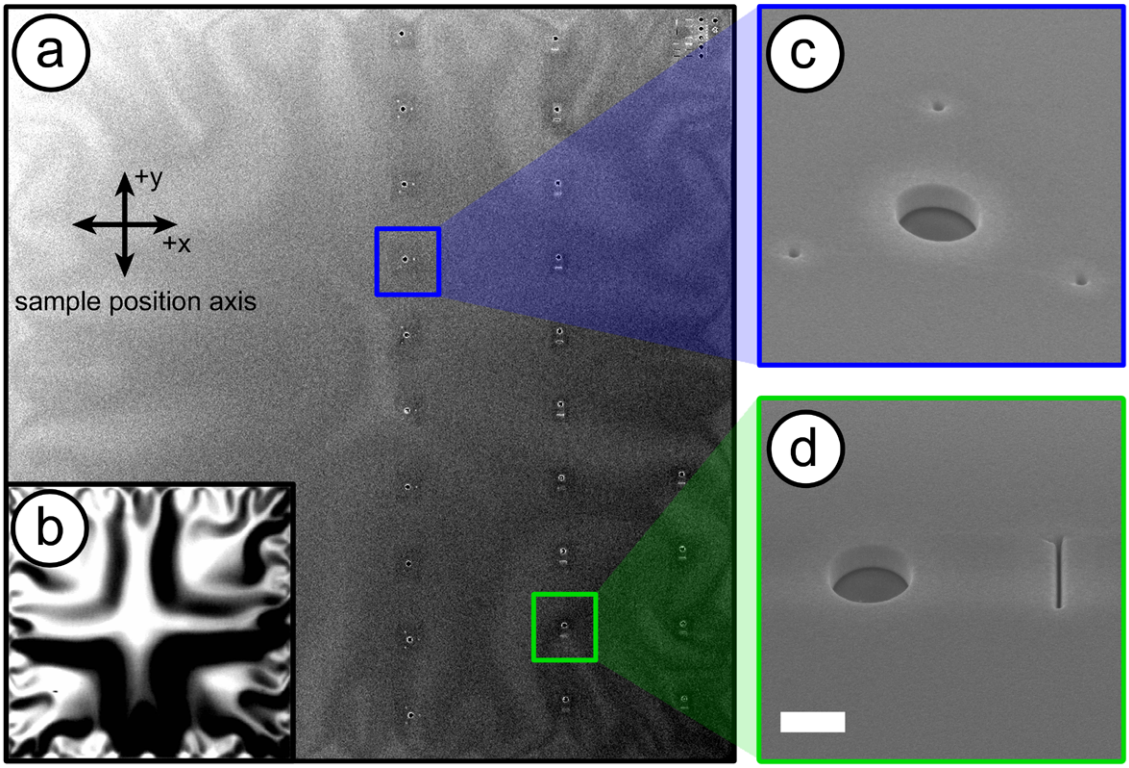

Figure 6.7: Sample fabrication for x-ray transmission experiments. (a) SEM of the membrane window. Two vertical columns of holographic devices, spaced evenly across the entire window, can be seen. Along the right side of the membrane some test devices for calibrating the dose of the FIB milling for patterning the devices. (b) Shows a microscope image of the membrane surface which demonstrates that the membrane was buckled when the magnetic film was deposited. (c) SEM view of a holographic device patterned for conventional FTH with pinhole references. A 1.5 micron sized FOV aperture is surrounded by three reference pin holes. (d) a holographic device used for HERALDO imaging. Here a 1.5 micron sized FOV aperture has been patterned in close proximity to an extended holographic reference slit. The white bar in (d) is 1.5 μm.

the resulting image is Fourier inverted to retrieve the final reconstruction. Both ends of the slit then produce a conjugate pair of images that revealed the magnetic domain structure within the FOV aperture. The FOV in holography experiments is restricted in size because the object aperture and reference structure have to remain within the coherent region of the beam, whilst separation conditions (presented in Guizar-sicairos *et. al* [93]) have to be obeyed to prevent cross-correlation terms overlapping in the reconstruction.

Aligning the Sample in the X-ray Beam

The sample stage was initially positioned by eye, so that the beam was approximately centred onto one of the membrane windows. The sample was then scanned vertically (y-axis) through the beam and the transmitted intensity was measured on the photodiode. Figure 6.8 (a) shows the measured intensity on the photodiode that reveals two broad peaks corresponding to the two membrane windows passing through the beam. The position of the sample along the horizontal axis (x-axis) was adjusted by a fine tuning screw on the diffraction chamber, this was capable of aligning the sample along in the horizontal direction with high precision to an accuracy <10 μm. Figure 6.8 (b) shows the measured intensity on the photodiode when the sample was scanned vertically so that the a single column of devices [seen in Figure 6.7 (a)] passed through the beam. Ten intense peaks can be seen that correspond to the vertical position of each device. The horizontal position of a selected device was fine tuned using the photodiode. Figure 6.8 (c) shows several vertical scans through an individual HERALDO device (an image of one is shown in the inset of Figure 6.7 (d)). Each intensity envelope is split into two peaks. The smaller of the peaks occurs as the reference slit passes through the most intense part of the x-ray beam. There is a small drop followed by a second peak as the FOV aperture moves into the most intense part of the beam. The relative intensity of the peaks for difference x positions was maximised to complete the positioning procedure. Any further fine tweaks to the sample position was performed by examining the intensity of the speckle in recorded CCD images. In Figure 6.8 (d), an

illustration of the sample is presented with dashed lines indicating the part of the sample scanned through the beam in Figures 6.8 (a-c). For clarity purposes, each of the dashed lines have been coloured and labelled with a letter that corresponds with the part of the figure to which they refer.

The beamstop was moved into the beam, replacing the photodiode, and imaging on the CCD commenced. A schematic of the HERALDO imaging process is illustrated in Figure 6.9.

To examine the magnetisation in a Co/Pt ML, the photon energy of the x-rays was tuned to the L_3 absorption edges of cobalt. Holograms were taken using both helicities of circularly polarised x-rays [see Figure 6.9 (b)]. The magnetic contrast was enhanced by subtracting two holograms that were recorded with opposite helicities of circularly polarised x-rays. This also removed the effects of charge scattering from the reconstruction. In the setup shown in Figure 6.9, a narrow reference slit was used as a holographic reference. Here, a linear differential filter [see Figure 6.9 (c)] was applied to the difference image, where the linear filters direction was determined directly from the diffraction pattern by the intense streak visible in Figure 6.9 (b). A Fourier transform was then taken to retrieve the reconstruction. Figure 6.9 (d) shows an MFM image of the magnetic film. It shows the perpendicular magnetised domains of the Co/Pt. The light and dark regions representing a magnetisation direction facing into and out of the page.

6.1.2 FIB Milling of Devices

The individual devices were fabricated using specified FIB settings, with the Au layer etched for specific milling exposure times for the different features. To fabricate the device's 1.5 μm FOV aperture, several apertures were milled into a corner of the Au film with different exposure times. Figure 6.10 shows five apertures milled in 10 second intervals, from 10-50 seconds (left to right). The FIB energy was 30 kV and the beam current was 30 pA. After a 50 second exposure, the FIB removed all the Au film within the 1.5 μm aperture, and stopped at the Si_3N_4 substrate.

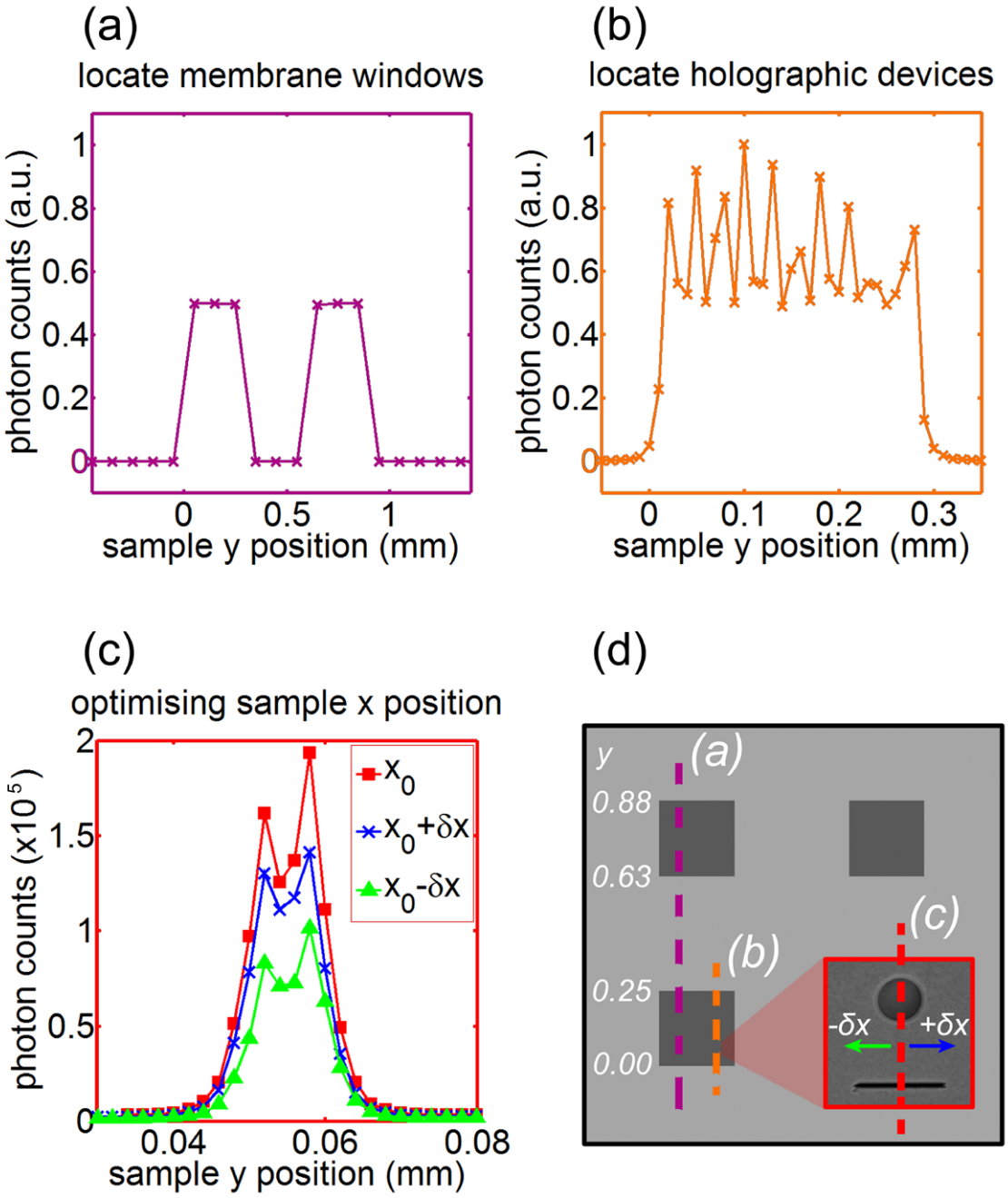

Figure 6.8: (a) The transmitted intensity is measured on a photodiode behind the sample. A coarse vertical scan of the sample through the beam reveals two intensity peaks corresponding to the two membrane windows. (b) The x-axis stage position is adjusted to the edge of the membrane and a second coarse of a single window reveals several peaks that correspond to the vertical positions of each holographic device. (c) A fine vertical scan over a particular device is performed for several x position values to improve the position coordinates relating to the device. The fine scan reveals two peaks corresponding to the reference slit (smaller peak) and FOV aperture (larger peak).

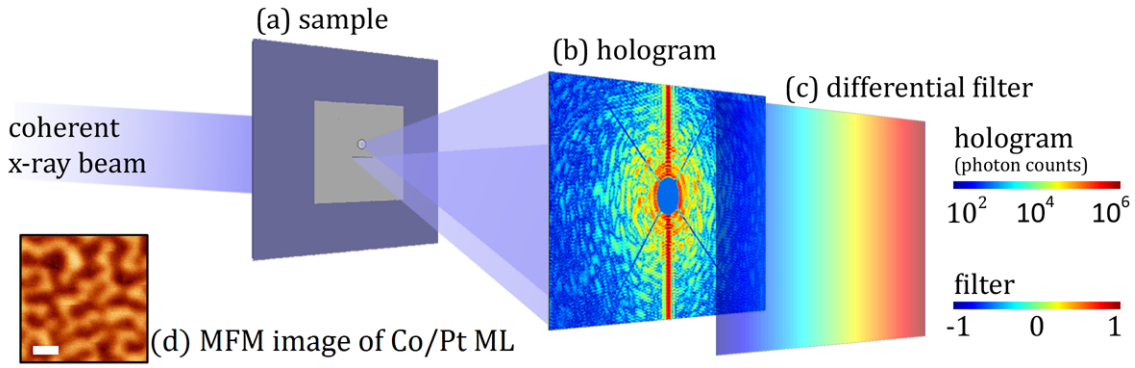

Figure 6.9: Transmission geometry experimental setup. (a) The object FOV and reference are illuminated by coherent x-rays. In this example the reference used is a narrow slit. (b) The scattered light from the object and reference forms an interference pattern in the far field that is recorded on the CCD camera. (c) A linear differential filter is multiplied by the hologram before performing a Fourier transform to retrieve the reconstructed image. Note that a filter is not required with conventional FTH using reference holes. The filter is defined by the directional derivative of the slit and is determined from the intense streak visible in the hologram. (d) An MFM image of the $[\text{Co}(0.5\text{ nm})/\text{Pt}(1\text{ nm})]_{30}$ ML film used in magnetic holography (white scale bar = 300 nm).

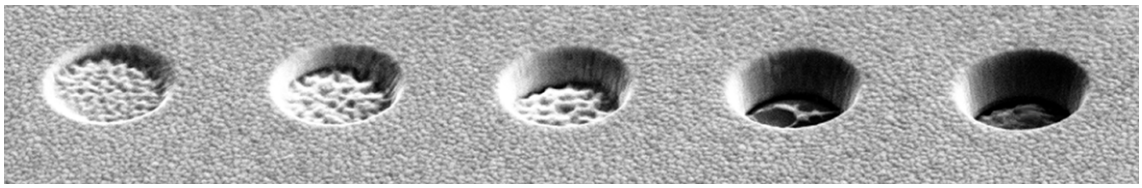

Figure 6.10: FIB milling FOV apertures. Apertures milled in 10 second intervals, from 10-50 seconds (left to right).

Having found the correct FIB milling time for the apertures, a dose test for the reference structures was performed. The reference dose tests are shown in Figure 6.11. A row of narrow hole were patterned into the Au film, with exposures times increasing in 1 second intervals. Beneath the holes, a row of extended reference slits were patterned, with exposure times increasing in 5 second intervals. Figure 6.11 (a) shows the dose test patterns from the back side of the sample where the Au film was deposited. The membrane is turned over and imaged again from the front side, or rather, the side in which the x-rays will exit the sample in the experiment. The dose tests from the front (exit) side of the sample is shown in Figure 6.11 (b). When defining the size of the reference structures, it is important to know the exit width of the structure because this will play a role in defining the resolution of the imaging technique. Enlargements of the reference hole and slit are shown in Figure 6.11 (b). In these examples a hole of size $\sim$70 nm was manufactured and slits were produced with a width of $\sim$30 nm.

Between the two rows of reference features, a series of 1.5 μm FOV apertures were milled with the same mill time of 50 seconds. They are visible in Figure 6.11 (a) but because they do not etch through the Si_3N_4 substrate, they are not visible in Figure 6.11 (b) when the membrane is imaged from the front side of the sample. It can be seen that the aperture in the centre contains a lump of Au that has not been removed by the FIB despite the etch time being calibrated for this film. It became apparent that the Au film contained large grains of Au that developed during the deposition of the layer. This resulted in many apertures containing Au grains that were not removed by the FIB, which in turn, created an obstruction within the FOV aperture that would strongly absorb soft x-rays, and in many cases would

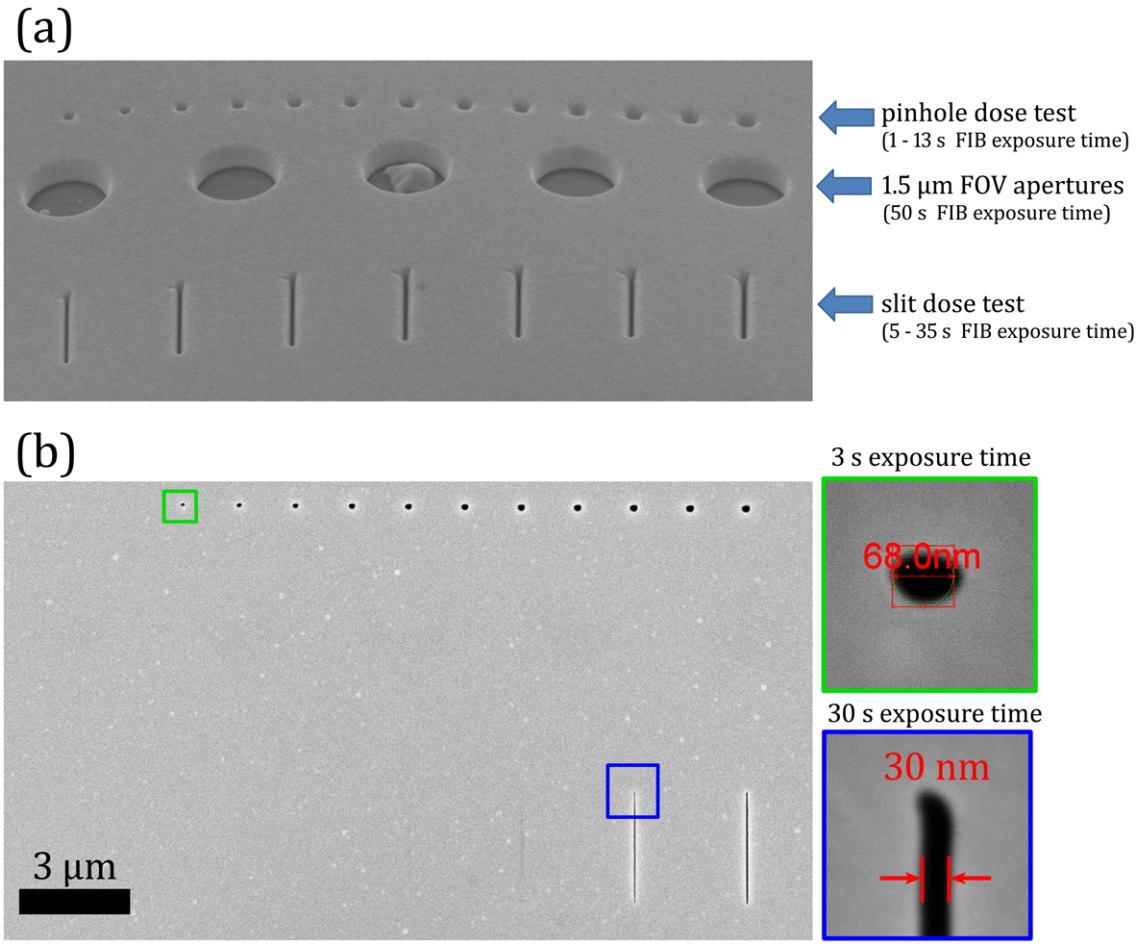

Figure 6.11: FIB milling reference structures. (a) Scanning electron micrograph of a dose array of test structures required for the holographic devices as imaged from the side of the Au mask. (b) The membrane is image from the front of the sample over the dose array region to determine suitable FIB etch times for the holographic references, so that they remove all the material whilst maintaining a narrow exit width.

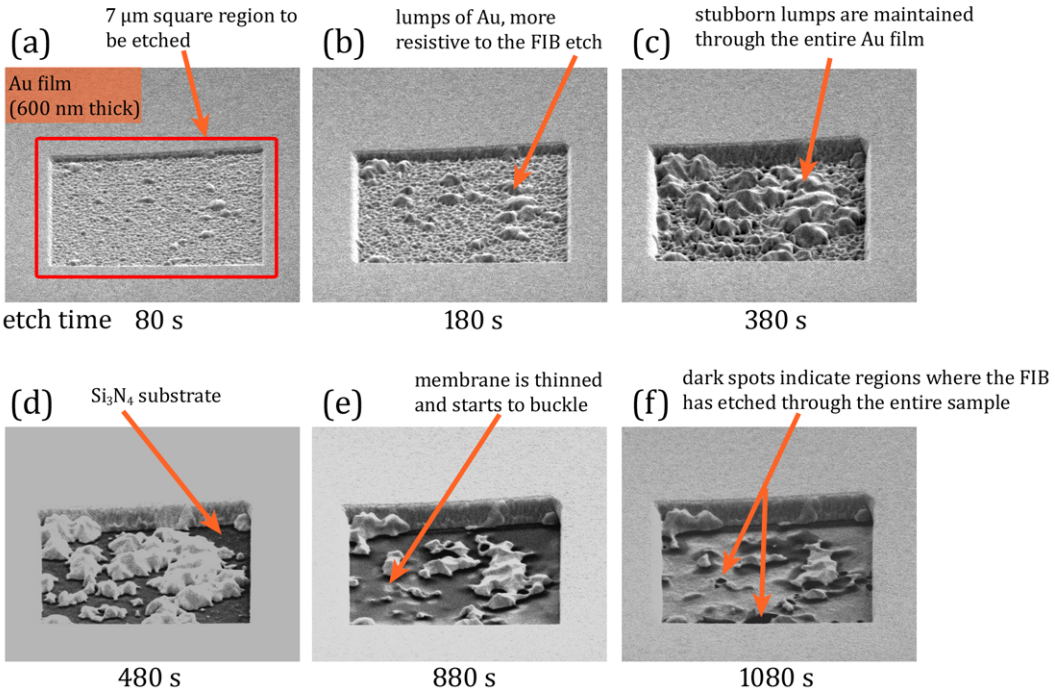

Figure 6.12: Nonuniform FIB milling of a 7×7μm square region in a gold film deposited with thermal evaporation onto a silicon nitrite membrane substrate. Problems arise and are outlined as the FIB etching time is increased to values that can completely remove the Au layer over an extended area.

severely reduce the magnetic contrast of these regions in the final reconstructed image.

During the course of the research it became apparent that due to the growth process of the Au, thick layers were being produced that would often not etch uniformly across the surface upon FIB milling. Figure 6.12 shows a series of SEM images that were taken at different time intervals as a 7 μm region of the gold film was etched with the FIB. The depth across the etched region is not uniform, but contains clusters of Au grains. In Figures 6.12 (a-c), one can see the grains becoming more apparent as the milling progresses through the film. After 480 second [Figure 6.12 (d)] the milling removes all the Au in some regions, reaching the Si_3N_4 membrane substrate, which appears as a dark grey colour in the image. In Figure 6.12 (e) the FIB has milled through almost all the substrate in certain parts and the thin magnetic film on the reverse side begins to buckle due to the

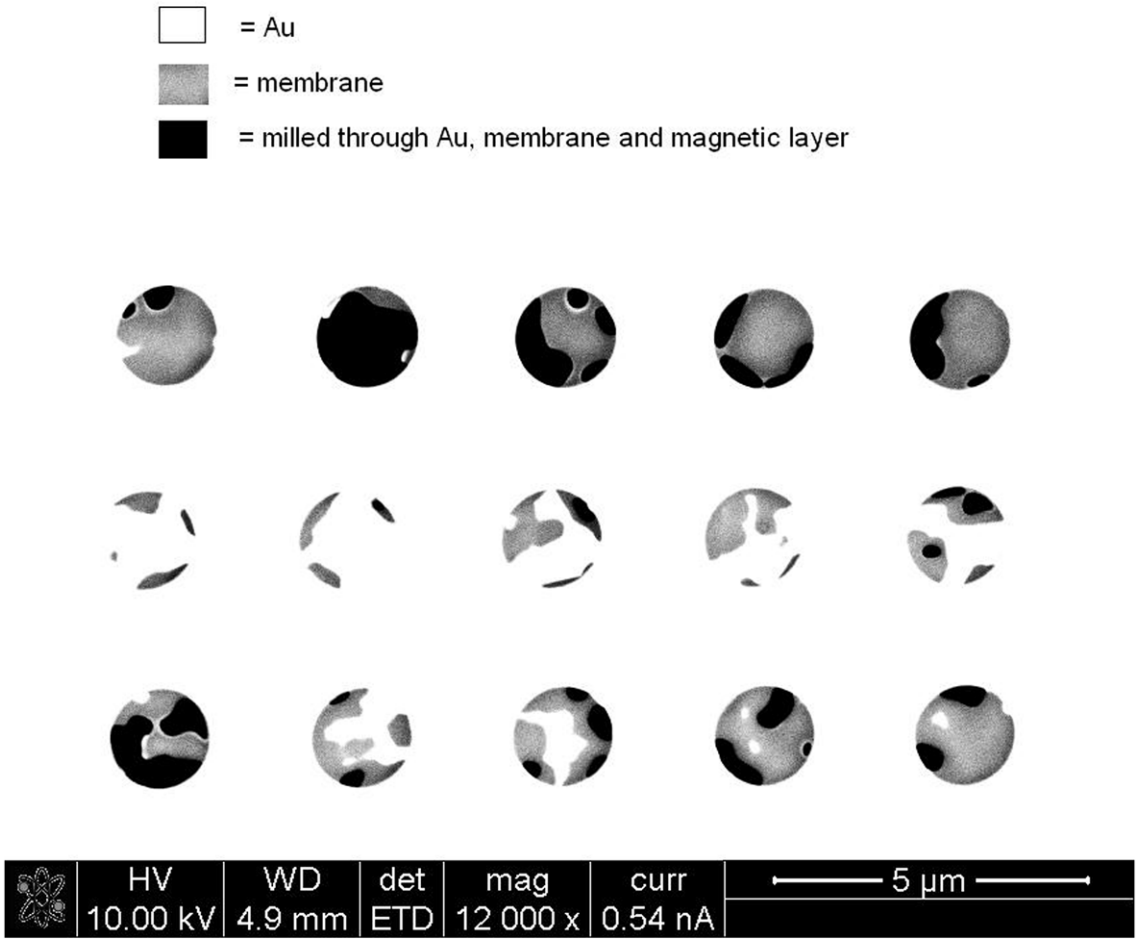

Figure 6.13: Nonuniform FIB milling of FOV apertures into thick Au films. Scanning electron micrograph of several 1.5 μm circular FOV apertures that were FIB milled into Au with the same milling time. The contrast in the SEM image indicates the material as shown in the key. Certain apertures can be seen to have been milled through the entire sample ensemble as revealed by dark black regions. Other apertures contain stubborn regions of Au that have not been completely removed, and would hinder the experiments if such apertures were used, by strongly absorbing the soft x-rays and not allowing them to transverse freely through the magnetic thin film of the reverse side of the silicon nitride membrane.

lack of a robust substrate. In close-by regions, there are however still large grains of Au. Eventually, in Figure 6.12 (f) the milling penetrates though the entire sample which appear as black in the SEM images.

The growth process of the Au forms nanoscopic islands across the surface of the substrate during the first stages of the deposition and the space between the islands fills as the gold layer becomes thicker. This became problematic when fabricating holographic devices. When milling several FOV apertures spaced across the membrane, there was no guarantee that all apertures would be completely clear of Au grains, and in some cases, the grains were so large that some of the devices themselves became unusable for the imaging experiment. Figure 6.13 shows several 1.5 μm apertures that were all milled for the same FIB exposure time of 60 second. The FIB beam energy was set at 30 kV and the beam current was 30 pA.

6.1.3 Improving the Fabrication of Apertures

For many samples, the large grains found in the Au film prevented the fabrication of effective devices for soft x-ray FTH. Increasing the thickness of the Si_3N_4 membrane to 200 nm, and reducing the size of the FOV apertures to 1 μm, both helped (but did not completely prevent the problem). By increasing the membrane substrate thickness from 100 nm to 200 nm decreases transmission of x-rays (with energy 800 eV) from $\sim$ 0.85 to 0.75 [279]. Lowering the sputtering power during the Au deposition results in smaller grains forming making them etch more uniformly with the rest of the Au film when exposed to the FIB [274]. A more satisfactory solution lies in the fact that thinner films of Au produce smaller stubborn grains. The small grains are easily removed by the FIB and only become problematic if they are allowed to develop as the Au film increases in thickness. Upon introducing a second metal to act as a spacer layer between several thin layers of gold, the hard grains are prevented. A Pd/Au multilayer can be used [13]. Here, both Au and Pd are high density metals and the Pd will strongly absorb soft x-rays and add to the effectiveness of the x-ray opaque mask. The spacer layer could equally be Cr [14] which will not absorb the soft x-rays as strongly as Pd, but is still effective at

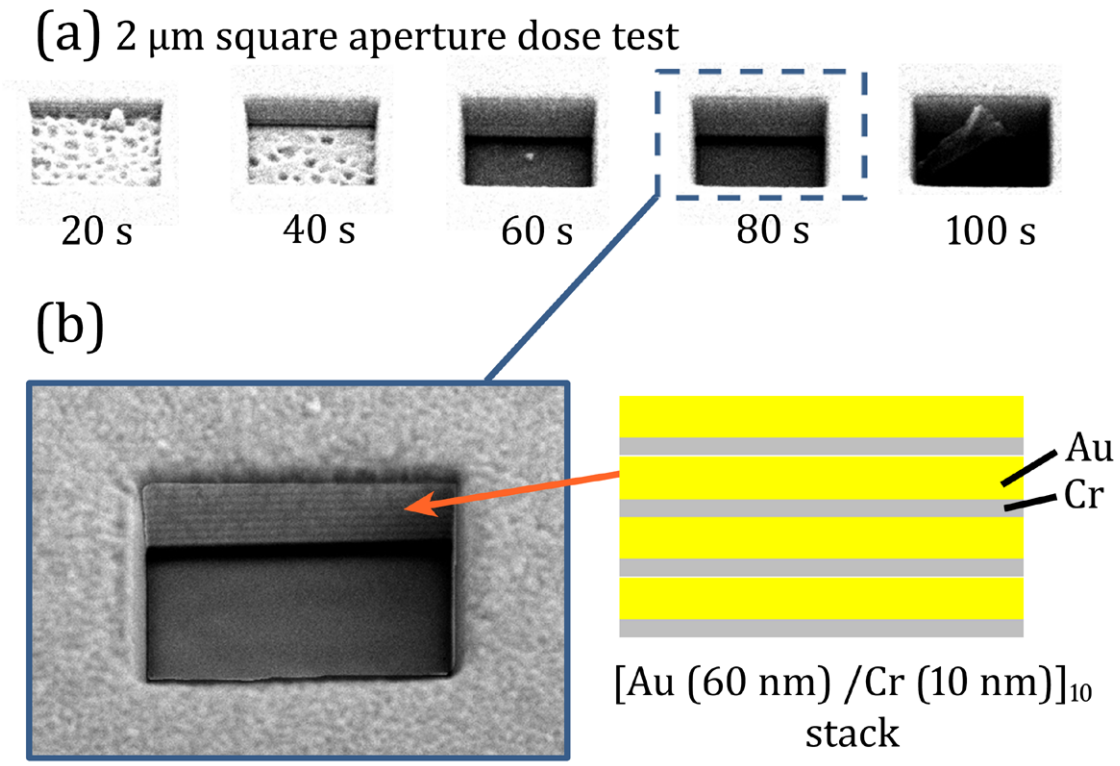

Figure 6.14: Au/Cr multilayer masks. (a) Dose array of a 2 μm square aperture showing exposure times to the FIB in seconds. The FIB beam energy was set at 30 kV and the beam current was 30 pA. (b) An enlarged view of the aperture with an 80 s mill time. The profile of the repeating Au/Cr layers can be seen.

preventing hard grains forming throughout the Au. Figure 6.14 (a) shows a dose test of 2 μm square apertures with exposures ranging from 20 to 100 s. The mask here was [[Au(60 nm)/Cr (10 nm)]$_{10}$] ML stack. Small grains formed in each of the gold layers but the Cr layer between each Au layer prevented grains from persisting through the entire thickness of the mask. The small grains could easily be removed with standard exposure to the FIB Figure 6.14 (b) shows an enlargement of the clean aperture with a schematic of the Au/Cr ML stack.

Sample that were manufactured with a single thick Au masks (where hard grains had formed) could be processed with a chemical etch to remove the majority of the Au rather than using a FIB. This process is illustrated in Figure 6.15. In Figure 6.15 (a) An etch mask was created by depositing a 20 nm Cr layer onto

the thick Au film. FIB was then used to etch a FOV apertures through the Cr and partly into the Au film, the result of which is shown in Figure 6.15 (b). The sample was then placed in a dilute solution of potassium iodide gold etchant for 90 s and rinsed with DW, IPA and acetone before drying with N_2 gas. The resulting aperture is shown in Figure 6.15 (c).

The etching procedure illustrated in Figure 6.15 (b) was not optimised and tests have not been carried out to investigate reducing the damage to the sides of the aperture (by the chemical etch solution) by reducing the total etch time. In the majority of cases the etchant did remove parts of the walls, making the aperture an irregular shape rather than the clean cut square, or circle. The etch also introduced an undercut as shown in Figure 6.16. The enlarged view of the undercut shown in Figure 6.16 (c) revealed the undercut to be ∼300 nm wide and ∼70 μm deep, and forms with a step-like profile. The irregular shape of the aperture due to the undercut should not present a problem for soft x-ray FTH reconstruction however samples created with this method of manufacture remain untested at present.

6.1.4 Beamstops

Beamstops are used in coherent x-ray diffractive imaging (CXDI) to protect the CCD camera from intense parts of the x-ray beam that pass though the sample with small scattering vectors. The x-rays with small scattering vectors are very bright and can potentially damage the CCD camera if the pixels are exposed for an excessive amount of time to the intense beam.

Two beamstops designs were used on IO6. The first was simply a piece of wire ∼400 μm wide which was positioned diagonally across the CCD. Some low-$\mathbf{q}$ information at the centre of the hologram will always be lost due to the beamstop, and whilst this is unavoidable, other defects in the reconstruction can be avoided by reducing the disturbance in the continuity across the rest of the hologram. The thick wire used for this beamstop causes a large strip of information to be lost from the hologram. The sudden change in intensity in the hologram across the boundary of the beamstop has a step like property that introduces periodic defects in the

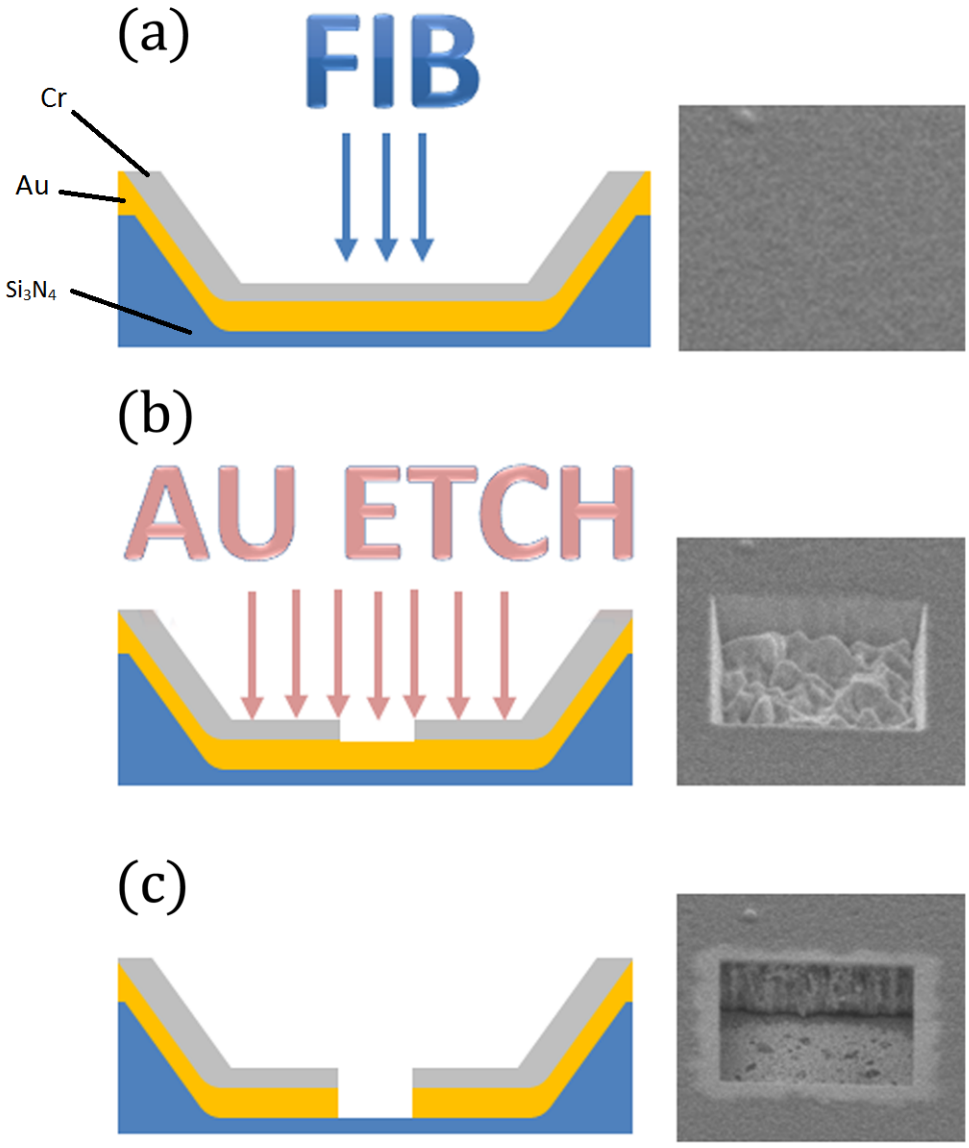

Figure 6.15: Chemically etched apertures. (a) 10 nm of Cr is deposited over the Au mask. FIB is then used to etch through the Cr and through parts of the Au beneath. (b) The sample is placed in chemical etchant to remove the Au in areas exposed to the FIB in (a). (c) The resulting aperture is clear of Au grains after an etch time of 90 seconds.

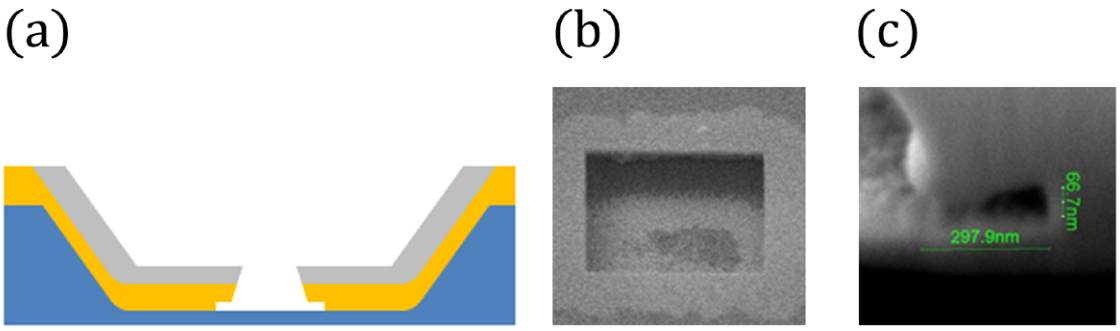

Figure 6.16: Chemically etched apertures - undercut. (a) In many incidences the walls of the aperture were not always preserved, as can been seen in the scanning electron micrograph in (b). (c) A profile of the aperture revealed a step-like undercut ∼300 nm wide and ∼70 μm deep.

reconstruction. Simulations of the expected defects caused by different beamstops are shown in Figure 6.17. To reduce the sudden step-like change in intensity, a smoothing function is often applied across the beamstop area to remove any sharp edges from the hologram [13]. A directional smoothing function was applied to the measured holograms over the shadow from the beamstop to reduce the presence of defects in the reconstruction. To reduce the loss of information in the hologram, a beamstop was designed with a central tungsten disc ∼600 μm in diameter on two ∼50 μm diameter crosswires.

6.2 Experimental Results

6.2.1 Conventional Magnetic FTH

Conventional pinhole references were used to image the out-of-plane domain structure in a $[Co(0.5\ nm)/Pt(1\ nm)]_{30}$ multilayer. Figure 6.18 (a) shows the hologram recorded for a single polarisation of light. The hologram was an accumulation of 100 images, each frame with an exposure time of 8 s on the full area of the CCD. A second hologram was recorded with the opposite helicity of light and was subtracted from the hologram in Figure 6.18 (a). The Fourier transform of the difference image is shown in Figure 6.18 (b). It reveals three pairs of conjugate

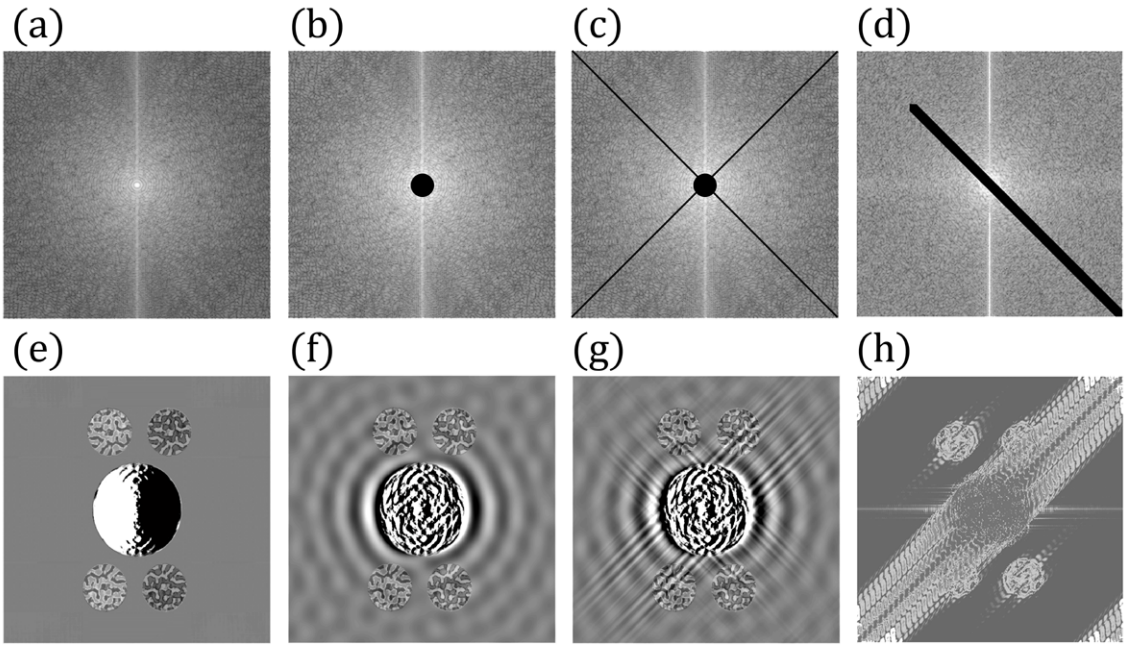

Figure 6.17: Simulated beamstop defects to the reconstruction. (a) A simulated hologram without the presence of a beamstop. (b) A small circular disc beamstop would be most ideal causing the least amount of disruption to the hologram whilst blocking the central bright beam. (c) A small circular disc is mounted on a pair of supporting crosswires. (d) A single wire is positioned across the centre of the hologram. Both (c) and (d) represent simulation of the beamstops used at stages in the Diamond experiments. (d) Prior to the the design used in (c), a thin wire was placed across the centre of the beam to block the central bright region from the CCD. (e-h) Simulated reconstructions from the holograms (a-d) respectively. (f) shows radial fluctuations in the phase resulting in a small distortion to the reconstructed object. (h) The introduction of the thin cross wires introduces diagonal streaks into the reconstruction which can lie across the object reference cross-correlations in certain geometries. (h) The wire used as a beamstop introduces large distortions to the reconstruction in the form of a thick diagonal streak at the centre, and streaks across the reconstructed objects.

images of the magnetic domains that lie within the FOV aperture. An SEM image of the holographic device, as viewed from the side of the Au mask, is shown in Figure 6.18 (c). Here a 1.5 μm FOV aperture is surrounded by three narrow reference pinholes which form the cross-correlations in the reconstruction. An SEM of the holographic device as view from the side of the magnetic film is shown in (d). The size of the narrow reference holes are $\sim$60 nm, which places the limit on the resolution of the final reconstruction.

A directional smoothing function was used to reduce the sharp edges introduced by the shadow of the wire beamstop on the CCD image, as seen in Figure 6.18 (a). The resulting hologram and the real part of its FT are shown in Figures 6.19 (a) and (b). The artifacts from the beamstop are significantly reduced in Figure 6.19 (b) which has enhanced the clarity of the reconstruction. The magnetic contrast of the domains in the image is solely due to absorption contrast and so the information is contained within the real part of the reconstruction. The variation in the contrast between the cross-correlations from the different pinhole references is believed to be caused by a phase gradient in the real part of the image as described by Scherz *et al.* [15]. A procedure to correctly centre the hologram in the image is performed using Fourier shift theorem, and the reconstructed image was multiplied by a plane wave $\exp(i\Delta qr)$. If the centre is not determined precisely with sub-pixel accuracy then a phase gradient remains that is thought to be the case in Figure 6.19 (b). A phase change may also arise from loss of low-$\mathbf{q}$ information due to the beamstop shadow or loss of high-$\mathbf{q}$ information due to the limited size of the CCD [15].

Figure 6.19 (c) shows an enlargement of the cross-correlation highlighted in Figure 6.19 (b). The light and dark areas in the FOV disc represent magnetic domains pointing in and out of the page. A line scan across the highlighted domain boundary is shown in Figure 6.19 (d). The resolution of the image was estimated by taking into account the typical width of a domain wall in CoPt multilayer films (typically <10 nm) [283]. The intensity profile in Figure 6.19 (d) was fitted with a hyperbolic tangent functions of the form $I = I_0\tanh[2(x - x_0)/w] + I_c$, where x_0 is the position of the centre of the domain wall, w is the width of the wall, and

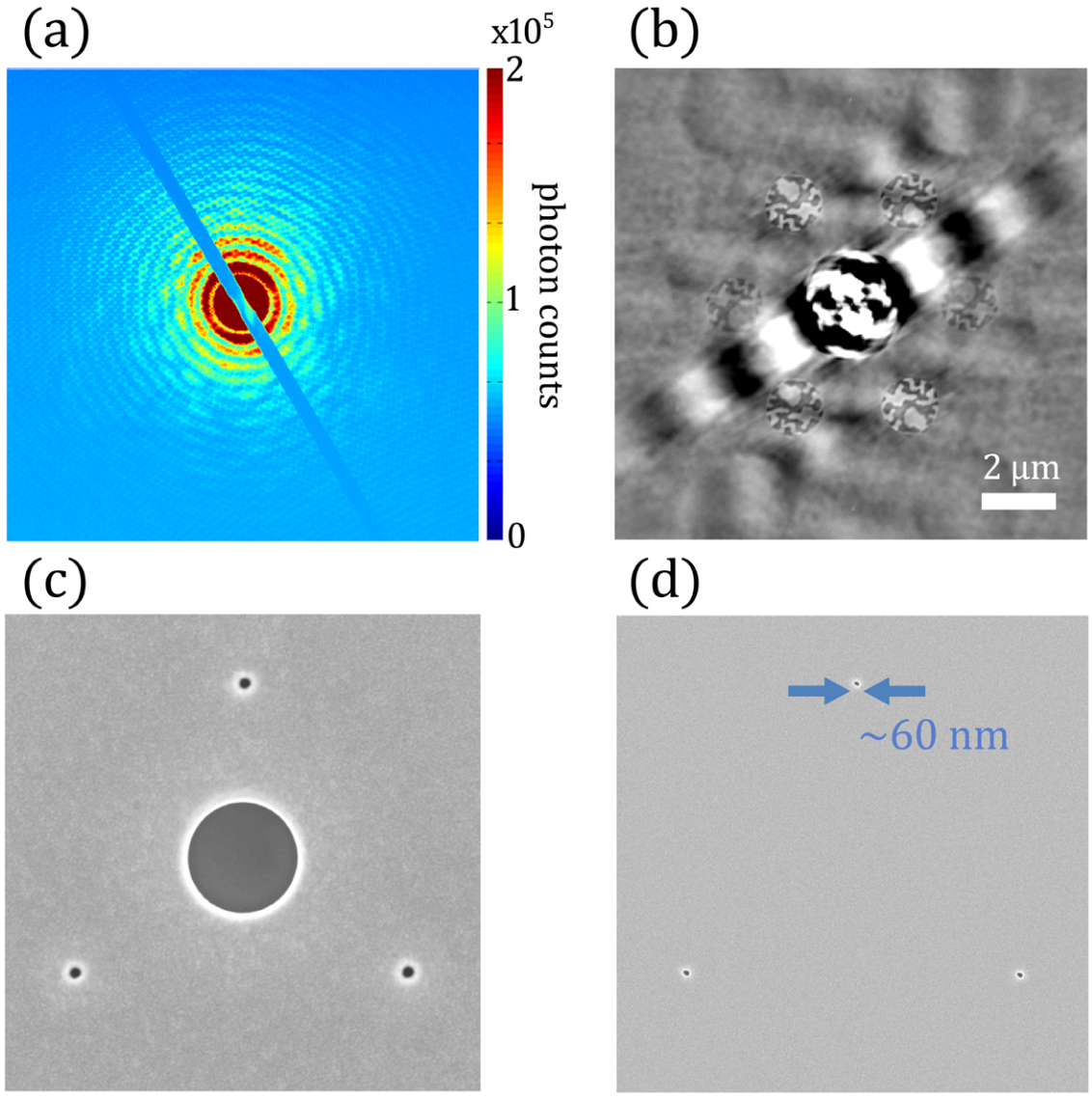

Figure 6.18: Imaging magnetic domains with pinhole references. (a) Hologram recorded with right circularly polarised x-rays with the beam energy set to the Co L_3 absorption edge (778 eV) (only the central 1200×1200 pixels are shown). (b) Fourier transform of a difference image between holograms recorded with opposite polarisation helicity. (c) Scanning electron micrograph of the holographic device, viewed from the backside of the sample. A 1.5 μm FOV aperture is surrounded by three narrow holographic reference pinholes, each $<$ 100 nm in diameter. The reconstruction shown in (b) reveals three pairs of conjugate images of the magnetic domains that lie within FOV aperture. Each pair of conjugate images result from the cross-correlations between the FOV aperture and one of the three reference pinholes shown in (c). (d) Scanning electron micrograph of the holographic device as viewed from the front side of the sample. The exit width of the reference pinholes range between 60 and 70 nm.

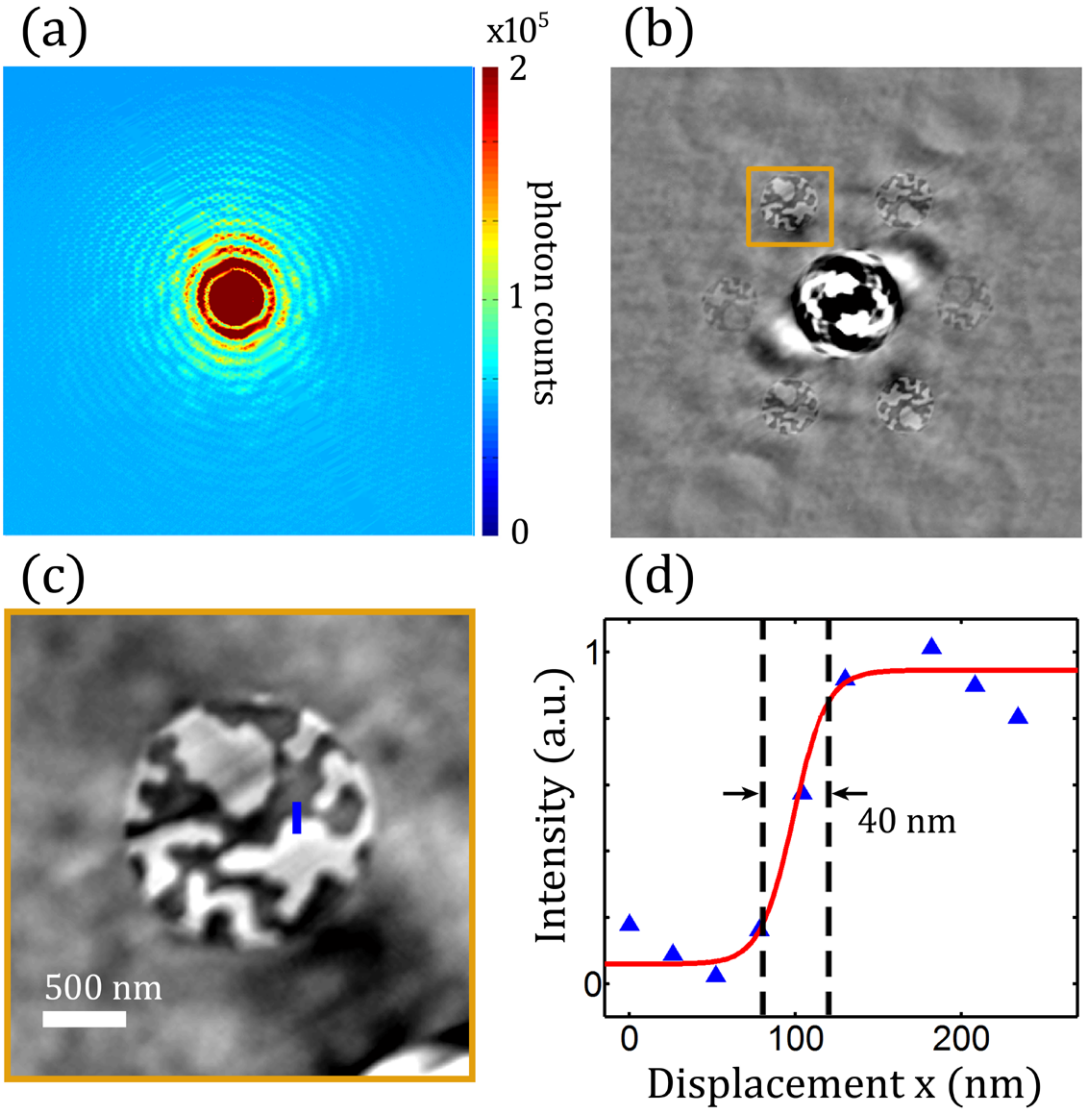

Figure 6.19: Reducing the shadow of the beamstop. (a) A direction smoothing function was applied to the area of the hologram where the beamstop shadow disrupted the continuity of the image (only the central 1200×1200 pixels of the hologram are shown). (b) The Fourier transform of (a) reveals a reconstruction with improved clarity due to reduced artifacts caused by the beamstop shadow. (c) An enlargement of the highlight cross-correlation in (b). The blue line indicates the region across a domain wall of the line scan in (d). (d) The intensity profile across a domain wall is shown by the blue triangle markers. The data was fitted with a hyperbolic tangent (red curve) and the resolved width of the domain wall is estimated as $w = 40 \pm 10$ nm.

I_0 and I_c are intensity offset values. The fitting is shown by the red curve and gives a width of the domain boundary $w \approx 40 \pm 10$ nm. This value corresponds with the resolution limited by a reference pinhole of size ~ 60 nm, as described in Chapter 3.

6.2.2 Magnetic Imaging Using Extended References

As shown in Figure 6.7, the Au mask on the backside of the sample was patterned with several holographic devices. In this section we present the results of reconstructions formed from an extended holographic references. A 1.5 μm FOV aperture was FIB milled into the Au mask with a narrow extended reference slit in close proximity. The reference slit was $\sim$2 μm in length and $\sim$30 nm wide. The straight wire beamstop used previously was replaced with the more sophisticated design consisting of the $\sim$600 μm diameter disc supported on two $\sim$50 μm diameter crosswires. Accumulations of 100 images, each frame with an exposure time of 8 s on the full area of the CCD, were recorded for the two opposite x-ray helicities under attenuated beam intensity. The total exposure time of 800 s should not be taken as being representative for the required image acquisition time, as steps to optimise this aspect of the measurements were not taken.

The difference image of the two holograms recorded with opposite helicities is shown in Figure 6.20 (a). An appropriate differential filter is determined from the streak visible in the hologram, and digitally multiplied with Figure 6.20 (a). A Fourier transform of this result is given in Figure 6.20 (b) and reveals the four object-reference cross-correlations. The reconstruction using conventional FTH references possessed a phase gradient, and likewise the phase in Figure 6.20 (b) was adjusted by multiplying the FT of the hologram with a plane wave to centre the hologram in the image. The reconstruction in Figure 6.20 (b) shows only the real part of the data which is related to the magnetic contrast. Figure 6.20 (c) shows an enlargement of one of the cross-correlations revealing a high resolution image of the magnetic domain structure in the Co/Pt. Line scans were taken across a domain wall in the horizontal and vertical direction. The line scans were

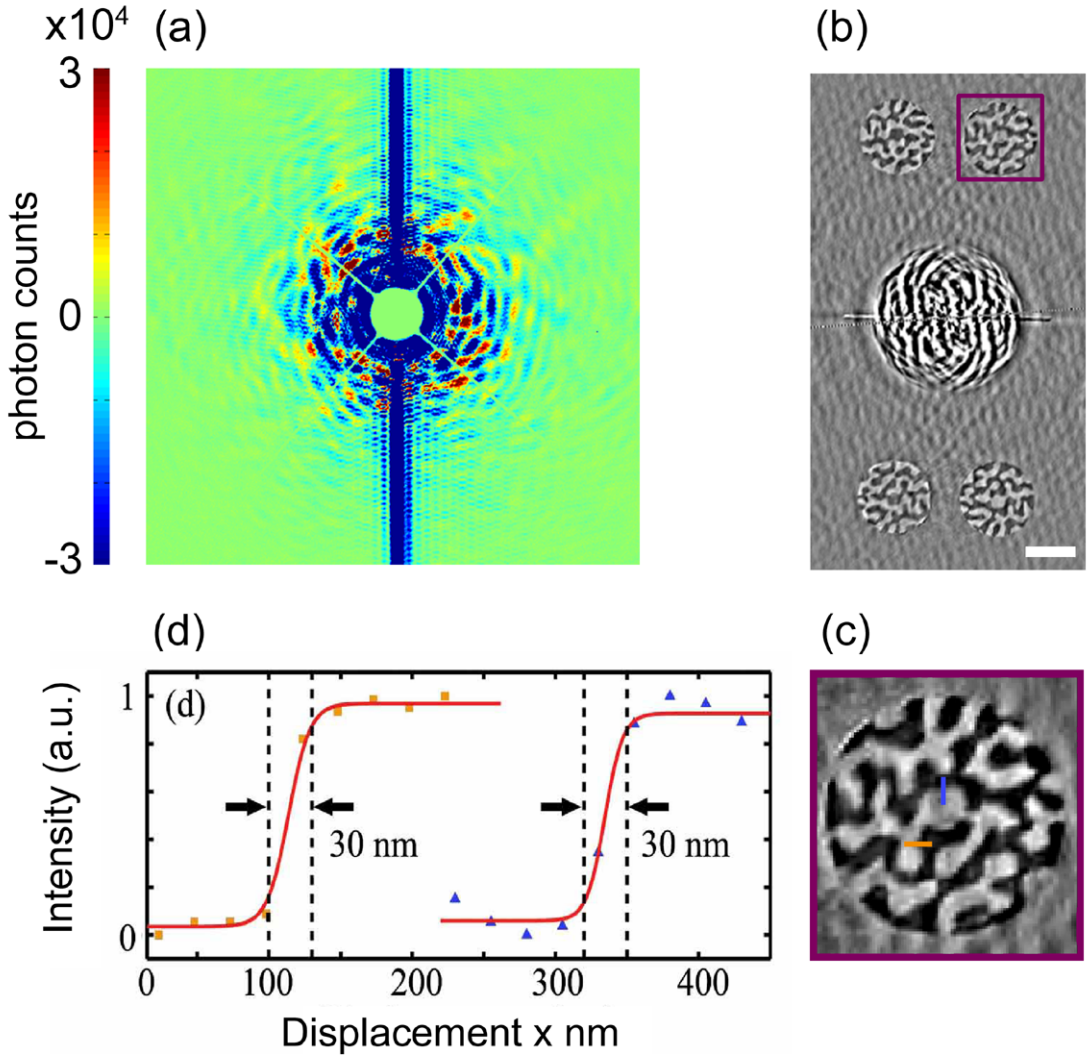

Figure 6.20: Imaging magnetic domains with extended references. (a) Difference image of holograms measured with opposite polarisation helicity. Only the central ∼500×500 pixels of the hologram are displayed. (b) Real part of the reconstruction data (white scale bar = 1 μm). (c) An enlargement of the cross-correlation highlighted in (b). The positions of the line scans in (d) are marked out with blue and orange lines. (d) The horizontal intensity profile across the domain wall (orange square symbols) corresponds to the resolution along the slit direction. The intensity profile across the domain vertically (blue triangle symbols) corresponds to the resolution across the width of the slit. The data was fitted using a hyperbolic tangent (red curves) which gave a resolved width of the domain wall as $w \approx 30 \pm 10$ nm in either direction. For clarity purposes, the line scans have been shifted an arbitrary amount along the x-axis to separate the data.

used to interpret the approximate resolution of the image, with the horizontal line scan corresponding to the resolution along the slit direction and the vertical scan across the width of the slit. The intensity profiles and hyperbolic tangent fitting functions across two domain walls are shown in Figure 6.20 (d). The regions of these line scans are highlighted in Figure 6.20 (c). From the hyperbolic tangent we obtain a width of the domain boundary $w \approx 30 \pm 10$ nm in both directions. This value is of the order of the sample period (∼30 nm) as determined by the maximum acceptance angle of the CCD, and equivalent to the width of the extended reference slit.

6.3 Conclusions

This chapter demonstrates holographic magnetic imaging using HERALDO which has been setup on the nanoscience beamline, IO6, at Diamond light source. Magnetic imaging with conventional FTH (using narrow reference holes) was performed to resolve the nanoscopic domain structure in a Co/Pt ML film. Measurements of the same sample film were performed using magnetic HERALDO imaging where a narrow slit was used as an extended holographic reference. The resolution achieved in our conventional FTH setup was limited by the size of the reference hole and estimated to be ∼40 nm from the resolvable size of a domain wall. In our HERALDO setup we found the resolution to be limited by the sample period (∼30 nm) which was also equivalent to the approximate width of the reference slit. We found that when using a narrow slit as an extended reference object, the resolution in the vertical and horizontal direction (the latter corresponds to HERALDO filtering) was the same within the error of the fitting function used to extract the resolved domain wall width. Compared with the conventional FTH method an expected benefit of using extended references is the reduced image acquisition time due to an increase in intensity through the reference. Another benefit of using an extended reference lies with the ease of manufacturing slits on the Nova 600 dual beam system compared with fabricating narrow holes. It was found that slits ∼30 nm wide could be produced whereas the smallest size of reference hole manufactured was

∼60 nm. We acknowledge that today, FTH masks can be routinely produced with reference holes of 30 nm size using FIB milling [12], but we believe the sensitivity to small changes in the milling time will have less effect on extended reference objects than narrow holes, and fabricating slits should prove easier to manufacture on many nanofabrication systems. It has been reported by Zhu *et al.* that holographic reference slits ∼15 nm wide have been manufactured [95] and it is believe that the HERALDO approach can provide superior resolution over the conventional FTH method.

Chapter 7

Off-normal Magnetic Imaging With HERALDO

In this chapter we present a method for imaging in-plane magnetism using holography with extended references. We achieved contrast of in-plane magnetic configurations by rotating the sample within the scattering chamber such that the surface plane was no longer perpendicular to the direction of the x-ray beam. When performing imaging in this off-normal incidence geometry, the in-plane magnetic vectors acquire a non-zero projection to the beam, and a SXRMS signal can be measured.

The off-normal geometry reported here is similar to the setup reported by Tieg *et al.*[23], where a narrow hole was milled at an inclined angle into a fixed holographic mask that allowed x-rays to pass through the mask as a point-like reference whilst the sample was rotated within the beam. An extended reference, however, offers more flexibility, and allows one to vary the incidence angle *in situ*.

To demonstrate the techniques sensitivity to in-plane magnetisation, we present images of flux closure ground states in thin ($\sim$50 nm) permalloy elements, less than 1 μm in lateral size. We then studied magnetostatic coupling in [Co/Pt]/NiFe systems and obtained images of an in-plane domain pattern which is imprinted into the permalloy (NiFe) layer by the stray fields generated from the adjacent Co/Pt domains.

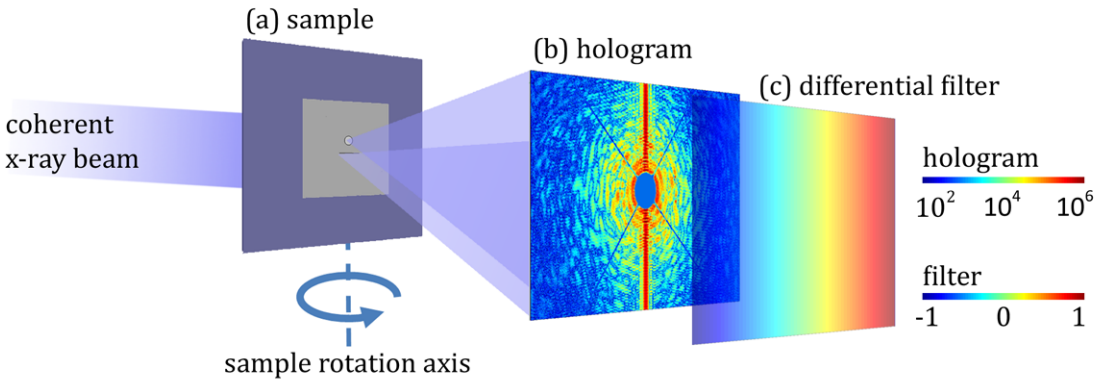

Figure 7.1: Experimental setup for off-normal incidence transmission FTH. (a) The sample was rotated about its vertical axis, perpendicular to the long axis of the reference slit and the x-ray beams direction. (b) When rotated within the beam, the slit still allows x-rays to pass through it. This would not occur if a conventional narrow hole was instead used for a holographic reference instead of an extended object. The reconstruction procedure has already been presented in Section 4.3, where a linear filter [shown in (c)] was digitally multiplied to the hologram before the Fourier inversion is performed.

7.1 Experimental Setup

The concept for this experimental setup is straight forward in nature and closely follows the method already presented in Chapter 6. Here, the sample was rotated by 30° or 45° about the vertical axis, perpendicular to the beams direction and the long axis of a holographic reference slit. A schematic of the setup is shown in Figure 7.2.

The sample-mask arrangement in the rotated geometry is shown in Figure 7.2 (a). This demonstrates the transmission of the x-ray beam through the reference slit. A scanning electron micrograph of the holographic device is shown in Figure 7.2 (b). A plan view of the experimental setup is shown in Figure 7.2 (c) where the tilt angle is set to $\alpha = 45°$. Figure 7.2 (d) illustrates the expected SXRMS signal strength associated with in-plane and out-of-plane magnetisation as a function of incident angle. The size of the FOV aperture from the perspective of the

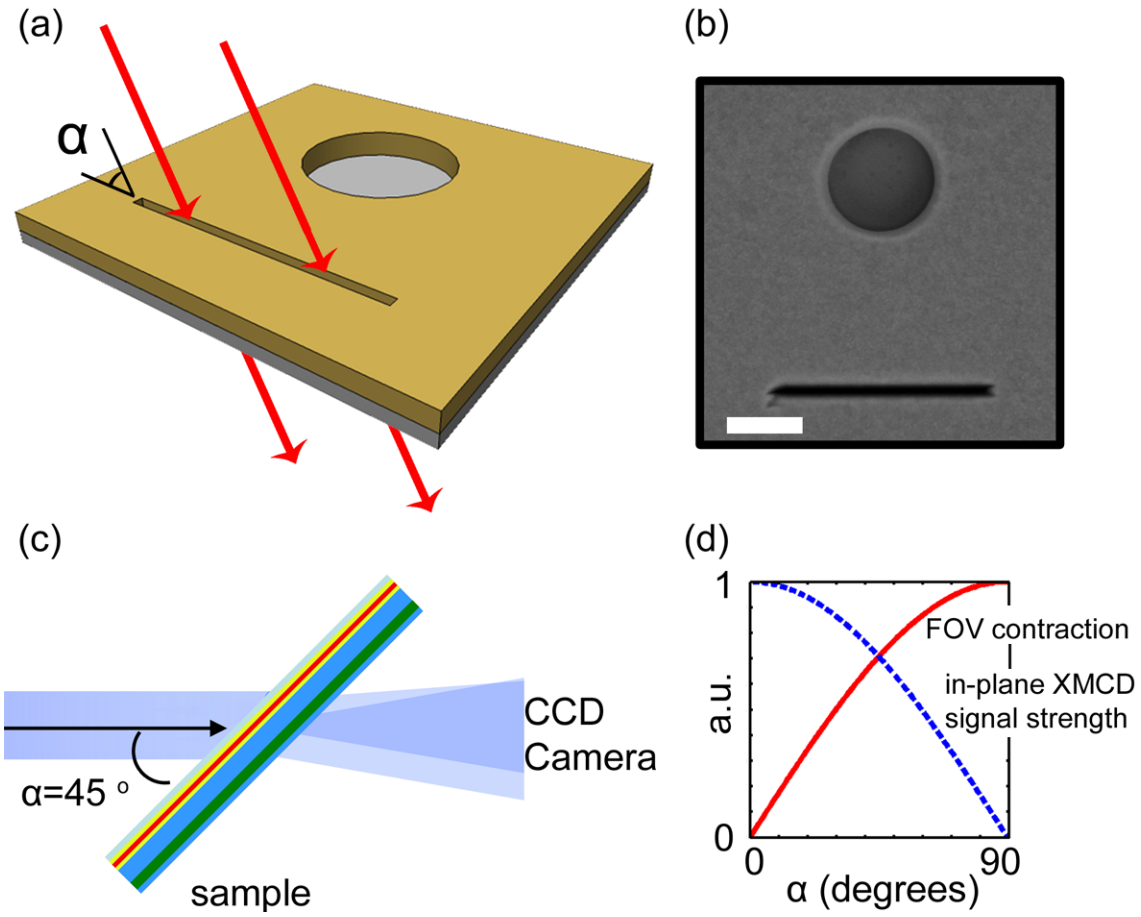

Figure 7.2: Schematic illustrating the passage of x-rays through a rotated sample. (a) Schematic indicating the sample orientation when rotated within the x-ray beam spot. (b) Scanning electron micrograph (SEM) of the reference slit and object aperture viewed from the side of the mask (scale bar=1 μm). (c) Experimental setup with the sample rotated to 45° within the beam spot which makes the XMCD signal sensitive to the in-plane magnetisation. (d) Illustration showing how the in-plane SXRMS signal is proportional to the cosine of the incident angle. The reconstructed FOV contracts in the direction perpendicular to the axis of rotation and is proportional to the sine of the incident angle. The SXRMS signal from out-of-plane magnetisation is also proportional to the sine of the incident angle.

beam will contract as the sample is rotated, but also the FOV aperture gradually becomes blocked by the mask (to what extent depending on the thickness of the $[Au/Cr]_{10}$ mask layer). The contraction is proportional to the sine of the angle of incidence that is equivalent to the reduction in the SXRMS signal from out-of-plane magnetic moments. At rotation $\alpha = 45°$, the $[Au/Cr]_{10}$ mask blocked ∼700 nm of the FOV aperture (which is equivalent to the thickness of the mask layer).

Off-normal transmission holography experiments were performed on IO6 at DLS and on the dragon beamline ID08 at the European Synchrotron Research Facility (ESRF). The experimental setups used at both beamlines was largely the same and were as described in Chapter 6. The differences in the details at the ESRF are outlined below.

ID08 beamline, ESRF

An external applied magnet field was generated by two poles mounted onto the diffraction chamber in a perpendicular geometry. Both pole pieces possessed a small hole to allow for the x-ray beam to pass through the chamber undisturbed. The 50 μm spatial filter pinhole was positioned 80 cm upstream from the sample. The CCD camera chip had 1300×1340 pixels, with 20 μm pixel size. This was positioned 500 mm downstream from the sample and allowed a maximum scattering vector $\mathbf{q}_{max} = 205\ \mu\text{m}^{-1}$ to be detected. This gave a pixel size in the reconstruction (or sampling period) of ∼30 nm. The focal point of the beam was set at 1 m behind the CCD.

The beamstop was a circular disc ∼700 μm in diameter. The samples were mounted onto a holder shown in Figure 7.3. The holder contained five 2 mm holes each with a 60° exit cone shape. The schematic of one of the wholes is shown in Figure 7.3 (a) with a cross section illustrating the 60 degree exit cone in Figure 7.3 (b). A photograph of the sample holder is shown in Figure 7.3(c). The design of the 2 mm holes stopped the scattered x-rays from becoming blocked by the sample holder when the sample was rotated within the x-ray beam (Figure 7.3 (d)). A similar sample holder design was used at DLS to prevent the x-rays becoming

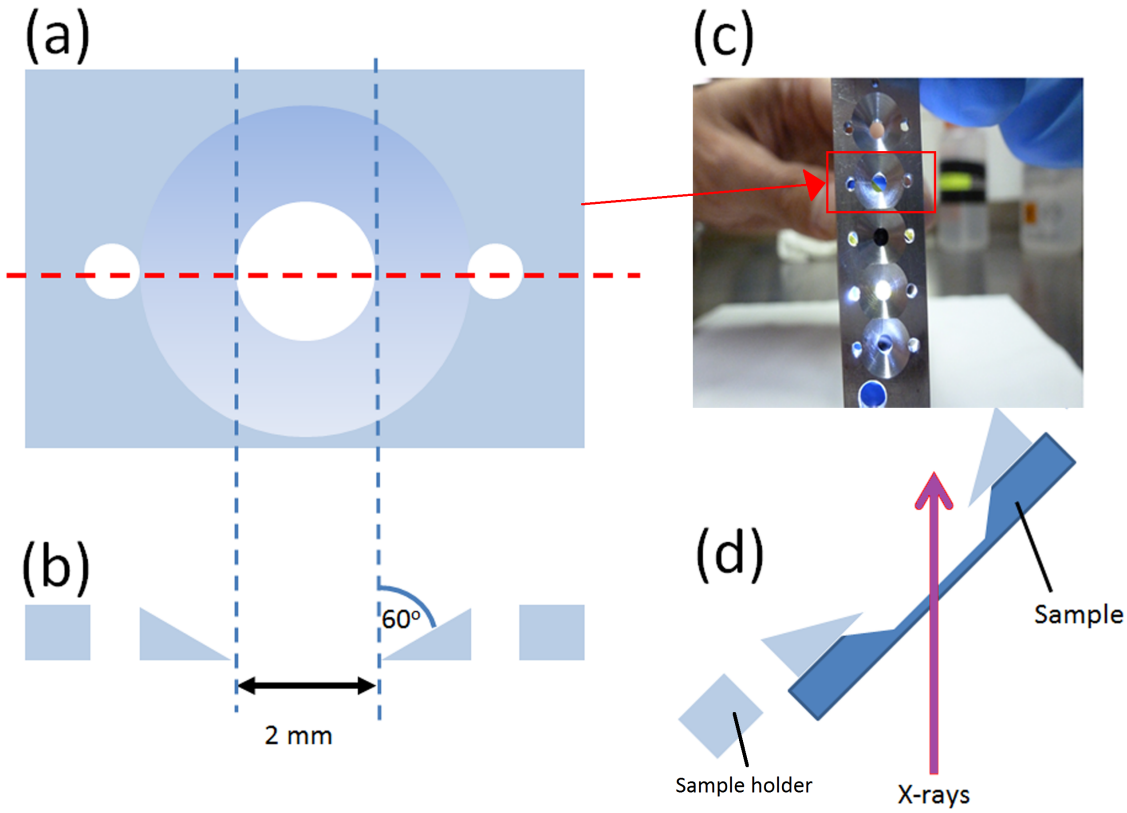

Figure 7.3: ESRF sample holder design for off-normal HERALDO. (a) A 2 mm hole was machined through the sample holder, with a 60° exit cone. (b) A cross-section of the hole shown in (a) taken across the dashed red line. Here the 60° exit cone of the hole can be seen. (c) A photograph of the sample holder which contained five 2 mm holes, each equivalent to the schematics shown in (a) and (b). (d) The sample was positioned over one of the 2 mm holes for the experiment. The 60° exit cone of the hole illustrated in (b) ensured that the light scattering through the sample would not be blocked by the holder, when the sample was rotated within the beam.

blocked by the holder when measuring in an off-normal geometry.

7.2 Imaging of Magnetic Vortex Structures

Magnetic films will form planar magnetic structures if the film thickness is below the magnetic exchange length [284]. Generally, the magnetisation in these films is

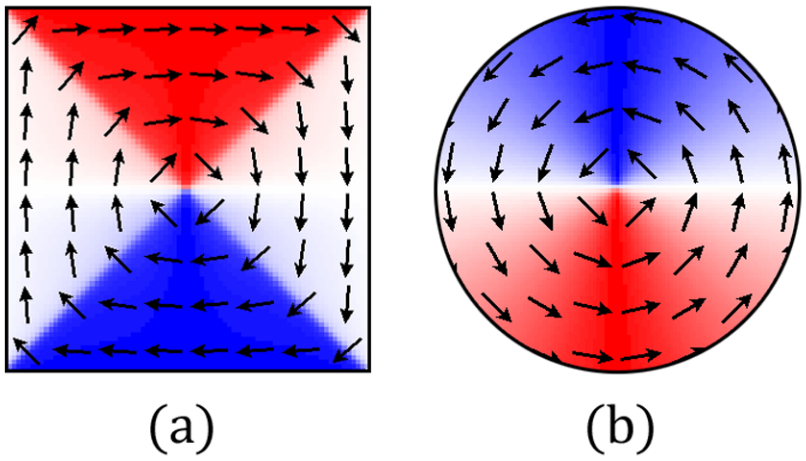

Figure 7.4: Micromagnetic simulation of the magnetic vortex structure in submicroscopic elements. (a) A simulation of a Laudau ground state that forms in flat square Py elements. (b) Simulation of a vortex ground state that typically occurs in nanoscopic Py discs. The blue, white and red colours signify different in-plane magnetisation directions that are then given by the arrows. The curling nature of the magnetic vectors forces an out-of-plane core at the centre of each element as discussed in Section 2.2.3.

forced into the plane of the film by demagnetising fields. An exception to this is the magnetic vortex, illustrated in Figure 7.4. These simulations were performed in OOMMF (see Appendix C for more details). They show that the magnetisation curls around the element with an out-of-plane core at the centre. In these simulations the permalloy thickness was 50 nm, and the lateral size of the elements was 1 μm.

From a data storage perspective, the ability to provide vortex ground states confined within lithographically manufactured circular or rectangular elements would be a great feat. The vortex structures exhibit low stray fields and so have a high magnetic stability. Also minimal cross-talk between adjacent vorticies would mean that a high bit densities could be achieved [284]. The potential application of vorticies in Random Access Memory (RAM) data storage systems is currently attracting enormous interest. Here it is important to be able to observe and understand the four degenerate states of the magnetic vortex (two levels of polarity (up/down)

and two levels of circulation), and lensless HERALDO imaging holds the potential to observe both both the chirality and the polarity in single elements, or even small arrays. Recent studies reported by Im *et al.* [2], have shown asymmetric phenomenon in large arrays of vorticies which may impose unforeseen difficulties in creating vortex based RAM data storage systems. The experimental observation of non-symmetric behavior, however, implies a biasing which could be applied to a logic device or a sensor [285].

The magnetisation dynamics of nanoscopic elements is verging outside the scope of this research thesis. However, a discussion of time resolved imaging shall be presented in Chapter 9. There we propose an experiment to extend the static measurements presented in this thesis into a time resolved stroboscopic holographic imaging technique.

7.2.1 Sample Design and Fabrication

To prepare samples for static measurements of flux closed magnetic vorticies, a $\sim$50 nm thick permalloy film was sputter-deposited onto the front side of a Si_3N_4 membrane and protected from oxidation by a 2 nm Ta capping layer. As previously described in Figure 6.7, an integrated $[Au/Cr]_{10}$ mask was patterned with holographic devices. The sample was then turned over within the FIB system so that the front side of the sample faced the FIB, and the fabrication of nano-sized elements was achieved by etching the continuous Py film. Material was milled away from the film over a 3-4 μm square region which left a single isolated square or disc element at the centre of the etched patch. Figure 7.5 (a) shows a dose array used to create 800 nm square elements in this fashion. In this example a 3 μm square region was FIB etched into the Py film. 4 μm regions were also used and in this situation the etch time was adjusted accordingly. This manufacturing approach could reliable pattern square elements down to 400 nm in lateral size before the sides became deformed and the element resembled a disc more so than a square with well defined edges. Figure 7.5 (b) shows equivalent dose array tests for disc elements.

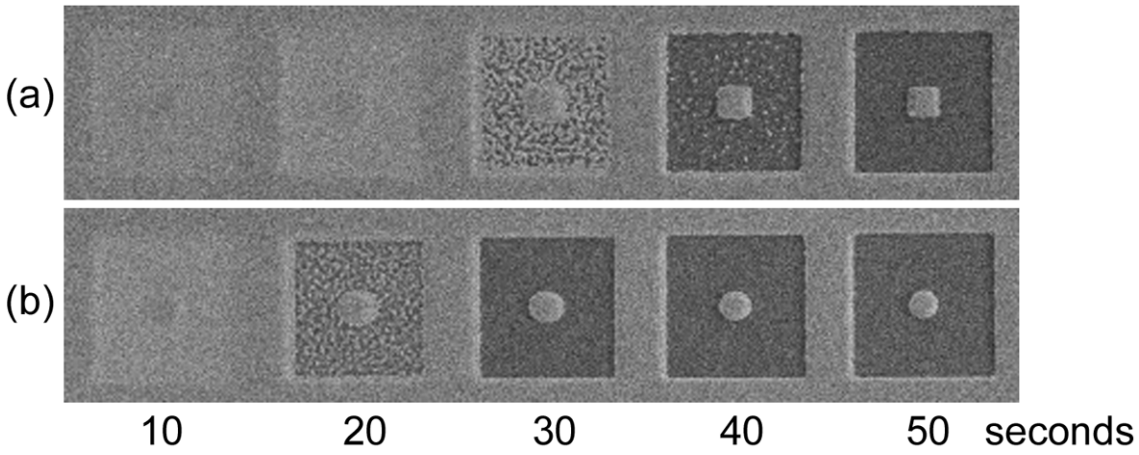

Figure 7.5: Fabricating permalloy nanoelements using FIB. (a) Scanning electron micrograph showing the 50 nm Py film with several 3×3 μm regions that were exposed to the FIB for a range of etch times. At the centre of each etched area, an 800 nm squares remained. (b) Shows an equivalent dose array for 800 nm disc elements. The etch times are shown beneath in seconds. A milling time of 50 seconds provided a square element completely isolated from the continuous film. Similarly an etch time of 30 seconds created a disc element completely isolated from the continuous film, however an etch time of 50 seconds was used to ensure the disc element was not elongated.

We found that discs down to sizes no smaller than 200 nm could be manufactured with this approach using the Nova 600 dualbeam system. To improve the edge roughness of these elements and manufacture yet smaller features, EBL would seem a more appropriate tool. However, for convenience of aligning the element with the holographic FOV aperture, FIB was the tool of choice during these development stages of the imaging technique.

Figure 7.6 illustrates specifically how the elements were positioned with respect to the FOV apertures in the holographic mask, and how each of the devices were positioned across the membrane window. The support frame of the membrane was $\sim$ 200 μm thick so with a sample rotation of 45° (as in Figure 7.2) the support frame blocked the x-rays from passing through approximately half of the membrane window. The holographic devices were thus machined in a single line along one edge of the membrane window. This is depicted in Figure 7.6 (c). The FOV apertures themselves became blocked by the holographic mask, and the curve illustrated in Figure 7.2 (d) suggests that a portion of the FOV aperture $\sim$700 nm in size was blocked. The elements were therefore offset from the centre of the FOV apertures as illustrated in Figures 7.6 (a) and (b). An SEM image of an 800 nm disc element, positioned within the FOV aperture is shown in Figure 7.6 (b). At the centre of the image there is Py disc, 800 nm in diameter. Here, a square FOV aperture (2 μm in size) was milled into the holographic Au/Cr mask on the back side of the membrane. This is visible as the darker shaded square immediately around the disc in Figure 7.6 (b). A small hole can been seen just outside the FOV aperture, close to the bottom left corner, which was milled through the mask to act as a reference marker to align the elements with the correct edge of the FOV aperture and prevent the mask from covering them during the experiment when the sample was rotated. The disc element was manufactured by FIB etching a 4 μm square region around the disc for a total etch time of 85 s.

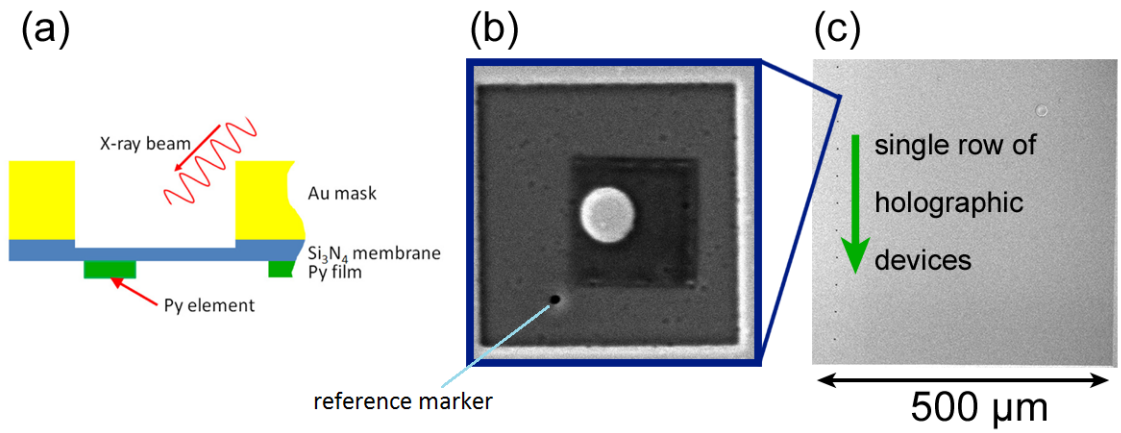

Figure 7.6: Positioning elements on the sample. (a) Profile schematic of the FOV aperture. (b) SEM image of an 800 nm disc positioned off centre from the FOV aperture so that the mask did not prevent the x-rays from passing through the element. A reference marker was used to position the element over the aperture. (c) SEM image of the front side of the sample showing the Py film. Several holographic devices were milled in a single line along one side of the membrane to prevent the membrane frame blocking the passage of x-rays through the holographic devices.

7.2.2 Static Imaging of the Ground State

A 800 nm Py element was imaged with HERALDO in both a normal and off-normal geometry with the photon energy of the beam tuned to the Fe L_3 absorption edge. The measurements were performed at beamline ID08 at the ESRF. Figure 7.7 (a) shows a scanning electron micrograph of the 800 nm disc which was positioned within a square 1.5 μm FOV aperture. A reconstruction of the scattering taken at zero applied field, with the sample plane normal to the incident x-ray beam, is shown in Figure 7.7 (b). It reveals a faint outline of the square aperture, but no structure can be seen within the FOV because the imaging is only sensitive perpendicular magnetisation.

Figure 7.7 (c) shows a reconstructed image measured in an external magnetic field of 250 mT applied perpendicular to the sample plane. The magnetisation in the disc aligns with the external field and its uniform out-of-plane domain state can be clearly seen. The normal to the plane was then rotated away from the beam direction. The position of the extended holographic reference slit was orientated such that the rotation axis was perpendicular to the long direction of the slit. Using such a configuration allowed the sample to be rotated allowing the x-rays to pass through the reference slit. In the measurements, the intensity of SXRMS signal is proportional to the projection of the magnetisation vector onto the direction of the incident beam, and so the in-plane magnetisation cannot be observed if the sample plane is orthogonal to the beam direction. When the sample is rotated to off-normal incidence, however, the in-plane magnetisation acquires a non-zero projection to the beam and permits non-zero contrast detection. Figure 7.7 (d) show the reconstructed disc imaged at remanence with the sample rotated to 30°. Here the magnetic vortex ground state of the disc is revealed. The three reconstructions in Figures 7.7 (a-c) contain unexplained artificial vertical lines which has reduced the quality of the reconstruction. Additional measurements of the same sample, which did not suffer from these artifacts, were taken at beamline IO6 at DLS and are shown in Figures 7.7 (e-h).

The same rotation angle of 30° was used at DLS to acquire in-plane contrast.

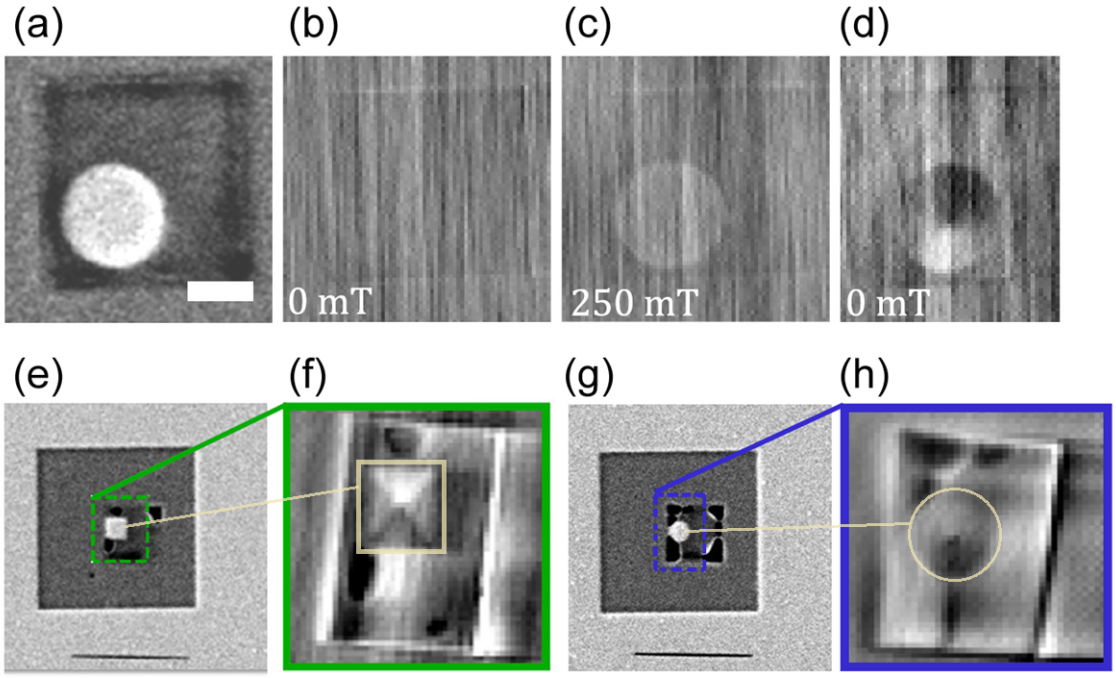

Figure 7.7: Imaging magnetic vortex ground states. (a) Scanning electron micrograph of an 800nm Py disc, positioned along the edge of a square 1.5 μm FOV aperture (white scale bar = 500 nm). (b) FTH reconstruction of (a), imaged at remanence with the sample plane normal to the x-ray beam. (c) Uniform magnetic domain state in the Py element when imaged at normal incidence under 250 mT field applied perpendicular to the film plane. (d) Magnetic vortex ground state, imaged at remanence with the sample plane rotated by 30° within the beam. (e) SEM of a holographic device revealing a 4 μm square region etched from the continuous Py film, leaving a 500 nm square at its centre. The region was milled so that the square element was aligned along one edge the holographic FOV aperture. The holographic reference slit can be seen in close proximity to the element, away from the 4 μm etched region. (f) Holographic reconstruction of the magnetic domain structure of the square element in (e). The dark regions around the square are artifacts which correlate to areas where the FIB has penetrated further through the membrane when the FOV aperture was machined into the integrated holographic mask. (g) Similar to (e), showing an SEM image of a holographic device used to image a 500 nm disc. (h) Holographic reconstruction of the magnetic vortex ground state of the disc element in (g).

In Figure 7.7 (e), a 500 nm square fabricated from the same 50 nm thick permalloy film is shown. The magnetic reconstruction is shown in Figure 7.7 (f), revealing a Landau ground state which typically forms in Py elements with these dimensions [286]. Figure 7.7 (g) shows an equivalent holographic device where a 500 nm disc was fabricated instead of a square element. Figure 7.7 (h) show the reconstruction of the magnetic vortex ground state of the disc.

7.2.3 Field Dependant Vortex Core Displacement

When an isolated permalloy element with a vortex ground state is introduced to an external magnetic field, the vortex core will be displaced from the centre of the element. We used HERALDO in an off-normal geometry to image vortex core displacement in a 50 nm thick Py square, 900 nm in lateral size, as a means of demonstrating the technique for imaging in-plane magnetic configurations within an applied magnetic field. The measurements were taken at beamline IO6 at DLS. An image of the inside of the chamber taken from one of the view ports is shown in Figure 7.8 (a). A close up view of the sample holder positioned between the two pole pieces of the magnet is shown in Figure 7.8 (b). The height of the x-ray beam is at the centre of the magnet pole pieces. The sample shown in Figure 7.8 (b) was rotated to an off-normal incidence angle of 30° and lowered into the beam. Figure 7.9 (a) shows a micromagnetic model performed in OOMMF showing the hysteresis loop of the Py square. The model was used to select a small range of specific field values with which to demonstrate vortex core displacement. The reconstructions of the square from the experiment and the corresponding external applied magnetic fields are shown in Figures 7.9 (b-e). The position of the vortex core is visible in all four images verging towards the edge of the element in Figure 7.9 (e). For clarity, an outline of the square element and the position of the vortex core has been drawn next to each image in Figures 7.9 (b-e). The displacement of the core from the centre of the element is seen to gradually increase with the applied field. The images were compared with the micromagnetic simulations performed in OOMMF as shown in Figures 7.9 (f-i). The discrepancies in the field values

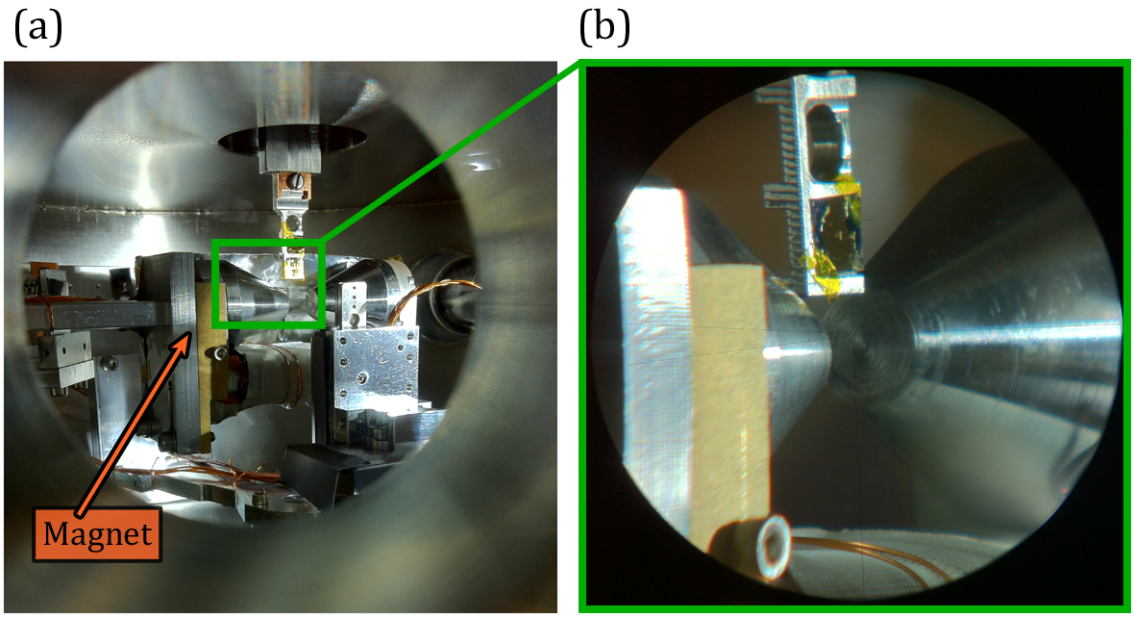

Figure 7.8: Inside view of the Scattering Chamber at DLS. (a) Image of the components inside the scattering chamber taken from one of the view ports. (b) Close up view of the sample aligned between the pole pieces of the magnet. The height of the x-ray beam is level with the centre of the magnet pole pieces. The sample holder was rotated by 30° before it was lowered into the beam.

required to displace the core between the simulations and experimental data is thought to be a result of the idealistic nature of the model.

7.3 Imaging Interlayer Coupling in [Co/Pt]/NiFe

In the context of magnetoelectronics and proposed applications of multilevel recording devices, FTH has previously been used to study domain replication in an all-perpendicular anisotropy system [16]. Here, the stray fields from a hard magnetic layer induced magnetisation in a soft layer. In this section we report on high resolution imaging of domain mimicking in a magnetic system, namely $[Co/Pt]_{30}$/Ta/Py, where the stray fields from a Co/Pt ML, imprints an in-plane domain pattern in an adjacent permalloy layer.

The interlayer coupling in the Co/Pt/Ta/Py has been reported on by Kinane *et al.* [57], where simulations suggested that large stray fields generated by the Co/Pt ML just above its surface, induced the magnetic moments in the Py by purely magnetostatic interactions. This caused the in-plane domain structure of the Py to replicate the out-of-plane domain structure of the Co/Pt ML in the model.

We used the chemical selectivity of soft x-ray holography to performed off-normal x-ray transmission HERALDO to separately image the domain structure in each of the magnetic layers in a [Co/Pt]/Ta/Py system. The measurements were performed at beamline IO6 at DLS using the experimental setup depicted in Figure 7.1. The sample was rotated to 45° within the x-ray beam so that out-of-plane magnetic structure of the Co/Pt, and in-plane structure of the Py could measured at one sample position by simply changing the energy of the x-ray beam to a respective L_3 absorption edge.

7.3.1 Sample Design and Fabrication

The magnetic films were sputter deposited onto the front side of the Si_3N_4 membranes with a thick Au/Cr mask deposited on the reverse side. FIB milling was

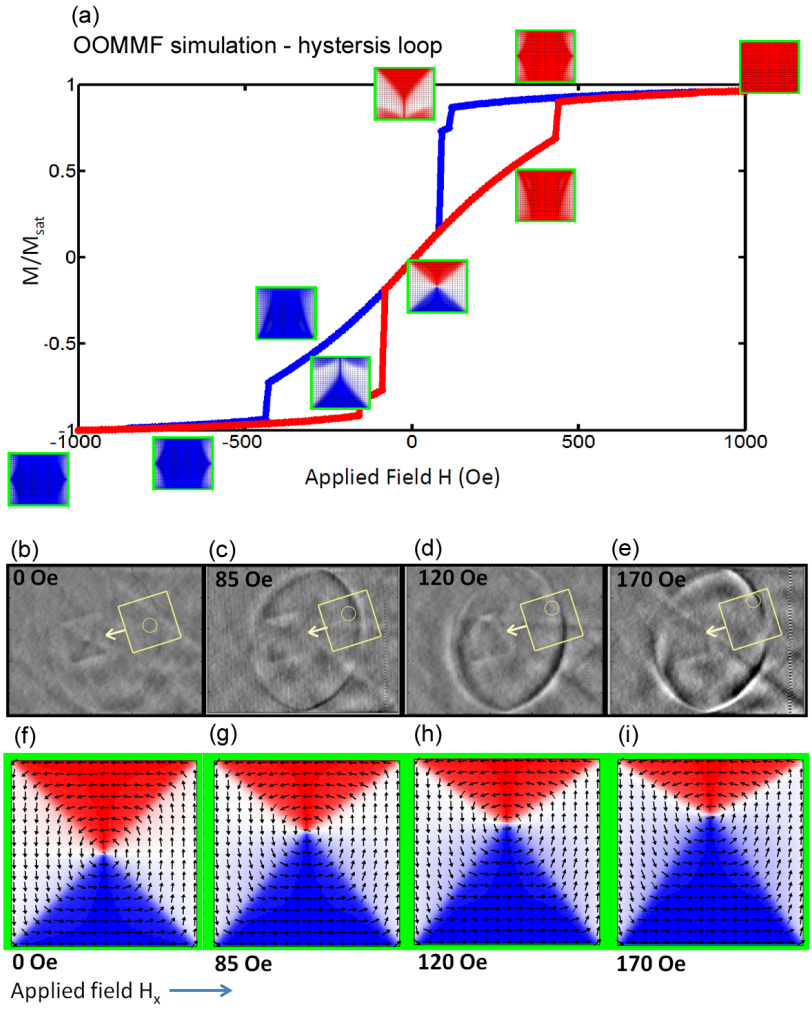

Figure 7.9: Vortex core displacement: experimental results and comparison to micromagnetic modelling. (a) OOMMF simulation showing a hysteresis loop of a 50 nm thick Py square, 900 nm in lateral size. Positions along the loop are marked with simulated images of the domain structure at these field values. (b-e) Experimental results. (b) Landau domain structure forms in the element at remanence. (c-e) The central core position of the Landau structure is displaced within an external applied field. The core position moves vertically up away from the centre with increasing field. The field values correspond to an in-plane field component in the direction H_x. (e-h) show OOMMF simulations of (b-e) respectively.

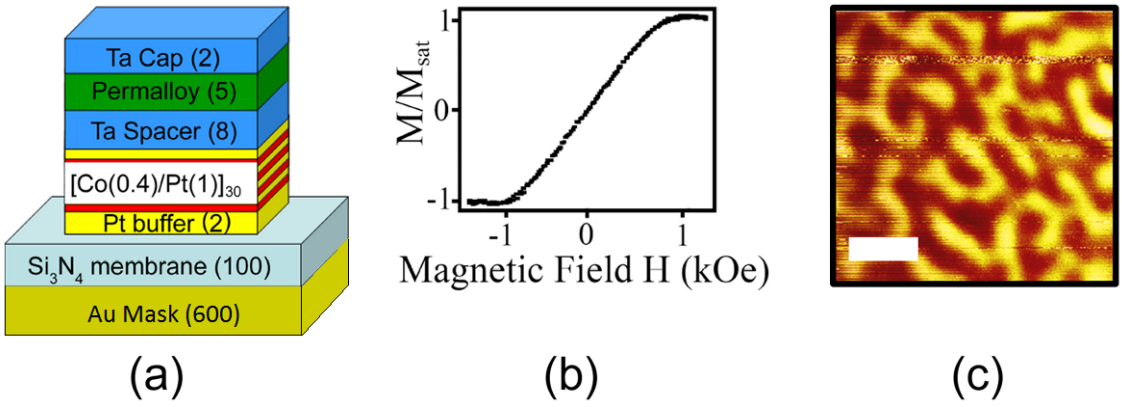

Figure 7.10: Characterisation of $[Co/Pt]_n$/Ta/Py films. (a) Sample structure of the $[Co/Pt]_{30}$/Ta/Py system with corresponding thickness values in nanometers in the parentheses. (b) Polar MOKE hysteresis loop of the magnetic film showing the in-plane response from the permalloy. (c) MFM image showing perpendicular maze domains of the buried Co/Pt at remanence (white scale bar = 500 nm).

used to pattern a circular 1.5 μm FOV aperture into the mask and close by reference slit, 3 μm long and ~30 nm wide. A schematic of the sample is shown in Figure 7.10 (a). The magnetic film was characterised with polar MOKE measurements [Figure 7.10 (b)] and MFM [Figure 7.10 (c)]. To preserve the as-deposited state of the samples during the HERALDO imaging, the characterisation was performed after the measurements with x-rays.

The polar MOKE hysteresis loops shown in Figure 7.10 (b) shows the characteristic field dependence for in-plane magnetic anisotropy. This is because the optical laser probe in the MOKE setup is a surface sensitive technique and therefore the hysteresis loop measures the response from only the top Py layer and not the buried Co/Pt ML. The out-of-plane maze domain pattern of the buried Co/Pt ML are shown in the MFM image presented in Figure 7.10 (c).

7.3.2 Domain Mimicking in [Co/Pt]/Py Systems

Figures 7.11 (a) and (b) show the magnetic speckle pattern from the Co/Pt ML. These difference images are a subtraction of two holograms recorded with opposite helicity at the Co L_3 absorption edge (778 eV). The sample surface in Figure 7.11

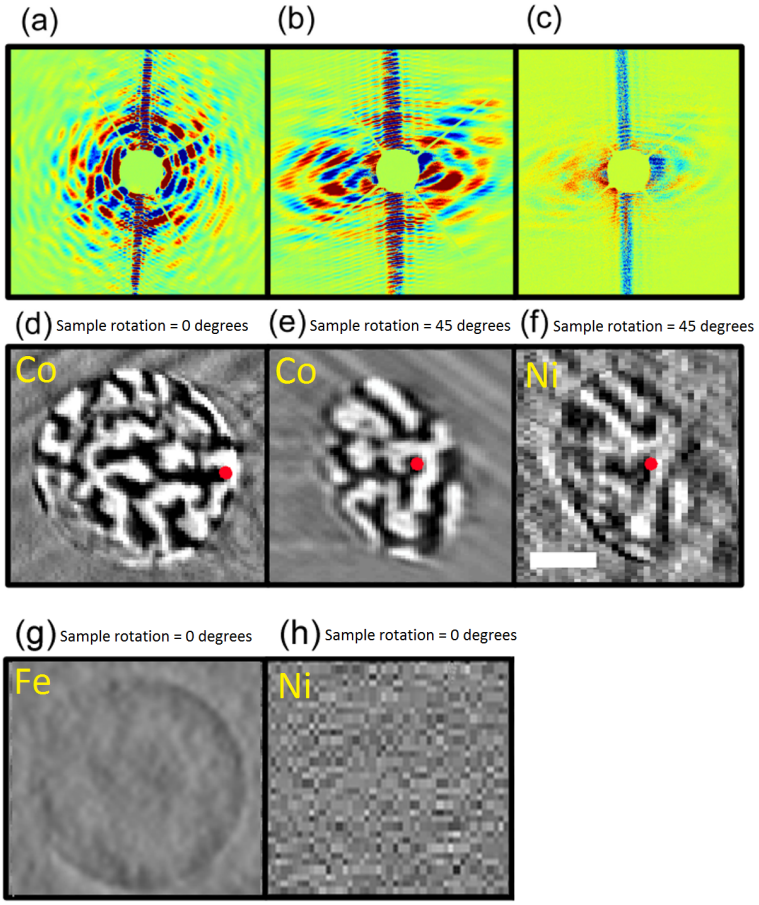

Figure 7.11: Interlayer coupling in $[Co/Pt]_n$/Ta/Py films. (a) Hologram with the sample surface perpendicular to the x-ray beam, recorded at the Co L_3 edge. (b) Hologram with the sample surface rotated to 45° to the beam, recorded at the Co L_3 edge. (c) Hologram with the sample surface rotated to 45° to the beam, recorded at the Ni L_3 edge. Only the central 500 × 500 pixels of the holograms in (a-c) are displayed. (d) Reconstruction of the hologram in (a) showing the domain structure in Co/Pt. (e) Reconstruction of the hologram in (b) showing the domain structure in Co/Pt when imaged at off normal incidence. (f) Reconstruction of the hologram in (c) showing the domain structure in Py when imaged at off normal incidence (white scale bar = 500 nm). The domain structure in the Py layer (f) closely follows the domain pattern of the Co/Pt (d,e). The red dot on the reconstructions (d-f) indicates the same spatial location on each. (g) Reconstruction of the sample with its surface perpendicular to the x-ray beam, recorded at the Fe L_3 edge. (h) Reconstruction of the sample with its surface perpendicular to the x-ray beam, recorded at the Ni L_3 edge.

(a) was normal to the beam and rotated to 45° in Figure 7.11 (b). The difference image at the Ni L_3 absorption edge recorded at 45° is presented in Figure 7.11 (c). Each of these hologram was an accumulation of 100 images for each helicity, each frame with an exposure time of 5 s under attenuated beam conditions. Figures 7.11 (d-f) shows the real part of the reconstruction of the holograms in Figures 7.11 (a-c). Figure 7.11 (d) shows a region in the form of a circular outline where the magnetisation appears to be lost. This to be due to the Co/Pt ML receiving a high dose of Ga ions during the FIB milling of the FOV aperture in those local areas that is believed to disrupt the perpendicular magnetic anisotropy in the Co/Pt ML [13]. The reconstruction in Figure 7.11 (e) only reveals part of the FOV aperture seen in Figure 7.11 (d) due to the holographic mask blocking regions of the FOV when the sample is in a rotated geometry. The exposed parts are shown in Figure 7.11 (e), and reveals the same magnetic domain configuration that can be seen in the Co/Pt at normal incidence [Figure 7.11 (d)]. For comparison a red dot has been used to indicate the sample spatial region in Figures 7.11 (d-f). It is revealed in Figure 7.11 (f) that the domain structure of Ni replicates the same configuration as the Co/Pt in Figure 7.11 (e), suggesting that the domains in the Py are indeed influenced by the magnetic texture of the Co/Pt ML. The magnetic contrast of the Ni pattern was found to be significantly reduced (compared to that of the Co edge), correlating with the reduced amount (and the magnetisation value) of Ni being probed.

We note that the resulting domain structure in Figure 7.11 (f) is the effect of the in-plane magnetisation components, and not the perpendicular ones; due to strong demagnetising effects (and as shown by the MOKE loops in Figure 7.10 (b)). To verify this, measurements were taken with sample plane normal to the beam direction at the Ni and Fe L_3 edges. Unfortunately the measurement at the Ni absorption edge [Figure 7.11 (h)] did not provide a consistent reconstruction, however the measurement at the Fe L_3 edge shown in Figure 7.11 (h) revealed a uniform contrast across the FOV, indicating a zero or uniform component of magnetisation with a direction out of the plane.

We also note that the images presented in Figure 7.11 represent a sample that had not been exposed to large magnetic fields, and that the domain structure in the Py layer is induced in its as-deposited state. We found the result of figure Figure 7.11 (f) rather surprising with the exact mimicking of the domain structure unexpected. Here we suggest a qualitative explanation for the observations.

The exact mimicking of the Co/Pt domain structure suggests that initially the magnetisation in the permalloy layer has a perpendicular component, which follows the perpendicular demagnetising field from the 'up' and 'down' moments in the Co/Pt ML. However, the perpendicular component in Py becomes suppressed by the demagnetising fields of the Py layer, and thus cannot produce any significant contribution to the observed magnetic contrast, as we observed in Figure 7.11 (h). The contrast we observed in Figure 7.11 (f) can only arise from the in-plane components, and a possible explanation is that this domain structure is induced by the in-plane dipole fields above the domain walls of the Co/Pt. The result of this however would not lead to the exact mimicking of the domains in the Co/Pt that we observed.

We performed micromagnetic modeling using OOMMF to simulate the response of the Py layer (see Appendix C for more details). In the model we used a cell size of $20 \times 20 \times 5$ nm^3 in a 1×1 μm^2 area. The Co/Pt ML was modeled as a continuous slab with an 8 nm thick nonmagnetic layer on top, which separated it from a 5 nm thick Py layer. In the simulation we first initiated the system in the random state, and examined the domain structures of the Co/Pt layer and the Py layer. The result of this is shown in Figure 7.12. The out-of-plane domain structure in the Co/Pt ML and Py layer is shown in Figures 7.12 (a) and (b) respectively. Here, the perpendicular components exhibit the same domain structure, though the Py layer in Figure 7.12 (b) has significantly smaller values, due to demagnetizing effect. The in-plane component of the Py layer is shown by arrows in Figure 7.12 (b) with a colour map of the in-plane domain structure shown in Figure 7.12 (c). From the simulation we see that the size of the Py in-plane domains replicates the microscopic lengths of the Co/Pt domains, however the direct mimicking of the

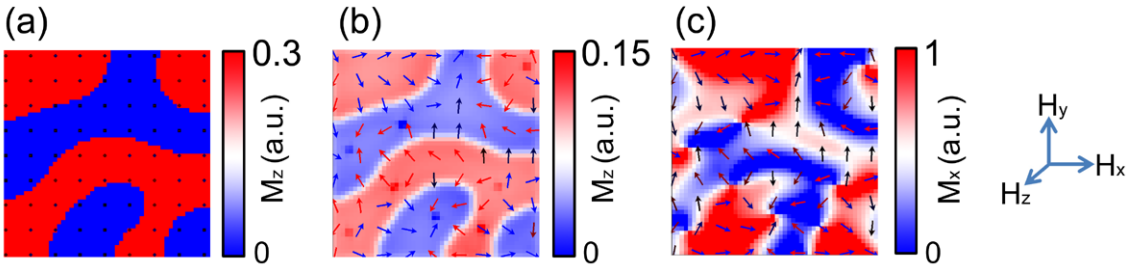

Figure 7.12: 1 μm^2 OOMMF simulation of interlayering coupling. (a) Out-of-plane magnetisation in Co/Pt at remanence. (b) Colour map showing the perpendicular magnetisation in the adjacent Py layer (separated by a nonmagnetic Ta spacer) with an overlay of the in-plane fields shown by the arrows. (c) A colour map of the in-plane domain structure in the Py in it's pristine state.

domain pattern is not observed in these simulations.

In Figure 7.13 a qualitative explanation of our proposition is presented. We suggest that when the Py layer is formed - typically starting from nanoscopic islands or a thin monatomic layer - the local moments in the Py follow the direction of the perpendicular demagnetising fields from the Co/Pt domains. This is shown in Figure 7.13 (a). At this stage the demagnetising effect of the Py is negligible. It is also our suggestion that contributions of perpendicular surface anisotropy helps in providing the out-of-plane component. As the space between the 'islands' is filled (or the layer becomes thicker) the demagnetising field in the Py increases and the moments tend towards the plane, as shown in Figure 7.13 (b). At this point the moments with 'down' directions are already coupled via exchange and form domains mimicking 'down' domains in Co/Pt. A similar situation can be expected from the moments with 'up' direction. At the same time the dipolar coupling between the domains will maintain the initially induced configuration. When the moments are tilted towards the plane, they remain in the same configuration resulting in the domain mimicking shown in Figure 7.13 (c). Whilst this configuration is not energetically ideal, it remains stable enough to exist until an external field is applied.

It is surprising that the orientation of magnetisation in different domains of the

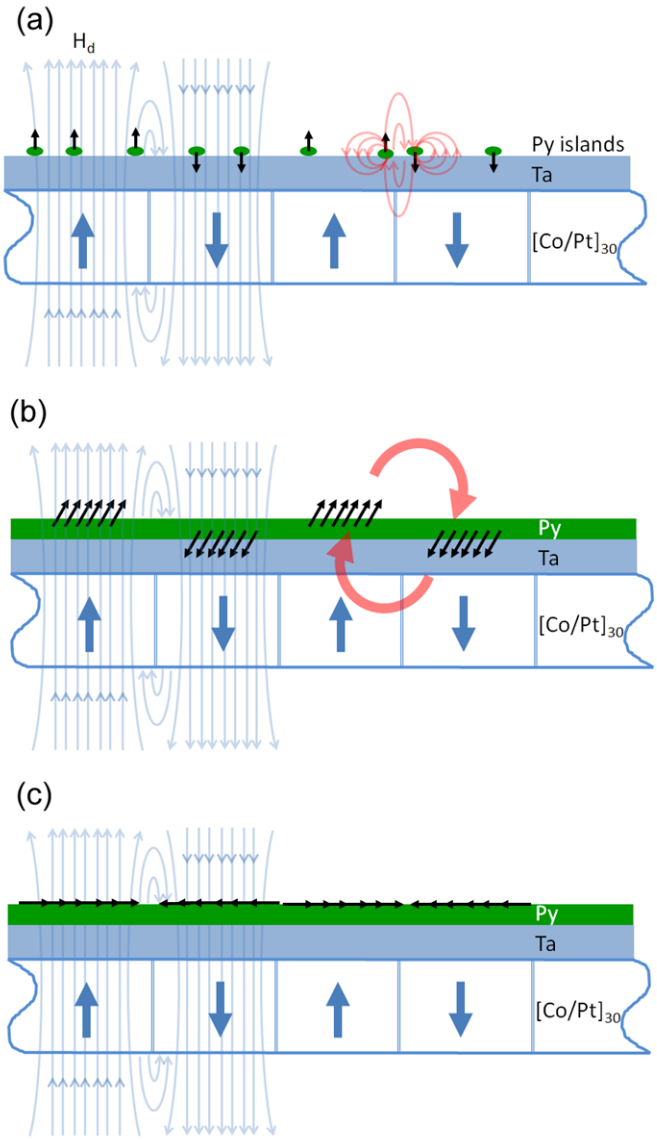

Figure 7.13: Qualitative explanation of domain mimicking. (a) During the deposition of the Py film onto the stack, nanoscopic islands (or a very thin layer) will typically form in the initial stages. The local moments in the 'islands' (or the monatomic layer) follow the direction of the perpendicular dipolar fields H_d. from the Co/Pt domains. At this point the demagnetising effect of the Py is negligible. (b) During the next stages of the deposition process, the space between the islands fill (or the layer becomes thicker). The demagnetising field increases and tends to incline the moments towards the plane. Here, the moments with 'down' directions are already exchange coupled and form domains mimicking the 'down' domains in the Co/Pt. Similarly the moments with an initial 'up' direction mimic the 'up' direction in the Co/Pt. (c) As the moments are tilted towards the plane they remain in the same configuration.

Py layer appear to follow the same preferred orientation in the film. This is seen in Figure 7.11 (f). If the plane was completely isotropic then the moments in different domains would be free to relax in any direction, thus resulting in different magnetic contrasts between the different domains, yet the observed Py pattern is nearly identical to that from in Co/Pt. This implies that the moments in both 'black' and 'white' domains follow an unaxial direction that has a non-zero projection onto the x-ray wave vector. It is thought that the preferred direction can be induced during the growth by the weak magnetic field present during the sputtering process. Magnetron plasma systems typically require fields to maintain plasma, or reduce the electron acceleration during the sputtering deposition, and typically fields between 10-50 Gauss are sufficient to influence the magnetisation in Py on a local scale. As a result, when the thickness of the layer is increased and the magnetic moments of Py begin to incline to the plane, they may preferentially settle to the direction of the applied field. This structure is however unstable, and after applying a saturating magnetic field, the domain pattern is erased and cannot be recovered. In the next section we discuss the results of imaging after application of a saturating field.

The Effect of a Magnetic Field on the Domain Mimicking

We believe that the in-plane structure may arise during the deposition process and stay unaffected until a reasonably large field is applied. Further imaging of the sample was carried out to investigate the effect of an applied magnetic field on the domain mimicking. A saturating field of 250 mT was applied perpendicular to the beam whilst the sample remained at a 45° angle to the beam, and the direction of the applied magnetic field. This provided an out- and in-plane field components of 176 mT. Figures 7.14 (a) and (b) show the domain configurations after the sample was reimaged at zero field having been exposed to the saturating applied magnetic field. They show an equivalent object FOV aperture and reference slit, on a different part of the sample, recorded at the Co and Ni L_3 edges, respectively. The magnetic configuration in the Co/Pt shows a maze domain structure which

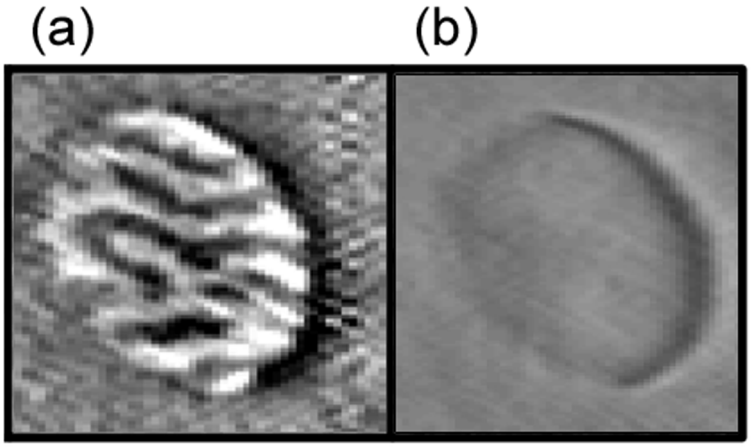

Figure 7.14: Effects of a magnetic field on interlayering coupling. (a) Reconstruction of the Co/Pt domains recorded at remanence after a saturating magnetic field was applied. (b) Reconstruction of the Py domains recorded at remanence after a saturating magnetic field was applied.

was found before the sample was introduced to the saturating field, however, the presence of a magnetic configuration was absent in the Py. Figure 7.14 (b) shows an image with uniform intensity, which is interpreted as a constant level of magnetisation in the Py layer. We speculate that after a saturating external field is applied, the magnetic structure is dominated by larger domains that form due to the local exchange coupling within the Py layer. In the pristine state, the remanent magnetisation is formed by small, uncorrelated regions, that are susceptible to local fields and tend to couple via exchange interaction as the preferred orientation becomes similar in neighbouring domains. In this state, it is possible for dipolar fields from the Co/Pt ML to induce a similar structure in Py layer. Once a saturating field is applied, larger domains form in Py layer that are now more difficult to decouple. Returning to zero field still produces an overall zero remanence (the hysteresis is negligible), however, the size of the domains is now of macroscopic size and unlikely to be verifiable, unless a domain wall passes directly through the FOV.

7.4 Conclusions

In summary, we have demonstrated magnetic HERALDO imaging by implementing the holographic technique at off-normal incidence. When applied to magnetic systems, off-normal magnetic HERALDO imaging provides sensitivity to in-plane magnetisation with the magnetic contrast obtained via SXRMS. We have presented images of flux closure ground states in permalloy elements less than 1 μm in lateral size and demonstrated displacement of the elements vortex core by imaging the sample in an external applied magnetic field.

Using an example of a complex magnetic system comprising of two types of magnetic components, perpendicular and in-plane, we demonstrated that both components can be resolved. We directly imaged the domain structure of different magnetic layers in a pristine $[Co/Pt]_{30}$/Ta/Py multilayer that showed that the out-of-plane domain structure in the Co/Pt ML is replicated by the in-plane domains of Py. OOMMF simulation suggest that large stray field generated by the Co/Pt domains influence the magnetic texture in the Py, and the size of the Py domains mimicked size of the domains in the Co/Pt. In the experimental images, the domains in the Py layer correlated spatially with the domains of the Co/Pt, with direct mimicking of the domain structure observed. It is suspected that the in-plane domain structure in the Py arises during the deposition stages of the film which cannot be accounted for in the OOMMF model. After exposing the sample to a saturating applied magnetic field, the induced in-plane structure of Py is inhibited. Once saturated, it is suspected that the Py layer forms its own domain structure which remains dominant within the layer in zero field.

Chapter 8

Progress Towards Establishing X-ray Holography in Reflection Geometry

The advantages of employing an FTH setup that performs in a reflection geometry have already been discussed in Chapter 4. For the purpose of magnetic imaging, a reflection technique would allow one to use FTH imaging to study samples that cannot be studied as thin films, or those that require a certain substrate other than a Si_3N_4 membrane. A reflection approach has the potential to be sensitive to in-plane and perpendicular magnetisation, and could prove a versatile imaging technique. In the current literature, soft x-ray holography recorded in reflection geometry has been used to reconstruct a high resolution image of a nonmagnetic nanostructured material [280] with incident angles of 17° used. A mask, containing an aperture hole and two reference holes, was separated from the sample plane, which splits the reflected light into an object wave and two reference waves. There is an added complexity to conventional transmission experiments, and the recovered complex wave at the mask has to be back-propagated to the sample surface. This places an effective working limit on the distance that separates the sample and the mask, and this depends on the size of the aperture in the mask and the energy of the incident beam.

In this chapter we present our progress towards establishing a holographic imaging technique in reflection geometry whereby the Bragg scattering from an object is reconstructed without the use of a mask. We manufactured object and reference structures using EBL and presented images of holograms recorded in a reflection geometry. The FFT of the holograms failed to show any structure of the object, and we discuss with regards to the signal strength why this might be. Later in the chapter we present methods for 'cutting-out' the reflected beam footprint around an object and reference, to mimic the design of the optical samples presented in Chapter 5. We used robust Si_3Ni_4 membrane substrates but discovered that lines of stress appear in the surface of the membrane after FIB machining was used to mill microscopic holes in the substrate. We propose a more suitable design for further experiments using FIB milling to induce surface roughness into a substrate and encourage diffuse Bragg scattering.

8.1 Preliminary Investigation into Reflection FTH at Soft X-ray Wavelengths

This section presents an investigation into establishing a lensless imaging technique in reflection geometry using non-magnetic structures.

8.1.1 Experimental Setup

An experiment was set up at BESSY using the soft x-ray beamline STG52 and the ALICE scattering chamber. A schematic of the end station at the beamline is shown in Figure 8.1 (a), with a photograph of the setup shown in Figure 8.1 (b).

The ALICE scattering chamber provided x, y, z motor positioning along with motor rotation of the sample stage about the z axis. An external port on the chamber was fitted with a CCD camera fixed at 45° to the beam direction. The sample was then placed into the chamber with its surface plane orthogonal to the beam. A 20 μm diameter pinhole was placed 20 mm upstream from the sample to filter the x-ray beam that defined the spot size of the beam. A photodiode

downstream from the sample was then used for positioning the sample by measuring the transmitted intensity across the thin membrane substrate. The sample stage was rotated such that the angle of incidence was 22.5°, and Bragg scattering from the sample was detected on the CCD camera. The detection plane was 300 mm from the sample. For these experiments a beam energy much lower than any of the ferromagnetic L_3 absorption edges was used. This was because generally, a lower energy beam will provide a higher reflective intensity [279]. We considered these experiments as initial proof of concept setups, performed to optimise the a geometry that could then be used for magnetic reflective FTH. For this reason a lower beam energy of 150 eV was used in order to improve the flux of the reflected beam compared with the expected reflection from a beam with an energy tuned to any of the ferromagnetic L_3 absorption edges. The holographic device that was initially positioned into the beam with the photodiode, was not necessarily inline with the centre of the stage rotation axis and upon rotating the sample, the x and y stage motor positions needed fine adjustment to reposition the device into the beam spot. Due to restrictions of the sample holder, it was not possible to measure the transmitted intensity (using the diode) through the sample whilst rotated at 22.5°. Adjustment's to the samples position whilst in the the rotated geometry were therefore controlled using the direct image of the Bragg scattering received at the CCD camera and position coordinates of the holographic device were determined using simple geometric calculations. For the case where the sample was rotated to 22.5° within the beam, the beam footprint was stretched over the holographic device, illuminating an elliptical area ∼20 μm in height and 50 μm wide on the sample. The expected footprint is illustrated as part of the inset in Figure 8.1 (a).

8.1.2 Sample Design and Fabrication

To determine the suitability of the setup in Figure 8.1, and to optimise the performance of measurements, microscopic reference and object features were fabricated onto Si_3N_4 membranes substrates. Figure 8.2 (a) shows a scanning electron micrograph of a letter 'E' surrounded by three circular reference pins. The length of the

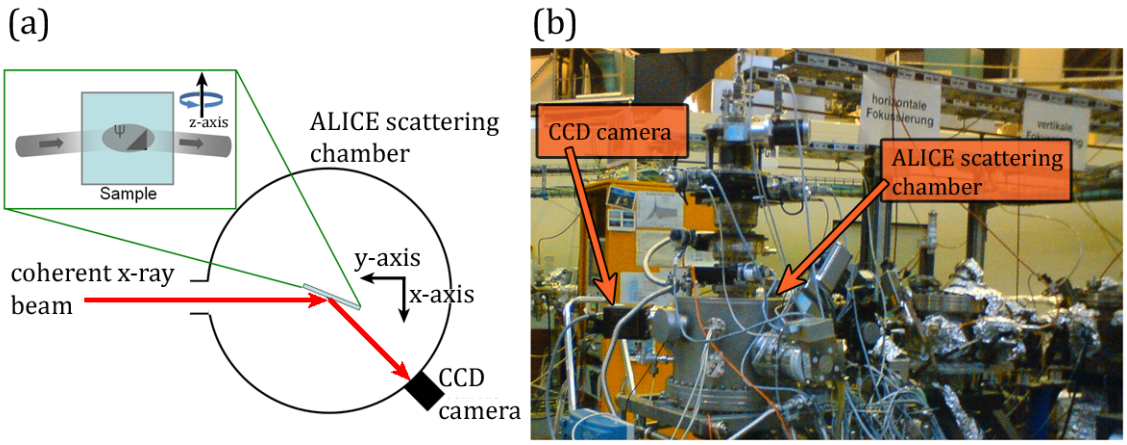

Figure 8.1: Experimental setup for reflection FTH at BESSY. (a) Schematic of the setup. The inset shows an example holographic device containing an object structure and extended reference triangle. It depicts the Bragg scattering of the input beam, directed towards the CCD detector. (b) Photograph of the beamline endstation.

letter was 10 μm, and the diameter of each pin structure was ~1 μm. Figure 8.2 (b) shows a test object, 10 μm in size, with a triangular extended reference, positioned to the right of the object. The lengths of the two sides that form the right angle of the triangle were each 15 μm in length. FIB was used to sharpen the corners of the triangle, results of which are shown in Figures 8.2 (b-c).

To fabricate the structures shown in Figure 8.2, the Si_3N_4 substrate was spin-coated with a bilayer of PMMA, and EBL was used to define the test object and near-by reference structure(s). 10 nm of Cr followed by 90 nm of Au was thermally evaporated onto the membrane substrate before lift-off, resulting in the holographic devices designed for imaging in reflection geometry.

8.1.3 Results and Discussion

When the beam was positioned over the reflective holographic device shown in Figure 8.2 (a), the photon count was ~43 000 counts for an exposure time of 1 second. Simulations shown in Figure 8.3 were performed to ensure that the sensitivity of the CCD was capable of detecting a speckle pattern from the light

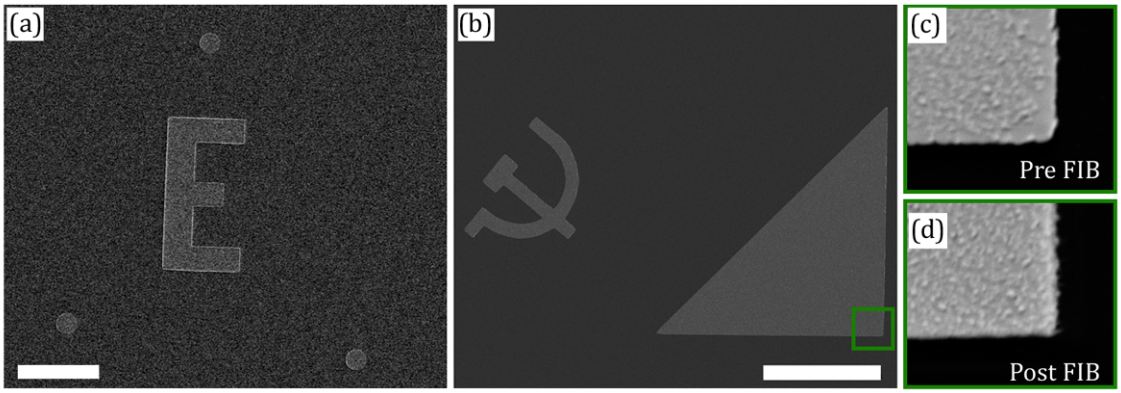

Figure 8.2: Non-magnetic test samples. (a) A 10 μm sized letter 'E' is surrounded by three holographic reference pin structures (each 1 μm in diameter). The object and reference was made from a 100 nm film of Au. (white scale bar = 5 μm). (b) A 10 μm object symbol is placed in close proximity to a triangular extended holographic reference structure. (white scale bar = 10 μm). (c) Enlargement of the corner highlight by the green box in (b). (d) FIB milling was used to sharpen each corner of the triangle.

scattered by the object letter 'E', and the three reference pin structures. The simulated holographic device is shown in Figure 8.3 (a) where the shape of the object along the horizontal axis has been modified to account for the rotation of the the sample in the beam. Figure 8.3 (b) shows a simulated hologram with the full dynamic range of the diffraction pattern. Because a beamstop was not used in the experiments, a large percentage of the counts received by the detector were from the specular reflection of the beam, and not from the scattered light from the object and reference pins. Due to the dynamic range of the 16-bit CCD chip, the full dynamic range of the diffraction pattern cannot be captured, and so we expect only photon counts above a certain threshold to be detected during the 1 second exposure [as shown in Figure 8.3 (c)]. From the geometry of the setup we can expect the scattering from the features shown in Figure 8.2 to have scattering vectors between $\mathbf{q}\sim$3-6 μm^{-1} corresponding to speckle $\sim$50 to 100 pixels radially from the centre of the hologram shown in Figure 8.3 (c). Figure 8.3 (d) shows a reconstruction of the modified hologram in Figure 8.3 (c) which shows a satisfactory

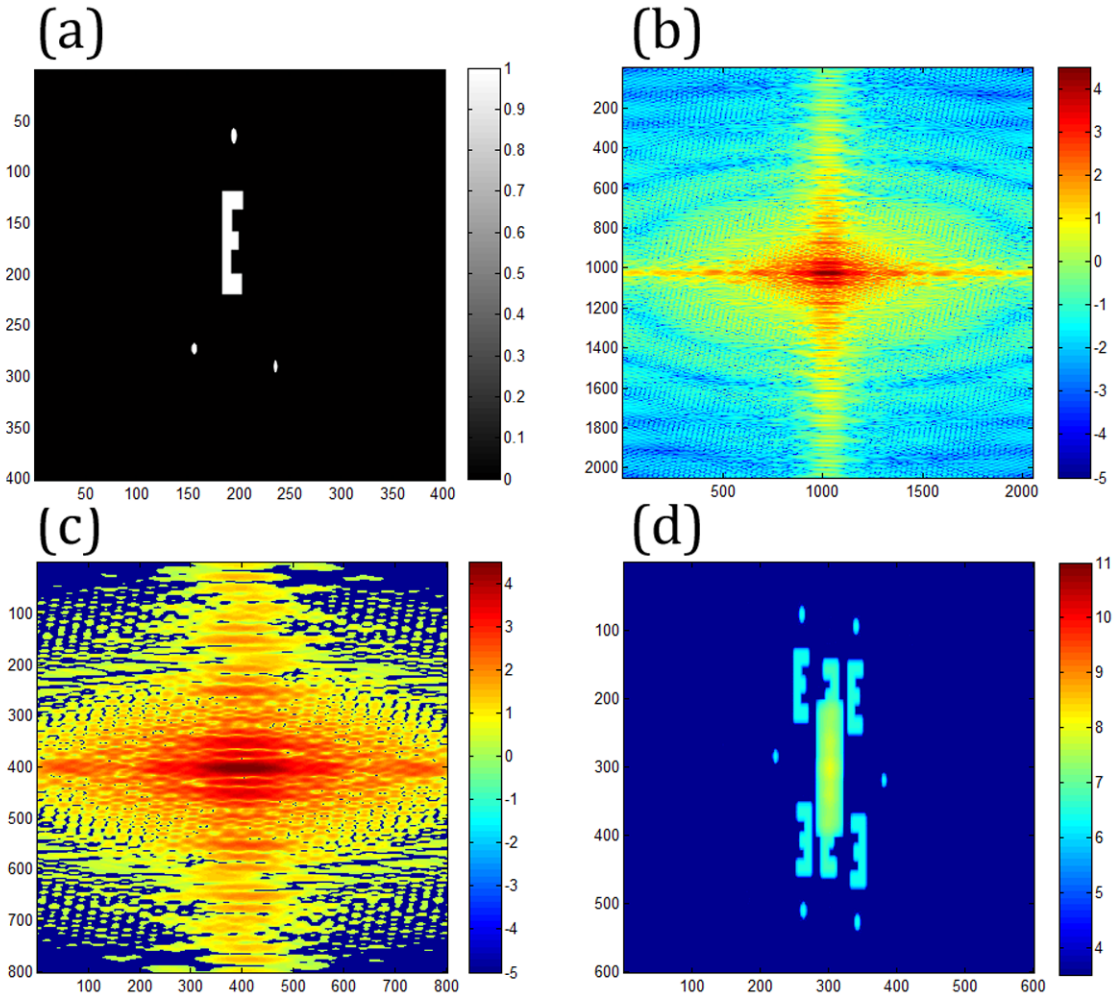

Figure 8.3: Simulations of reflection FTH. (a) Reflective holographic device with pin structure references as seen by the x-ray been in the rotated geometry. (b) Simulated hologram of (a), showing the full dynamic range of scattering normalised to the maximum photon count of the experimental data (log scale colour bar). The view of the hologram in (b) has been enlarged to show only the central 800×800 pixels around the centre of the hologram. (c) The dynamic range of the hologram in (b) has been reduced to mimic the expected dynamic range available in the experiment. (d) IFT reconstruction of (c) revealing the object reconstructions of the letter 'E' shown in (a).

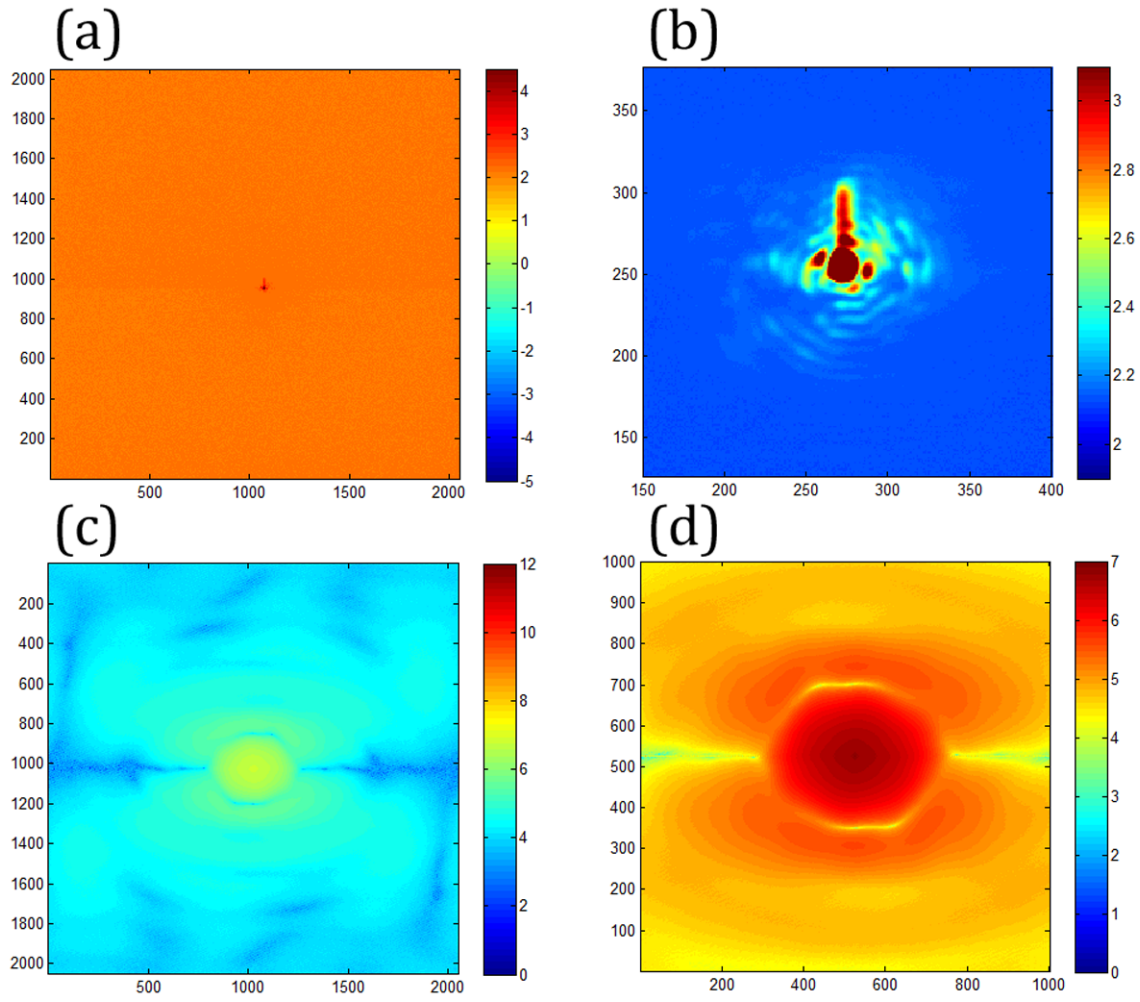

Figure 8.4: (a) Hologram recorded in reflection geometry, of an object letter 'E' surrounded by three reference pin structures. Accumulation of 100 images with a maximum photon count detected in each frame ∼43 000 counts (the colour bar shows a log scale). (b) Enlarged view of the central 250×250 pixels showing the region of the hologram with scattering vectors expected from the test object. (c) FFT reconstruction of (a). (d) Enlarged view of the central 1000×1000 pixels of the reconstruction, highlighting the position where the cross-correlations between the object and reference pins was expected to be found. No structure is visible in these reconstructions.

reconstruction of the object letter 'E'.

Figure 8.4 (a) shows the measured reflection hologram of the 'E' structure and three reference pins shown in Figure 8.2 (a). The hologram was an accumulation of 100 recorded diffraction patterns, each frame with an exposure time of 1 s. An enlargement of the central 250×250 pixels of the hologram is shown in Figure 8.4 (b). Figure 8.4 (c) shows a full sized FFT of Figure 8.4 (a) revealing little structure. An enlargement of the central 1000×1000 pixels of the reconstruction is shown in Figure 8.4 (d), where the position of the reconstructed letter 'E' is expected to form within. Unfortunately the reconstruction did not reveal any structure resembling the illuminated object and because the contribution to the Bragg scattering signal from the reference pin structures was too small, and does not provide interference fringes with enough contrast to reconstruct the object. The weak signal from the reference could be significantly improved by using extended reference structures.

Reflection HERALDO

The sample with a triangular extended reference (shown in Figure 8.2 (b)) was used to test HERALDO imaging in reflection. Simulations of the device in the rotated geometry are shown in Figure 8.5. Figure 8.5 (a) shows a simulated hologram with the full dynamic range of the diffraction pattern. Similar to the case in Figure 8.3 (c), a hologram with the expected scattering for the reflection HERALDO measurements are shown in Figure 8.5 (b). For a reconstruction from a corner, the unit vectors pointing along the edges of the corner are estimated from the streaks in the hologram, and the product of the measured hologram and the differential filter is calculated. The IFT is then computed to retrieve the reconstruction of the object [94]. Figure 8.5 (c) shows the differential filter associated with the right angle corner of the triangular reference. The resulting IFT after applying this differential filter is shown in Figure 8.5 (d).

Our experimental data shown in Figure 8.6 revealed interesting scattering patterns recorded by the CCD camera. Figure 8.6 (a) presents the recorded Bragg scattering from the holographic device without the use of a beamstop. The holo-

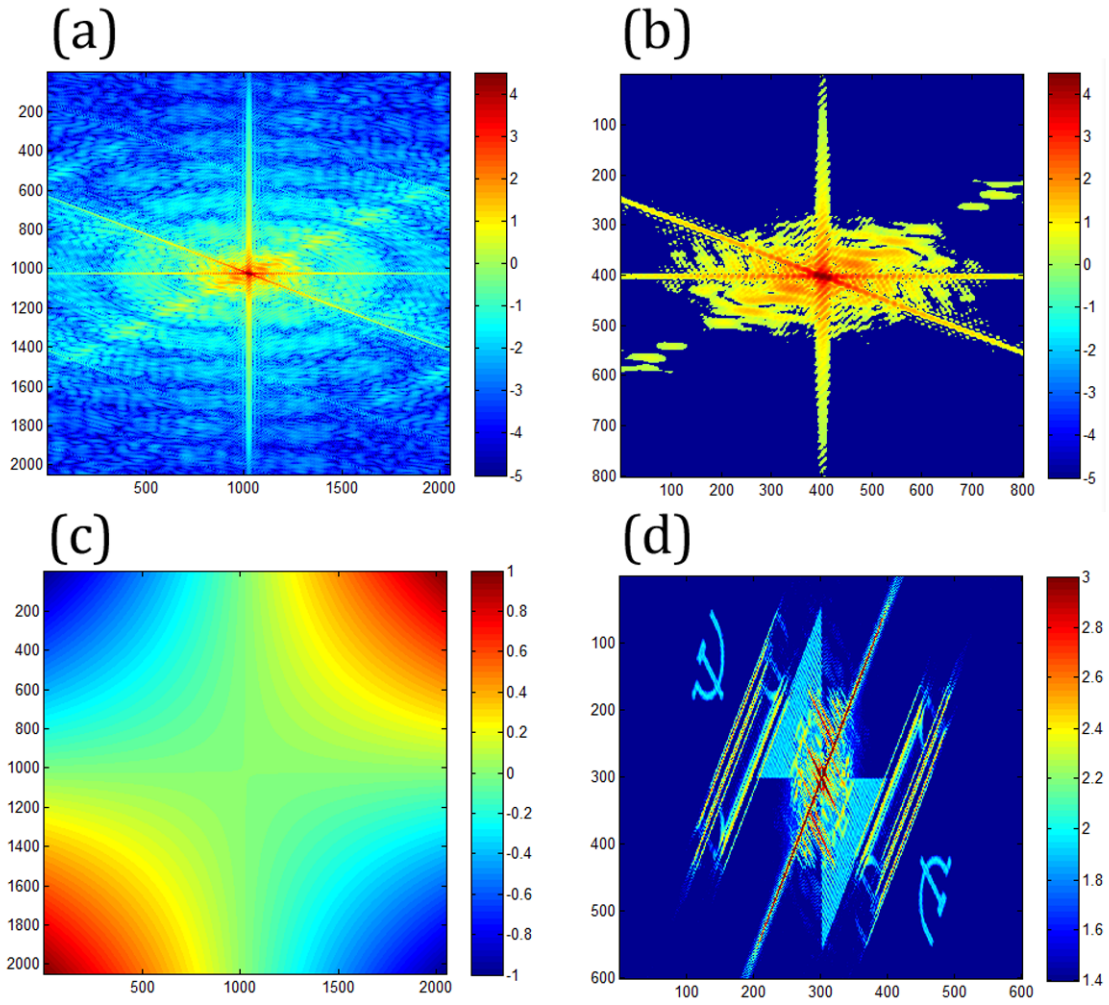

Figure 8.5: Simulations of reflection HERALDO. (a) Hologram recorded in reflection, showing the full dynamic range of scattering normalised to the maximum photon count of the experimental data (log scale colour bar). (b) The dynamic range of the hologram in (a) has been reduced to mimic the expected dynamic range available in the experiment without the use of a beamstop. The view of the hologram in (b) has been enlarged to show only the central 800×800 pixels around the centre of the hologram. (c) differential filter applied to the hologram before an IFT is computed to give the reconstruction shown in (d).

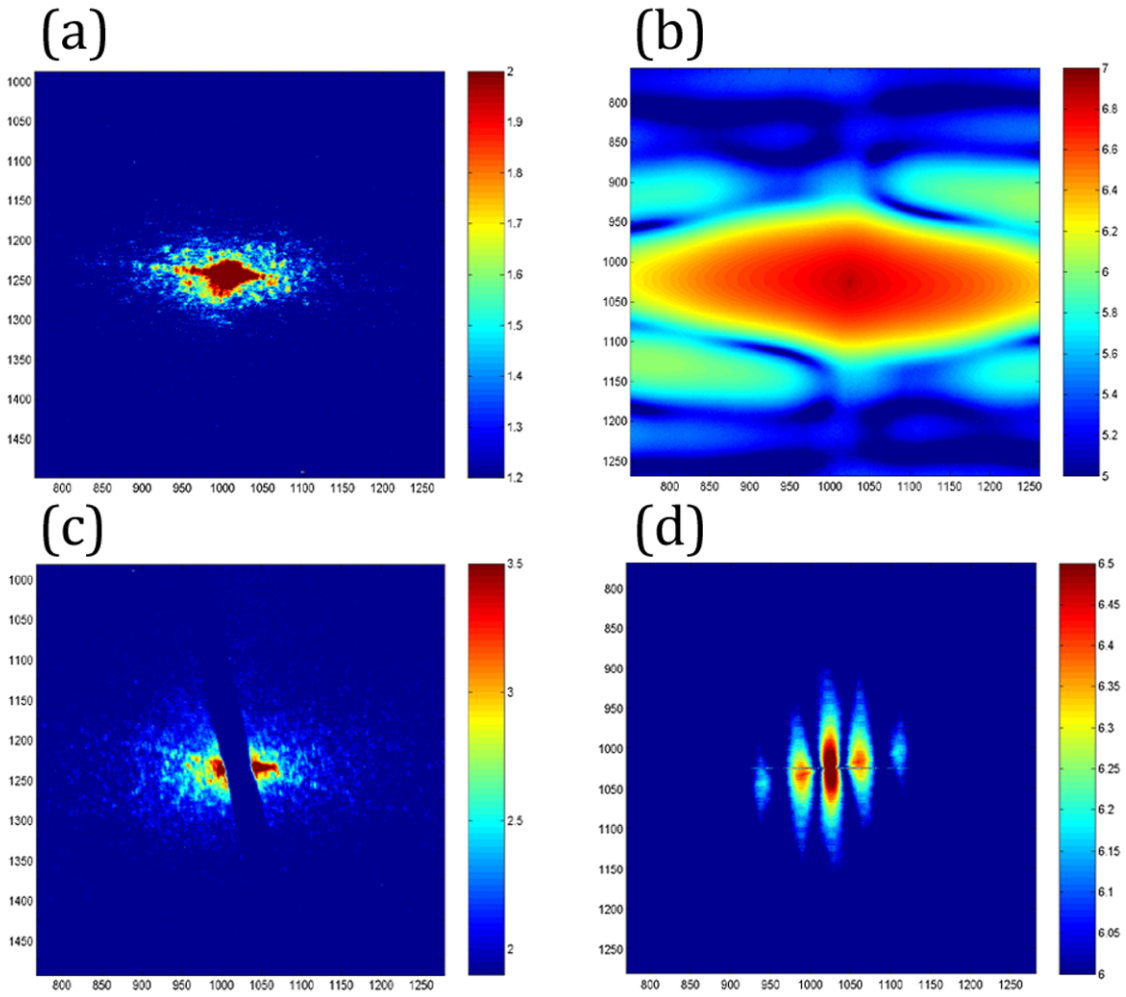

Figure 8.6: (a) Hologram recorded in reflection geometry, of an object symbol in close proximity to a triangular extended reference. The maximum photon count detected for each frame this accumulation was ∼41 000 counts. The colour bar shows an arbitrary log scale. (b) FFT of (a). (c) Recorded hologram after implementing the use of a beamstop to block the central specular reflected beam, the maximum photon count for this single, 1000 s exposure was ∼38 000 counts. (d) FFT of (c).

gram was an accumulation of 20 images, each frame with an exposure time of 40 s under attenuated beam intensity. Figure 8.6 (b) reveals the FFT of Figure 8.6 (a) contain no features resembling an autocorrelation between the object and triangle reference.

We took measurements with a beamstop in position to block the central portion of the reflected beam. Longer exposures could now be recorded without over saturating the CCD and a higher dynamic range of the Bragg scattering from the holographic device was recorded. The hologram in Figure 8.6 (c) shows a single image with an exposure time of 1000 s. The maximum photon count after this exposure time was ∼35 000. This demonstrates how information at larger scattering angles away from the blocked central region became more visible after the introduction of a beamstop. A prominent steak is visible in the hologram that is characteristic of scattering from a straight edge (expected from our extended reference triangle). The Fourier transform of Figure 8.6 (c) is shown in Figure 8.6 (d), yet, this did not reveal any structure structure resulting from the cross-correlation between the object and reference triangle.

The total reflective area from the reference increased by ∼50× when using the extended triangle compared with the pin structures in Figure 8.2 (a). Even with this expected increase in signal, a reconstruction revealing the structure of the object was not achieved. A strong possibility for this result is that the total counting time is insufficient to record the interference fringes with a suitable contrast to reconstruct the object. Increasing the overall counting by two orders of magnitude may well make the technique impractical for experimental use and so a solution was sought in increasing the total reflectivity by measuring reflective holograms at shallow incidence.

8.2 Reflection FTH at Shallow Incidence

Modifying the angle of incidence from 22.5°, to shallow angles <10° will significantly enhance the strength of the reflected signal [279]. In this section, we use a setup with an angle of incidence set to 6.7°. We also manufactured samples that reduced

the reflected footprint from the structurally smooth substrate in the immediate areas around the holographic device via FIB milling. Large regions of the 100 nm thin Si_3N_4 membrane substrate were removed with the FIB and allowed a reflective holographic device to be suspended over a non reflective region of the sample substrate. This design mimicked the samples developed optically, where a non-reflective mask was used to implement holography in reflection geometry.

We found that a device positioned over a narrow bridge caused undesired stress to the surface of the membrane that produced distortions to the recorded scattering pattern. This, in turn, introduced many artifacts into the FFT of the hologram. We discuss employing FIB milling to induce artificial surface roughness in the substrate surrounding the holographic device to encourage diffuse scattering, as an alternative to 'cutting out' the background. This approach would not lead to distortions in the FFT to the extent of cutting away areas of the substrate, and make reconstructions of the object more distinguished at low levels of signal.

8.2.1 Experimental Setup

Experiments were performed at beamline BL13-3 at the Stanford Synchrotron Radiation Lightsource (SSRL). A schematic of the setup is shown in Figure 8.7 (a). A 50 μm pinhole was placed 250 mm upstream from the sample to prove a beam with sufficient spatial coherence. A close up of the inside of the chamber is given in Figure 8.7 (b), and shows the sample holder downstream from a guard support containing a 20 μm pinhole that was used to define the spot size on the sample.

A CCD camera was mounted to the chamber so that its plane was perpendicular to the beam (as would be the case for standard transmission experiments). The connecting tube from the chamber to the CCD allowed the CCD to be rotated around the chamber to shallow angles which was then fixed at 13.4°. The sample was positioned into the beam using the same procedure as described in Section 8.1.1. Once aligned, the sample was rotated such that the plane of the sample formed an incidence angle of 6.7° with the beam. The Bragg scattering was then detected at the CCD, 350 mm downstream from the sample.

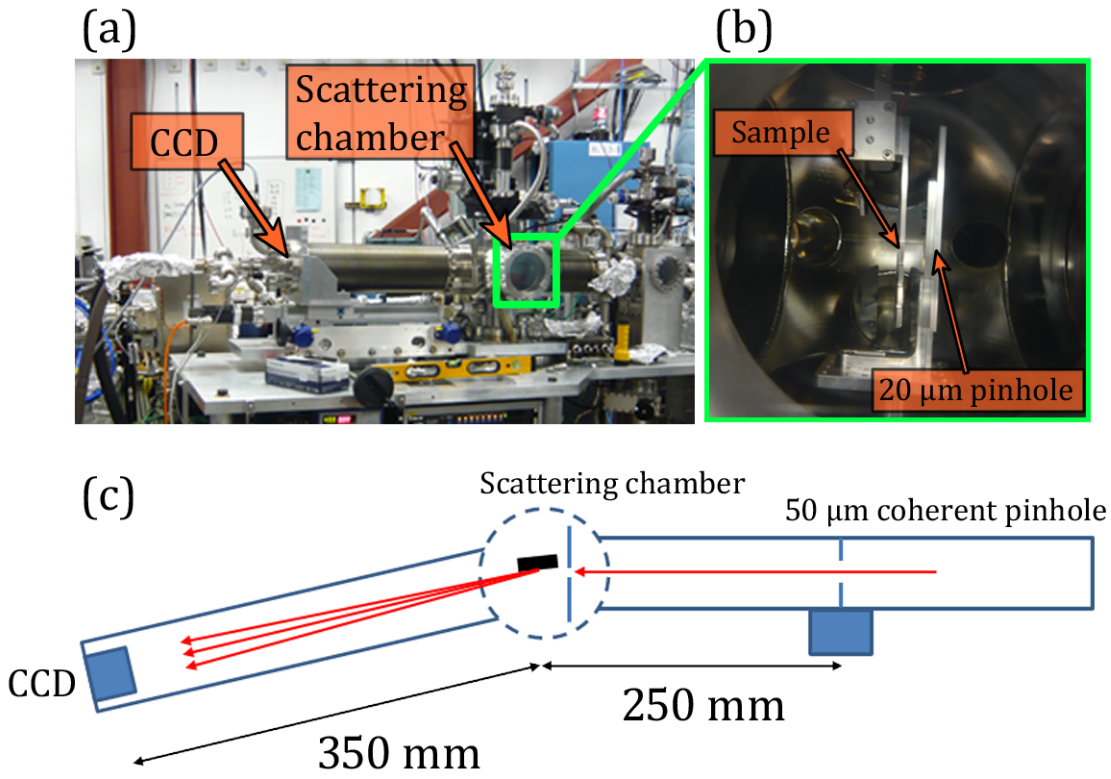

Figure 8.7: Experimental setup for reflection FTH at SSRL. (a) Photograph of the beamline endstation. (b) The inside of the scattering chamber with the sample at normal incidence to the beam. A 20 μm pinhole is positioned upstream from the sample to define the spot size of the input beam. (c) A schematic showing the experimental setup. The sample here was rotated within the beam and measurements were recorded at a shallow incident angles of 6.7°.

8.2.2 Results and Discussion

Figure 8.8 (a) shows a sample with a device similar to the one shown in Figure 8.2 (a). Here an object (10 μm in size) is positioned in close proximity to two reference pin structures (each 1 μm in diameter). An enlargement of the object is shown in Figure 8.8 (b). Figure 8.8 (c) shows the Bragg scattering pattern of the device recorded in reflection at shallow incident (angle of incidence = 6.7°). Figure 8.8 (d) shows the FFT of Figure 8.8 (c). Here, no reconstruction of the object symbol is revealed.

Adapting The Sample Design

To manufacture samples with large regions cut out of the Si_3N_4 substrate, we constructed narrow bridges using FIB milling. An example is shown in Figure 8.9 (a)). Here we demonstrate that a bridge structure ∼600 nm wide and ∼5 μm long can be comfortably manufacture without the membrane surface along the bridge bucking or becoming damaged. The purpose of the bridge is then to support the holographic device suspended over a non reflective region, much like the optical design where a mask was implemented to 'cut out' any reflection from regions around the holographic device.

A bridge was fabricated around a holographic device similar to the device shown in Figure 8.2 (a). Large regions of the sample substrate were removed via FIB milling so that the holographic device was suspended over a non reflective region of the sample either side of it. The size of the two regions removed by the FIB was 30×30 μm. They were separated by 25 μm to accommodate the object and three reflective pins structure. The holographic device held by the bridge structure is shown in Figure 8.10 (a). An enlargement of the object is shown in Figure 8.10 (b). Figure 8.8 (c) shows the Bragg scattering pattern of the device recorded in reflection at shallow incident (angle of incidence= 6.7°). Here, there are distortion to the hologram that are due to the scattering from the edges of the bridge, and the distorted membrane surface caused by the added strain to the membrane substrate. Figure 8.8 (d) shows the FFT of Figure 8.8 (c). Here, no reconstructed structure

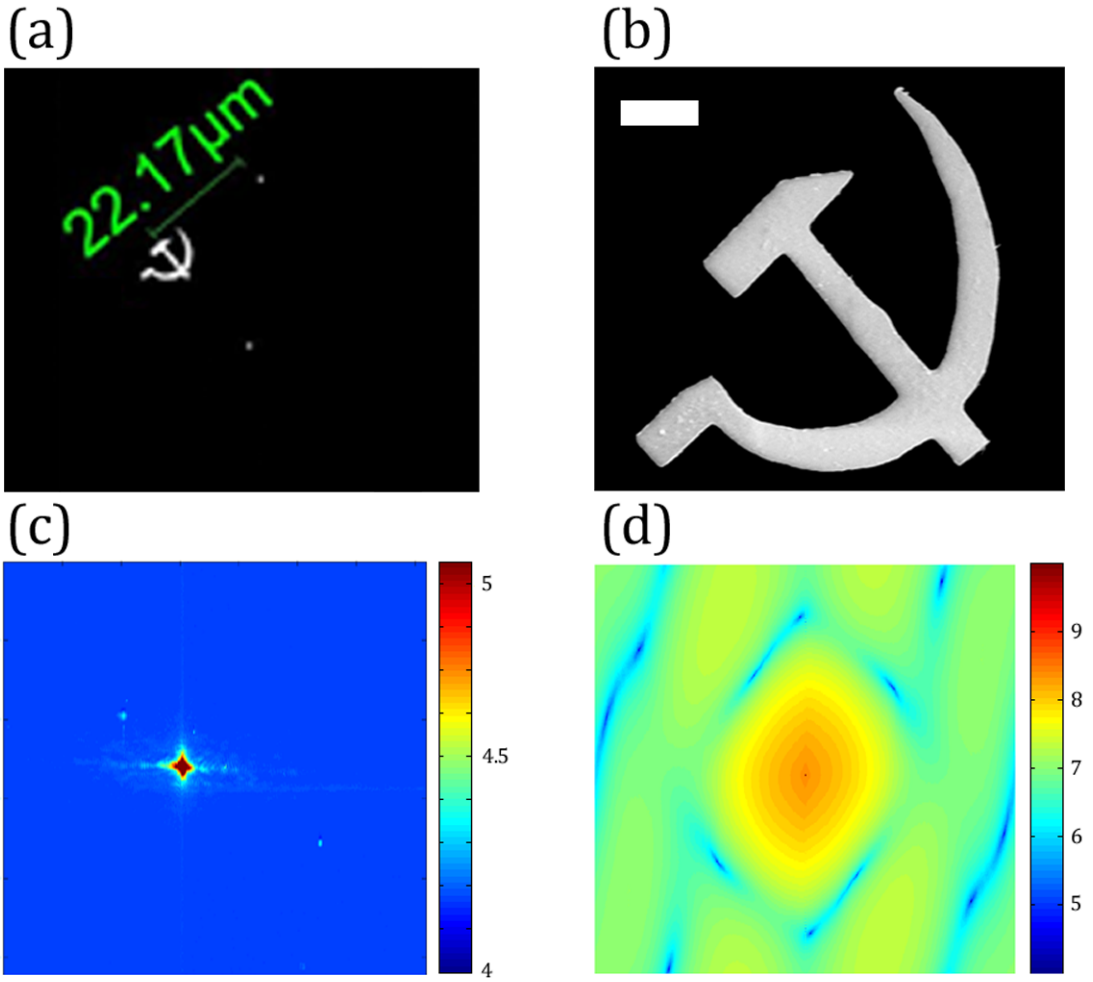

Figure 8.8: Shallow incidence reflection FTH. (a) SEM image of the reflective holographic device. (b) Enlargement of the object symbol (white scale bar = 2 μm). (c) Bragg scattering pattern of the device shown in (a), measured with an incident angle of 6.7°. FFT of the hologram shown in (c). Only the central 450×450 pixels are shown. No structure that resulting from the cross-correlation between the object and reference pin was found in this reconstruction.

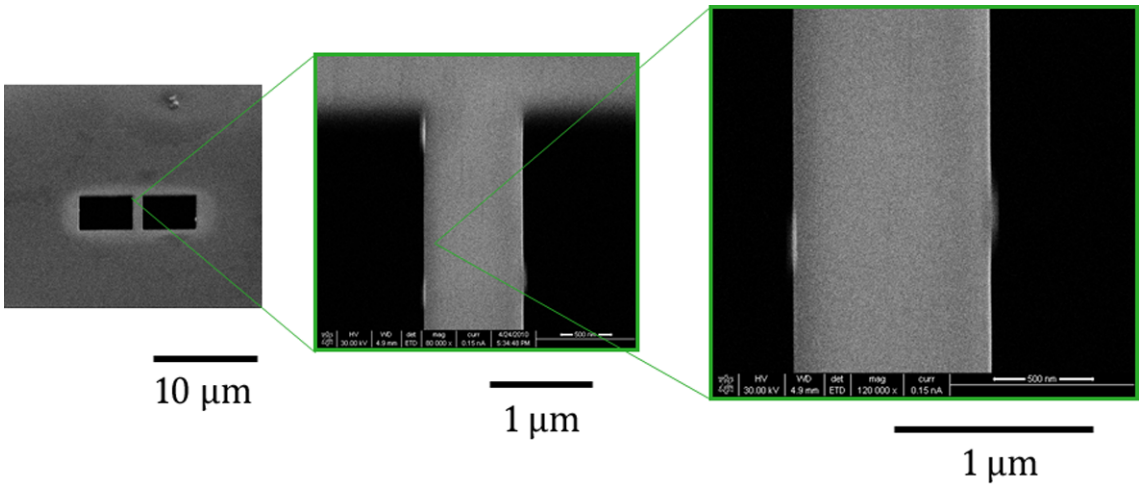

Figure 8.9: FIB milling bridge structures. (a) Two 10×5 μm regions are milled through a 100nm thin Si_3Ni_4 membrane. The separation between the milled regions was 600 nm. This creates a bridge in which a reflective holographic device can be positioned, to suspend it in the centre of an unreflective region of the sample substrate. (b) close up of the bridge. (c) The surface of the membrane along the bridge appear structurally intact after FIB was employed to remove large regions either side of the remaining bridge structure.

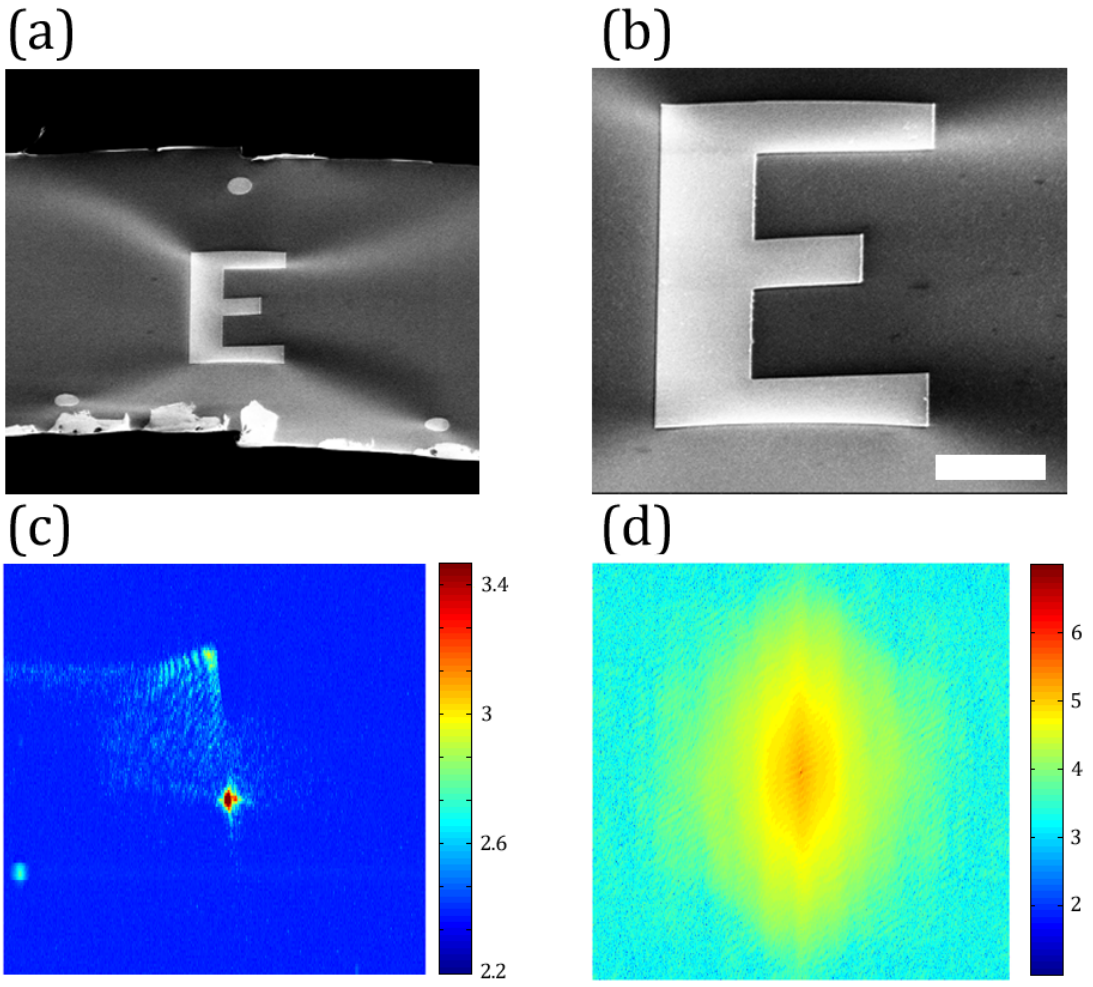

Figure 8.10: Shallow incidence reflection of suspended FTH devices. (a) SEM image of the reflective holographic device. (b) Enlargement of the object (white scale bar = 2 μm). Stress line can been seen across the membrane originating from the holographic object that is due to the added strain on the thin membrane when large regions were cut away with FIB milling, (c) Bragg scattering pattern of the device shown in (a), measured with an incident angle of 6.7°. FFT of the hologram shown in (c). Only the central 550×550 pixels are shown. No structure resulting from the cross-correlation between the object and reference pin was found in this reconstruction. Additional artifacts are apparent in the reconstruction due to the distortions in the measured hologram.

of the object was revealed, which is due to low levels of signal in the recorded scattering pattern. The distortions to the hologram caused by the buckling of the membrane has introduced artifacts into the reconstruction but at this stage it is unclear what effect this may have on a reconstruction of the objects structure. In principle, this should inhibit visibility of the object reconstruction.

We propose two alternative approaches to avoid defects to the membrane structure which are demonstrated in Figure 8.11. Figure 8.11 (a) shows a holographic device suspended on a platform as shown in Figure 8.10 (a), however, the width of the bridge has been increased to 40 μm for added stability to the membrane substrate. Figure 8.11 (b) shows a close up of the holographic device. No lines of stress where the membrane has buckle are apparent.

By increasing the width of the bridge, the background footprint becomes more prominent in the reflection and the setup become less favourable. We therefore propose to use samples that mimic a second design that proved successful in the optical regime. Figure 8.11 (c) shows a bridge structure that could be used to suspend a reflective holographic device over a non reflective region of the sample substrate. A 60 nm Au film was deposited onto a Si substrate and exposed to a FIB. The FIB was used to induce artificial roughness to the surface of the substrate, that strongly reduces the amplitude of reflected light at soft x-ray wavelengths [279]. Optically, we used chemical etching to promote diffuse scattering over the substrate to ensure the reflected light, in regions other than the reflective holographic device, were low in amplitude. This method of inducing artificial surface roughness into the substrate would permit one to use a variety of substrates rather than being limited to a thin membrane substrate that need to be cut away with FIB milling. This latter method is therefore favoured over the previous and holds potential for further investigation into reflection holography at soft x-ray wavelengths.

8.3 Conclusions

In summary, we have presented our progress towards establishing holography in reflection geometry at soft x-ray wavelengths. We addressed the problem of low

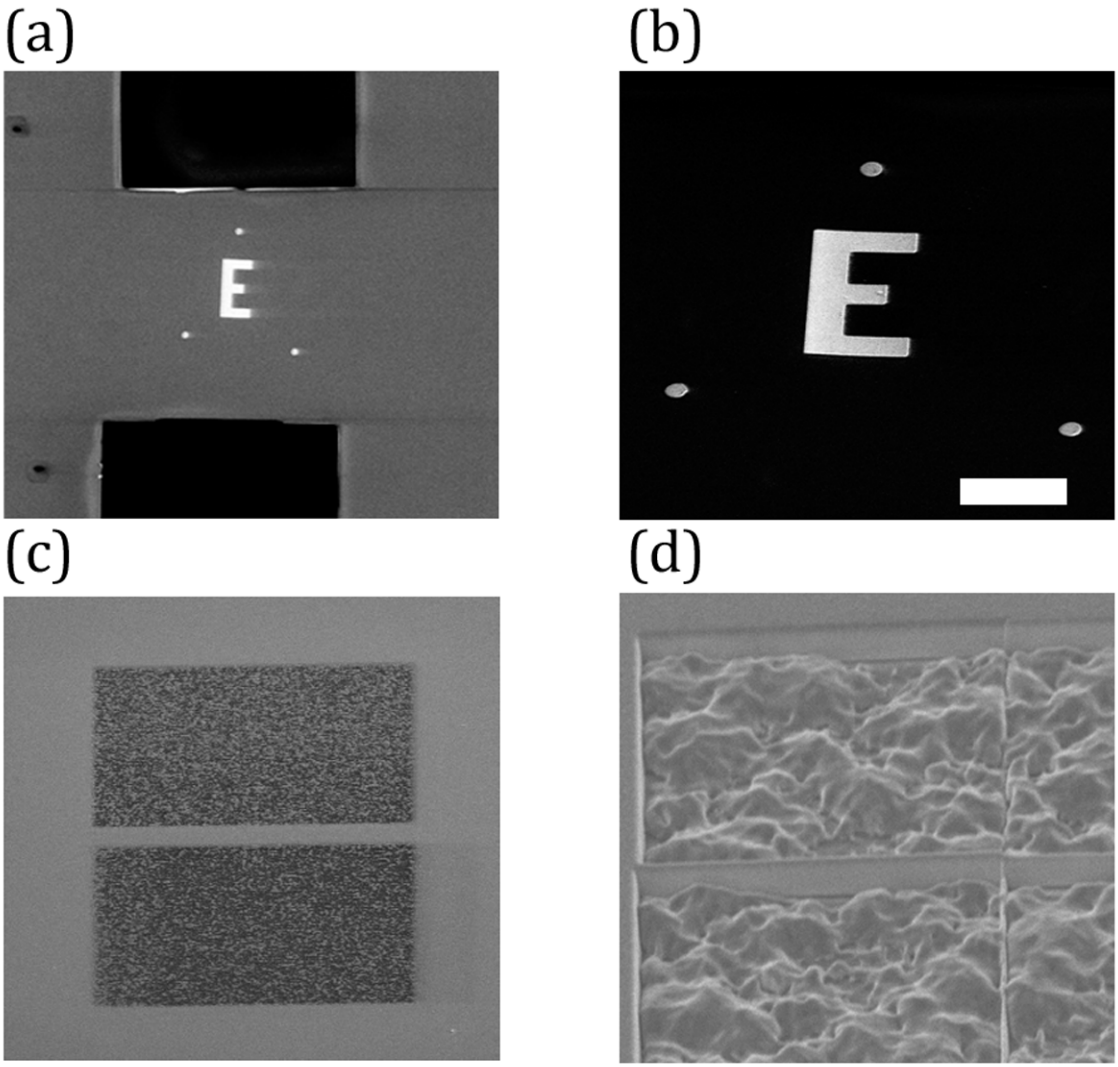

Figure 8.11: Improving sample designs. (a) A holographic device is suspended on a wide bridge support structure. The wider bridge reduces the strain on the membrane substrate and no line of stress are visible. (b) Close up of the holographic device shown in (a) view at an angle of 52° above the object and reference structures. (c) Artificial roughness is induced into a thin film of Au by exposing the surface to FIB etching. A 60 nm Au film was deposited onto a Si substrate but in principle, a number of substrates and materials with a range of thicknesses could be used for this approach. (d) A close up of a 500 nm thick Au film, which has been etched with FIB. The depth of the etch has removed material from the Au film giving a surface roughness on the order of 10 nm. The induced surface roughness is thought to strongly encourage diffuse scattering at soft x-ray wavelengths and strongly mimic the setup which has already been presented optically in Chapter 5.

reflected signal from point-like holographic references by manufacturing extended reference structures. For this reason, FIB milling used to sharpen the corners of the extended reference object. Our experimental approaches were based around the methods that proved most successful in the optical regime, which we have presented in Chapter 5.

We have shown that a narrow bridge can be manufactured into a 100 nm thin Si_3Ni_4 substrate, with lateral dimension of 600×5000 nm. This bridge structures were built around a reflective holographic device to suspend the device over a non reflective, or rather, non existing region of the sample substrate. This approach was designed to mimic the experiments performed optically, where a non reflective mask was used to block reflected light in all regions other than the holographic device. In cases where the width of the narrow bridge was equivalent to the lateral dimensions of the holographic device to which it supported, lines of stress appeared in the membrane surface, which we believed introduced artifacts into the reconstruction of the recorded hologram. At this stage, the extent to which the artifacts reduce the clarity of a reconstruction of the object is unclear. We found that increasing the width of the bridge to for a 20 μm sized device, avoided stress lines forming in the surface.

By inducing artificial roughness into a structurally smooth surface, we propose a new method of suspending a reflective holographic device over a non-reflective region of the substrate. This will reduce specular reflection from the substrate without the need for cutting away sections of a membrane substrates. Test samples were manufactured using FIB etching to induce roughness on the order of 10 nm, into a 60 nm Au film. Measurements of these samples have not been taken.

An approach based on a simple closed-form algorithm developed by, and demonstrated optically in transmission by Podorov *et. al* [91, 92], could also prove to be valuable for achieving an FTH reconstructions in reflection geometry at soft x-ray wavelengths. Here, a holographic reference is not used. Instead the object is confined within a sharp rectangular support aperture that allows one to reconstruct the complex scalar wavefield of the object from the far field coherent diffraction

pattern.This approach, like reflection HERALDO, would solve the issue with weak signals reflected from the reference.

The future of reflection holography in the x-ray regime requires further experiments before the technique can be utilised for magnetic imaging. One approach would be to select a substrate such as silicon, which has a shallow critical angle where the reflection of x-rays is incredibly small. For energies of 500 eV the reflection intensity of thick silicon is expected to be about 0.5 for a 3 degree angle of incidence and 0.01 for a 4 degree angle of incidence [279]. Compared with a thick gold mirror where the reflected intensity is about 0.3 for a 4 degree angle of incidence. Under these parameters, imaging the reflected light from a silicon substrate with gold features at a 4 degree angle of incidence would provide an much stronger reflected signal from the golder compared with that of the silicon. Combined with HERALDO imaging this setup could allow for strong reflections from a gold object and extended reference compared with the light reflected from a silicon substrate. By removing the background reflection from the substrate, the signal-to-noise ratio in the recorded scattering pattern would in principle take on a significant improvement.

An approach for reflection FTH has already been reported by Roy *et al.* [280]. This technique could be implemented for magnetic imaging by tunning the x-ray energy to a resonant absorption edge of the magnetic material. Here, a Fourier transform mask is separated from the sample and placed between the scattering plane and the detector. After the light has reflected from the sample, it passes through the mask before it is recorded by the detector. The reflected beam is split into an object wave and a reference wave after the beam has been reflected from the sample surface. This has been illustrated in Figure 8.12. In this setup it is important to minimise the distance between the holographic mask and the sample. this is because the reconstruction of the hologram recorded on the detector has to be back-propagated to the sample surface. Two effects limit how far the back-propagation can be calculated. Firstly, the object aperture acts as a low pass filter on the diffracted wave and secondly, Fresnel zones become apparent when

back-propagating the aperture and this causes Fresnel ringing in the image which is amplified with the propagating distance. To avoid these effects overwhelming the recovered image at the sample surface, Roy *et al.* [280] reported on a working limit, defined by a Fresnel number no great than 5. For an electromagnetic wave passing through an aperture and hitting a screen, the Fresnel number F is defined as,

$$Fresnelnumber = \frac{a^2}{L\lambda} \tag{8.1}$$

where a is the aperture diameter, L is the distance of the aperture to the screen and λ is the wavelength of the radiation.

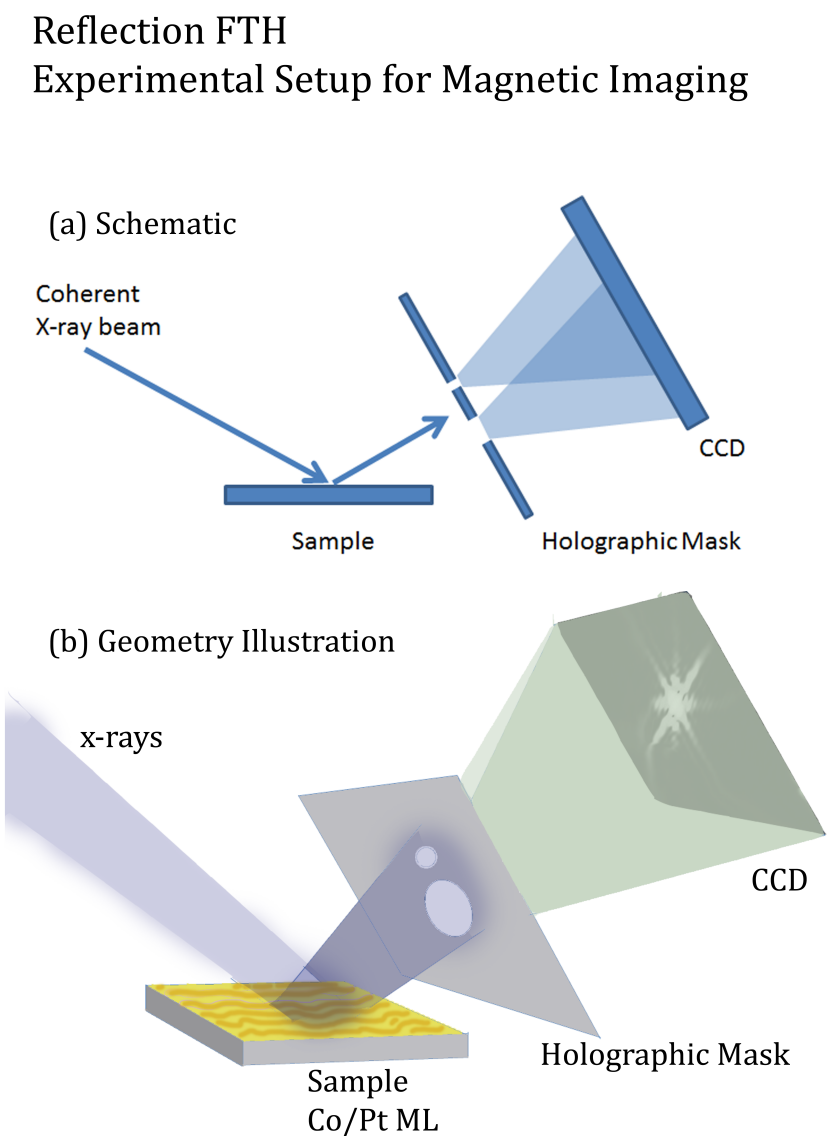

Figure 8.12: (a) Experimental schematic for reflection FTH of magnetic nanostructures. Here a traditional transmission FTH mask is placed in the path of the beam reflected from the sample. The mask splits the beam into a reference and object wave that interfere at the detector. (b) Illustration of the reflection FTH experimental setup reported by Roy *et al.* [280]. In this experiment the setup makes use of coherent soft x-ray resonant magnetic scattering to image a Co/Pt ML film. The electric field amplitude at the holographic mask needs to be back-propagated to the samples surface and providing the mask is sufficiently close to the sample (as defined in [280])

Chapter 9

Summary and Outlook

In this thesis we have discussed two holography experimental setups that extends x-ray magnetic holography for simultaneous imaging of in-plane and out-of-plane magnetic components. The two geometries are:

- Transmission holography at off-normal incidence
- Reflection holography

9.0.1 Transmission Holography at Off-Normal Incidence

The main motivation for investigating an off-normal transmission geometry was to provide a high resolution lensless imaging technique suitable for imaging magnetic structure in samples where the directions of the magnetic vectors lie in the plane of the sample. In conventional FTH very little work has been reported where holography has been used to image magnetic specimen where the direction of magnetisation lies in the plane of the sample [23]. This is due to limitations associated with the experimental geometries of magnetic imaging with holography. We have shown that by using the HERALDO technique, a magnetic sample can be easily rotated within an x-ray beam to gain sensitivity to in-plane magnetic contrast.

A method reported by Tieg *et al.* demonstrated that FTH can be used to image in-plane magnetisation using holographic reference holes at inclined angles. However, the spatial resolution of this approach was limited by the fabrication of

the reference holes, which is technically challenging because it requires FIB milling of narrow holes through a thick ($\sim$ 800 nm) layers of gold, with the sample plane rotated within the FIB beam.

In this thesis we have used extended holographic references to perform off-normal transmission holography and demonstrated that the technique is capable of simultaneous imaging in-plane and out-of-plane magnetic components in nanopatterned structures with a high spatial resolution. An advantage of using extended references over the pinholes used in conventional FTH is that the approach decouples the spatial resolution from the image contrast. In conventional FTH, to improve the contrast one typically has to increase the signal of the reference source by using larger pinholes, which comes at a cost of reducing the resolution of the reconstructed image. By using a narrow slit to provide the holographic reference beam, the reference signal can be increased without comprising the spatial resolution. Due to current limitations of nanofabrication tools, it would be impractical to manufacture a series of reference pinholes that would provide sufficient image contrast for images with sub-10 nm spatial resolutions (as described in [287]. Due to the decoupling of the reference size from the spatial resolution made possible with HERALDO, however, this dilemma can be avoided.

As a proof of concept, we have demonstrated that HERALDO can be used for in-plane measurements and presented magnetic structure in permalloy films and sub-micron elements. We presented images of a magnetic vortex ground state in a 900 nm square and 900 nm disc structure that was patterned by by FIB milling, and demonstrated displacement of the vortex core in the presence of an external applied magnetic field.

The techniques capability for simultaneously imaging in-plane and out-of-plane magnetisation was utilised in a study of a $[Co/Pt]_30/Ta/Py$ multilayers stack. In this structure the Co/Pt multilayer exhibits perpendicular magnetic anisotropy and so the magnetic moments face in and out of the samples plane. During the deposition stage, the Permalloy is sputtered onto the stack. It was found that magnetic stray field from the Co/Pt can influence the domain structure via dipolar coupling.

From HERALDO images recorded at the Co and the Ni absorption edges, it was found that the at spatial structure of the Permalloy mimicked the magnetisation state of the Co/Pt beneath. Micromagnetic simulations of the sample showed that the Co/Pt caused the real-space period of the domains in the Permalloy to match the real space period of the domains in the Co/Pt. Whilst no direct correlation of the spatial domains could be seen in the simulation, it highlights the important factor that theoretical predictions alone can not accurately describe magnetic systems alone.

9.0.2 Reflection Holography

The main motivation for investigating reflection holography was to provide a lensless imaging technique, complimentary to transmission holography at off-normal incidence, but also suitable for imaging magnetic materials with in-plane magnetisation. In the reflection geometry the substrate for growing magnetic samples would not be limited to Si_3N_4 membranes because the sample would not necessarily have to be transparent in the soft x-ray regime.

In this thesis progress has been made toward developing a technique for imaging sample systems that can only be grown as bulk crystals, or films that require specific substrates that cannot be implemented in a x-ray transmission geometry. Reflection holograms of non magnetic metal objects recorded in the optical regime have been presented, which revealed reconstructions in three experimental geometries. In each of the three geometries the angles of incidence was changed (i.e. angle of incidence=45°, 22.5° or 8°). These experiments were used to investigate different geometries that could be used in the x-ray regime for investigating magnetic imaging.

In the x-ray regime, holograms of non-magnetic test samples were recorded at various angles of incident, close to the geometries that were tested in the optical regime. It was not possible to reconstruct a real-space image of the test objects in any of these experiments due to a lack of signal strength which resulted in the holograms lacking sufficient fringe contrast required for a reconstruction.

9.0.3 Future Work

Improve OOMMF model of [Co/Pt]$_3$0/Ta/Py systems

The OOMMF simulations presented in Section 7.3.2 did not agree with the experimental results revealing the magnetic structure in the permalloy layer of a [Co/Pt]$_3$0/Ta/Py system. To improve this model a simulation of a much larger area may reveal agreements between the simulations and experimental findings. The current model simulates the magnetisation within a 1×1 μm square region and this may not be representative of a magnetic film of the system and it is possible that the boundaries of 'film' in the simulation cause an undesired effect on the magnetisation.

Field dependent studies of [Co/Pt]$_3$0/Ta/Py systems

It was observed in Section 7.3.2 that a saturating out- and in-plane field components of 176 mT caused a break down of the dipolar coupling between the Co/Pt and Py in the[Co/Pt]$_3$0/Ta/Py systems. A full investigation of the coupling and external applied magnetic fields would be required to further our understanding of this system and to fully evaluate our conclusions presented in Section 7.3.2. An aim of future investigations will be to image the evolution of the domain structure as a function of the applied field, and thereby study different stages of the reversal mechanism in these thin film systems.

Investigate Coupling as a Function of [Co/Pt]$_n$ Repeats in [Co/Pt]$_n$/Ta/Py systems

During this thesis several magnetic films of [Co/Pt]$_n$/Ta/Py systems were deposited where a different number of [Co/Pt]$_n$ multilayer (ML) repeats was used before the Ta/Py layers were deposited ontop. Polar hysteresis loops of the Co/Pt ML and the [Co/Pt]$_n$/Ta/Py systems for Co/Pt ML with different numbers of repeats is presented in secrefMagneto-Optical Effects. In the experiments only the sample where $n = 30$ was investigated as it provided the structure with the highest coercive field. An investigation into the coupling of films with few repeats could

be performed, however more importantly, an investigation of films with a greater number of repeats could be performed to investigate whether the coupling between the Co/Pt and Py could be preserved in the presence of high external applied fields due to the stronger stray fields of the Co/Pt ML.

Investigation of isolated [Co/Pt]$_3$0/Ta/Py elements

It was recently proposed that synchronised arrays of spin-torque nanooscillators (STNOs) could be manufactured by patterning a magnetic multilayered thin films and provide a nanoscale microwaves source for spintronic applications [34].

Characterising the magnetic states on the submicroscopic scale is still a challenge, yet leading on from the work presented in this thesis, imaging of the magnetic states in patterned structures, such as STNOs, could be performed. Here, the analysis of perpendicular and in-plane components of magnetisation is essential for understanding the characteristics of coupling between the 'fixed' and the 'free' magnetisation layers. As demonstrated in the Section 7, off-normal magnetic HERALDO imaging can provide simultaneous imaging of in-plane and out-of-plane magnetisation in [Co/Pt]$_3$0/Ta/Py films. Patterning this films would serve as an example of an STNO systems where the fixed layer has a perpendicular magnetised component while the free layer has in-plane magnetisation, where such a combination normally leads to a maximum spin-transfer torque.

Development of scanning HERALDO imaging at off-normal incidence

By separating the magnetic sample from the optics part of the setup (i.e. the holographic mask), holography can be implemented in a scanning mode [12, 80]. The holographic mask can remain stationary whilst the sample is scanned across the FOV aperture in the mask. This could be implemented with extended references in an off-normal geometry to provide an x-ray holographic microscope for imaging in-plane magnetisation (Figure 9.1). In using an extended reference, it is important to note that imaging a magnetic thin film would be problematic because the extended reference would typically by pass through the magnetic film and be split up into

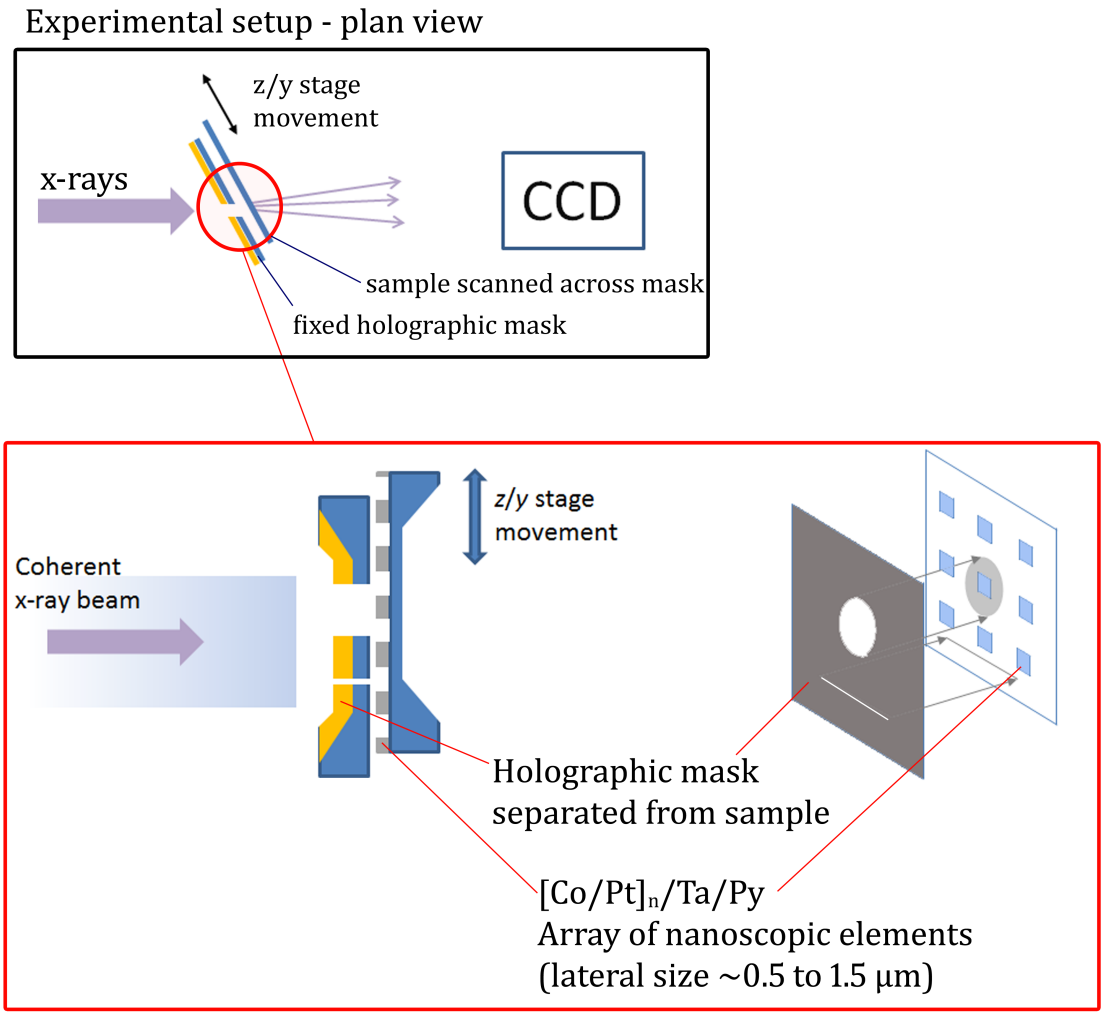

Figure 9.1: Experimental setup for scanning HERALDO imaging. The scanning setup could be used to increase the field of view of HERALDO imaging without compromising the spatial resolution of the setup. Whilst imaging magnetic thin films would be problematic due to magnetic domain boundaries appearing within the extended reference, using an extended slit as a reference could be implemented to image arrays of magnetic nanostructures.

sections by magnetic domain boundaries. This would result in many images of the sample forming in the HERALDO reconstruction due to the sharp edges that the magnetic domain boundaries provide within the reference. Nevertheless, if a narrow reference slit was used, it would be possible to image isolated or arrays of magnetic nanostructures, providing the spacing between the nanoscopic elements in one of the lateral direction was greater than the width of the extended reference slit. This would provide a way for imaging arrays of magnetic nanostructures without compromising the spatial resolution of the magnetic HERALDO imaging technique.

Time-resolved magnetic HERALDO imaging

Vortex Core Gyration

With growing interest toward dynamic studies where the use of femtosecond pulses provides a coherent source, a limited number of photons are available for each image and so larger reference signals are desirable in FTH experiments which the HERALDO technique can provide.

In future experiments examining the dynamic properties nanostructures would allow one to observe the precession of magnetic moments in the 'fixed' and the 'free' layers, and investigate the possibility of synchronising the precession of moments in different patterns of elements [34].

Vortex closure domains are fascinating nanoscopic magnetic structures with complex dynamic behavior. Having demonstrated lensless imaging of vortex flux closure ground states in permalloy elements in this dissertation, the development of a time-resolved stroboscopic holographic imaging technique, with contrast of in-plane and out-of-plane magnetisation would be a highly desirable step forward for lensless magnetic FTH. An experimental setup as reported by Marcham *et al.* [230, 288] could be implemented to stroboscopically record time-resolved images with transmission holography.

Directing an RF field into the coplanar waveguide across a magnetic element would produce an in-plane magnetic field that excites vortex gyration [289, 290],

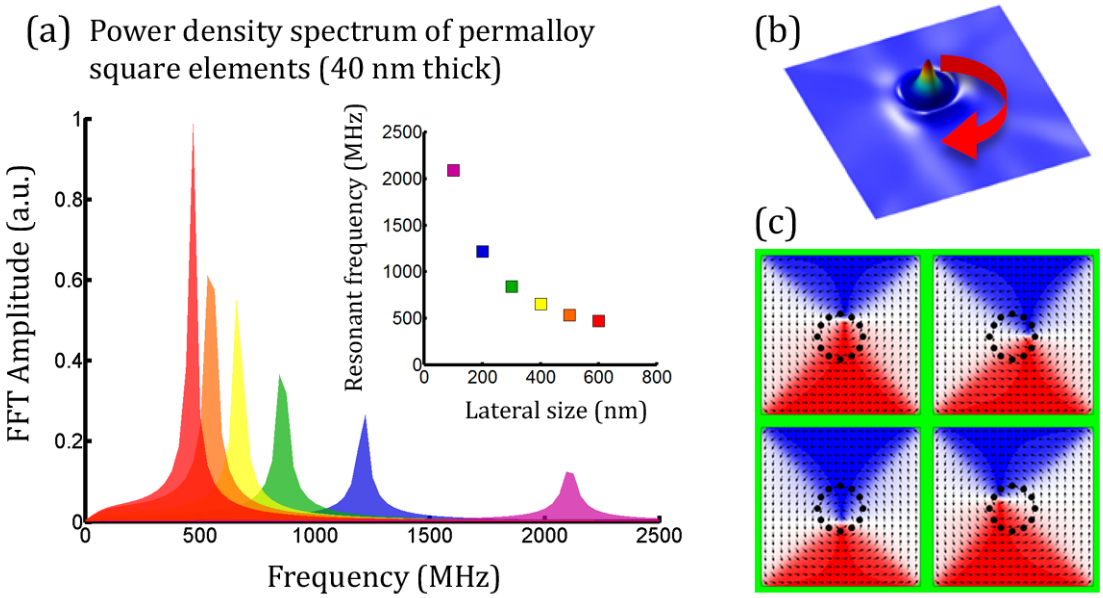

Figure 9.2: OOMMF simulation for time-resolved stroboscopic imaging. (a) Amplitude and frequency of the gyrotropic mode for elements of different size. (b) Simulated vortex precession. M_z component of a 40×500×500 nm Py element. (c) M_x-component configurations of the element in (b) at different stages of an RF field (5 Oe) cycle.

and magnetic dynamics could be studied via HERALDO imaging by adopting a similar experimental setup presented by Vansteenkiste *et al.* [291]. Figure 9.2 shows simulations preformed in OOMMF to discern the gyrotropic mode of a 500×500×40 nm Py element.

Future Reflection Holography Experiments

For magnetic imaging in reflection geometry an experimental setup as reported by Roy *et al.* [280] could be implemented (Figure 9.3). Here the holographic mask is separated from the sample film, so that light reflected form the sample is split into an object and reference beam. The electric field amplitude at the holographic mask needs to be back-propagated to the samples surface. It was reported by Roy *et al.* [280] that the ringing from back-propagating the object hole becomes problematic for a Fresnel number of ∼5 (where the Fresnel number=a^2/Lλ, with a the size of

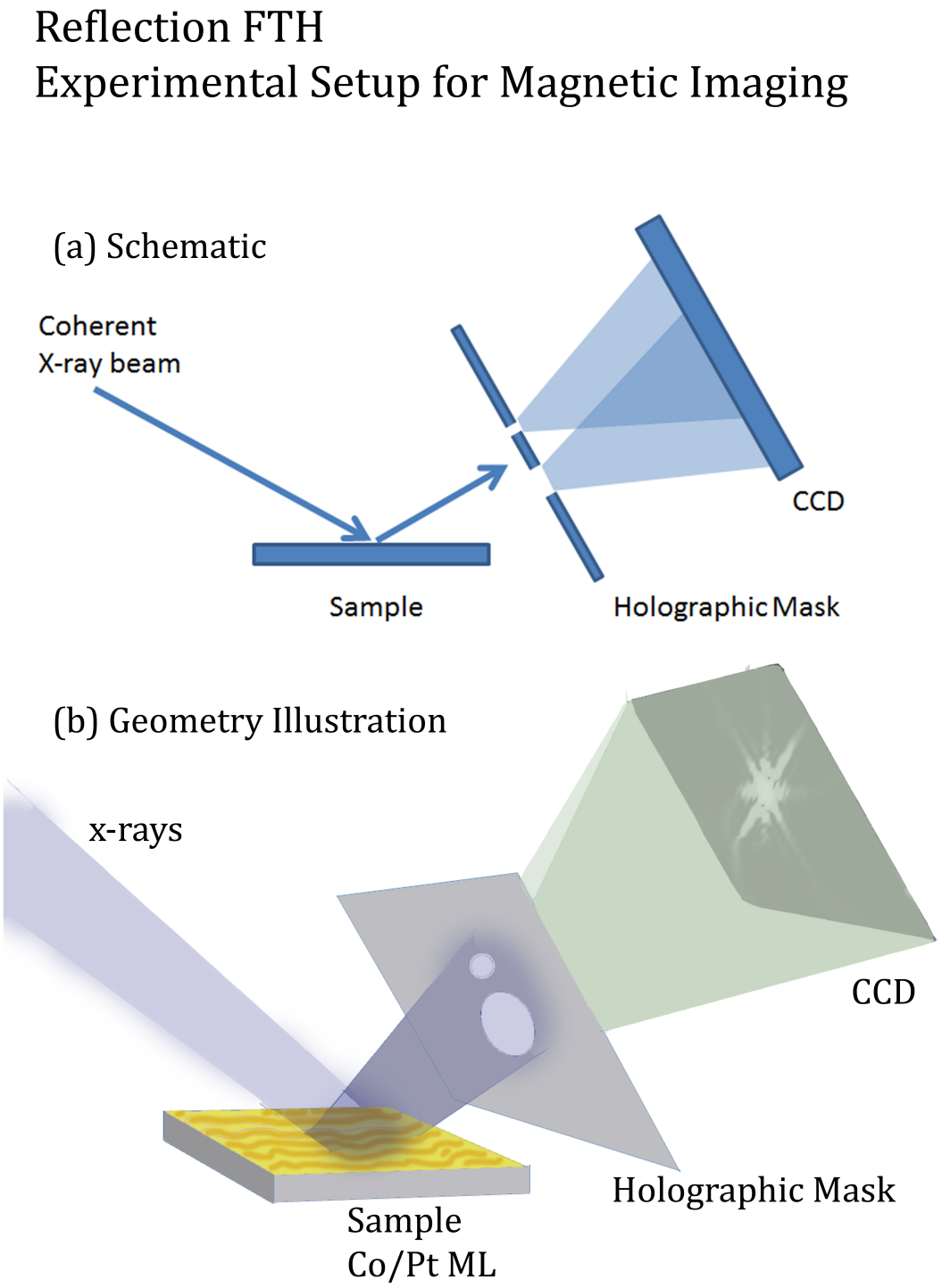

Figure 9.3: (a) Experimental schematic for reflection FTH of magnetic nanostructures. Here a traditional transmission FTH mask is placed in the path of the beam reflected from the sample. The mask splits the beam into a reference and object wave that interfere at the detector. (b) Illustration of the reflection FTH experimental setup reported by Roy *et al.* [280]. In this experiment the setup makes use of coherent soft x-ray resonant magnetic scattering (Beutier *et al.* [292, 51]) to image a Co/Pt ML film.

the aperture, L the distance to the mask from the sample, and λ is the incident wavelength). If we consider an aperture with a diameter of 2 μm, and a beam energy corresponding to the Co L_3 absorption edge (778 eV), this corresponds to a propagation limit of $\sim$500 μm.

Providing these experimental conditions are met in that the mask can be positioned sufficiently close to the sample surface, combining the experimental setup of Roy *et al.* [280] with the soft x-ray coherent scattering setup reported by Beutier *et al.* [51] we expect that real-space images of the magnetic domain structure in the Co/Pt film could be achieved.

Appendix A

Coordinate systems

Plane	**Horizontal coordinate**	**Vertical coordinate**
Source	ξ	η
Sample	x	y
Far field	u	v
	q_x	q_y
Real space reconstruction	X'	Y'

Appendix B

Basic Fourier Theorems

Shift Theorem

If $f(x)$ has a Fourier transform $F(u)$, then $f(x-a)$ has the Fourier transform $e^{-2\pi iau}F(u)$. This means that if a given function is shifted by an amount a in a positive direction, no change in the amplitude of the Fourier component is expected. The only change expected in the Fourier transform is a change in the phase. Derivation taken from [263]:

$$\begin{aligned}\int_{-\infty}^{\infty} f(x-a)e^{-i2\pi xu}\mathrm{d}x &= \int_{-\infty}^{\infty} f(x-a)e^{-i2\pi(x-a)u}e^{-i2\pi xau}\mathrm{d}(x-a) \\ &= e^{-i2\pi au}F(u).\end{aligned} \tag{B.1}$$

Convolution Theorem

The convolution between two functions f and g is defined as a new function $h(x)$ where,

$$h(x) = f(x) * g(x) = \int_{-\infty}^{\infty} f(u)g(x-u)\mathrm{d}u \tag{B.2}$$

Cross-correlation

The cross-correlation of functions $f(x)$ and $g(x)$ is equivalent to the convolution of $f^*(-x)$ and $g(x)$. The cross-correlation between two functions f and g is defined

as,

$$\begin{aligned} f(x) \otimes g(x) &= f^*(-x) * g(x) \\ &= \int_{-\infty}^{\infty} f^*(u) g(x+u) \mathrm{d}u \end{aligned} \tag{B.3}$$

Derivative Theorem

If $f(x)$ has the Fourier transform $F(u)$, then the derivative $f'(x)$ has the Fourier transform $i2\pi u F(u)$ [263].

Derivative of a Cross-correlation

The derivative of a cross-correlation is equal to the cross-correlation of either function with the derivative of the other [263].

$$[h \otimes g(x,y)]' = h \otimes g'(x,y) = h' \otimes g(x,y) \tag{B.4}$$

Linear Differential Operator and the Cross-correlation

From the principles above we obtain the expression for the derivative of a cross-correlation between a holographic reference $r(x)$ and an object $g(x,y)$,

$$[r(x) \otimes g^*(x,y)]' = r \otimes g'^*(x,y) = r' \otimes g^*(x,y). \tag{B.5}$$

Taking the Fourier transform of Figure B.5 we have

$$i2\pi u[R(u)G^*(u,v)] = -R(u)[i2\pi u G(u,v)]^* = [i2\pi u R(u)]G^*(u,v). \tag{B.6}$$

where $R(u)$ and $G(u,v)$ are the Fourier transforms of $r(x)$ and $g(x,y)$, respectively.

Appendix C

OOMMF modelling software

The Object Oriented MicroMagnetic Framework (OOMMF)

OOMMF is a micromagnetic simulation software. The software simulates the magnetism inside a two dimensional material by taking the approach that the magnetisation is made up of millions of spins [1]. Typically the user defines the size and shape of the material, the material properties, the cell size of the simulation mesh, the method to solve the magnetisation in the material and any external applied fields.

Simulating the Vortex Core Displacement in a Permalloy Element

A colourmap was used to define the Permalloy (Py) element as a square magnetic free layer. The size of the Py element was then set by specifying in the code that the dimensions of the input colourmap was 900×900×50 nm. Anything coloured white in the images was defined as the magnetic free layer, and anything black defined as a default universe with no magnetic properties. The input image is shown in Figure C.1 with a grey background around it so that the square element can be seen. The properties of the magnetic free layer were then defined to have values K_u=0 MJ/m^3, M_{sat}=0.86 MA/m, and A=13 pJ/m (typical values for Py). The cell size used was 20×20×5 nm^3. To form the initial vortex state, energy minimisation

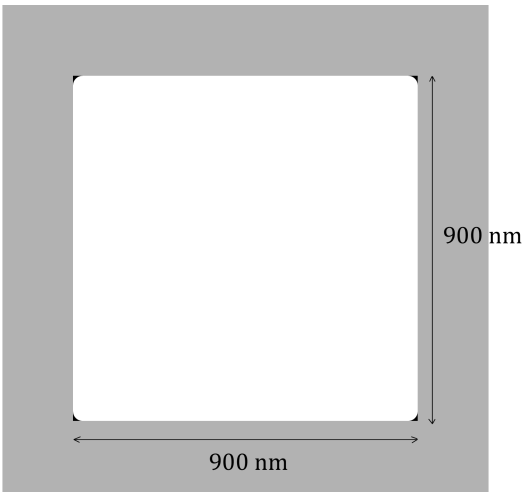

Figure C.1: The colourmap shown was input to define the starting magnet state of the permalloy free layer. Any part of the image coloured white was defined as the magnetic free layer. Any parts coloured black were defined as the default universe with no magnetic properties. A grey background has been used in this figure to highlight which areas of the colourmap were white and which were black. The grey area was not apart of the colourmap input into the model. A Runga Kutta solver was used to simulate the magnetisation in the element as the system relaxed in zero applied field.

of the magnetisation in the magnetic free layer was performed with a Runga Kutta solver. The system relaxed in zero applied field (with a stopping parameter that defined as $\mathrm{d}m/\mathrm{d}t$=0.001). The magnetic square relaxed into a vortex state and the OOMMF software output was a vector field map of this magnetic state. An image of the vector map is shown in Figure C.2

The magnetisation in the element within an external applied magnetic field was then simulated which showed displacement of the vortex core. For this simulation, the vector field map of the vortex state was input as the starting magnetisation state of the Py element.

The external applied magnetic field was defined by x, y, and z field components and a simulated vector map of the magnetisation state of the Py element within the applied magnetic field was output by the software. The OOMMF software was programmed to output a vector field map for many x, y, and z field components

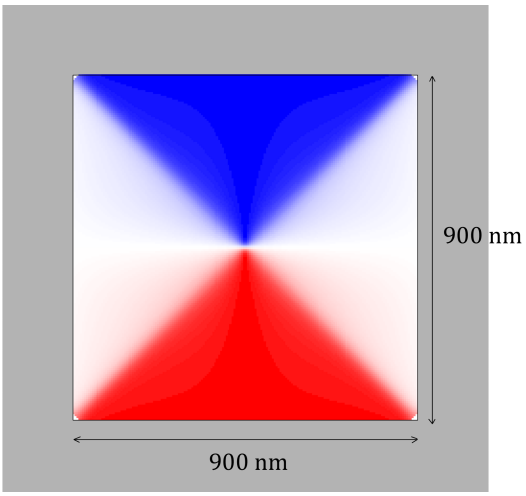

Figure C.2: The vector field map shown here was input as the starting magnetisation state of the permalloy square before simulating its responce to an applied magnetic field.

by specifying, a start and end value for each of the field components, along with a number that determined how many vector field maps to output at evenly spaced steps across the field range specified. This was input into the OOMMF code in the form (with all values given in kOe),

[start x field component, start y field component, start z field component, end x field component, end y field component, end z field component, steps]

The simulation was performed in three stages defined as,

Step one: take measurements with x and z field components increasing from 0 Oe to 500 Oe in 20 steps. The y component of magnetisation is zero at all times. These field components were chosen to correspond with the magnetic fields applied in the off-normal x-ray HERLAOD experiment presented in Section 7

[0, 0, 0.00, 0.5, 0, 0.5, 100]

Step two: take measurements with x and z field components decreasing from 500 Oe to -500 Oe in 40 steps

[0.50, 0, 0.5, -0.50, 0, -0.5, 200]

Step three: take measurements with x and z field components increasing from -500 Oe to 0 Oe in 20 steps

[-0.50, 0, -0.5, 0.0, 0, 0, 100]

Simulating the [Co/Pt]$_n$/Ta/Py Stack

The Co/Pt ML was modeled as a continuous slab with the perpendicular anisotropy constant K_u=0.21 MJ/m^3 and magnetisation M_sat=0.26 MA/m derived from our VSM data [57]. The exchange stiffness constant was A=4.6 pJ/m. The size of the slab was defined as a 1×1 μm region. The cell size of the simulation was 5×5×5 nm^3. The simulation output a vector field map of the magnetisation state of the Co/Pt.

A second simulation was then performed to model the response of the Py layer in a [Co/Pt]$_n$/Ta/Py Stack. The vector field map of the Co/Pt ML describe above was input as the starting magnetisation state of the Co/Py ML in the stack. The Ta layer was magnetically dead and the Py was defined as a magnetic free layer with K_u=0 MJ/m^3, M_{sat}=0.86 MA/m, and A=13 pJ/m. The cell size used was 5×5×5 nm^3. The magnetisation of the Py layer was relaxed (using a stopping parameter dm/dt=0.25), and the software output a vector field map of the magnetisation in the Py layer.

Bibliography

[1] *The Object Oriented MicroMagnetic Framework (OOMMF).* `http://math.nist.gov/oommf/`

[2] M.-Y. Im, P. Fischer, K. Yamada, T. Sato, S. Kasai, Y. Nakatani, T. Ono, *Symmetry breaking in the formation of magnetic vortex states in a permalloy nanodisk.*, Nature communications 3 (2012) p. 983.

[3] V. Uhlí, M. Urbánek, L. Hladík, J. Spousta, M.-Y. Im, P. Fischer, N. Eibagi, J. J. Kan, E. E. Fullerton, T. Sikola, *Dynamic switching of the spin circulation in tapered magnetic nanodisks.*, Nature nanotechnology 8 (5) (2013) p. 341–6.

[4] J. Vogel, W. Kuch, M. Bonfim, J. Camarero, Y. Pennec, F. Offi, K. Fukumoto, J. Kirschner, A. Fontaine, S. Pizzini, *Time-resolved magnetic domain imaging by x-ray photoemission electron microscopy*, Applied Physics Letters 82 (14) (2003) p. 2299.

[5] D. Gabour, *A New Microscopy Principle*, Nature 161 (1948) p. 777.

[6] D. Gabour, *Microscopy by Reconstructed Wave Fronts: I1*, Proc. Phys. Soc. B 64 (1951) p. 449.

[7] S. Eisebitt, J. Lüning, W. F. Schlotter, M. Lörgen, O. Hellwig, W. Eberhardt, J. Stöhr, *Lensless imaging of magnetic nanostructures by X-ray*, Nature 432 (December) (2004) p. 885–888.

[8] H. El-Sum, P. Kirkpatrick, *Microscopy by reconstructed wavefronts*, Physical Review 85 (4) (1952) p. 763–763.

[9] D. Gabour, *Holography 1948-1971, Nobel Lecture* (1971).

[10] E. Leith, J. Upatnieks, *Wavefront Reconstruction with Continuous-Tone Objects*, Journal of the Optical Society of America 53 (1963) p. 1377.

[11] O. Hellwig, S. Eisebitt, W. Eberhardt, W. F. Schlotter, J. Luning, J. Stöhr, *Magnetic imaging with soft x-ray spectroholography*, Journal of Applied Physics 99 (2006) p. 08H307.

[12] D. Stickler, R. Frömter, H. Stillrich, C. Menk, C. Tieg, S. Streit-nierobisch, M. Sprung, C. Gutt, L.-m. Stadler, O. Leupold, G. Grübel, H. P. Oepen, *Soft x-ray holographic microscopy*, Applied Physics Letters 96 (4) (2010) p. 042501.

[13] S. Streit-Nierobisch, D. Stickler, C. Gutt, L.-M. Stadler, H. Stillrich, C. Menk, R. Fromter, C. Tieg, O. Leupold, H. P. Oepen, G. Grubel, *Magnetic soft x-ray holography study of focused ion beam-patterned Co/Pt multilayers*, Journal of Applied Physics 106 (8) (2009) p. 083909.

[14] C. Tieg, E. Jimenez, J. Camarero, J. Vogel, C. Arm, B. Rodmacq, E. Gautier, S. Auffret, B. Delaup, G. Gaudin, B. Dieny, R. Miranda, *Imaging and quantifying perpendicular exchange biased systems by soft x-ray holography and spectroscopy*, Applied Physics Letters 96 (7) (2010) p. 072503.

[15] A. Scherz, W. F. Schlotter, K. Chen, R. Rick, J. Stöhr, J. Luning, I. McNulty, C. Gunther, F. Radu, W. Eberhardt, O. Hellwig, S. Eisebitt, *Phase imaging of magnetic nanostructures using resonant soft x-ray holography*, Physical Review B 76 (21) (2007) p. 214410(5).

[16] T. Hauet, C. Günther, B. Pfau, M. Schabes, J.-U. Thiele, R. Rick, P. Fischer, S. Eisebitt, O. Hellwig, *Direct observation of field and temperature induced domain replication in dipolar coupled perpendicular anisotropy films*, Physical Review B 77 (18) (2008) p. 184421.

[17] O. Hellwig, C. M. Gunther, F. Radu, A. Menzel, W. F. Schlotter, J. Luning, S. Eisebitt, *Ferrimagnetic stripe domain formation in antiferromagnetically-coupled Co/PtCo/NiCo/Pt multilayers studied via soft x-ray techniques*, Applied Physics Letters 98 (17) (2011) p. 172503.

[18] M. Kläui, *personal communications* (2012).

[19] F. Buttner, M. Schneider, C. M. Gunther, F. Vaz, L. Bert, D. Berger, M. Kläui, S. Eisebitt, *Automatable sample fabrication process for pump-probe X-ray holographic imaging*, Optics express 21 (25) (2013) p. 30563–30572.

[20] M. Sacchi, H. Popescu, N. Jaouen, M. Tortarolo, F. Fortuna, R. Delaunay, C. Spezzani, *Magnetic imaging by Fourier transform holography using linearly polarized x-rays.*, Optics express 20 (9) (2012) p. 9769–9776.

[21] S. Flewett, C. M. Günther, C. V. K. Schmising, B. Pfau, J. Mohanty, F. Büttner, M. Riemeier, M. Hantschmann, M. Kläui, S. Eisebitt, *Holographically aided iterative phase retrieval.*, Optics express 20 (28) (2012) p. 29210–6.

[22] T. Wang, D. Zhu, B. Wu, C. Graves, S. Schaffert, T. Rander, L. Müller, B. Vodungbo, C. Baumier, D. Bernstein, B. Bräuer, V. Cros, S. de Jong, R. Delaunay, A. Fognini, R. Kukreja, S. Lee, V. López-Flores, J. Mohanty, B. Pfau, H. Popescu, M. Sacchi, A. Sardinha, F. Sirotti, P. Zeitoun, M. Messerschmidt, J. Turner, W. Schlotter, O. Hellwig, R. Mattana, N. Jaouen, F. Fortuna, Y. Acremann, C. Gutt, H. Dürr, E. Beaurepaire, C. Boeglin, S. Eisebitt, G. Grübel, J. Lüning, J. Stöhr, A. Scherz, *Femtosecond Single-Shot Imaging of Nanoscale Ferromagnetic Order in Co/Pd Multilayers Using Resonant X-Ray Holography*, Physical Review Letters 108 (26) (2012) p. 267403.

[23] C. Tieg, R. Frömter, D. Stickler, S. Hankemeier, A. Kobs, S. Streit-nierobisch, C. Gutt, G. Grübel, H. P. Oepen, *Imaging the in-plane magnetization in a Co microstructure by Fourier transform holography.*, Optics express 18 (26) (2010) p. 27251.

[24] S. D. Bader, *Magnetism in low dimensionality*, Surface Science 500 (13) (2002) p. 172–188.

[25] A. B. Smith, *Bubble-domain Memory Devices*, Dedham, Mass: Artech House, 1974.

[26] T. H. O'Dell, *Magnetic bubbles*, Wiley; First Edition edition, 1974.

[27] T. H. O'Dell, *Magnetic bubble domain devices*, Reports on Progress in Physics 49 (1986) p. 589–620.

[28] M. Julliere, *Tunneling between ferromagnetic films*, Physics Letters A 54 (3) (1975) p. 225–226.

[29] J. Moodera, L. Kinder, T. Wong, R. Meservey, *Large magnetoresistance at room temperature in ferromagnetic thin film tunnel junctions*, Physical Review Letters.

[30] T. Miyazaki, N. Tezuka, *Giant magnetic tunneling effect in Fe/Al2O3/Fe junction*, Journal of Magnetism and Magnetic Materials 139 (3) (1995) p. L231 – L234.

[31] L. Berger, *Emission of spin waves by a magnetic multilayer traversed by a current*, Phys. Rev. B 54 (13) (1996) p. 9353–9358.

[32] J. Slonczewski, *Current-driven excitation of magnetic multilayers*, Journal of Magnetism and Magnetic Materials 159 (1-2) (1996) p. L1–L7.

[33] D. C. Ralph, M. D. Stiles, *Spin transfer torques*, Journal of Magnetism and Magnetic Materials 320 (7) (2008) p. 1190–1216.

[34] A. Slavin, *Microwave sources: Spin-torque oscillators get in phase*, Nat Nano 4 (8) (2009) p. 479–480.

[35] A. Brataas, K. M. D. Hals, *Spin-orbit torques in action*, Nat Nano 9 (2) (2014) p. 86–88.

[36] J. A. Katine, E. E. Fullerton, *Device implications of spin-transfer torques*, Journal of Magnetism and Magnetic Materials 320 (7) (2008) p. 1217–1226.

[37] S. K. Sinha, E. B. Sirota, S. Garoff, H. B. Stanley, *X-ray and neutron scattering from rough surfaces*, Phys. Rev. B 38 (4) (1988) p. 2297–2311.

[38] G. van der Laan, *Soft X-ray resonant magnetic scattering of magnetic nanostructures*, Comptes Rendus Physique 9 (5-6) (2008) p. 570–584.

[39] M. Sacchi, C. F. Hague, L. Pasquali, A. Mirone, J.-M. Mariot, P. Isberg, E. M. Gullikson, J. H. Underwood, *Optical Constants of Ferromagnetic Iron via 2p Resonant Magnetic Scattering*, Phys. Rev. Lett. 81 (7) (1998) p. 1521–1524.

[40] T. P. A. Hase, I. Pape, B. K. Tanner, H. Dürr, E. Dudzik, G. van der Laan, C. H. Marrows, B. J. Hickey, *Soft-x-ray resonant magnetic diffuse scattering from strongly coupled Cu/Co multilayers*, Phys. Rev. B 61 (6) (2000) p. R3792—-R3795.

[41] J. F. MacKay, C. Teichert, D. E. Savage, M. G. Lagally, *Element Specific Magnetization of Buried Interfaces Probed by Diffuse X-Ray Resonant Magnetic Scattering*, Phys. Rev. Lett. 77 (18) (1996) p. 3925–3928.

[42] B. T. Thole, G. van der Laan, G. A. Sawatzky, *Strong Magnetic Dichroism Predicted in the M4,5 X-Ray Absorption Spectra of Magnetic Rare-Earth Materials*, Phys. Rev. Lett. 55 (19) (1985) p. 2086–2088.

[43] G. van der Laan, B. T. Thole, G. A. Sawatzky, J. B. Goedkoop, J. C. Fuggle, J.-M. Esteva, R. Karnatak, J. P. Remeika, H. A. Dabkowska, *Experimental proof of magnetic x-ray dichroism*, Phys. Rev. B 34 (9) (1986) p. 6529–6531.

[44] J. Stöhr, Y. Wu, B. D. Hermsmeier, M. G. Samant, G. Harp, S. Koranda, D. Dunham, B. P. Tonner, *Stohr1993.pdf*, Science 259 (1993) p. 658–661.

[45] J. Stöhr, S. Jose, H. A. Padmore, S. Anders, T. Stammler, A. L. Source, L. Berkeley, M. R. Scheinfein, *PRINCIPLES OF X-RAY MAGNETIC*, surface review 5 (6) (1998) p. 1297–1308.

[46] H. A. Dürr, E. Dudzik, S. S. Dhesi, J. B. Goedkoop, G. van der Laan, M. Belakhovsky, C. Mocuta, A. Marty, Y. Samson, *CHIRAL MAGNETIC DOMAIN STRUCTURES IN ULTRATHIN FEPD FILMS*, Science 284 (5423) (1999) p. 2166–2168.

[47] K. Chesnel, M. Belakhovsky, S. Landis, B. Rodmacq, E. Dudzik, S. P. Collins, S. S. Dhesi, G. der Laan, *Magnetic coupling in Co/Pt multilayers studied by soft X-ray resonant magnetic scattering*, Magnetics, IEEE Transactions on 37 (4) (2001) p. 1661–1663.

[48] K. Chesnel, M. Belakhovsky, S. Landis, J. Toussaint, S. Collins, G. van der Laan, E. Dudzik, S. Dhesi, *X-ray resonant magnetic scattering study of the magnetic coupling in Co/Pt nanolines and its evolution under magnetic field*, Physical Review B 66 (2) (2002) p. 024435.

[49] K. Chesnel, E. E. Fullerton, M. J. Carey, J. B. Kortright, S. D. Kevan, *Magnetic memory in ferromagnetic thin films via exchange coupling*, Phys. Rev. B 78 (13) (2008) p. 132409.

[50] K. Chesnel, M. Belakhovsky, G. van der Laan, F. Livet, A. Marty, G. Beutier, S. P. Collins, A. Haznar, *Tracking the local reversal processes in nanostructures by magnetic speckles*, Phys. Rev. B 70 (18) (2004) p. 180402.

[51] G. Beutier, A. Marty, F. Livet, G. van der Laan, S. Stanescu, P. Bencok, *Soft X-ray coherent scattering: instrument and methods at ESRF ID08.*, The Review of scientific instruments 78 (9) (2007) p. 093901.

[52] G. Beutier, G. van der Laan, A. Marty, F. Livet, *Back-illuminated CCD for coherent soft X-ray imaging*, The European Physical Journal - Applied Physics 42 (02) (2008) p. 161–167.

[53] G. Beutier, A. Marty, K. Chesnel, M. Belakhovsky, J.-c. Toussaint, B. Gilles, G. V. D. Laan, S. Collins, E. Dudzik, *Soft X-ray resonant magnetic scattering from FePd thin films : a study of the micromagnetic components*, Physica B 345 (2003) p. 143–147.

[54] M. S. Pierce, R. G. Moore, L. B. Sorensen, S. D. Kevan, O. Hellwig, E. E. Fullerton, J. B. Kortright, *Quasistatic X-Ray Speckle Metrology of Microscopic Magnetic Return-Point Memory*, Phys. Rev. Lett. 90 (17) (2003) p. 175502.

[55] M. S. Pierce, C. R. Buechler, L. B. Sorensen, J. J. Turner, S. D. Kevan, E. A. Jagla, J. M. Deutsch, T. Mai, O. Narayan, J. E. Davies, K. Liu, J. H. Dunn, K. M. Chesnel, J. B. Kortright, O. Hellwig, E. E. Fullerton., *Disorder-Induced Microscopic Magnetic Memory*, Phys. Rev. Lett. 94 (1) (2005) p. 17202.

[56] M. S. Pierce, C. R. Buechler, L. B. Sorensen, S. D. Kevan, E. A. Jagla, J. M. Deutsch, T. Mai, O. Narayan, J. E. Davies, K. Liu, G. T. Zimanyi, H. G. Katzgraber, O. Hellwig, E. E. Fullerton, P. Fischer, J. B. Kortright, *Disorder-induced magnetic memory: Experiments and theories*, Phys. Rev. B 75 (14) (2007) p. 144406.

[57] C. J. Kinane, A. K. Suszka, C. H. Marrows, B. J. Hickey, T. R. Charlton, S. Langridge, *Soft x-ray resonant magnetic scattering from an imprinted magnetic*, Notes (2006) p. 23–25.

[58] S. Eisebitt, M. Lörgen, W. Eberhardt, J. Luning, J. Stöhr, E. E. Fullerton, C. T. Rettner, O. Hellwig, G. Denbeaux, *Polarization effects in coherent scattering from magnetic specimen : Implications for x-ray holography , lensless imaging , and correlation spectroscopy*, Physical Review B 68 (2003) p. 104419.

[59] I. McNulty, J. Kirz, C. Jacobsen, E. H. Anderson, M. R. Howells, D. P. Kern, *High-Resolution Imaging by Fourier Transform X-ray Holography*, Science 256 (5059) (1992) p. 1009–1012.

[60] J. R. Fienup, *Phase retrieval algorithms: a comparison*, Appl. Opt. 21 (15) (1982) p. 2758–2769.

[61] J. R. Fienup, *Phase-retrieval algorithms for a complicated optical system*, Applied Optics 32 (10) (1993) p. 1737–1746.

[62] J. Miao, P. Charalambous, J. Kirz, D. Sayre, *Extending the methodology of X-ray crystallography to allow imaging of micrometre-sized non-crystalline specimens*, Nature 400 (1999) p. 342–344.

[63] J. E. TREBES, S. B. BROWN, E. M. CAMPBELL, D. L. MATTHEWS, D. G. NILSON, G. F. STONE, D. A. WHELAN, *Demonstration of X-ray Holography with an X-ray Laser*, Science 238 (4826) (1987) p. 517–519.

[64] I. K. Robinson, I. A. Vartanyants, G. J. Williams, M. A. Pfeifer, J. A. Pitney, *Reconstruction of the Shapes of Gold Nanocrystals Using Coherent X-Ray Diffraction*, Phys. Rev. Lett. 87 (19) (2001) p. 195505. `http://link.aps.org/doi/10.1103/PhysRevLett.87.195505`

[65] E. H. Anderson, K. O. Hodgson, *Phase retrieval of diffraction patterns from noncrystalline samples using the oversampling method*, Physical Review B (2003) p. 1–6.

[66] J. J. Turner, X. Huang, O. Krupin, K. a. Seu, D. Parks, S. Kevan, E. Lima, K. Kisslinger, I. McNulty, R. Gambino, S. Mangin, S. Roy, P. Fischer, *X-Ray Diffraction Microscopy of Magnetic Structures*, Physical Review Letters 107 (3) (2011) p. 033904.

[67] J. R. Fienup, *Reconstruction of a complex-valued object from the modulus of its Fourier transform using a support constraint*, J. Opt. Soc. Am. A 4 (1) (1987) p. 118–123.

[68] H. He, S. Marchesini, M. Howells, U. Weierstall, G. Hembree, J. C. H. Spence, *Experimental lensless soft-X-ray imaging using iterative algorithms: phasing diffuse scattering*, Acta Cryst. A 59 (2003) p. 143–152.

[69] D. Zhu, B. Wu, R. Rick, J. Stöhr, A. Scherz, *Phase retrieval in x-ray lensless holography by reference beam tuning*, Optics Letters 34 (17) (2009) p. 2604–2606.

[70] A. Scherz, D. Zhu, R. Rick, W. F. Schlotter, S. Roy, J. Lüning, J. Stöhr, *Nanoscale Imaging with Resonant Coherent X˜Rays: Extension of Multiple-Wavelength Anomalous Diffraction to Nonperiodic Structures*, Phys. Rev. Lett. 101 (7) (2008) p. 76101.

[71] S. Marchesini, H. N. Chapman, R. A. London, A. Szoke, *Coherent X-ray diffractive imaging : applications and limitations*, Optics express 11 (19) (2003) p. 2344–2353.

[72] C. M. Günther, O. Hellwig, A. Menzel, B. Pfau, F. Radu, D. Makarov, M. Albrecht, A. Goncharov, T. Schrefl, W. F. Schlotter, R. Rick, J. Lüning, S. Eisebitt, *Microscopic reversal behavior of magnetically capped nanospheres*, Physical Review B 81 (2010) p. 06441.

[73] B. Pfau, C. M. Gunther, E. Guehrs, T. Hauet, H. Yang, L. Vinh, X. Xu, D. Yaney, R. Rick, S. Eisebitt, O. Hellwig, *Origin of magnetic switching field distribution in bit patterned media based on pre-patterned substrates*, Applied Physics Letters 99 (6) (2011) p. 062502.

[74] J. Stöhr, S. Anders, *X-ray specto-microscopy of complex materials and surfaces*, IBM Journal of Research and Development 44 (4) (2000) p. 535–551.

[75] C. Tsang, N. Heiman, K. Lee, *Exchange induced unidirectional anisotropy at FeMnNi80Fe20 interfaces*, Journal of Applied Physics 52 (3).

[76] J. M. Daughton, *Magnetoresistive memory technology*, Thin Solid Films 216 (1) (1992) p. 162–168.

[77] W. H. Meiklejohn, C. P. Bean, *New Magnetic Anisotropy*, Phys. Rev. 102 (5) (1956) p. 1413–1414.

[78] J. Camarero, J. Sort, A. Hoffmann, J. M. Garc\'\ia-Mart\'\in, B. Dieny, R. Miranda, J. Nogués, *Origin of the Asymmetric Magnetization Reversal Behavior in Exchange-Biased Systems: Competing Anisotropies*, Phys. Rev. Lett. 95 (5) (2005) p. 57204.

[79] F. Romanens, S. Pizzini, F. Yokaichiya, M. Bonfim, Y. Pennec, J. Camarero, J. Vogel, J. Sort, F. Garcia, B. Rodmacq, B. Dieny, *Magnetic relaxation of exchange biased PtCo multilayers studied by time-resolved Kerr microscopy*, Phys. Rev. B 72 (13) (2005) p. 134410.

[80] H. Search, C. Journals, A. Contact, M. Iopscience, I. P. Address, *Overcoming the field-of-view restrictions in soft x-ray holographic imaging*, Journal of Physysics: Conference Series 211 (2010) p. 012024.

[81] W. F. Schlotter, R. Rick, K. Chen, *Multiple reference Fourier transform holography with soft x-rays*, Applied Physics Letters 89 (16) (2006) p. 163112.

[82] S. Marchesini, S. Boutet, A. E. Sakdinawat, M. J. Bogan, S. Bajt, A. Barty, H. N. Chapman, M. Frank, S. P. Hau-riege, Szoke Abraham, C. Cui, D. A. Shapiro, M. R. Howells, J. C. H. Spence, J. W. Shaevitz, J. Y. Lee, J. Hajdu, M. M. Seibert, *Massively parallel X-ray holography*, Nature Photonics Letters 2 (September) (2008) p. 3–6.

[83] B. Pfau, R. Mitzner, B. Siemer, S. Roling, H. Zacharias, O. Kutz, I. Rudolph, C. M. Gu, D. Schondelmaier, R. Treusch, S. Eisebitt, *Sequential femtosecond X-ray imaging*, Nature Photonics 5 (February) (2011) p. 99–102.

[84] S. Flewett, S. Schaffert, J. Mohanty, E. Guehrs, J. Geilhufe, C. Günther, B. Pfau, S. Eisebitt, *Method for Single-Shot Coherent Diffractive Imaging of Magnetic Domains*, Physical Review Letters 108 (22) (2012) p. 223902.

[85] Y. Nishino, Y. Tanaka, M. Okada, M. Okaya, Y. Uozaki, K. Nozaki, M. Yabashi, M. Nagasono, K. Tono, H. Kimura, H. Ohashi, S. Matsui, T. Ishikawa, E. Matsubara, *Femtosecond Snapshot Holography with Extended Reference Using Extreme Ultraviolet Free-Electron Laser*, Applied Physics Express 3 (10) (2010) p. 102701.

[86] B. Pfau, C. M. Günther, S. Schaffert, R. Mitzner, B. Siemer, S. Roling, H. Zacharias, O. Kutz, I. Rudolph, R. Treusch, S. Eisebitt, *Femtosecond*

pulse x-ray imaging with a large field of view, New Journal of Physics 12 (9) (2010) p. 095006.

[87] C. Gutt, L. Stadler, A. P. Mancuso, A. Schropp, B. Pfau, C. M. Günther, R. Könnecke, J. Gulden, B. Reime, J. Feldhaus, E. Weckert, I. A. Vartanyants, O. Hellwig, F. Staier, R. Barth, M. Grunze, A. Rosenhahn, D. Stickler, H. Stillrich, R. Frömter, H. P. Oepen, M. Martins, T. Nisius, T. Wilhein, B. Faatz, N. Guerassimova, K. Honkavaara, V. Kocharyan, R. Treusch, E. Saldin, S. Schreiber, E. A. Schneidmiller, M. V. Yurkov, S. Eisebitt, G. Grübel, *Resonant magnetic scattering with soft x-ray pulses from a free-electron laser operating at 1 . 59 nm*, Physical Review B 79 (2009) p. 212406.

[88] B. Pfau, C. M. Günther, R. Könnecke, E. Guehrs, O. Hellwig, W. F. Schlotter, S. Eisebitt, *Magnetic imaging at linearly polarized x-ray sources.*, Optics express 18 (13) (2010) p. 13608–15.

[89] W. F. Schlotter, J. J. Turner, M. Rowen, P. Heimann, M. Holmes, O. Krupin, M. Messerschmidt, S. Moeller, J. Krzywinski, R. Soufli, M. Fernández-Perea, N. Kelez, S. Lee, R. Coffee, G. Hays, M. Beye, N. Gerken, F. Sorgenfrei, S. Hau-Riege, L. Juha, J. Chalupsky, V. Hajkova, a. P. Mancuso, A. Singer, O. Yefanov, I. a. Vartanyants, G. Cadenazzi, B. Abbey, K. a. Nugent, H. Sinn, J. Lüning, S. Schaffert, S. Eisebitt, W.-S. Lee, A. Scherz, a. R. Nilsson, W. Wurth, *The soft x-ray instrument for materials studies at the linac coherent light source x-ray free-electron laser.*, The Review of scientific instruments 83 (4) (2012) p. 043107.

[90] P. C. Mehta, Chander Bhan, R. Hyadaynath, *Multiple imaging by lensless Fourier transform holography*, Journal of Optics (paris) 10 (3) (1979) p. 133–136.

[91] S. G. Podorov, K. M. Pavlov, D. M. Paganin, *A non-iterative reconstruction method for direct and unambiguous coherent diffractive imaging*, Optics Express 15 (16) (2007) p. 9954–9962.

[92] S. G. Podorov, A. I. Bishop, D. M. Paganin, K. M. Pavlov, *Mask-assisted deterministic phase-amplitude retrieval from a single far-field intensity diffraction pattern: two experimental proofs of principle using visible light*, Ultramicroscopy 111 (7) (2011) p. 782–787.

[93] M. Guizar-sicairos, J. R. Fienup, *Holography with extended reference by autocorrelation linear differential operation*, Optics Express 15 (26) (2007) p. 17592–17612.

[94] M. Guizar-sicairos, J. R. Fienup, *Direct image reconstruction from a Fourier intensity pattern using HERALDO*, Optics Letters 33 (22) (2008) p. 2668–2670.

[95] D. Zhu, M. Guizar-Sicairos, B. Wu, A. Scherz, Y. Acremann, T. Tyliszczak, P. Fischer, N. Friedenberger, K. Ollefs, M. Farle, J. Fienup, J. Stöhr, *High-Resolution X-Ray Lensless Imaging by Differential Holographic Encoding*, Physical Review Letters 105 (4) (2010) p. 043901.

[96] M. Guizar-sicairos, D. Zhu, J. R. Fienup, B. Wu, A. Scherz, J. Stöhr, *The application of differential and integral operators*, Optics Letters 35 (7) (2010) p. 928–930.

[97] D. Gauthier, M. Guizar-sicairos, X. Ge, W. Boutu, B. Carré, J. R. Fienup, H. Merdji, *Single-shot Femtosecond X-Ray Holography Using Extended References*, Physical Review Letters 105 (9) (2010) p. 1–4.

[98] J. Camarero, E. Jimenez, J. Vogel, C. Tieg, P. Perna, A. Bollero, F. Yakhou-Harris, C. Arm, B. Rodmacq, E. Gautier, S. Auffret, B. Delaup, G. Gaudin, B. Dieny, R. Miranda, *Exploring the limits of soft x-ray magnetic holography: Imaging magnetization reversal of buried interfaces (invited)*, Journal of Applied Physics 109 (7) (2011) p. 07D357.

[99] P. Langevin, *Magnétisme et théorie des électrons. (Magnetism and the theory of electrons)*, Annales de chimie et de physique (8) 5 (1905) p. 70–127.

[100] P. Weiss, *L'hypothése du champ moléculaire et la propriété ferromagnétique (The hypothesis of the molecular field and the property of ferromagnetism)*, Journal de Physique Radium 6 (1907) p. 661–690.

[101] L. D. Landau, E. Lifshitz, *On the theory of the dispersion of magnetic permeability in ferromagnetic bodies*, Physikalische Zeitschrift der Sowjetunion 8 (1935) p. 153–169.

[102] A. Hubert, R. Schäfer, *Magnetic Domains*, Springer, 2000.

[103] A. Aharoni, *Introduction to the Theory of Ferromagnetism*, Vol. 50, Oxford Science Publications, 1997.

[104] R. C. O'Handley, *Modern Magnetic Materials: Principles and Applications*, John Wiley and Sons, Inc., 2000.

[105] J. Stöhr, *Exploring the microscopic origin of magnetic anisotropies with X-ray magnetic circular dichroism (XMCD) spectroscopy*, Journal of Magnetism and Magnetic Materials 200 (13) (1999) p. 470–497.

[106] T. O. Paine, L. I. Mendelsohn, F. E. Luborsky, *Effect of Shape Anisotropy on the Coercive Force of Elongated Single-Magnetic-Domain Iron Particles*, Phys. Rev. 100 (4) (1955) p. 1055–1059.

[107] J. A. Osborn, *Demagnetizing Factors of the General Ellipsoid*, Physical Review 67 (11) (1945) p. 351–357.

[108] J. H. Van Vleck, *A Survey of the Theory of Ferromagnetism*, Rev. Mod. Phys. 17 (1) (1945) p. 27–47.

[109] A. Aharoni, *Demagnetizing factors for rectangular ferromagnetic prisms*, Journal of Applied Physics 83 (6) (1998) p. 3432–3434.

[110] R. M. Bozorth, D. M. Chapin, *Demagnetizing Factors of Rods*, Journal of Applied Physics 13 (5) (1942) p. 320–326.

[111] R. I. Joseph, E. Schlömann, *Demagnetizing Field in Nonellipsoidal Bodies*, Journal of Applied Physics 36 (5) (1965) p. 1579–1593.

[112] L. Landau, E. Lifshits, *ON THE THEORY OF THE DISPERSION OF MAGNETIC PERMEABILITY IN FERROMAGNETIC BODIES*, Phys. Zeitsch. der Sow. 8 (14) (1935) p. 153–169.

[113] T. L. Gilbert, *A phenomenological theory of damping in ferromagnetic materials*, Magnetics, IEEE Transactions on 40 (6) (2004) p. 3443–3449.

[114] C. Kittel, *Theory of the Structure of Ferromagnetic Domains in Films and Small Particles*, Phys. Rev. 70 (11-12) (1946) p. 965–971.

[115] C. Kittel, *Physical Theory of Ferromagnetic Domains*, Rev. Mod. Phys. 21 (4) (1949) p. 541–583.

[116] Z. Huang, *High Accuracy Numerical Method of Thin-Film Problems in Micromagnetics*, Journal of Computational Mathematics 21 (1) (2003) p. 33–40.

[117] C. Schneider, O. de Haas, D. Tietjen, U. Muschiol, N. Cramer, Z. Celinski, A. Oelsner, M. Klais, C. Ziethen, O. Schmist, G. Schönhense, N. Zema, S. Zennaro, *Size dependence of magnetic domain patterns in exchange-biased Permalloy/NiO microstructures*, Journal of Physics D: Applied Physics 35 (20) (2002) p. 2472–2478.

[118] A. Subramani, D. Geerpuram, A. Domanowski, V. Baskaran, V. Metlushko, *Vortex state in magnetic rings*, Physica C: Superconductivity 404 (1-4) (2004) p. 241–245.

[119] A. Hubert, *Theorie der Domänenwände in Geordneten Medien (Theory of Domain Walls in Ordered Media)*, Springer Berlin Heidelberg, 1974.

[120] B. A. Lilley, *Energies and widths of domain boundaries in ferromagnets*, Philosophical Magazine 41 (1950) p. 792–813.

[121] S. Rohart, *Basic concepts on magnetisation reversal: magnetic field and temperature influence, Lecture* (2011).

[122] L. Néel, *Énergie des parois de Bloch dans les couches minces (Bloch wall energy in thin films)*, Comptes Rendus de l'Académie des Sciences 241 (1955) p. 533–536.

[123] F. B. Humphrey, M. Redjdal, *Domain walls in nano-thin permalloy films*, physica status solidi (a) 201 (8) (2004) p. 1771–1776.

[124] J. C. Slonczewski, *Theory of domain wall motion in magnetic films and platelets*, Journal of Applied Physics 44 (4) (1973) p. 1759–1770.

[125] I. K. Schuller, S. Kim, C. Leighton, *Magnetic superlattices and multilayers*, Journal of Magnetism and Magnetic Materials 200 (February) (1999) p. 571–582.

[126] R. Wu, A. J. Freeman, *Recent Progress in First Principles Investigations of Magnetism of Surfaces and Thin Films*, in: Magnetism in Metals, Kongelige Danske Videnskabernes Selskab, 1997, Ch. Rare earth, pp. 133–148.

[127] D. Weller, Y. Wu, J. Stöhr, M. Samant, B. Hermsmeier, C. Chappert, *Orbital magnetic moments of Co in multilayers with perpendicular magnetic anisotropy*, Physical review. B, Condensed matter 49 (18) (1994) p. 12888–12896.

[128] W. B. Zeper, F. J. a. M. Greidanus, P. F. Carcia, C. R. Fincher, *Perpendicular magnetic anisotropy and magneto-optical Kerr effect of vapor-deposited Co/Pt-layered structures*, Journal of Applied Physics 65 (12) (1989) p. 4971.

[129] S. Uba, L. Uba, A. Yaresko, A. Perlov, V. Antonov, R. Gontarz, *Optical and magneto-optical properties of Co/Pt multilayers*, Physical review. B, Condensed matter 53 (10) (1996) p. 6526–6535.

[130] K. Sato, H. Ikekame, Y. Tosaka, K. Tsuzukiyama, Y. Togami, M. Fujisawa, *Fundamental studies and application of short-wavelength magneto-optical effect in Pt-based multilayers*, Journal of Magnetism and Magnetic Materials 126 (1-3) (1993) p. 572–576.

[131] Y. Ochiai, S. Hashimoto, K. Aso, *Co/Pt and Co/Pd ultrathin-multilayered films as new magneto-optical recording materials*, Magnetics, IEEE Transactions on 25 (5) (1989) p. 3755–3757.

[132] A. Rahmim, *Analysis of coherent resonant x-ray scattering and reconstruction of magnetic domains*, Ph.D. thesis, The University of British Columbia (1999).

[133] X. M. Cheng, V. I. Nikitenko, a. J. Shapiro, R. D. Shull, C. L. Chien, *Unusual magnetization reversal in [CoPt][sub 4] multilayers with perpendicular anisotropy*, Journal of Applied Physics 99 (8) (2006) p. 08C905.

[134] C. Bran, A. B. Butenko, N. S. Kiselev, U. Wolff, L. Schultz, O. Hellwig, U. K. Rö\ssler, A. N. Bogdanov, V. Neu, *Evolution of stripe and bubble domains in antiferromagnetically coupled [(Co/Pt)8/Co/Ru]18 multilayers*, Phys. Rev. B 79 (2) (2009) p. 24430.

[135] J. Choi, J. Wu, C. Won, Y. Z. Wu, A. Scholl, A. Doran, T. Owens, Z. Q. Qiu, *Magnetic Bubble Domain Phase at the Spin Reorientation Transition of Ultrathin Fe/Ni/Cu(001) Film*, Phys. Rev. Lett. 98 (20) (2007) p. 207205.

[136] V. Karoutsos, P. Poulopoulos, M. Angelakeris, E. T. Papaioannou, *Magnetic Force Microscopy on Co / Pt multilayers*, Solid State Phenomena 152 (2009) p. 241–244.

[137] P. Fischer, M.-Y. Im, S. Kasai, K. Yamada, T. Ono, A. Thiaville, *X-ray imaging of vortex cores in confined magnetic structures*, Physical Review B 83 (21) (2011) p. 212402.

[138] K. W. Chou, A. Puzic, H. Stoll, D. Dolgos, G. Schutz, B. Van Waeyenberge, A. Vansteenkiste, T. Tyliszczak, G. Woltersdorf, C. H. Back, *Direct observation of the vortex core magnetization and its dynamics*, Applied Physics Letters 90 (20) (2007) p. 202505.

[139] R. Antos, Y. Otani, *Simulations of the dynamic switching of vortex chirality in magnetic nanodisks by a uniform field pulse*, Phys. Rev. B 80 (14) (2009) p. 140404.

[140] S. Bohlens, B. Krüger, A. Drews, M. Bolte, G. Meier, D. Pfannkuche, *Current controlled random-access memory based on magnetic vortex handedness*, Applied Physics Letters 93 (14) (2008) p. 142508.

[141] K. Nakano, D. Chiba, N. Ohshima, S. Kasai, T. Sato, Y. Nakatani, K. Sekiguchi, K. Kobayashi, T. Ono, *All-electrical operation of magnetic vortex core memory cell*, Applied Physics Letters 99 (26) (2011) p. 262505.

[142] N. Kikuchi, S. Okamoto, O. Kitakami, Y. Shimada, S. G. Kim, Y. Otani, K. Fukamichi, *Vertical bistable switching of spin vortex in a circular magnetic dot*, Journal of Applied Physics 90 (12) (2001) p. Kikuchi2001.

[143] K. Yamada, S. Kasai, Y. Nakatani, K. Kobayashi, H. Kohno, A. Thiaville, T. Ono, *Electrical switching of the vortex core in a magnetic disk*, Nat Mater 6 (4) (2007) p. 270–273.

[144] M. Curcic, B. Van Waeyenberge, A. Vansteenkiste, M. Weigand, V. Sackmann, H. Stoll, M. Fähnle, T. Tyliszczak, G. Woltersdorf, C. H. Back, G. Schütz, *Polarization Selective Magnetic Vortex Dynamics and Core Reversal in Rotating Magnetic Fields*, Physical Review Letters 101 (19) (2008) p. 197204.

[145] A. N. Bogdanov, U. K. Rössler, *Chiral Symmetry Breaking in Magnetic Thin Films and Multilayers*, Phys. Rev. Lett. 87 (3) (2001) p. 37203.

[146] M. Faraday, *On the Magnetization of Light and the Illumination of Magnetic Lines of Force*, Philosophical Transactions of the Royal Society London 136 (1846) p. 1–20.

[147] J. Kerr, *On rotation of the plane of polarization by reflection from the pole of a magnet*, Philosophical Magazine (5) 3 (1877) p. 321–343.

[148] H. Williams, F. Foster, E. Wood, *Observation of magnetic domains by the Kerr effect*, Physical Review 82 (1951) p. 119–120.

[149] C. Fowler, E. Fryer, *Magnetic domains on silicon iron by the longitudinal Kerr effect*, Physical Review 86 (1952) p. 426.

[150] H. Ebert, *Magneto-optical effects in transition metal systems*, Reports on Progress in Physics 59 (1996) p. 1665–1735.

[151] F. Schmidt, A. Hubert, *Domain observations on CoCr layers with a digitally enhanced Kerr microscope.*, Journal of Magnetism and Magnetic Materials 61 (1986) p. 307–320.

[152] R. L. Conger, G. H. Moore, *Direct Observation of HighSpeed Magnetization Reversal in Films*, Journal of Applied Physics 34 (4).

[153] R. J. Hicken, J. Wu, *Observation of ferromagnetic resonance in the time domain*, Journal of Applied Physics 85 (8).

[154] P. S. Keatley, V. V. Kruglyak, P. Gangmei, R. J. Hicken, *Ultrafast Magnetisation Dynamics of Spintronic Nanostructures*, Philosophical Transactions A: Mathematical, Physical and Engineering Sciences 369 (1948) (2011) p. 3115–3135.

[155] P. Keatley, V. Kruglyak, A. Neudert, E. Galaktionov, R. Hicken, J. Childress, J. Katine, *Time-resolved investigation of magnetization dynamics of arrays of nonellipsoidal nanomagnets with nonuniform ground states*, Physical Review B 78 (21) (2008) p. 214412.

[156] E. Beaurepaire, J.-C. Merle, A. Daunois, J.-Y. Bigot, *Ultrafast Spin Dynamics in Ferromagnetic Nickel*, Phys. Rev. Lett. 76 (22) (1996) p. 4250–4253.

[157] M. R. Freeman, R. R. Ruf, R. J. Gambino, *Picosecond pulsed magnetic fields for studies of ultrafast magnetic phenomena*, Magnetics, IEEE Transactions on 27 (6) (1991) p. 4840–4842.

[158] W. K. Hiebert, A. Stankiewicz, M. R. Freeman, *Direct Observation of Magnetic Relaxation in a Small Permalloy Disk by Time-Resolved Scanning Kerr Microscopy*, Phys. Rev. Lett. 79 (6) (1997) p. 1134–1137.

[159] M. R. Freeman, J. F. Smyth, *Picosecond time-resolved magnetization dynamics of thin-film heads*, Journal of Applied Physics 79 (8) (1996) p. 5898–5900.

[160] S. Tamaru, J. A. Bain, R. J. M. van de Veerdonk, T. M. Crawford, M. Covington, M. H. Kryder, *Measurement of magnetostatic mode excitation and relaxation in permalloy films using scanning Kerr imaging*, Phys. Rev. B 70 (10) (2004) p. 104416.

[161] P. S. Keatley, V. V. Kruglyak, A. Neudert, M. Delchini, R. J. Hicken, J. R. Childress, J. a. Katine, *Time- and vector-resolved magneto-optical Kerr effect measurements of large angle precessional reorientation in a 22 μm2 ferromagnet*, Journal of Applied Physics 105 (7) (2009) p. 07D308.

[162] A. Barman, V. V. Kruglyak, R. J. Hicken, A. Kundrotaite, M. Rahman, *Anisotropy, damping, and coherence of magnetization dynamics in a 10 μm square Ni81Fe19 element*, Applied Physics Letters 82 (18) (2003) p. 3065.

[163] H. Hopster, H. P. Oepen, *Magnetic Microscopy of Nanostructures*, Springer Berlin Heidelberg New York, 2005.

[164] M. A. Schofield, M. Beleggia, Y. Zhu, G. Pozzi, *Characterization of {JEOL} 2100F Lorentz-TEM for low-magnification electron holography and magnetic imaging*, Ultramicroscopy 108 (7) (2008) p. 625–634.

[165] S. McVitie, J. N. Chapman, *Reversal Mechanisms in Lithographically Defined Magnetic Thin Film Elements Imaged by Scanning Transmission Electron Microscopy*, Microscopy and Microanalysis 3 (02) (1997) p. 146–153.

[166] A. K. Petford-Long, J. N. Chapman, *Lorentz Microscopy*, in: Magnetic Microscopy of Nanostructures, Springer Berlin Heidelberg, 2005, pp. 67–86.

[167] M. Mankos, M. R. Scheinfein, J. M. Cowley, *Electron Holography and Lorentz Microscopy of Magnetic Materials*, in: P. W. Hawkes (Ed.), Advances in Imaging and Electron Physics, Vol. 98 of *Advances in Imaging and Electron Physics*, Elsevier, 1996, pp. 323–426.

[168] A. Tonomura, *Electron Holography*, Springer Series in Optical Sciences, Springer, 2010.

[169] J. M. Cowley, *Twenty forms of electron holography*, Ultramicroscopy 41 (4) (1992) p. 335–348.

[170] A. Tonomura, *Electron-Holographic Interferometry*, in: Electron Holography, Springer Berlin Heidelberg, 1999, pp. pp 78–132.

[171] R. E. Dunin-Borkowski, T. Kasama, A. Wei, S. L. Tripp, M. J. Hÿtch, E. Snoeck, R. J. Harrison, A. Putnis, *Off-axis electron holography of magnetic nanowires and chains, rings, and planar arrays of magnetic nanoparticles.*, Microscopy research and technique 64 (5-6) (2004) p. 390–402.

[172] T. Kasama, R. E. Dunin-Borkowski, M. Beleggia, *Electron Holography of Magnetic Materials*, in: F. A. M. Ramírez (Ed.), Holography - Different Fields of Application, InTech, 2011, Ch. 3, pp. 53–80.

[173] F. Junginger, M. Klaui, D. Backes, S. Krzyk, U. Rudiger, T. Kasama, R. E. Dunin-Borkowski, J.-M. Feinberg, R. J. Harrison, L. J. Heyderman, *Quantitative determination of vortex core dimensions in head-to-head domain walls using off-axis electron holography*, Applied Physics Letters 92 (11) (2008) p. 112502.

[174] M. Huber, J. Zweck, D. Weiss, *Experimental observation of switching in ferromagnetic nanoscale double disks*, Physical Review B 77 (5) (2008) p. 1–6.

[175] S. D. Pollard, L. Huang, K. S. Buchanan, D. a. Arena, Y. Zhu, *Direct dynamic imaging of non-adiabatic spin torque effects.*, Nature communications 3 (May) (2012) p. 1028.

[176] E. Bauer, *Low energy electron microscopy*, Reports on Progress in Physics 57 (1994) p. 895–938.

[177] E. Bauer, W. Telieps, *Emission and Low Energy Reflection Electron Microscopy*, in: Surface and Interface Characterization by Electron Optical Methods, Springer US, 1988, pp. 195–233.

[178] E. Bauer, T. Duden, H. Pinkvos, H. Poppa, K. Wurm, *LEEM studies of the microstructure and magnetic domain structure of ultrathin films*, Journal of Magnetism and Magnetic Materials 156 (13) (1996) p. 1–6.

[179] E. Bauer, *Spin-polarized low-energy electron microscopy*, in: Handbook of Microscopy, 2nd Edition, VCH, Weinheim, New York, 1997, pp. 751–759.

[180] R. J. Celotta, D. T. Pierce, G. C. Wang, S. D. Bader, G. P. Felcher, *Surface Magnetization of Ferromagnetic Ni(110): A Polarized Low-Energy Electron Diffraction Experiment*, Phys. Rev. Lett. 43 (10) (1979) p. 728–731.

[181] T. Duden, E. Bauer, *Magnetization Wrinkle in Thin Ferromagnetic Films*, Phys. Rev. Lett. 77 (11) (1996) p. 2308–2311.

[182] H. Pinkvos, H. Poppa, E. Bauer, J. Hurst, *Spin-polarized low-energy electron microscopy study of the magnetic microstructure of ultra-thin epitaxial cobalt films on W(110)*, Ultramicroscopy 47 (4) (1992) p. 339–345.

[183] H. Pinkvos, H. Poppa, E. Bauer, G.-M. Kim, *A Time-Resolved Spleem Study of Magnetic Microstructure in Ultrathin Co Films on W(110)*, in: Magnetism and Structure in Systems of Reduced Dimension, Springer US, 1993, pp. 25–31.

[184] E. D. Tober, G. Witte, H. Poppa, *Variable temperature and ex situ spin-polarized low-energy electron microscope*, Journal of Vacuum Science & Technology A 18 (4).

[185] K. Koike, K. Hayakawa, *Observation of magnetic domains with spin-polarized secondary electrons*, Applied Physics Letters 45 (5).

[186] K. Koike, H. Matsuyama, K. Hayakawa, *Spin-Polarized Scanning Electron Microscope Equipped with a Thumb-Size Spin Detector*, Japanese Journal of Applied Physics 27 (7A) (1988) p. L1352.

[187] R. Allenspach, *Spin-polarized scanning electron microscopy*, IBM Journal of Research and Development 44 (4) (2000) p. 553–570.

[188] T. Kohashi, K. Koike, *A Spin-Polarized Scanning Electron Microscope with 5-nm Resolution*, Japanese Journal of Applied Physics 40 (11B) (2001) p. L1264.

[189] S. Hankemeier, R. Frömter, N. Mikuszeit, D. Stickler, H. Stillrich, S. Pütter, E. Vedmedenko, H. Oepen, *Magnetic Ground State of Single and Coupled Permalloy Rectangles*, Physical Review Letters 103 (14) (2009) p. 147204.

[190] M. P. Seah, W. A. Dench, *Quantitative electron spectroscopy of surfaces: A standard data base for electron inelastic mean free paths in solids*, Surface and Interface Analysis 1 (1) (1979) p. 2–11.

[191] M. R. Scheinfein, J. Unguris, M. H. Kelley, D. T. Pierce, R. J. Celotta, *Scanning electron microscopy with polarization analysis (SEMPA)*, Review of Scientific Instruments 61 (1990) p. 2501–2527.

[192] S. Hankemeier, *The Magnetic Fine Structure of Thin-Film Elements*, Ph.D. thesis, Hamburg (2010).

[193] Y. Iwasaki, K. Bessho, J. Kondis, H. Ohmori, H. Hopster, *In-situ observation of magnetization process of soft magnetic films by spin-polarized secondary electron microscopy*, Applied Surface Science 113114 (0) (1997) p. 155–159.

[194] G. Steierl, G. Liu, D. Iorgov, J. Kirschner, *Surface domain imaging in external magnetic fields*, Review of Scientific Instruments 73 (12).

[195] H. Hopster, H. P. Oepen, *SEMPA Studies of Thin Films , Structures , and Exchange Coupled Layers*, in: Magnetic Microscopy of Nanostructures, Springer Berlin Heidelberg New York, 2005, pp. 137–167.

[196] J. Unguris, *Scanning Electron Microscopy with Polarization Analysis (SEMPA) and its Applications*, in: Magnetic Imaging and its Applications to Materials, Academic Press, San Diego, CA, 2000, pp. 167 – 303.

[197] J. Unguris, S.-H. Chung, D. T. Pierce, D. G. Seiler, A. C. Diebold, R. McDonald, C. M. Garner, D. Herr, R. P. Khosla, E. M. Secula, *SEMPA Imaging for Spintronics Applications*, AIP Conference Proceedings 931 (2007) p. 472–476.

[198] Y. Martin, H. K. Wickramasinghe, *Magnetic imaging by force microscopy with 1000 A resolution*, Applied Physics Letters 50 (20) (1987) p. 1455–1457.

[199] J. J. Sáenz, N. García, P. Grütter, E. Meyer, H. Heinzelmann, R. Wiesendanger, L. Rosenthaler, H. R. Hidber, H. Güntherodt, *Observation of magnetic forces by the atomic force microscope*, Journal of Applied Physics 62 (10).

[200] G. Binning, Q. Quate, C. Gerber, *Atomic force microscope*, Phys. Rev. Lett. 56 (1986) p. 930–933.

[201] P. Grutter, H. J. Mamin, D. Rugar, *Magnetic Force Microscopy (MFM)*, in: H.-J. Guntherodt, R. Wiesendanger (Eds.), Scanning Tunneling Microscopy, Springer, Berlin, Heidelberg, New York, 1992, pp. 151–207.

[202] S. Porthun, L. Abelmann, C. Lodder, *Magnetic force microscopy of thin film media for high density magnetic recording*, Journal of Magnetism and Magnetic Materials 182 (12) (1998) p. 238–273.

[203] H. Hopster, H. P. Oepen, *Magnetic Microscopy of Nanostructures*, Springer Berlin Heidelberg New York, 2005.

[204] Q. Zhong, D. Inniss, K. Kjoller, V. Elings, *Fractured polymer/silica fiber surface studied by tapping mode atomic force microscopy*, Surface Science 290 (1-2) (1993) p. L688–L692.

[205] L. Abelmann, A. V. D. Bos, C. Lodder, *Towards higher resolution in Magnetic Force Microscopy*, in: Magnetic Microscopy of Nanostructures, 2005th Edition, Springer, 2005, Ch. 12, pp. 254–283.

[206] L. Abelmann, S. Porthun, M. Haast, C. Lodder, A. Moser, M. E. Best, P. J. A. van Schendel, B. Stiefel, H. J. Hug, G. P. Heydon, A. Farley, S. R. Hoon, T. Pfaffelhuber, R. Proksch, K. Babcock, *Comparing the resolution of magnetic force microscopes using the CAMST reference samples*, Journal of Magnetism and Magnetic Materials 190 (12) (1998) p. 135–147.

[207] E. Betzig, J. K. Trautman, R. Wolfe, E. M. Gyorgy, P. L. Finn, M. H. Kryder, C. Chang, *Near-field magneto-optics and high density data storage*, Applied Physics Letters 61 (2).

[208] S. V. Kalinin, A. Gruverman, *Scanning Probe Microscopy*, in: Electrical and Electromechanical Phenomena at the Nanoscale, Springer, 2007, Ch. Kalinin200.

[209] G. Binnig, H. Rohrer, *Scanning Tunneling Microscopy*, IBM Journal of Research and Development 30 (4).

[210] H. F. Ding, W. Wulfhekel, C. Chen, J. Barthel, J. Kirschner, *A combined magnetic force and spin-polarized scanning tunneling microscopy study of the closure domain pattern of Co(0001)*, Materials Science and Engineering: B 84 (12) (2001) p. 96–101.

[211] S. Y. Yamamoto, S. Schultz, *Scanning magnetoresistance microscopy (SMRM): Imaging with a MR head*, Journal of Applied Physics 81 (8).

[212] B. L. T. Plourde, D. J. Van Harlingen, *design of a scanning Josepson junction microscope for submicron resolution magnetic imaging*, Review of Scientific Instruments 70 (1999) p. 4344–4347.

[213] R. C. Black, A. Mathai, F. C. Wellstood, E. Dantsker, A. H. Miklich, D. T. Nemeth, J. J. Kingston, J. Clarke, *Magnetic microscopy using a liquid nitrogen cooled YBa2Cu3O7 superconducting quantum interference device*, Applied Physics Letters 62 (17).

[214] A. M. Chang, H. D. Hallen, L. Harriott, H. F. Hess, H. L. Kao, J. Kwo, R. E. Miller, R. Wolfe, J. van der Ziel, T. Y. Chang, *Scanning Hall probe microscopy*, Applied Physics Letters 61 (16).

[215] T. Eimuller, *Magnetic imaging of nanostructured systems with Transmission X-ray Microscopy*, Ph.D. thesis, Wurzburg (2002).

[216] H. Hopster, H. P. Oepen, *Scanning Probe Methods for magnetic Imaging*, in: Magnetic Microscopy of Nanostructures, Springer Berlin Heidelberg New York, 2005, pp. 285–307.

[217] G. Schütz, W. Wagner, W. Wilhelm, P. Kienle, R. Zeller, R. Frahm, G. Materlik, *Absorption of Circularly Polarised X-Rays in Iron*, Physical Review Letters 58 (7) (1987) p. 737–740.

[218] J. Stöhr, *X-ray magnetic circular dichroism spectroscopy of transition metal thin films*, Jouenal of Electron Spectroscopy and Related Phenomena 75 (95) (1995) p. 253–272.

[219] U. Fano, *Spin Orientation of Photoelectrons Ejected by Circularly Polarized Light*, Physical Review A 178 (1) (1969) p. 131–136.

[220] C. Schneider, *Soft X-ray Photoelectron Emission Microscopy (X-PEEM)*, in: Neutron and X-ray Spectroscopy, Springer, 2006, pp. 271–295.

[221] J. Stöhr, H. C. Siegmann, *Magnetism*, Springer Berlin Heidelberg, 2006.

[222] J. Feng, A. Scholl, *Photoemission Electron Microscopy (PEEM)*, in: Science of Microscopy, Springer New York, 2007, Ch. 9, pp. pp 657–695.

[223] A. Locatelli, E. Bauer, *Recent advances in chemical and magnetic imaging of surfaces and interfaces by XPEEM*, Journal of Physics: Condensed Matter 20 (9) (2008) p. 093002.

[224] G. Schönhense, *Imaging of magnetic structures by photoemission electron microscopy This*, Journal of Physics: Condensed Matter 11 (1999) p. 9517–9547.

[225] E. Bauer, *A brief history of PEEM*, Journal of Electron Spectroscopy and Related Phenomena 185 (10) (2012) p. 314–322.

[226] S. A. Nepijko, N. N. Sedov, G. Schönhense, *Measurement of magnetic fields and domain structures using a photoemission electron microscope*, in: P. W. Hawkes (Ed.), Advances in Imaging and Electron Physics, Vol. 113 of *Advances in Imaging and Electron Physics*, Elsevier, 2000, pp. 205–248.

[227] R. Nakajima, J. Stöhr, Y. Idzerda, *Electron-yield saturation effects in L-edge x-ray magnetic circular dichroism spectra of Fe, Co, and Ni*, Physical Review B 59 (1999) p. 6421.

[228] S. Heun, Y. Watanabe, *Photoelectron Spectroscopy with a Photoemission Electron Microscope*, in: Nanoscale Spectroscopy and Its Applications to Semiconductor Research, Springer, 2002, pp. 157–171.

[229] D. Neeb, A. Krasyuk, A. Oelsner, S. a. Nepijko, H. J. Elmers, A. Kuksov, C. M. Schneider, G. Schönhense, *Sub-nanosecond resolution x-ray magnetic circular dichroism photoemission electron microscopy of magnetization processes in a permalloy ring*, Journal of Physics: Condensed Matter 17 (16) (2005) p. S1381–S1395.

[230] M. K. Marcham, *Phase-Resolved Ferromagnetic Resonance Studies of Thin Film Ferromagnets*, Ph.D. thesis, Exeter (2012).

[231] C. M. Schneider, *From Magnetodynamics to Spin Dynamics in Magnetic Heterosystems*, in: Nanostructured Materials for Magnetoelectronics, Springer Berlin Heidelberg, 2013, pp. 1–23.

[232] G. Schönhense, *Surface magnetism studied by photoelectron spectromicroscopy with high spatial and time resolution*, Journal of Electron Spectroscopy and Related Phenomena 137140 (0) (2004) p. 769–783.

[233] C. M. Schneider, A. Krasyuk, S. A. Nepijko, A. Oelsner, G. Schönhense, *Accessing fast magnetization dynamics by XPEEM: Status and perspectives*, Journal of Magnetism and Magnetic Materials 304 (1) (2006) p. 6–9.

[234] T. H. Schmidt, U. Groh, R. Fink, E. Umbach, O. Sschaff, W. Engel, B. Richter, H. Kuhlenbeck, R. Schlogl, H.-J. Freund, A. M. Bradshaw, D. Preikszas, P. Hartel, R. Spehr, H. Rose, G. Lilienkamp, E. Bauer, G. Benner, *XPEEM with energy-filtering: Advantages and first results from SMART project*, Surface Review and Letters 09 (01) (2002) p. 223–232.

[235] R. Fink, M. R. Weiss, E. Umbach, D. Preikszas, H. Rose, R. Spehr, P. Hartel, W. Engel, R. Degenhardt, R. Wichtendahl, H. Kuhlenbeck, W. Erlebach, K. Ihmann, R. Schlögl, H.-J. Freund, A. M. Bradshaw, G. Lilienkamp, T. Schmidt, E. Bauer, G. Benner, *SMART: a planned ultrahigh-resolution spectromicroscope for BESSY II*, Journal of Electron Spectroscopy and Related Phenomena 84 (13) (1997) p. 231–250.

[236] J. Feng, E. Forest, a. a. MacDowell, M. Marcus, H. Padmore, S. Raoux, D. Robin, A. Scholl, R. Schlueter, P. Schmid, J. Stöhr, W. Wan, D. H. Wei, Y. Wu, *An x-ray photoemission electron microscope using an electron mirror aberration corrector for the study of complex materials*, Journal of Physics: Condensed Matter 17 (16) (2005) p. S1339–S1350.

[237] G. Schmahl, D. Rudolph, B. Niemann, O. Christ, *Zone-plate X-ray microscopy*, Quarterly Reviews of Biophysics 13 (03) (1980) p. 297–315.

[238] W. Chao, B. D. Harteneck, J. A. Liddle, E. H. Anderson, D. T. Attwood, *Soft X-ray microscopy at a spatial resolution better than 15 nm.*, Nature 435 (7046) (2005) p. 1210–3.

[239] D. T. Attwood, *Soft X-Rays and Extreme Ultraviolet Radiation: Principles and Applications*, 1st Edition, Cambridge University Press, 1999.

[240] T. Eimüller, T. C. Ulbrich, E. Amaladass, I. L. Guhr, T. Tyliszczak, M. Albrecht, *Spin-reorientation transition in CoPt multilayers on nanospheres*, Phys. Rev. B 77 (13) (2008) p. 134415.

[241] J. Kirz, C. Jacobsen, M. Howells, *Soft X-ray microscopes and their biological applications*, Quarterly Reviews of Biophysics 28 (01) (1995) p. 33–130.

[242] G. Schmahl, D. Rudolph, B. Niemann, J. P. Thieme, G. Schneider, *Röntgenmikroskopie (x-ray microscopy)*, Naturwissenschaften 83 (1996) p. 61 – 70.

[243] P. Fischer, T. Eim, G. Sch, G. Denbeaux, *Imaging Magnetic Domain Structures with Soft X-Ray Microscopy*, Structural Chemistry 14 (1) (2003) p. 39–47.

[244] J. C. Andrews, S. Brennan, P. Pianetta, H. Ishii, J. Gelb, M. Feser, J. Rudati, A. Tkachuk, W. Yun, *Full-field transmission x-ray microscopy at SSRL*, Journal of Physics: Conference Series 186 (2009) p. 012002.

[245] C. Jacobsen, S. Williams, E. Anderson, M. T. Browne, C. J. Buckley, D. Kern, J. Kirz, M. Rivers, X. Zhang, *Diffraction-limited imaging in a scanning transmission x-ray microscope*, Optics Communications 86 (34) (1991) p. 351–364.

[246] C. Jacobsen, J. Kirz, S. Williams, *Resolution in soft X-ray microscopes*, Ultramicroscopy 47 (13) (1992) p. 55–79.

[247] H. Stoll, A. Puzic, B. van Waeyenberge, P. Fischer, J. Raabe, M. Buess, T. Haug, R. Höllinger, C. Back, D. Weiss, G. Denbeaux, *High-resolution imaging of fast magnetization dynamics in magnetic nanostructures*, Applied Physics Letters 84 (17).

[248] S. Kasai, P. Fischer, M.-Y. Im, K. Yamada, Y. Nakatani, K. Kobayashi, H. Kohno, T. Ono, *Probing the Spin Polarization of Current by Soft X-Ray Imaging of Current-Induced Magnetic Vortex Dynamics*, Physical Review Letters 101 (23) (2008) p. 1–4.

[249] A. Puzic, B. Van Waeyenberge, K. W. Chou, P. Fischer, H. Stoll, G. Schütz, T. Tyliszczak, K. Rott, H. Brückl, G. Reiss, I. Neudecker, T. Haug, M. Buess, C. H. Back, *Spatially resolved ferromagnetic resonance: Imaging of ferromagnetic eigenmodes*, Journal of Applied Physics 97 (10) (2005) p. 10E704.

[250] P. Fischer, M.-Y. Im, *Imaging Nanoscale Magnetic Structures With Polarized Soft X-Ray Photons*, IEEE PHOTONICS JOURNAL 2 (2) (2010) p. 260–264.

[251] J.-S. Kim, M.-A. Mawass, A. Bisig, B. Krüger, R. M. Reeve, T. Schulz, F. Büttner, J. Yoon, C.-Y. You, M. Weigand, H. Stoll, G. Schütz, H. J. M. Swagten, B. Koopmans, S. Eisebitt, M. Kläui, *Synchronous precessional motion of multiple domain walls in a ferromagnetic nanowire by perpendicular field pulses.*, Nature communications 5 (2014) p. 3429.

[252] P. A. Sloan, *Time-resolved scanning tunnelling microscopy for molecular science.*, Journal of physics. Condensed matter : an Institute of Physics journal 22 (26) (2010) p. 264001.

[253] A. Furube, Y. Tamaki, R. Katoh, *Time-Resolution Estimation of a Femtosecond Time-Resolved SNOM Having an Apertured Cantilever Tip*, Journal of the Korean Society 47 (August) (2005) p. 76–79.

[254] B. T. Thole, P. Carra, F. Sette, G. van der Laan, *X-ray circular dichroism as a probe of orbital magnetization*, Phys. Rev. Lett. 68 (12) (1992) p. 1943–1946.

[255] P. Carra, B. T. Thole, M. Altarelli, X. Wang, *X-ray circular dichroism and local magnetic fields*, Phys. Rev. Lett. 70 (5) (1993) p. 694–697.

[256] J. Stöhr, H. König, *Determination of Spin- and Orbital-Moment Anisotropies in Transition Metals by Angle-Dependent X-Ray Magnetic Circular Dichroism*, Phys. Rev. Lett. 75 (20) (1995) p. 3748–3751.

[257] J. Stöhr, *Exploring the microscopic origin of magnetic anisotropies with X-ray magnetic circular dichroism (XMCD) spectroscopy*, Journal of magnetism and magnetic materials 200 (1999) p. 470–497.

[258] Silson Ltd., *personal communications* (2010).

[259] A. Einstein, *Strahlungs-Emission und Absorption nach der Quantentheorie*, Deutsche Physikalische Gesellschaft 18 (1916) p. 318–323.

[260] CVI Melles-Griot, *Melles-Griot LGX1 Product Catalog.*
`www.cvimellesgriot.com`

[261] Orazio Svelto, *Principles of Lasers*, 5th Edition, Springer, 2010.

[262] M. Born, E. Wolf, *Principles of Optics*, 7th Edition, Cambridge University Press, 1999.

[263] R. N. Bracewell, *The Fourier Tansform and Its Applications*, 3rd Edition, McGraw-Hill, 1999.

[264] J. W. Goodman, *Introduction to Fourier Optics*, 2nd Edition, McGraw-Hill, 1996.

[265] G. W. Stroke, *An Introduction to Coherent Optics and Holography*, 2nd Edition, Academic Press Inc., 1969.

[266] H. He, M. Howells, S. Marchesini, H. N. Chapman, U. Weierstall, H. A. Padmore, J. C. H. Spence, *Use of extended and prepared reference objects in experimental Fourier transform X-ray holography*, Applied Physics Letters 85 (13) (2004) p. 2454–2456.

[267] B. Enders, K. Giewekemeyer, T. Kurz, S. Podorov, T. Salditt, *Non-iterative coherent diffractive imaging using a phase-shifting reference frame*, New Journal of Physics 11 (4) (2009) p. 043021.

[268] P. M. Platzman, N. Tzoar, *Magnetic Scattering of X Rays from Electrons in Molecules and Solids*, Physical Review B 2 (9) (1970) p. 3556–3559.

[269] F. de Bergevin, M. Brunell, *Diffraction of X-rays by magnetic materials. I. General formulae and measurements on ferro- and ferrimagnetic compounds*, Acta Crystallographica Section A 37 (3) (1981) p. 314–324.

[270] D. Gibbs, D. R. Harshman, E. D. Isaacs, D. B. McWhan, D. Mills, C. Vettier, *Polarization and Resonance Properties of Magnetic X-Ray Scattering in Holmium*, Physical Review Letters 61 (10) (1988) p. 1241–1244.

[271] J. D. J. Ingle, S. R. Crouch, *Spectrochemical Analysis*, Prentice Hall, 1988.

[272] J. P. Hannon, G. T. Trammell, M. Blume, D. Gibbs, *X-ray Resonance Exchange Scattering*, Physical review letters 61 (10) (1988) p. 1245–1248.

[273] A. P. Hitchcock, K. P. Lam, S. Kalirai, Y. Mozharivskj, V. Svitlyk, K. Harding, J. Wang, *Nanoscale Magnetism Studied with Soft X-ray Spectromicroscopy*, La Physique au Canada 67 (1) (2011) p. 7–10.

[274] W. F. Schlotter, *Lensless Fourier Transfrom Holography With Soft X-rays*, Ph.D. thesis, Stanford (2007).

[275] Princeton Instruments, *Glossary of Terms* (2013).
`http://www.princetoninstruments.com`

[276] J. T. Winthrop, C. R. Worthington, *X-ray microscopy by successive Fourier transformation*, Physical review letters 15 (1965) p. 124.

[277] E. Guehrs, A. M. Stadler, S. Flewett, S. Frömmel, J. Geilhufe, B. Pfau, T. Rander, S. Schaffert, G. Büldt, S. Eisebitt, *Soft x-ray tomoholography*, New Journal of Physics 14 (1) (2012) p. 013022.

[278] A. C. Kak, S. Malcolm, *Algorithms for Reconstruction with Nondiffracting Sources*, in: Principles of Computerized Tomographic Imaging, No. 1, IEEE Press, 1988, p. 49.

[279] *The Center for X-Ray Optics* (2013).
`http://www.cxro.lbl.gov/`

[280] S. Roy, D. Parks, K. A. Seu, R. Su, J. J. Turner, W. Chao, E. H. Anderson, S. Cabrini, S. D. Kevan, *Lensless X-ray imaging in reflection geometry*, Nature Photonics Letters 5 (4) (2011) p. 243–245.

[281] Diamond Light Source, *IO6 - Branch line* (2013).
`http://www.diamond.ac.uk/Home/Beamlines/I06/branch.html`

[282] V. Ziebart, O. Paul, H. Baltes, *Strongly buckled square micromachined membranes*, Journal of Microelectromechanical Systems 8 (4) (1999) p. 423–432.

[283] S. Hashimoto, Y. Ochiai, *Co/Pt and Co/Pd multilayers as magneto-optical recording materials*, Journal of Magnetism and Magnetic Materials 88 (1-2) (1990) p. 211–226.

[284] S. B. Choe, Y. Acremann, A. Scholl, A. Bauer, A. Doran, J. Stöhr, H. a. Padmore, *Vortex core-driven magnetization dynamics.*, Science (New York, N.Y.) 304 (5669) (2004) p. 420–2.

[285] Y. Lynn, *New Phenomenon in Nanodisk Magnetic Vortices* (2012). `http://newscenter.lbl.gov`

[286] T. Shinjo, T. Okuno, R. Hassdorf, K. Shigeto, T. Ono, *Magnetic vortex core observation in circular dots of permalloy*, Science (New York, N.Y.) 289 (5481) (2000) p. 930–932.

[287] J. Geilhufe, B. Pfau, M. Schneider, F. Büttner, C. M. Günther, S. Werner, S. Schaffert, E. Guehrs, S. Frömmel, M. Kläui, S. Eisebitt, *Monolithic focused reference beam X-ray holography.*, Nature communications 5 (2014) p. 3008.

[288] M. K. Marcham, P. S. Keatley, A. Neudert, R. J. Hicken, S. a. Cavill, L. R. Shelford, G. van der Laan, N. D. Telling, J. R. Childress, J. a. Katine, P. Shafer, E. Arenholz, *Phase-resolved x-ray ferromagnetic resonance measurements in fluorescence yield*, Journal of Applied Physics 109 (7) (2011) p. 07D353.

[289] B. Van Waeyenberge, A. Puzic, H. Stoll, K. W. Chou, T. Tyliszczak, R. Hertel, M. Fähnle, H. Brückl, K. Rott, G. Reiss, I. Neudecker, D. Weiss, C. H. Back, G. Schütz, *Magnetic vortex core reversal by excitation with short bursts of an alternating field.*, Nature 444 (7118) (2006) p. 461–4.

[290] A. Vansteenkiste, K. W. Chou, M. Weigand, M. Curcic, V. Sackmann, H. Stoll, T. Tyliszczak, G. Woltersdorf, C. H. Back, G. Schütz, B. Van Waeyenberge, *X-ray imaging of the dynamic magnetic vortex core deformation*, Nature Physics 5 (5) (2009) p. 332–334.

[291] A. Vansteenkiste, J. De Baerdemaeker, K. Chou, H. Stoll, M. Curcic, T. Tyliszczak, G. Woltersdorf, C. Back, G. Schütz, B. Van Waeyenberge, *Influence of domain wall pinning on the dynamic behavior of magnetic vortex structures: Time-resolved scanning x-ray transmission microscopy in NiFe thin film structures*, Physical Review B 77 (14) (2008) p. 144420.

[292] G. Beutier, *E TUDE DE NANOSTRUCTURES MAGNÉTIQUES PAR DIFFRACTION RÉSONANTE ET COHÉRENTE DES RAYONS X MOUS*, Ph.D. thesis, Doctoral School of Physics, Grenoble (2005).